The Twin-Probe Method: Improving the Accuracy of Langmuir Probes on Small Spacecraft

by

Omar Jesus Leon

A dissertation submitted in partial fulfillment
of the requirements for the degree of
Doctor of Philosophy
(Applied Physics)
in the University of Michigan
2020

Doctoral Committee:

Professor Brian E. Gilchrist, Chair
Professor John E. Foster
Dr. Linda H. Krause, NASA Marshall Space Flight Center
Professor Mark J. Kushner
Jason A. Vaughn, NASA Marshall Space Flight Center

Omar Jesus Leon

omarleon@umich.edu

ORCID iD: 0000-0002-2370-2991

This dissertation is in honor of everyone who has helped me along my academic journey and helped me reach this point in my academic career.

To my parents, Margarita Puentes, Jesus León, and Francisco Ales, who raised me to be studious and encouraged my scientific endeavors.

To Pierre Avila and Emily McGehee for their close friendships and long hours of conversation during both the best and worst of times.

To the Dance Revolution community, a wonderfully supportive group of dancers; especially to Laura Geldys for her infectious passion for dancing; and to Guadalupe Madrigal, Irene Vargas Salazar, and Alex Escobar for their endless patience and sense of adventure.

ACKNOWLEDGMENTS

I feel very fortunate to have the opportunity to acknowledge so many amazing people whom I've had the pleasure of knowing throughout my academic career. Research is not an endeavor undertaken by a single person. It is a collaborative venture with many components and moving pieces. Each person's contribution goes toward improving humanity bit by bit.

First and foremost, I would like to thank my advisor, Professor Brian E. Gilchrist, whose experience and dedication to his students gave me every opportunity to grow as a scientist. I could probably write a second thesis on everything Brian has taught me, but I feel it's best to just list the top three lessons: First, while it's important for a team to be productive and efficient, the well-being of the team members is more important. Second, words matter; choose them wisely. And third, you can get a PhD on three seconds of data.

I would also like to thank each and every member of my dissertation committee. Dr. Linda Krause was my first research host at NASA Marshall Space Flight Center (MSFC) and introduced me to the NASA/Air Force Spacecraft Charging Analyzer Program (NASCAP-2K), a program fundamental to my research. Her attention to detail and natural curiosity greatly elevated the quality of my research. Any project with which she is involved is guaranteed to pose interesting and fundamental questions that expand the forefront of science and technology. Jason Vaughn was my NASA mentor and host to a series of experiment campaigns at NASA MSFC that are integral to my graduate career. During our four-year collaborative effort, Jason's tremendous experience in ground chamber tests and space environmental effects helped ensure the campaign's focus on the proper measurements, questions, and implementation.

Professor Mark Kushner was one of my first instructors at the University of Michigan and introduced me to the Michigan Institute for Plasma Science and Engineering (MIPSE). His systems-level approach to solving problems has given me a deeper, more complete understanding of plasma physics through his precise inquiry. Finally, Professor John Foster provided me with the opportunity to perform many plasma physics experiments that I would not have had the chance to perform otherwise. His varied research interests highlighted the interdisciplinary nature of plasmas, and his excitement for new plasma applications provided plenty of motivation and assurance that I was on the right path.

I must also recognize the extraordinary efforts of Grant Miars. Grant and I began our graduate careers in the same year and worked closely on multiple experiment campaigns and proposals. We have traveled the world together, visiting two continents and three countries. There were many times during our graduate student careers where we would go through a ”100-hour workweek,” and without a doubt in my mind, those weeks were made much easier because we did them together. We definitely earned the title, ”Gromar,” in those early years. Grant unsurprisingly defended his dissertation successfully, and he is well on his way to perform many more noteworthy feats in his career.

I'd also like to take a moment to recognize many others in the space plasma community. Dr. Walter Hoegy and I have collaborated for many years and co-created the Plasma Spacecraft Interaction Codes for Low Earth Orbit (PSIC-LEO) to better understand spacecraft charging effects on Langmuir probe operation. Dr. David Cooke, Dr. Iverson Bell, Dr. Gian Luca Delzanno, Dr. Sven Bilén, Dr. Keiichi Ogasawara, and Dr. John Williams have all provided either software, hardware, and/or support- not to mention the many riveting hours of conversation I've had with each of them. Dr. David Cooke in particular provided much needed NASCAP-2K technical support that greatly improved simulation accuracy and provided a path for future modeling studies. Dr. Iverson Bell trained Grant and me on many important skills necessary for a graduate student, including experimental methods, publication timeline, and bureaucratic protocol.

Dr. Bell also introduced us to the Plasmadynamics and Electric Propulsion Laboratory (PEPL) where Grant and I performed some of our first experiments. From PEPL, I would like to thank Dr. Scott Hall, Dr. Tim Collard, Dr. Ethan Dale, Dr. Sarah Cusson, Dr. Marcel Georgin, Ben Wachs, Eric Viges, and Dr. JP Sheehan. Every member of PEPL has shown me many facets of plasma applications beyond my own, and it was a joy to interact with everybody in and out of the lab.

It is because of Dr. Bell, that the MiTEE satellite mission exists. Through MiTEE I became familiar with the process of developing and building a satellite. My involvement in MiTEE was often made difficult because my own research pulled me to other states, and I am very grateful to the many undergraduate and master's students that have worked on MiTEE. I want to thank Derek Cheyne and Thomas von Bibra for their work on the hardware and testing of the Langmuir probe. I've had the pleasure of witnessing Derek's growth as a scientist and engineer as he transitioned from working on the Langmuir probe deployer to leading troubleshooting efforts during MiTEE's day-in-the-life testing. I'd also like to thank Yuchen Liu for programming and troubleshooting the Langmuir probe FPGA, and Allison Hancock for leading the charge on the finalization of the MITEE software, a herculean task made even more difficult by recent pandemic protocols. Additionally, the University of Michigan's Space Physics Research Laboratory (SPRL) provided immeasurable support, and I'd like to recognize the efforts of Curt Cooper, Bradley Angelocci, and Bret Bronner for their aide and expertise with MiTEE's Langmuir probe.

During my research at NASA MSFC, I had the pleasure of working with Jason Vaughn, Dr. Linda Krause, Todd Schneider, Dr. Kenneth Wright, Dr. Jesse McTernan, and many others. Todd Schneider was always available to provide technical support, and without him I'd still be trying to find everything at the MSFC laboratory. His assistance greatly expedited and streamlined the experiment campaign.

I'd like to give a special thanks to Dr. McTernan, whose compassion left a lasting impression. During my time at NASA MSFC, Dr. McTernan and I worked in the same vacuum chamber on synergistic projects. Outside of the laboratory, he welcomed me into his home, gave me a seat at his table, and invited me to share meals with his wonderful family. I wish many blessings to Dr. McTernan and his family; I'm forever grateful for their generosity and warmth.

The University of Michigan Applied Physics program has been incredibly supportive and provided a great space for collaboration and connection. Dr. Cagliyan Kurdak, Lauren Segall, and Cynthia McNabb all work tirelessly to ensure Applied Physics students feel heard and have the best opportunity for success in their graduate studies. On more than one occasion, they reached out to me of their own accord and offered support when natural disasters could have potentially affected my family or me. Additionally, I met and studied with many brilliant minds in the Applied Physics program, including Dr. Catherine Ayuso, Dr. Justin Easley, Joseph Iafrite, Robert W VanDervort, Dr. Paul Cambell, Dr. Marcel Georgin, Morgan Whitcomb, and many others. I would be remiss if I didn't individually thank Dr. Justin Easley and Ashley Jackson. We met in the summer of 2014 and have spent countless hours together since then. We studied together, ran many grueling miles together, looked after each other's homes, and shared endless laughs. I look forward to when we are all in the same region again. Thank you dearly for your friendship, company, and for being my first family in Michigan.

My academic journey did not begin with the University of Michigan, and so I want to thank many people who helped me and worked with me as an undergraduate student at Florida International University (FIU). I want to extend a special thanks to Dean Juan Carlos Espinosa, Professor Werner Boeglin, Dr. Ramona Valenzuela Perez, David Jones, Dr. Rafael A. Badui, Adrianna Angulo, Carlos Lopez, Daniela Blagoeva, Douglas Laurence, Lauren Perez, and Pierre Avila. In particular, I'd like to recognize the mentorships of Dean Juan Carlos Espinosa, Professor Werner Boeglin, David Jones,

and Dr. Ramona Valenzuela Perez; I hope to one day give back to others like they have given to me.

I want to recognize the invaluable assistance of all of those who proofread this dissertation: Amanda Webster, Professor Brian Gilchrist, Emily McGehee, Grant Miars, Dr. Justin Easley, Lauren Perez, and Pierre Avila. Special recognition must be made for Amanda Webster who graciously edited the majority of the dissertation for grammar and spelling. This dissertation is made all the better with their proofing skills and endless support.

Finally, I want to recognize the many funding sources that made my research possible. This research was funded by a NASA Space Technology Research Fellowship, Grant NNX16AM62H. It was through NASA that I was able to attend many conferences, perform cutting-edge research, and present my work to members of Congress. Additionally, support was provided by MIPSE and the University of Michigan's Horace H. Rackham School of Graduate Studies. My first source of funding was through the University of Michigan Applied Physics Imes-Moore Fellows Program, which was a pivotal funding source in my early years as a graduate student.

TABLE OF CONTENTS

DEDICATION . . . . **ii**

ACKNOWLEDGMENTS . . . . **iii**

LIST OF FIGURES . . . . **x**

LIST OF TABLES . . . . **xvii**

LIST OF APPENDICES . . . . **xviii**

LIST OF ABBREVIATIONS . . . . **xix**

LIST OF SYMBOLS . . . . **xx**

ABSTRACT . . . . **xxii**

CHAPTER

1 Introduction **1**

- 1.1 Research Motivation 1
- 1.2 Basic Properties of a Plasma 3
- 1.3 Langmuir Probe as a Plasma Diagnostic Tool in Space 5
  - 1.3.1 Langmuir Probes in Space: A Brief Overview 8
  - 1.3.2 The Spacecraft to Probe Conductive Surface Area Ratio Problem 10
  - 1.3.3 Attempts at Resolving the Issue 16
  - 1.3.4 Problem Statement 18
- 1.4 Dissertation Overview 19

2 Ionospheric Plasmas and Langmuir Probe Theory **21**

- 2.1 Representative Structure of Planetary Ionospheres 21
  - 2.1.1 Earth's Ionosphere 23
  - 2.1.2 Venus' Ionosphere 26
  - 2.1.3 Mars' Ionosphere 27
- 2.2 Plasma Current Collection to a Planar Surface 28
- 2.3 Cylindrical Probe Current Collection 32
  - 2.3.1 Electron Current Collection 35
  - 2.3.2 Ion Current Collection 37
- 2.4 Sources of Error 40
  - 2.4.1 Photoelectrons 40

2.4.2 Secondary Electrons 41
2.4.3 Auroral Precipitation 42
2.4.4 Electromotive Force 43
2.4.5 Work Function 44
2.4.6 Transient Effects 45
2.4.7 Probe End Effects 46

3 The Twin-Probe Method 47

3.1 Formulation of the Twin-Probe Method 47
3.2 Implementation Considerations 52
3.2.1 Sheath Expansion 52
3.2.2 RC Time Constant 54
3.3 Calibrating for Additional Current Sources 56
3.3.1 Photoelectrons 56
3.3.2 High Impedance Probe Floating Potential 58
3.3.3 High-Impedance Measured with Variable Angle of Attack 58
3.3.4 Work Function 59

4 Plasma Spacecraft Interaction Codes for Low Earth Orbit: Twin-Probe Method Modeling using Analytic Methods 61

4.1 General Procedure and Assumptions 62
4.2 Object Current Collection 64
4.2.1 Langmuir Probe Current Collection 64
4.2.2 CubeSat Current Collection 65
4.3 Spacecraft Charging Behavior and its Effects on Langmuir Probe I-V Curves 66
4.3.1 Spacecraft Charging Impact on Electron Temperature Measurements 71
4.3.2 Spacecraft Charging Impact on Electron Density Measurements . 73
4.4 Twin-Probe Correction Analysis 75
4.4.1 Accuracy of Twin-Probe Correction for Electron Temperature Measurements 76
4.4.2 Accuracy of Twin-Probe Correction for Electron Density Measurements 77
4.4.3 Magnitude of Twin-Probe Correction 79
4.4.4 Importance of Proper Input Resistance for Accurate Tracking of Spacecraft Potential 81

5 Experiments 84

5.1 Experiment Description 84
5.1.1 Chamber and Plasma Source 84
5.1.2 Notional CubeSat and Instrumentation 87
5.1.3 Twin-Probe Method Setup 88
5.2 Hollow Cathode Plume Homogeneity and Controls 90
5.3 Results 94

5.3.1 Spacecraft Charging 95
5.3.2 Plasma Plume Ions 106
5.3.3 Electron Energy Distribution Function 116
5.3.4 Electron Temperature 117
5.3.5 Electron Density 122
5.4 Comparing PSIC-LEO Model to Experiment Results 127

6 Applications and System Level Design 131

6.1 Interpretation of Simulation and Experiment Results 131
6.2 Optimal System Design for Small Spacecraft 135
6.3 Applications for Future Missions 141
6.3.1 CODEX 141
6.3.2 MiTEE-I and MiTEE-II 143

7 Summary, Future Work, and Conclusion 146

7.1 Summary of Research 147
7.2 Recommendations for Future Work 149
7.2.1 Improvements to PSIC-LEO Codes 150
7.3 Conclusion 150

BIBLIOGRAPHY 152

APPENDICES 169

LIST OF FIGURES

1.1 Examples of different common Langmuir probe geometries. 5
1.2 Example of a Langmuir probe current voltage relationship. 7
1.3 Symmetric double probe circuit comprised of identical, cylindrical Langmuir probes. 10
1.4 Modeled potentials of each probe in a symmetric double probe as a function of the applied bias between the two probes. 12
1.5 Asymmetric double probe configuration comprised of a Langmuir probe and spacecraft. 13
1.6 Experimentally measured potentials of the spacecraft and Langmuir probe in an asymmetric double probe configuration as a function of the applied bias between the two probes. 15
1.7 Comparison of charging effects on I-V characteristics for small and large area ratios. 16

2.1 Energy exchanges between neutral and charged particles in an ionosphere. . . . 22
2.2 Ion, electron, and neutral particle densities in the ionosphere as a function of altitude. 23
2.3 Ion, electron, and neutral particle temperatures in the ionosphere as a function of altitude. The solid lines correspond to measurements during solar minimum and the dashed lines correspond to measurements during solar maximum. . . . 24
2.4 Daytime ion densities at Venus. 26
2.5 Electron temperature measurements of Venus at solar cycle maximum electron temperatures as a function of zenith angle. 27
2.6 Chemistry of ions in both the Venusian and Martian ionospheres. 28
2.7 Calculated and measured day side ion density profiles at Mars. 28
2.8 Components of particle velocity relative to planar surface. 29
2.9 Normalized electron currents collected by a planar surface as a function of potential relative to the ambient plasma. 30
2.10 Normalized ion currents collected by a planar probe as a function of potential relative to the ambient plasma. 32
2.11 Approximate charged particle trajectories for: (a) thin sheath collection and (b) thick sheath collection. 33
2.12 Varying coaxial sheaths sizes surrounding a cylindrical Langmuir probe of constant size. There are 3 sheath categories (denoted by dotted lines) considered based on the ratio of sheath radius to probe radius: thin sheath, transitional sheath, thick sheath. Relative sheath sizes are not to scale. 33

2.13 Components of particle velocity in cylindrical coordinates. 34
2.14 Normalize electron current collected by a cylindrical probe as a function of potential relative to the ambient plasma. 36
2.15 Normalized ion current collected by a cylindrical probe as a function of potential relative to the ambient plasma. 39
2.16 Illustration of charge effects due to photoelectrons. Side (a) presents a negatively charged conductor without the presence of solar photons. Side (b) presents a positively charged conductor due to solar radiation. 41
2.17 SEY curves from electron impact. 42
2.18 Particle precipitation from the Earth's magnetosphere. Auroral precipitation originates from magnetic reconnection. 43
2.19 a) Effective circuit for work function variation due to surface contaminants. b) Hysteresis effects on I-V curve due to contaminants. 45

3.1 Example of measured I-V curve correction using the twin-probe method. The red bundle of solid dots corresponds to sweeps referenced against the spacecraft. The blue bundle of solid lines are sweeps corrected using the twin-probe method, and the single black line of circles is a control sweep referenced against the chamber. 48
3.2 General schematic of depicting current flow between the LP, spacecraft, high-impedance probe, and the ambient plasma. 49
3.3 Diagrams of spacecraft's charging response to positive and negative applied biases to an LP. 51
3.4 Sheath thickness as a function of negative spacecraft voltage and plasma density. The sheath thickness becomes increasingly large with decreasing plasma density. 53
3.5 General circuit for a high-impedance probe. 54
3.6 Comparing current collection difference between a sunlit and shadowed probe in a low-density plasma. 57
3.7 Modeled floating potential of a cylindrical probe for various angles relative to the plasma flow. $0°$ corresponds to a probe oriented parallel to the plasma flow and $90°$ represents a probe oriented perpendicular to the plasma flow. 59

4.1 Spacecraft potential (blue) and LP potential (red) with respect to the ambient plasma. For small enough area ratios, the LP potential does not reach the plasma potential. 67
4.2 Calculated potentials with respect to the plasma. 67
4.3 Example I-V curve and derivative for a Langmuir probe that does not reach the plasma potential. The x-axis is the applied potential between the LP and spacecraft and so the LP potential relative to the plasma is not shown (this is similar to LP operations without a twin-probe system). 68
4.4 Plasma potential percent error estimates of uncorrected I-V sweeps. For area ratios of 60 and below, the spacecraft greatly impacts the I-V curve leading to incorrect identification of the plasma potential. 69

4.5 Percent change between spacecraft potential relative to the plasma at different applied biases to the LP and the spacecraft's floating potential. LP V_F corresponds to the applied bias when the LP is at its floating potential, LP V_P is the applied bias when the LP is at the plasma potential, $V_A = 0V$ corresponds to an applied bias of $0\,\mathrm{V}$, and $V_A = 10V$ corresponds to an applied bias of $10\,\mathrm{V}$. The top figure has all four biases and the bottom figure considers all of the biases except LP V_P. 70
4.6 Deviation of uncorrected measurements from modeled electron temperature. . 72
4.7 Semilog linearization of the electron current at different area ratios. The electron currents were individually normalized by their respective minimum value and the potentials of the uncorrected current were shifted to start at the same position as the modeled current. 72
4.8 Percent error of single point methods for estimating of the electron density. The negative percent error indicates an underestimation. 73
4.9 Percent error of electron density calculated using the OML fit method. 74
4.10 Linearized electron saturation regime by squaring the currents. The electron currents were individually normalized by their respective minimum value and the potentials of the uncorrected current were shifted to start at the same position as the modeled current. 74
4.11 Modeled twin-probe corrected Langmuir probe sweeps. 76
4.12 Electron temperature percent error estimates of twin-probe corrected sweeps. . 77
4.13 Electron density percent error estimates of twin-probe corrected I-V sweeps using the thermal current method. 78
4.14 Details on the electron saturation regime probed by corrected sweeps. 78
4.15 Percent error of twin-probe corrected electron density measurements using the OML methods. 79
4.16 Magnitude of twin-probe correction of electron temperature when compared to uncorrected measurements. 80
4.17 Magnitude of twin-probe correction of electron density measurements when compared to uncorrected measurements. 81
4.18 Percent error estimates of twin-probe corrected I-V sweeps when the correction is accomplished using the modeled ”measured” spacecraft potential instead of the calculated spacecraft potential. 82
4.19 Effect of high-impedance input resistance on measured spacecraft potential. . . 82

5.1 NASA MSFC chamber description. 85
5.2 NASA MSFC chamber plasma source mechanical drawings and electrical schematic. 86
5.3 Internal structure of the CubeSat. The Teflon cubes in the corners and Kapton layers isolate the individual faces from each other. The RPA is mounted in the center of the CubeSat (top of the image). 87
5.4 The two configurations of the experiment are shown: a) an unmounted LP setup and b) a mounted LP setup. 89

5.5 Twin-probe circuitry for unmounted and mounted probe configurations. The high-impedance probe was isolated from the CubeSat using a $1\,\mathrm{G\Omega}$ sense resistor, Langmuir probe 1 in this configuration. 90
5.6 Ion and electron densities measured in representative plasma plume. 91
5.7 Representative electron temperature of plasma plume. Slight bias towards the north side of the plume. 92
5.8 Radial and axial ion velocities from hollow cathode source. 93
5.9 Floating potential map of the plasma plume for an unbiased and biased cathode. 93
5.10 This plot is an example of a properly implemented high-impedance measurement where all sweeps lie very close to one another. 95
5.11 The points represent the maximum negative potential for densities below $1 \times 10^{13}\,\mathrm{m}^{-3}$ where the SC potential becomes more positive as the area ratio increases. 96
5.12 Transient effects on spacecraft charging and ion density measurements. 98
5.13 Spacecraft charging behavior for two different elapsed times between sweeps. . 99
5.14 Transient effects observed at different plasma densities and area ratios. 100
5.15 Rotation about the CubeSat's Z-axis and Y-axis. 101
5.16 Twin-probe LP corrections as the CubeSat rotates about its Y-axis. The high-impedance probe changes its angle of attack relative to the ion drift velocity as the CubeSat rotates (sweeping probe remains in the same location and orientation). 102
5.17 Plasma potential of twin-probe corrected I-V curves indicate that the high-impedance probe's floating potential varies as the CubeSat rotates around its Y-axis. 102
5.18 Twin-probe LP corrections for a rotating CubeSat adjusted by their individual plasma potentials. The high-impedance probe changes its angle of attack relative to the ion drift velocity as the CubeSat rotates (sweeping probe remains in the same location and orientation). 103
5.19 Percent change between corrected and uncorrected plasma property estimates for a high-impedance probe that is perpendicular to the plasma flow, parallel to the flow in the spacecraft ram, and parallel to the plasma flow in the spacecraft wake. The area ratio is 482. 103
5.20 Maximum spacecraft potential induced by LP operation as the CubeSat rotates the high-impedance probe around its Y-axis. The high-impedance probe changes its angle of attack relative to the ion drift velocity as the CubeSat rotates (sweeping probe remains in the same location and orientation). 104
5.21 Twin-probe LP corrections as the CubeSat sweeping probe rotates around its Y-axis (high-impedance probe remains in the same location and orientation). All sweeps have been adjusted by their respective plasma potential; thus, $0\,\mathrm{V}$ corresponds to the measured plasma potential. 105
5.22 High-impedance measurements of spacecraft potentials as the CubeSat rotates around its Y-axis. The swept probe rotates with the CubeSat. 106
5.23 Ion energy distribution functions representing plasma plumes with no charge exchange ions and a significant charge exchange ion population. 108

5.24 Comparing chamber and satellite measurements ion current relative to angle of attack. 110
5.25 Ram and total ion current collection for differently sized ram direction areas for Z-axis ($0.13\,\mathrm{m}^2$ surface area) and Y-axis rotations ($0.11\,\mathrm{m}^2$ surface area). . 112
5.26 Ram and wake current collection for differently sized ram direction areas for Z-axis ($0.13\,\mathrm{m}^2$ surface area) and Y-axis rotations ($0.11\,\mathrm{m}^2$ surface area). . . . 113
5.27 Ion density measurements where only a single drifting ion population was present at the location of measurements. 115
5.28 Example electron energy distribution measurement of the plasma source at NASA MSFC. 116
5.29 The potential difference method uses the difference between the plasma and floating potential to estimate the electron temperature. 119
5.30 The integral method integrates the electron current between the floating and plasma potential. 119
5.31 Examples of log-linear analysis methods and results. 120
5.32 The plot presents the percent change in correction of temperature measurements as the area ratio is changed for densities between $1 \times 10^{12}\,\mathrm{m}^{-3}$ to $1 \times 10^{13}\,\mathrm{m}^{-3}$. 121
5.33 Plot of failed linearization of the electron current between each sweep's respective electron saturation regime due to small sheath-to-probe radius ratio. Each sweep has been normalized and the biases have been adjusted so they all begin at the same potential and the same arbitrary unit. 123
5.34 The thermal current method estimates the electron density from the current measured at the plasma potential. 124
5.35 The single point OML method estimates the electron density assuming the attractive potential dominates random thermal motion. The ion density is a constant value in this example. 125
5.36 Example of idea OML fit results and linearization. 126
5.37 The plot presents the percent change in correction of density measurements as the area ratio is changed for densities between $1 \times 10^{12}\,\mathrm{m}^{-3}$ to $1 \times 10^{13}\,\mathrm{m}^{-3}$. . 127
5.38 Measured spacecraft potential and Langmuir probe potential. The red line corresponds to Langmuir probe potentials and blue lines correspond to the spacecraft potential. 128
5.39 Measured spacecraft potential and Langmuir probe potential. The red line corresponds to Langmuir probe potentials and blue lines correspond to the spacecraft potential. 129

6.1 Ion energy in relation to ion density and spacecraft charging. 132
6.2 Example of the location of measurements used for thermal current and single point OML methods of determining electron density. 135
6.3 CAD representation of fully deployed CODEX satellite. 142

A.1 Example of simulated 3U CubeSat, guarded Langmuir probe, and boom structure. 171

A.2 Nested grid example surrounding an object composed of a CubeSat and Langmuir probe. 172
A.3 Gaussian pillboxes to calculate surface charges on insulators (in green) and on conductors (in blue). 174
A.4 Potential structure of quasi-neutral plasma and biased structures within simulation space. 176
A.5 General plasma properties are inputted in the LEO environment tab. 177
A.6 Problem tab of *Nascap-2K* that determines which properties are calculated. . . 179
A.7 Applied potentials tab of *Nascap-2K* that determines the initial surface potentials of the object. 180
A.8 Surface current subtab of the particles tab. 181
A.9 Particle generation advanced options window. 182
A.10 Time-dependent subtab of the particles tab. 183
A.11 Sheath size and shape variation with potential changes for the densest ionospheric plasma. v_i indicated the direction of the ion velocity, and the black outline provides a rough estimate of the sheath edge. 185
A.12 Sheath size and shape variation with potential changes for the sparsest ionospheric, F-region plasma. v_i indicated the direction of the ion velocity, and the black outline provides a rough estimate of the sheath edge. 186
A.13 Tracked oxygen particles around a 3U CubeSat object. 1 out of every 7 tracked macroparticle is shown. 188
A.14 Tracked hydrogen particles around a 3U CubeSat object. 1 out of every 7 macroparticles are shown. 188
A.15 Sheath size and shape variation with potential changes for the densest ionospheric plasma composed of various ratios of oxygen and hydrogen ions. . 189
A.16 Rotation about the CubeSat's Z-axis and Y-axis. Rotation arrows not necessarily indicative of true rotation. 190
A.17 Ion current collection dependence on Z-axis rotation. 191
A.18 Ion current collection dependence on Y-axis rotation. 192
A.19 Ion current collection by a scaled up 3U CubeSat for various potentials and ram surface areas. 193
A.20 Spacecraft charging behavior for the same probe operated from 1U, 2U, and 3U CubeSat reference. 195

C.1 Minimum uncertainty of the floating potential method. 213
C.2 Minimum uncertainties of plasma potential measurements using various methods. 215
C.3 Minimum uncertainty of the ion density using the single point approximation of the full ion current expression. 220
C.4 Minimum uncertainties of ion density measurements using a fit of the full ion current collection expression. 221
C.5 Minimum uncertainty of the dominant ion drift speed approximation. 223
C.6 Minimum uncertainty of the dominant accelerating potential approximation. . . 224
C.7 Minimum uncertainty of the electron current calculation using a linear ion current estimate. 226

C.8 Minimum uncertainty of the potential difference method in a stationary plasma. 228
C.9 Minimum uncertainty of the potential difference method in a flowing plasma. . 229
C.10 Minimum uncertainty of the integral method in a flowing plasma. 231
C.11 Linear fit to determine electron temperature example and estimate of step size required for proper fitting. 232
C.12 Minimum uncertainty of the single point method as a function of step size relative to electron temperature. 234
C.13 Minimum uncertainty of the EEDF fit method as a function of the ratio between the potential step size and electron temperature. 236
C.14 Minimum uncertainty of the thermal current method as a function of the ratio between the probe potential and electron temperature. 238
C.15 Linearizing electron saturation regime using natural logarithms. 240
C.16 Minimum uncertainty for estimating electron density using an OML approximation. 241
C.17 Minimum uncertainty of the EEDF integral point method as a function of the ratio between potential step size and electron temperature. 243

D.1 Retarding potential analyzer mechanical drawing. 245
D.2 Ideal I-V characteristics of RPA measurements of a single drifting ion species. 248
D.3 Minimum uncertainty of ion properties measured by an RPA when a single ion population is present. 250
D.4 Ideal I-V characteristics of RPA measurements of a drifting ion species and a smaller CEX ion population. 251
D.5 Minimum uncertainty of amplitude of distribution under various constraints. . 253
D.6 Minimum uncertainties of the properties of each ion energy distribution functions composed of $25\,\%$ CEX and $75\,\%$ main population. 254
D.7 Minimum uncertainties of the properties of each ion energy distribution functions composed of $50\,\%$ CEX and $50\,\%$ main population. 255

LIST OF TABLES

2.1 Temporal limits of LP slew rates based on ion sheath transit, ion sheath formation in a flowing plasma, and the resonance between probe potential and plasma oscillations for a range of possible densities found in the Earth's ionosphere. 46
2.2 Temporal limits of LP slew rates, in milliseconds, based on sheath capacitance for 3 voltage step sizes and a range of possible densities found in the Earth's ionosphere. 46
2.3 Temporal limits of LP slew rates, in milliseconds, based on stray capacitance for 3 voltage step sizes, and a range of possible densities found in the Earth's ionosphere, and a stray capacitance of $1\,\mathrm{pF}$. 46

3.1 Impedance probe potential errors and settling time constants relative to plasma density. 56

5.1 Range of plasma parameters measured during the experiment. 87
5.2 Range of plasma parameters for example measurement set. 94
5.3 Range of plasma parameters for measurement sets in fig. 5.11. 97
5.4 Range of parameters for measurement sets in fig. 5.14. 100
5.5 Range of parameters for measurement sets in figs. 5.25 and 5.26. 113

6.1 Example of various probe dimensions for a notional 3U CubeSat platform. Guard dimensions are included in the area ratio calculation; the guard length is $2.5 \times 10^{-2}\,\mathrm{m}$, and the guard diameter is equal to the probe diameter. 139
6.2 Estimated ion and electron currents to various LP dimensions and densities for notional 3U CubeSat system. Electron thermal current was calculated using eq. 2.10 and minimum ion drift current was calculated using eq. 2.19 for oxygen with $5\,\mathrm{eV}$ drift energy. 139
6.3 Impedance probe settling time constants relative to plasma density for MiTEE mission with a $10\,\mathrm{m}$. 145

A.1 Simulated ram and wake currents for various ion compositions. 187

LIST OF APPENDICES

A NASA/Air Force Spacecraft Charging Analyzer Program Modeling 169

B Plasma Spacecraft Interaction Codes for Low Earth Orbit Code 197

C Langmuir Probe Analysis with Uncertainties 211

D Retarding Potential Analyzer Analysis with Uncertainties 245

LIST OF ABBREVIATIONS

AE Atmospheric Explorer

BEM Boundary Element Method

EEDF electron energy distribution function

IEDF ion energy distribution function

I-V current-voltage

ISS International Space Station

FWHM full width half maximum

LEO low Earth orbit

LP Langmuir probe

m-NLP multi-Needle Langmuir probe

Nascap-2K NASA/Air Force Spacecraft Charging Analyzer Program

NASA MSFC NASA Marshall Space Flight Center

OML orbit motion limited

PIC particle-in-cell

PSIC-LEO Plasma Spacecraft Interaction Codes for Low Earth Orbit

PVO Pioneer Venus Orbiter

RPA retarding potential analyzer

LIST OF SYMBOLS

A_p Probe area

A_{SC} Spacecraft area

$\vec{B}$ Magnetic field

ϵ_0 Vacuum permittivity

I_e Electron current sourced from plasma

I_i Ion current sourced from plasma

I_{net} Net current sourced from plasma

I_{pe} Photoelectron current

I_{see} Secondary electron emission current

k_B Boltzmann constant

m_e Electron mass

m_i Ion mass

N_e Electron density

N_i Ion density

ϕ Potential of conductor with respect to plasma

ϕ_{LP} Potential of Langmuir probe with respect to plasma

ϕ_{SC} Potential of spacecraft with respect to plasma

q Unit electric charge

r_p Probe radius

r_s Sheath radius

T_e Electron temperature

T_i Ion temperature

V_A Applied potential of Langmuir probe

V_F Floating potential

$\vec{v}_i$ Ion drift velocity

V_P Plasma potential

$\vec{v}_{SC}$ Orbital velocity of spacecraft

ABSTRACT

A Langmuir probe (LP) is a versatile and effective in-situ space plasma instrument for measuring ion and electron densities, and electron temperatures. However, utilizing LPs on very small spacecraft presents challenges that are not experienced on larger, more traditional spacecraft. In particular, a key issue for LP operation on these very small satellites is the negative spacecraft potential induced during LP sweeps due to the limited ion current collection to the spacecraft relative to the electron current collected by the LP. This induced spacecraft charging reduces the accuracy of measurements made by the LP. To mitigate these charging effects, laboratory plasma experiments and computer modeling confirmed that the spacecraft potential can be tracked during LP sweeps using a second, identical probe configured for high impedance potential measurements. By correcting for changes to the spacecraft potential, the LP sweeps can be reconstructed as if they were referenced against a stable potential, providing more accurate measurements of the ambient plasma's properties. This dual probe measurement is referred to here as the twin-probe method (TPM).

This dissertation focuses on the efficacy of the twin-probe method and identifies barriers that must be addressed to maximize its impact. Particle-in-cell simulations were performed using the NASA/Air Force Spacecraft Charging Analyzer Program (NASCAP-2K) to understand which physical processes and system parameters are most critical when analyzing spacecraft charging behavior. A separate MATLAB program called the Plasma-Spacecraft Interaction Codes for Low Earth Orbit (PSIC-LEO) was developed using analytic equations to model spacecraft charging effects on LP current voltage (I-V) curves. Finally, an experiment campaign, performed at NASA Marshall Space Flight Center (MSFC), studied the TPM in a laboratory plasma that approximates a high-density, low-Earth orbit environment.

Through these investigations, it was determined that induced spacecraft charging effects result in LP I-V characteristics which overestimate electron temperature and underestimate electron density. Furthermore, regions of the I-V curves have additional non-linear characteristics due to the spacecraft's induced potential, making traditional Langmuir probe theory more difficult to apply. The TPM is shown to correct I-V curves to provide more accurate estimates of plasma properties. The magnitude of the TPM correction is dependent on the area ratio, defined as the conductive spacecraft surface area divided by the probe surface area. Greater spacecraft charging and, consequently, larger I-V curve corrections when using the TPM, are observed as the area ratio decreases. The method's largest impact occurs for area ratios below 300. While the TPM is effective for area ratios greater than 300, overlap between measurement uncertainty and the magnitude of correction prevents definitive claims of a maximum area ratio for which twin-probe implementation is necessary. Moreover, since the TPM mitigates the effects of spacecraft charging, but does not mitigate the charging itself, a minimum area ratio of 50 is recommended for this method. Below this area ratio, the TPM can be used, but the spacecraft may charge too negatively to allow the Langmuir probe to reach the plasma potential, reducing the number of useful plasma properties obtained from the incomplete I-V curve. Finally, novel capabilities brought about using a combination of Langmuir probes and other satellite instruments are identified. These capabilities include expanding the measurable range of plasma ion distributions using charged particle energy analyzers and calibrating for environmental effects (like photoelectron current).

CHAPTER 1

Introduction

Scientific probing of space plasmas has a long history with many applications and surprising discoveries. Over time, our analysis techniques became more sophisticated, our questions more specific, and our technologies more advanced. One of our more versatile tools for probing such plasmas is the science and engineering workbench known as the satellite. Satellites allow us to carry multiple instruments within or near space plasmas to understand internal interactions, composition, and coupling to external sources. As electrical components miniaturized and manufacturing techniques improved, satellites were built more compactly and at an increasingly cost-effective price. However, miniaturization brought forth new challenges for maintaining accuracy and precision when utilizing well-known instruments. In this chapter, the need for small satellites and their wide-ranging impact on space science will be highlighted in order to motivate the development of science-enabling technology found at the heart of this dissertation.

1.1 Research Motivation

The first time a Langmuir probe (LP) was used to study the Earth's ionosphere was on a V-2 rocket in 1947 [1]. A little over a decade later, after many sounding rocket missions, Sputnik 3 was launched with a Langmuir probe, marking one of the first instances of LP implementation on a satellite [2]. Since these early years, the LP instrument has proven to be a versatile plasma diagnostic tool used to determine many plasma properties, including, but not limited to, the electron and ion density, electron temperature, and spacecraft floating potential [3]. Its versatility allowed scientists to probe the ambient plasma environment while supporting additional instruments, such as ion energy analyzers. Traditionally, satellite missions had to carry multiple experiments to justify their costs. For instance, the Pioneer Venus Orbiter (PVO) carried 17 separate experiments for a mission that lasted over a decade [4]. The total cost of building the PVO and operating it for the first 10 years (the spacecraft orbited Venus from 1980 to 1992) was roughly \$125 million [5]. Adjusted for inflation, from 1992 to today, this is equivalent to just over \$225 million. For comparison, as recently as 2018, the average cost of a small explorer (SMEX) mission—spacecraft that are typically $200\,\mathrm{kg}$ to $300\,\mathrm{kg}$—is roughly \$200 million [6, 7]. While traditional spacecraft missions have greatly advanced space science and technology, their large costs are prohibitively expensive for most countries. Even for countries that can fund these projects, the number of missions that can be funded are understandably limited.

With the miniaturization of electrical components and improved manufacturing techniques, very small spacecraft have gained popularity as a science platform. A subset of small satellites is the CubeSat. CubeSats are a standard for satellites denoted by size and mass. The base unit of measurement is a 1U CubeSat, corresponding to a $10\,\mathrm{cm}$ cube that weighs up to $1.33\,\mathrm{kg}$ [8]. Due to their modular nature, a 1U CubeSat could be an individual spacecraft or part of a larger spacecraft. Common sizes for CubeSats are the 1U, 2U, 3U, 6U, 12U, and 27U CubeSat [9]. Part of the attraction of CubeSats are their low cost and rapid development time. CubeSats are often built with commercial, off-the-shelf electronics, and the cost of building a CubeSat averages at around \$250,000, with some reaching a few million dollars when special made components or instruments are used [10]. While launching a single satellite is expensive, typically costing \$20 million for a launch to low Earth orbit (LEO), an increase in ride shares has significantly dropped the barrier for putting a small satellite on a launch vehicle [11]. For instance, Nanoracks charges \$85,000 for the deployment of a 1U CubeSat [12] and Spaceflight prices a 3U CubeSat deployment to LEO at \$295,000 [13]. These comparatively lower costs combined with design-to-completion timescales that are typically on the order of 18 to 24 months [8], make CubeSats a viable option for countries trying to break into the space science industry, universities running student-led space missions, and industries interested in rapid prototyping and development. Multiple summaries on the benefits and recent trends related to CubeSats have already been published, including the increase of CubeSat launches and countries funding CubeSat missions [11]; the multi-CubeSat deployment system, P-POD [14]; how CubeSats lower the barrier of entry into space for developing nations [15]; and the feasibility of CubeSats as a science platform [9].

Of interest to this dissertation are the benefits that small spacecraft provide for proof-of concept missions and the development of science-enabling technologies. For instance, efforts into developing formation flying between multiple small and very small spacecraft have been underway [16, 17]. Formation flights would allow for long-term, multi-point measurements and high-resolution mappings of the ionosphere that are only available when multiple probes are in the same localized region of the plasma [18].

Furthermore, LP development has also improved by taking advantage of the CubeSat platform. The multi-Needle Langmuir probe (m-NLP) has been developed to make high-frequency measurements of the plasma's electron density [19]. Additionally, the "Instrument Sonde de Langmuir (ISL)," composed of a guarded cylindrical probe and a new, guarded, segmented spherical probe, has been developed and tested on a CubeSat platform [20]. However, the small CubeSat frame introduces interesting engineering and science challenges when implementing Langmuir probes. There is a distinct complication with current balance between a Langmuir probe and small spacecraft; specifically, Langmuir probe operation induces a negative charge on the spacecraft chassis. This variable spacecraft potential impacts instrument measurements, such as overestimating electron temperature and underestimating electron density. This dissertation focuses on the effects of spacecraft charging on LP current-voltage (I-V) characteristics, and studies a method of correcting impacted curves using the tracked spacecraft potential from an additional high-impedance probe..

1.2 Basic Properties of a Plasma

A plasma, in steady state, is a quasi-neutral, gaseous fluid composed of charged and neutral particles that exhibits collective behavior [21]. While accurately predicting their dynamics is an involved task requiring both fluid and electrodynamic physics; due to their nature, all plasmas share many of the same basic physical properties. To begin, the quasi-neutrality of plasmas implies that an imbalance of positively and negatively charged particles can exist locally, but globally, the density of positively charged ions must equal the sum of electron density and negatively charged ion density, such that

$$\sum_{i}^{N} M_i^+ = \sum_{i}^{N} M_i^- + e_i^- \tag{1.1}$$

where M^+ is the density of positively charged ions, M^- is the density of negatively charged ions, and e^- is the density of free electrons. Here, it is implicitly assumed that all ions are singly charged.

When an external point charge perturbs the plasma, free electrons respond to the external field by creating an ion- or electron-rich boundary around the charge, shielding the bulk of the plasma from the resultant external fields. The natural radial length scale that describes the distance over which external fields are screened is called the Debye length, and it is described by eq. 1.2. The plasma's effectiveness in screening external fields is proportional to its electron temperature and inversely proportional to the electron density. The region between any external charge and the boundary of the shielded plasma is called the sheath. This region is typically a few Debye lengths, λ_D, wide and does not adhere to the principles of quasi-neutrality [22].

$$\lambda_D = \sqrt{\frac{\epsilon_0}{q^2}}\sqrt{\frac{k_B T_e}{N_e}} \tag{1.2}$$

Additionally, the plasma's response time to the perturbations is not infinitely small. Since electrons are the more mobile charge carriers in a plasma, they are displaced due to an external charge's perturbations. Coulombic interactions between the displaced electrons and positively charged ions act as a restorative force, counteracting the perturbation and returning the plasma to a charge-neutral state. The characteristic time scale of the plasma is the time it takes for charge neutrality to be restored, and, in a cold, non-magnetized plasma, it is mainly governed by the electrons. This characteristic time scale for a collisionless plasma is called the electron plasma frequency, ω_{pe} (described by eq. 1.3 in units of $\mathrm{rad\,s^{-1}}$). While the Debye length restricts the distances over which time-independent electric fields mostly affect the plasma, the electron plasma frequency is the period of oscillation over which time-dependent electric fields perturb the plasma [22].

$$\omega_{pe} = \sqrt{\frac{q^2 N_e}{\epsilon_0 m_e}} \tag{1.3}$$

Therefore, for an ionized gas to be considered a plasma, it must generally adhere to the following criteria [23]:

1. $L >> \lambda_D$: The size of the plasma must be much greater than its Debye length so Debye shielding can take place, allowing for collective behavior.
2. $N_e \lambda_D^3 >> 1$: The average distance between free electrons must be smaller than the Debye length.
3. $\nu_{pe} >> \nu_{en}$: The electron plasma frequency must be greater than the electron-neutral collision frequency, ensuring the electrons do not achieve equilibrium with neutrals ($\nu_{pe} = \omega_{pe}/2\pi$).

There are many examples of plasmas found in nature. For instance, our sun, like most stars, is a plasma, and even the solar wind emitted from the sun is a plasma. As solar wind jets across the solar system, it interacts with astronomical bodies such as planets, moons, and comets, and their surrounding environments. In some cases, like on Earth, a strong magnetic field shields the planet's atmosphere from the high-energy particles in the solar wind, which instead couple with the magnetosphere and ionosphere. In the absence of an intrinsic magnetic field, like on Venus and Mars, the ionosphere can be stripped away, have holes, and, in severe cases, the atmosphere itself can be directly affected. These interactions and a general discussion on the properties of ionospheres are discussed in section 2.1. Regardless of the form of the plasma, studying it helps scientists model the coupling between the different regions surrounding astronomical bodies, create effective plans for interplanetary travel, study the composition and life of stars, and much more.

1.3 Langmuir Probe as a Plasma Diagnostic Tool in Space

To understand plasmas, whether in nature or in vacuum chambers, it is necessary to somehow probe the plasma for its properties, such as ion and electron density, charged particle distributions, flow velocity, etc. One such plasma instrument is called the Langmuir probe, which is, at its core, a conductor of known geometry that collects current from the plasma. Examples of different LP geometries are shown in fig. 1.1. The planar LP (fig. 1.1a) was used to study ion current emission from an ion plume (the work is detailed by *Miars* [24]). The cylindrical LP (fig. 1.1b) was one of many used in an experiment campaign to study the twin-probe method at NASA Marshall Space Flight Center (NASA MSFC) (see chapter 5 for experiment details). The spherical LP (fig. 1.1c) was used as part of preliminary plasma laboratory studies at NASA MSFC to prepare for the twin-probe method experiment campaign.

(a) Planar LP. (b) Cylindrical LP. (c) Spherical LP.

Figure 1.1: Examples of different common Langmuir probe geometries.

From the relationship between a probe's collected current and its potential relative to the ambient plasma, many properties can be derived. The most common application is determining ion and electron densities, N_i and N_e respectively, and electron temperature, T_e [25, 26]. In this section, a general overview of I-V characteristics is explained; a more in-depth study on the current collection of planar and cylindrical surfaces is given in sections 2.2 and 2.3; and a detailed description of cylindrical LP analysis can be found in appendix C.

As with any conductor in a plasma, Langmuir probes collect current from various environmental sources. The plasma itself provides ion and electron current, I_i & I_e respectively; photoelectron emission, I_{pe}, can be a non-negligible source of current when the conductor is illuminated by a photon source (like the sun) [27]; and secondary electron emission, I_{see}, is another available source of current [28]. As a result, for a given potential relative to the ambient plasma environment, ϕ, the net current, I_{net}, to a conductor is

$$I_{net}\left(\phi\right) = I_e\left(\phi\right) - I_i\left(\phi\right) - I_{pe}\left(\phi\right) - I_{see}\left(\phi\right) + I_{misc}\left(\phi\right) \tag{1.4}$$

where I_{misc} is any other current source not previously mentioned. Without an external bias, a conductor will naturally arrive at a potential where the net current is 0, known as the floating potential, V_F. In the absence of additional current sources, such as photoelectrons or secondary electron emission, this potential will typically be a few electron temperatures negative of the plasma potential, due to the higher mobility of the electrons [22].

When operating a Langmuir probe, it is impossible to reference the plasma directly, and so it is instead referenced against a reference electrode, such as a spacecraft chassis, when in space, or Earth ground, for ground-based experiments. In this discussion it is assumed that the reference electrode is a spacecraft and the Langmuir probe has a cylindrical geometry (the shape of the probe affects the I-V curves). The applied voltage between the LP and the spacecraft, V_A, is equivalent to the difference between the potential of the LP with respect to the ambient plasma, ϕ_{LP}, and the potential of the spacecraft with respect to the ambient plasma, ϕ_{SC} (see eq. 1.5).

$$V_A = \phi_{LP} - \phi_{SC} \tag{1.5}$$

In section 1.3.2, the case of a finite spacecraft-to-probe area ratio (from here on referred to as area ratio) is discussed. With this finite area ratio, it is recognized that a LP in space in reality has two probe surfaces that must be considered, which is called a double probe. However, in this initial discussion, the spacecraft is assumed to be infinitely larger than the Langmuir probe. As the LP is swept from negative to positive bias with respect to spacecraft electrical common, the net LP current governed by eq. 1.4 is measured, producing I-V curves. To understand which plasma properties can be obtained from the I-V curves, each section of the curve will now be briefly discussed. Figure 1.2 is an example I-V curve for a probe biased relative to the spacecraft and can be used to follow along for the remaining discussion in this subsection.

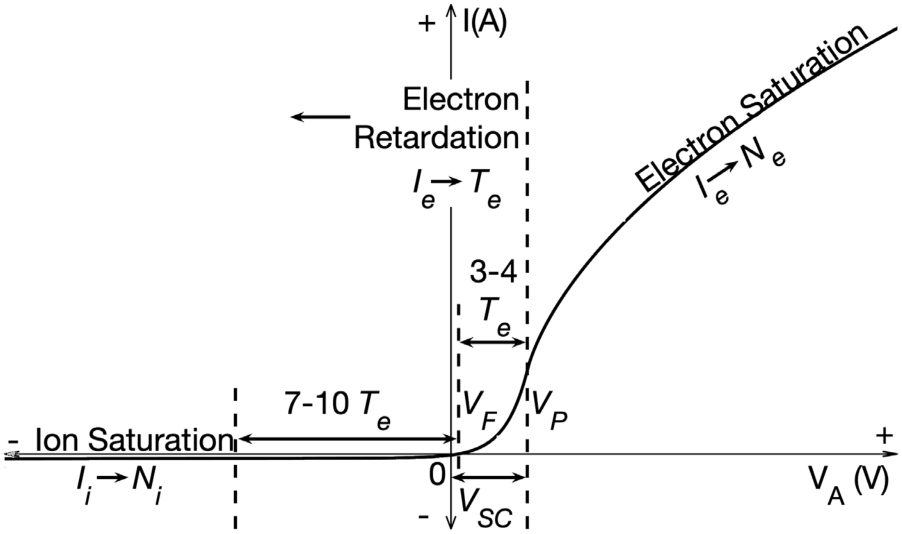

Figure 1.2: Example of a Langmuir probe current voltage relationship. For a probe referenced against the satellite, its I-V curve is divided into three bias regions: 1) an ion saturation region well below the floating potential, 2) an electron retardation region below the plasma potential, and 3) an electron saturation region above the plasma potential.

To begin, the I-V curves are framed by two distinct potentials: the Langmuir probe floating potential, V_F, and the plasma potential, V_P. As previously mentioned, the floating potential is the potential at which all currents collected by the conductor are balanced (sum of the currents is 0). The plasma potential is the potential at which the LP is equipotential with the ambient plasma, and is denoted by a change in concavity in the I-V characteristics. Referring to eq. 1.5, when the LP is at the plasma potential, $\phi_{LP} = 0$, and so $V_A = -\phi_{SC}$. Therefore, when operating in space, the measured plasma potential is an estimate of the spacecraft's potential relative to the plasma. As a result, both the Langmuir probe and spacecraft have their own floating potentials, which do not have to be the same. Thus, the LP I-V curve will very rarely pass through the origin of the coordinates. In fact, due to the different equilibrium potentials of the probe and spacecraft, the floating potential of the probe will more likely be found when the LP is biased positive with respect to the spacecraft [29]. This behavior was also noted by *L. G. Smith* for bipolar Langmuir probes, also referred to as double Langmuir probes, on sounding rockets [30]. Then, when V_A is

0, the LP is at the spacecraft's floating potential. Since the spacecraft's floating potential is more negative than the LP's floating potential, a net negative current will be measured from the LP. This difference in spacecraft and LP floating potentials is graphically presented in fig. 1.6 and discussed in its accompanying text.

When the probe is at the plasma potential, it neither attracts nor repels any charged particle. As the probe is biased above the plasma potential, ions are repelled and electrons are attracted. Since this region is nearly completely dominated by electron current, I_e, it is called the electron saturation regime, and the characteristics of this regime are used to estimate the plasma's electron density. For potentials more negative than the plasma potential, ions are accelerated and electrons are repelled, in a region called the electron retardation regime. However, in the bias region between the floating potential and plasma potential, the electron current is still greater than the ion current due to the increased mobility of the electrons. With careful manipulation of the curve, the electron temperature can be extracted from this bias region. Finally, at potentials seven to ten electron temperatures more negative than the floating potential (as determined by fig. C.4b), the electron current is fully extinguished by the retarding potential, and only the accelerated ion current remains, in a region referred to as the ion saturation regime. Using known properties of the plasma and spacecraft, such as the plasma's ion distribution and the satellite's orbital velocity, the ion density can be obtained in this bias region.

To summarize, analyzing the LP's I-V characteristics can provide the plasma ion density, N_i; the LP floating potential, V_F; the plasma electron temperature, T_e; the plasma potential, V_P, or, equivalently, the spacecraft floating potential, ϕ_F; and the plasma electron density, N_e. Furthermore, depending on the situation there are two possible electrical references that are discussed in this dissertation. When the LP is referenced against the spacecraft common or chamber wall, the bias of the LP is referred to as V_A. This notation is primarily used for physical measurements. When the LP, or any conductor, is referenced against the plasma, the bias of the conductor is referred to as ϕ (or ϕ_x, where x is LP (Langmuir probe), SC (spacecraft), or HI (high-impedance probe) when appropriate). This notation is used in the context of numerical simulations where it is more convenient to discuss current collection behavior as a function of probe potential relative to the plasma.

1.3.1 Langmuir Probes in Space: A Brief Overview

Langmuir probe implementation has seen great successes in many regions of the solar system. The very first use of a Langmuir probe in space was in 1947 aboard a V-2 rocket to study the E-region of Earth's ionosphere [1]. Since then, rocket-borne missions have been used to study the lower ionosphere and test developing plasma instrument technologies [31]. For instance, measurements of the electron energy distribution function (EEDF) in the solar quiet focus of the E-region revealed the existence of a high energy tail in the electron distribution, which helped explain anomalous regions of relatively high T_e that had not been understood at the time [32].

To study the high altitude regions of the ionosphere and beyond, satellites of many sizes and levels of sophistication are used. Two important missions in this regime are the Atmospheric Explorer (AE) mission that studied the physical processes that dominate the ionosphere [33], and the Dynamics Explorer (DE) mission, which focused on interactions between the Earth's atmosphere, ionosphere, and magnetosphere [34]. The Langmuir probes on the AE satellites provided electron temperature and plasma density measurements, while supporting more specialized instruments. Some important results from the AE mission were providing high-resolution measurements of photoelectron flux in the thermosphere [35], demonstrating the existence of plasma shear and rotational convection reversals on closed field lines [36], and characterizing electron acceleration in the aurora [37]. Meanwhile, the DE missions demonstrated strong coupling between the magnetosphere and thermospheric dynamics, and provided data to develop fully coupled ionosphere-thermosphere models [38]; identified a variety of ion outflows, such as polar wind [39]; and studied the heating of electrons that can produce suprathermal electron bursts [40]. Smaller, more specialized, spacecraft also play an important role in the ionosphere. For instance, the DEMETER micro-satellite mission employs Langmuir probes to help analyze anomalous variations in the ionosphere related to seismic activity on Earth [41].

Further still, satellites sent to other astronomical bodies used Langmuir probes to study their plasma environments. The PVO was an extensive 12-year study of Venus's ionosphere [42]. Beyond supporting other instruments, the Langmuir probes were used to identify local ionospheric depletion regions (known as "ionospheric holes") in the night side of Venusian ionosphere [43, 44], observe the location of the ionopause [45], and monitor solar irradiance [46]. The last two missions to discuss are for satellite operations around non-planetary bodies. The Rosetta spacecraft studied the plasma environment around the Wirtanen comet for nearly two years [47]. Measurements have so far determined that the cometary plasma has a strong correlation with solar illumination and neutral density [48]. Finally, the Parker Solar Probe, previously known as Solar Probe Plus, is the first spacecraft to fly into the low solar corona, and seeks to understand the solar corona's structure and dynamics [49]. Initial findings from the Parker Solar Probe allowed for estimates on the amount of dust ejected from the solar system [50], and revealed more detailed dynamics on the electron population within newly formed solar wind [51].

1.3.2 The Spacecraft to Probe Conductive Surface Area Ratio Problem

When the basics of Langmuir probes were discussed in section 1.3, it was briefly mentioned that the spacecraft was assumed to be infinitely larger than the LP. In reality, the spacecraft conductive surface area to LP conductive surface area (from here on simply called “area ratio”) is finite, and the magnitude of the area ratio is a useful metric for predicting how spacecraft size may affect the I-V characteristics of a LP. Indeed, when a LP is referenced against a spacecraft, it is being operated as an asymmetric double probe [52]. In a double probe system, a bias between two electrodes is applied and the current between them is measured. The system electrically floats, so there is no net current between it and the ambient plasma environment, regardless of the potential between the electrodes [53].

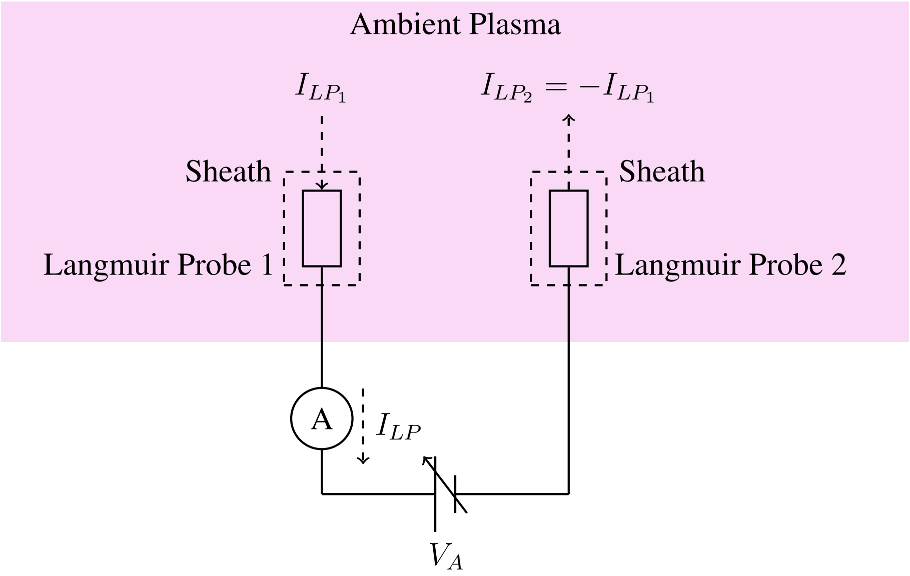

Figure 1.3: Symmetric double probe circuit comprised of identical, cylindrical Langmuir probes.

Before discussing the asymmetric double probe case that describes the LP/spacecraft system, consider the simpler symmetric double probe scenario for two cylindrical Langmuir probes. A simple circuit of a symmetric double probe is shown in fig. 1.3 and is used as a reference. In this idealized example, the two probes are identical and sufficiently separated to be outside of each other’s sheaths while sampling the same plasma environment. Thus, there are no issues due to differences in work functions, and the same current equations (detailed in section 2.3) can be used to describe the net current to both probes.

The applied potential between the two probes is

$$V_A = \phi_{LP_1} - \phi_{LP_2} \tag{1.6}$$

where ϕ_{LP_1} is the potential of Langmuir probe 1 (LP_1) relative to the ambient plasma and ϕ_{LP_2} is the potential of Langmuir probe 2 (LP_2) relative to the ambient plasma. Since the net current between a double probe system and the ambient plasma must be 0, and unaffected by the applied bias, the total current of the system is

$$I_{LP} = I_{e_{LP_1}} - I_{i_{LP_1}} = I_{i_{LP_2}} - I_{e_{LP_2}} \tag{1.7}$$

where $I_{e_{LP_1}}$ and $I_{e_{LP_2}}$ is the electron current to Langmuir probe 1 and 2, respectively;$I_{i_{LP_1}}$ and $I_{i_{LP_2}}$ is the ion current to Langmuir probe 1 and 2, respectively; and I_{LP} is the current between the probes. As a point of clarification, the net current to LP_1 is equal but of opposite sign to the net current collected by LP_2.

To understand how this current balance requirement affects the current collections of each probe, refer to the modeled potential curves of each probe shown in fig. 1.4. First, as a sanity check, when the applied potential between the probes is 0, the two probes are at the same potential relative to the plasma because they are identical probes in the same plasma. As the applied potential becomes increasingly positive, LP_1 is biased positive relative to LP_2, and LP_1 collects increasingly more electron current. For the same density and temperature, the thermal electron flux is roughly 170 times greater than the thermal flux of atomic oxygen ions (O^+), the dominant ion species in the LEO ionospheric environment. This is equivalent to the square root of the ratio of the atomic oxygen mass to the electron mass. Additionally, it is assumed that the only currents collected by the LP or spacecraft are charged particles sourced from the plasma. Consequently, to balance the increased electron current to LP_1, LP_2 will charge negatively to repel electrons and attract more ions to its surface. LP_2's induced negative potential then limits the potential of LP_1 with respect to the plasma, ϕ_{LP_1}. Equivalently, when V_A becomes increasingly negative, LP_2 is biased positive relative to LP_1, and ϕ_{LP_1} becomes increasingly negative. ϕ_{LP_1}'s induced negative charging will, in turn, limit ϕ_{LP_2}. Regardless of the applied potential, neither probe reaches the plasma potential (denoted on the y-axis of fig. 1.4 as $0\,\mathrm{V}$). As a result, only ion density and electron temperature estimates can be obtained from symmetric double probe operation. A full description of double probe analysis and the underlying physics is described by *Johnson et. al.* and *L. Schott* [54, 55].

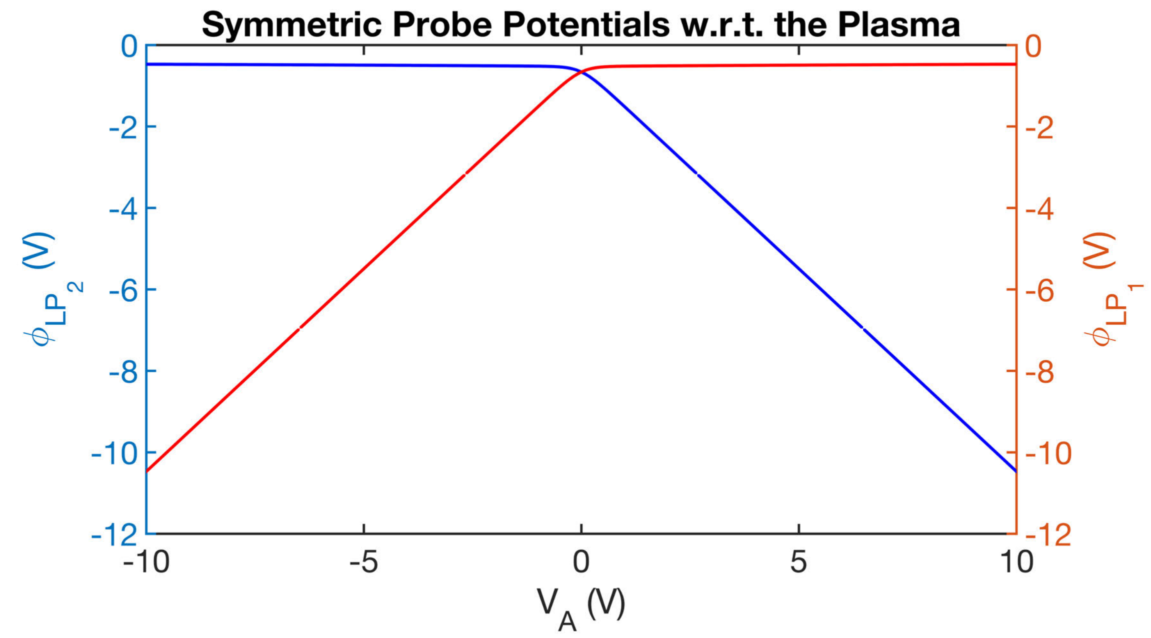

Figure 1.4: Modeled potentials of each probe in a symmetric double probe as a function of the applied bias between the two probes.

The same treatment as the symmetric double probe can be used to understand the asymmetric double probe configuration that describes the Langmuir probe/spacecraft system. The pictorial representation in fig. 1.5 provides a basic circuit diagram. Again, since the currents to the LP and spacecraft must sum to zero,

$$\begin{aligned} & I_{LP}\left(\phi_{LP}\right) - I_{SC}\left(\phi_{SC}\right) = 0 \\ \implies & I_{e_{LP}}\left(\phi_{LP}\right) - I_{i_{LP}}\left(\phi_{LP}\right) - \left(I_{e_{SC}}\left(\phi_{SC}\right) - I_{i_{SC}}\left(\phi_{SC}\right)\right) = 0 \\ \implies & A_{LP}\left(j_{e_{LP}}\left(\phi_{LP}\right) - j_{i_{LP}}\left(\phi_{LP}\right)\right) = A_{SC}\left(j_{e_{SC}}\left(\phi_{SC}\right) - j_{i_{SC}}\left(\phi_{SC}\right)\right) \\ \therefore\, & j_{e_{LP}}\left(\phi_{LP}\right) - j_{i_{LP}}\left(\phi_{LP}\right) = \frac{A_{SC}}{A_{LP}}\left(j_{e_{SC}}\left(\phi_{SC}\right) - j_{i_{SC}}\left(\phi_{SC}\right)\right) \end{aligned} \tag{1.8}$$

where j is the current density; the subscripts i and e represent the ions or electrons, respectively; and the subscripts LP and SC represent the Langmuir probe or spacecraft, respectively. Exact analytic expressions for the current collection of a general cuboid do not exist, but simplifying assumptions can be made to understand how the area ratio affects the LP's I-V characteristics.

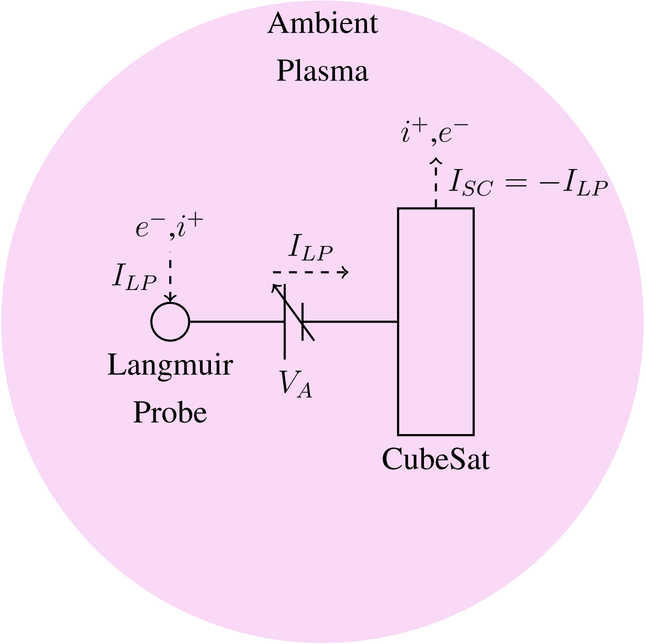

Figure 1.5: Asymmetric double probe configuration comprised of a Langmuir probe and spacecraft.

Equation 1.8 is written in terms of the spacecraft and LP potentials relative to the plasma, which are potentials that are not directly controlled. However, these potentials are related by the applied voltage, which is directly controlled, as shown in eq. 1.5. When the applied bias to the probe is negative, ϕ_{LP} is also negative, and the Langmuir probe collects net ion current. In this regime, eq. 1.8 simplifies to

$$-j_{i_{LP}}\left(\phi_{LP}\right) = \frac{A_{SC}}{A_{LP}} j_{e_{SC}}\left(\phi_{SC}\right).$$

Since the electron current density is greater than the ion current density, the spacecraft can balance the ion current to the probe by collecting electron current to its chassis with no noticeable change to ϕ_{SC}.

As the applied bias is increased, the electron current to the LP also increases. Eventually, the applied bias is sufficiently positive such that the LP collects only electrons. In this regime, eq. 1.8 simplifies to

$$j_{e_{LP}}\left(\phi_{LP}\right) = -\frac{A_{SC}}{A_{LP}} j_{i_{SC}}\left(\phi_{SC}\right).$$

Where before, the larger electron current density aided in current balance, now the spacecraft must compensate for the smaller ion current density with its size. On very large spacecraft, this current requirement does not pose any problems, since the spacecraft current collection area is much larger than the probe, and currents can be balanced by very small changes to the spacecraft potential. Indeed, *Szuszczewicz* found that an area ratio of 1×10^4 guarantees a fixed spacecraft potential, but an area ratio of at least 1×10^3 is typically sufficient and in agreement with *Smith* and *Bettinger* [56, 30, 52]. An extreme example of a large spacecraft and probe combination is the International Space Station (ISS) and its Wide-Sweep Langmuir Probe (WLP). The WLP is a spherical Langmuir probe of surface area $0.032\,\mathrm{m}^2$ [57] and the total surface area of the ISS is at least $378\,\mathrm{m}^2$ [58]; resulting in an area ratio of approximately 1.2×10^4, which grew as more sections and solar panels were added to the ISS. As an additional example, the Cassini spacecraft carried a guarded spherical Langmuir probe with a total conductive surface area of $8.9 \times 10^{-3}\,\mathrm{m}^2$ [59]. When approximating the spacecraft as a cylinder with a length of $6.8\,\mathrm{m}$ and diameter of $4\,\mathrm{m}$ [60], the area ratio between Cassini and its Langmuir probe was 1.24×10^4.

On small spacecraft, whose area ratio is less than 1000, the current collection area ratio isn't sufficiently large enough to balance the currents. As a result, the CubeSat will negatively charge to collect enough ion current to balance the electron current collected by the LP [3, 61]. This negative charging directly affects and limits the LP potential relative to the plasma. An example of a small spacecraft that detected this spacecraft charging behavior is the DEMETER satellite. Its maximum possible conductive surface area is $0.3\,\mathrm{m}^2$ and it carried a guarded LP with total area $7.07 \times 10^{-4}\,\mathrm{m}^2$ [62, 20], resulting in a maximum area ratio of approximately 433.

To understand how the unstable spacecraft potential affects LP I-V curves, consider the measured spacecraft potential example shown in fig. 1.6 and the I-V curve example shown in fig. 1.7. Starting with fig. 1.6, the measured spacecraft potential and Langmuir probe potential are with respect to a high-impedance probe floating potential. This method is discussed in section 3.1 with experiment details provided in section 5.1. Comparisons between fig. 1.6 and fig. 1.4 highlight the effects of referencing the LP against an electrode larger than itself. In this case, ϕ_{SC} is analogous to ϕ_{LP_2} and ϕ_{LP} is analogous to ϕ_{LP_1}. When the LP is biased negative relative to the spacecraft, the two plots are identical because the reference electrode (ϕ_{SC} and ϕ_{LP_2}, respectively) are balancing ion current to the LP with electron current to their surfaces. When the applied bias is 0, ϕ_{SC} and ϕ_{LP} are no longer at the same floating potential due to their size difference, shape difference, and difference in materials. As is seen in fig. 1.7 and noted in section 1.3, this floating potentials difference is directly responsible for a non-zero measured current collection when the applied bias is $0\,\mathrm{V}$. When the LP is biased positive relative to the spacecraft, the spacecraft will increasingly charge negative to balance electron current to the LP with ion current to its own surface.

Just like in the symmetric case (fig. 1.4), the spacecraft's induced negative potential limits ϕ_{LP}. However, ϕ_{LP} is not so limited by ϕ_{SC} that it will not reach and surpass the plasma potential for the example area ratio. As will be discussed in section 4.3, there exists a minimum area ratio for which ϕ_{LP} will reach the plasma potential.

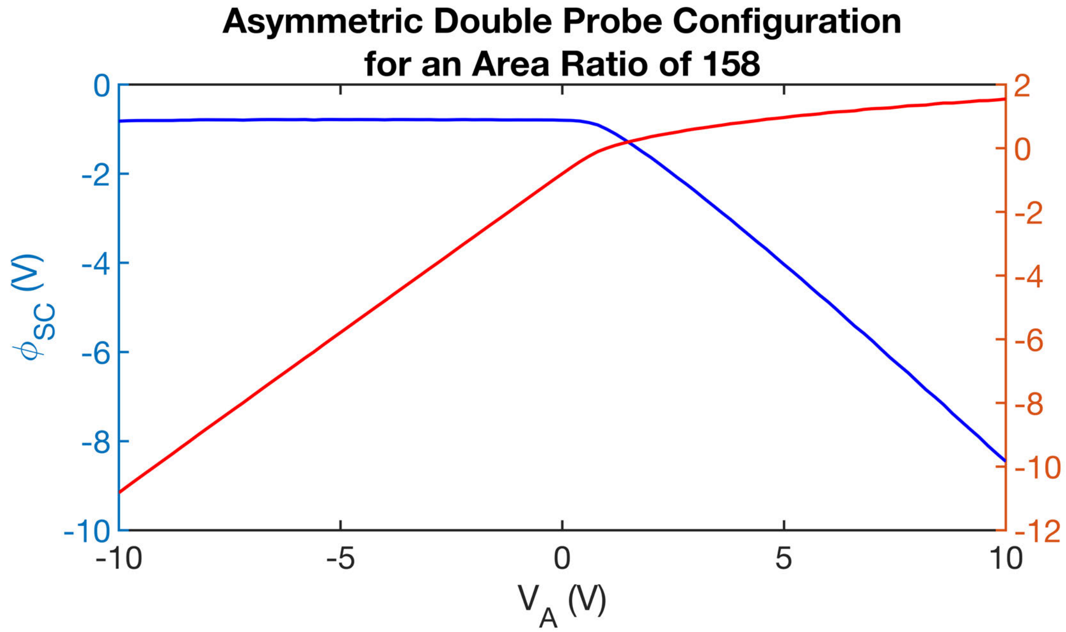

Figure 1.6: Experimentally measured potentials of the spacecraft and Langmuir probe in an asymmetric double probe configuration as a function of the applied bias between the two probes.

The variable potential of the spacecraft directly impacts the measured I-V characteristics of the swept LP. In fig. 1.7, experiment data of two Langmuir probe curves in the same plasma environment, but different area ratios, is shown. A description of the experiment is provided in chapter 5. The curve for an area ratio of 1.4×10^4 corresponds to a Langmuir probe referenced against a vacuum chamber, and is analogous to a Langmuir probe referenced against very large spacecraft. The curve for an area ratio of 158 corresponds to a Langmuir probe referenced against a 3U CubeSat, where the probe-satellite system is electrically isolated from the chamber, mimicking a satellite in space. For ease of comparison, the curves have each been adjusted by their respective measured plasma potentials; in this case, $0\,\mathrm{V}$ corresponds to the probe being equipotential with the plasma. As expected, for sufficiently negative applied biases, there is little difference in the I-V characteristics because the spacecraft potential is not significantly impacted by ion current collection to the LP. As the applied bias increases, the increased electron current to the probe induces a negative potential on the spacecraft, and in turn, produces I-V characteristics that are shallower when compared to I-V curves obtained from stable electrical references. Without a method of correcting the data for induced spacecraft charging or actively controlling the spacecraft potential, the I-V curves of Langmuir probes operating from small satellites consistently overestimate the electron temperature, underestimate the electron density, and provide a spacecraft potential that is somewhere between its natural floating potential and its maximal charged state.

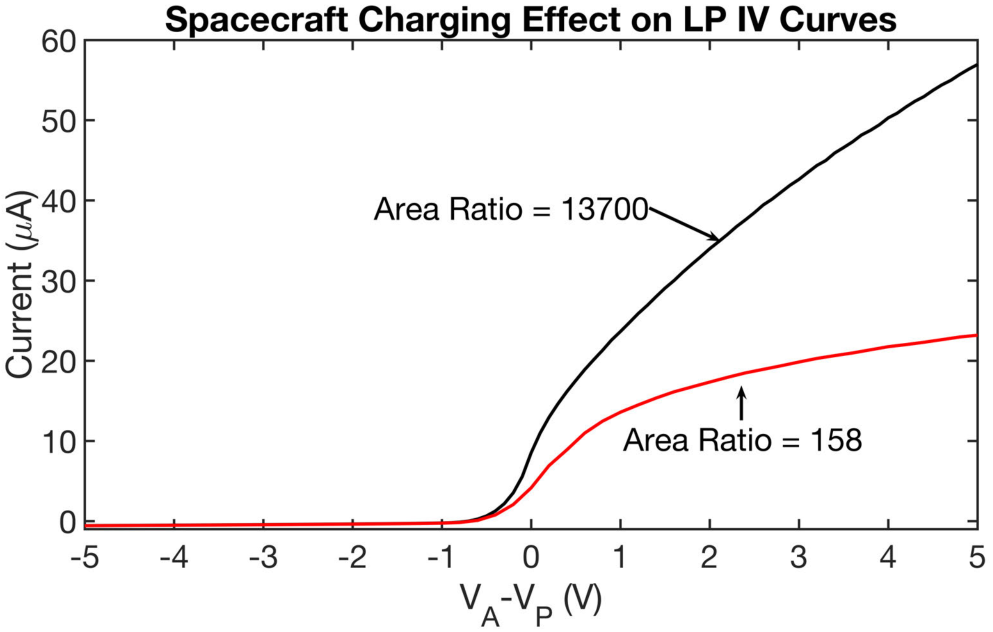

Figure 1.7: Comparison of charging effects on I-V characteristics for small and large area ratios.

1.3.3 Attempts at Resolving the Issue

The problem of spacecraft charging during LP operations is a well-known phenomenon that has affected rocket-borne missions and satellites alike [3]. The first time a Langmuir probe was utilized on a satellite (the third Sputnik mission), measurement inaccuracies due to spacecraft charging were experienced, resulting in hotter electron temperature estimates [2]. By the 1960s, the impact on LP measurements due to spacecraft charging was sufficiently known, such that that the design of the Ariel I satellite included several measures to improve spacecraft conductivity and the area ratio. These measures included building the satellite out of a high work function metal, coating the majority of the surface with evaporated gold to improve surface conductivity, and ensuring the probe area was very small compared to the satellite area ($0.13\,\%$) [63]. Additionally, to understand why Langmuir probe-borne electron temperature estimates from the second Atmospheric

Explorer mission, Explorer 32, deviated strongly with accompanying radar-derived temperature estimates, the impact of spacecraft charging due to probe operation was carefully studied. While only two-thirds of the spacecraft surface was conductive, the resultant spacecraft-to-probe area ratio was sufficiently large to only introduce a $5\,\%$ error for probe-derived electron temperature measurements [64]. Thus, area ratio was not viewed a significant contributor to the Explorer 32 temperature estimate discrepancy.

Similarly, the very first instance of Langmuir probe implementation on a rocket had issues of area ratio impacting the LP I-V curve [1, 65]. Interestingly, for a period of time, symmetric double Langmuir probes were ejected from rockets to study the Earth's ionosphere without worrying about issues of payload charging. An example of such probes is the dumbell electrostatic probe developed at the University of Michigan, which consisted of at least two guarded hemispherical Langmuir probes, a DC power supply, and a radio transmitter [66]. Since these probes were symmetric double probes, only ion density and electron temperature measurements could be obtained for various low altitude ionospheric conditions [67]. In a case where the LP system was not ejected from the rocket body, when testing an instrument suite designed to probe the Earth's ionosphere, *Bettinger* determined that the DC Langmuir probes' potential relative to the plasma environment was severely limited by an induced negative charge on the payload body, due to an area ratio of 20, rendering swept LP measurements unusable [29]. More recently, *Barjatya et. al.* noted that LP operation on the NASA Sudden Atom Layer sounding rocket's payload induced negative charging on the payload's surface as well [68]. Moreover, *Bekkeng et. al.* noted that payload charging on the rocket missions ECOMA 7, 8, and 9 impacted electron density estimates on fixed bias Langmuir probe measurements [69]. Finally, several CubeSats have encountered satellite charging as a result of LP operation, including DEMETER, CubeStar, and NorSat-1 [20, 70, 19].

Over time, many additional techniques to mediate these spacecraft charging issues have been developed for very small satellites. For instance, on the Dynamic Ionosphere CubeSat Experiment (DICE), LP sweeps are often restricted to potentials near or below the floating potential to ensure a minimally affected spacecraft potential, while guaranteeing the ion density can be estimated from LP sweeps [71]. Chamber experiments have shown that increasing the frequency of LP sweeps by up to $3\,\mathrm{kHz}$ diminishes distortions on the LP I-V curve due to the frequency response of the reference electrode's (i.e. a spacecraft's or rocket's) sheath impedance; thus, negating the effects of spacecraft charging on electron temperature measurements [72]. The Ex-Alta 1 and Hoopoe satellites used a 4 LP configuration, called the m-NLP system, in conjunction with a thermionic emitter to make rapid measurements of electron density without knowledge of electron temperature or spacecraft potential [73]. The thermionic emitter is used to balance the electron current to the probes as part of an active spacecraft charge control scheme.

So far, the discussed methods have either focused on a specific region of the LP I-V curve, introduced RF circuitry to circumvent the issues attributed to small area ratios, or utilize active beam emission. While these systems can be used as a traditional DC Langmuir probe, doing so would result in an I-V curve that is affected by the unstable spacecraft potential. In order to maintain the full operation capability of the DC Langmuir probe while operating on small spacecraft, the satellite potential must be tracked during probe operation. Such a system could conceivably consist of two LPs where one probe is operated as a traditional LP and the other tracks the spacecraft potential. Some small spacecraft have discussed using this method to mitigate the effects of spacecraft charging, but other factors have limited the impact of the technique. For instance, the DEMETER mission carried the ISL where the cylindrical probe could be swept relative to the spacecraft, while the guard of the spherical probe tracked the change in spacecraft potential. Initial tests demonstrated that sweeping the cylindrical probe by its full bias range did disturb the spacecraft potential, but the sweep range was reduced to minimize interference [20]. The Mars Atmosphere and Volatile Evolution (MAVEN) mission also carried two LPs to track the spacecraft potential during LP sweeps [74]. However, due to the sparse Martian ionosphere and significant photoelectron current, it was determined that the spacecraft potential variation is negligible during probe operation [75]. Finally, the PicoSatellite for Atmospheric and Space Science Observations (PICASSO) CubeSat carries the sweeping Langmuir probe (SLP) instrument. This instrument consists of four individual LPs, each having the capability to measure the spacecraft floating potential, or be operated in a swept mode [76]. This mission is slated for launch in 2020 [77].

1.3.4 Problem Statement

There is clear interest and motivation for mitigating the effects of satellite charging when Langmuir probes are operated on small spacecraft. A promising method for dealing with the effects of an unstable satellite electrical reference is to track the spacecraft potential during Langmuir probe sweeps. While satellites and rockets have flown iterations of this method, and several theoretical studies have been made on spacecraft charging during probe operation, little published material exists discussing experimental investigations on the efficacy of this technique. Therefore, this work seeks to study how much affected Langmuir probe I-V curves can be corrected using the tracked spacecraft potential. Specifically, an instrument package consisting of two identical cylindrical probes, each with a high-impedance and sweep mode, is used to experimentally study spacecraft charging and its impact of I-V curves. This Langmuir probe technique, referred to here as the twin-probe method, is detailed in chapter 3. To understand the affordances and constraints of the twin-probe method, this work seeks to answer the following questions:

1. Can the spacecraft potential be tracked accurately enough during Langmuir probe operation to properly correct I-V curves?
    (a) What system level design choices limit the effectiveness of the twin-probe method?
    (b) Does probe orientation, size, or shape affect the efficacy of the twin-probe method?
    (c) What environmental effects limit accuracy?
2. Can spacecraft charging behavior during Langmuir probe operation be predicted by analytic expressions?
    (a) How does spacecraft charging affect the Langmuir probe's I-V characteristics in ways that cannot be resolved using the twin-probe method?
    (b) What is the impact of individual spacecraft conductive surface areas on spacecraft charging?
3. How can the twin-probe method be used synergistically with other space plasma instruments?

1.4 Dissertation Overview

The seven chapters and four appendices of the dissertation are organized as follows:

- Chapter 1 introduces the small satellite as a science platform and motivates the research presented in this dissertation.
- Chapter 2 demonstrates the fundamentals of Langmuir probe current collection and discusses the general structure of the ionosphere.
- Chapter 3 details the twin-probe technique and its uncertainties.
- Chapter 4 discusses the Plasma Spacecraft Interaction Codes for Low Earth Orbit (PSIC-LEO) simulations used to understand the interactions between the Langmuir probes, small spacecraft, and ambient plasma environment.

- Chapter 5 describes experiments performed at NASA MSFC where the feasibility of the twin-probe method was studied. The results of the experiments are analyzed to understand when the method is the most effective.
- Chapter 6 describes the scope of the results and applications for future space missions.
- Chapter 7 concludes the dissertation and discusses future work.
- Appendix 1 provides an overview of the *NASA/AIR Force Spacecraft Charging Analyzer Program (Nascap-2K)* and highlights many top level physical phenomena that informs assumptions for the PSIC-LEO simulations and interpretation of results in the experiments.
- Appendix 2 contains the PSIC-LEO source code.
- Appendix 3 provides a complete description of the cylindrical LP data analysis used throughout the dissertation.
- Appendix 4 provides details the retarding potential analyzer (RPA) data analysis used for the experiment.

CHAPTER 2

Ionospheric Plasmas and Langmuir Probe Theory

A Langmuir probe is a conducting structure biased relative to an electrical reference (e.g. a grounded vacuum chamber, a satellite in space, etc.) to make in situ measurements of its plasma environment. In this dissertation, the primary focus will be on plasmas in space or simulate/scaled space plasmas in vacuum chambers. In this chapter, the fundamentals of steady state plasma current collection by a planar surface and cylindrical Langmuir probe used in this dissertation are described, as well as the basic composition of the planetary ionospheres where these instruments are utilized.

2.1 Representative Structure of Planetary Ionospheres

An example of a plasma that exists around all astronomical bodies with an atmosphere in our solar system is their respective ionospheres [78]. An ionosphere acts as a buffer between its atmosphere and the rest of space. An in-depth study of the commonalities of the ionospheres in our solar system can be found in *Nagy et. al.* [79], but a short description of these commonalities are detailed below.

The atmosphere surrounding these bodies is ionized by either interactions with solar photons or highly energetic particles of cosmic and solar origins [80]. The ionospheric plasma is typically balanced by two opposing processes: 1) ionization produces the plasma; and 2) recombination removes ions and free electrons. An in-depth study of the ionization, recombination, and other energy loss processes (see fig. 2.1) involving ionospheric electrons can be found in *Takayanagi et. al.* [81]; however, a summary of the processes is as follows. Ionization primarily occurs through photo-ionization from solar X-rays or UV radiation and, to a lesser extent, secondary ionization from high energy particle collisions. Since ionization is dominated by photo-ionization, the ionosphere's structure exhibits diurnal behavior and is heavily influenced by sun spot activity [82, 83, 84]. Charged particle cooling occurs through collisions that result in excitation or scattering; and with sufficient cooling, electrons will recombine with positive ions neutralizing the ionization.

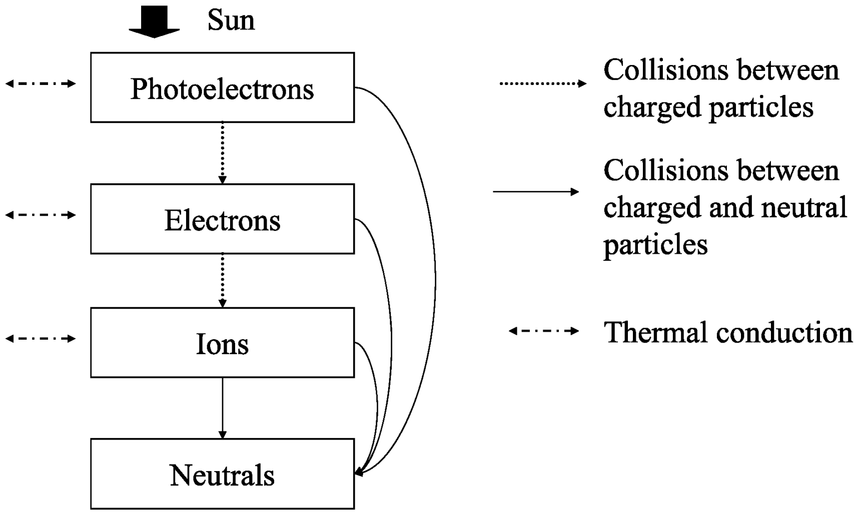

Figure 2.1: Energy exchanges between neutral and charged particles in an ionosphere. Figure extracted from *Witasse et. al.* [80, p. 239].

The various effects of ionization, energy transfer, and recombination lead to a largely vertical stratification where an ionosphere can be divided into regions based on general characteristics such as temperature and composition [85]. The thermal profiles of an ionosphere can be divided into three regions. At lower levels, neutrals, ions, and electrons are in thermal equilibrium due to inelastic collisions. Above this, electrons are hotter than neutrals due to a suprathermal population, while ions and neutrals continue to maintain thermal equilibrium. Finally, at the highest altitudes, ions are no longer thermalized with neutrals due to an increase in electron-ion collisions. The exact altitudes of these regions vary between astronomical bodies due to the complex nature of ionospheres and atmospheres [80].

Examples of planetary ionospheres are quickly described in sections 2.1.1 to 2.1.3, but this thesis focuses primarily on operations in the Earth's ionosphere. However, the twin-probe method is applicable in any situation where the spacecraft cannot balance the current to a Langmuir probe without significantly charging.

2.1.1 Earth's Ionosphere

The Earth's ionosphere extends from about 90 km to 2000 km above the Earth's surface and is protected from external energetic particles, such as solar wind, by the Earth's intrinsic magnetic field [86]. It is composed of multiple atoms and molecules such as helium, oxygen, and nitrogen, and their corresponding ions, as well as electrons (see fig. 2.2). Furthermore, it is divided into layers (D,E, F, and topside) based on several factors including but not limited to composition, ionization rates, and density [87, 88]. The F region has the largest plasma densities, ranging from 10^{10} to nearly 10^{13} m^{-3}, and exists from 150 km to 600 km above the Earth [89, 90]. Finally, fig. 2.3 shows the temperatures for ions, electrons, and neutral particles in the F-region.

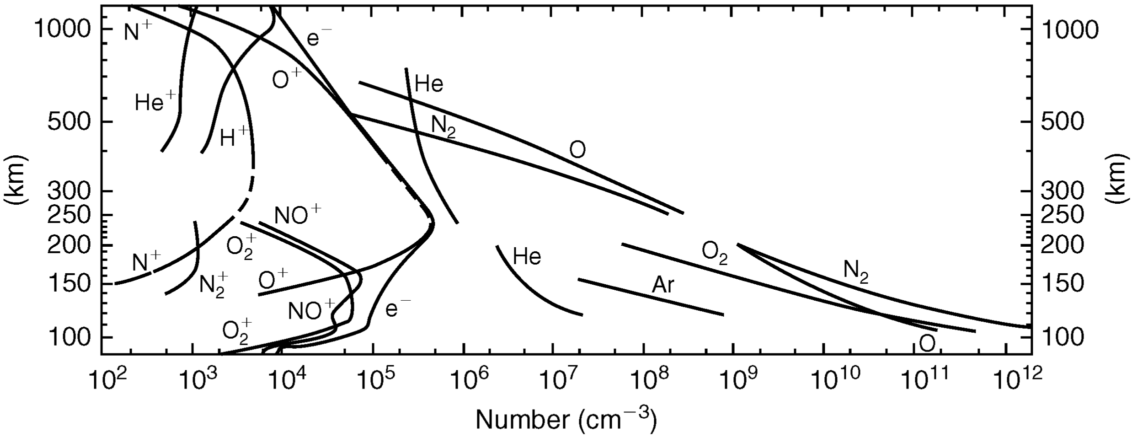

Figure 2.2: Ion, electron, and neutral particle densities in the ionosphere as a function of altitude. Figure from *The Earth's Ionosphere* [91, p. 6].

To properly model and predict the current collection of a conductor in the ionosphere, it is necessary to understand the ion and electron velocity distribution functions. The electron distribution function is divided into two regions: a low energy thermal region and a high energy suprathermal region [92, 93]. The low energy thermal region has been modeled, and experimentally confirmed, as Maxwellian [63, 94, 92, 95]. In this thesis, only the thermal electron population is considered. The high energy tail of the electron distribution, while significant for many processes, only accounts for roughly 1% of the total electron population [63].

For the ion population, singly ionized atomic oxygen is assumed to be the only ion species collected, as it is the dominant ion species in LEO, which is any orbit below 2000 km [96] (see fig. 2.2). In quiet, steady state conditions the ion distribution function is also assumed to be Maxwellian [97]. While this general assumption holds for these studies, in regions of the ionosphere where electric fields are large or where ion drifts differ sufficiently from neutral thermal speeds, the ion distribution function deviates strongly from a Maxwellian distribution [98, 99, 100, 101, 102].

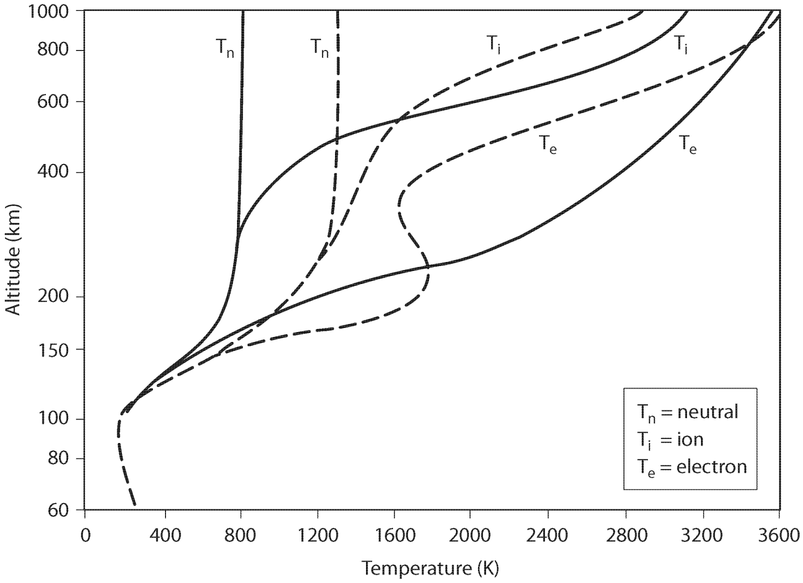

Figure 2.3: Ion, electron, and neutral particle temperatures in the ionosphere as a function of altitude. The solid lines correspond to measurements during solar minimum and the dashed lines correspond to measurements during solar maximum. Figure from *Fundamentals of Spacecraft Charging* [89, p. xvii].

For in-situ measurements made in the ionosphere, the ionospheric plasma is said to be mesothermal with respect to the orbital velocity of the spacecraft. That is, the orbital velocity is greater than the ion thermal speed but less than the electron thermal speed. As a result, the distribution function for ions collected by an Earth-orbiting body is treated as a drifting Maxwellian population where the drift term is the spacecraft's velocity [103]. Additionally, the mesothermal nature of the ionosphere produces ram and wake structures around the spacecraft. On the ram side of the spacecraft, slower moving ions are compressed against the spacecraft body leading to current collection enhancement in this region. In the wake of the spacecraft (opposite of the ram side), particles can only get behind the spacecraft through random thermal motion. Thus, the wake of the spacecraft is largely devoid of ions when compared to the ambient plasma environment, and a significant drop in current collection is observed in the wake region [104, 105]. Pictorial representations on ram/wake effects on the potential structure around the spacecraft are shown in figs. A.11a and A.11b and comparisons between ram and wake current collection are given in table A.1.

The presence of the Earth's magnetic field complicates current collection theory because charged particles will gyrate along magnetic filed lines, introducing anisotropies in the charged particle velocity distribution function [26]. While many theories for Langmuir probe current collection in a magnetized plasma exist, there is no complete, analytical treatment for LP current collection in a mesothermal magnetized plasma [106]. Furthermore, the physical gyroradii of the ions and electrons can be considered against their length scales. Using the typical F region parameters quoted by *Huba* [107], the electron gyroradius is $2.5 \times 10^{-2}\,\mathrm{m}$, the ion gyroradius is $4.3\,\mathrm{m}$, and the ion cyclotron frequency is $1.8 \times 10^{2}\,\mathrm{rad\,s^{-1}}$. First, the mesothermal nature of the spacecraft velocity implies that the ions will appear to have a preferential drift from the spacecraft's reference frame; thus, in the period of the ion cyclotron motion ($0.035\,\mathrm{s}$) the spacecraft will travel about $280\,\mathrm{m}$. Since the distance the spacecraft travels is much greater than the ion gyroradius, the ion motion will appear to have negligible effects due to the ambient magnetic field from the frame of reference of the spacecraft/LP system.

Regarding the magnetic field's effects on electron current, two cases must be considered: 1) the case where the LP is biased positive with respect to the spacecraft and the LP collects net electron current, and 2) the case where the LP is biased negative and the spacecraft can collect electrons. In the first case, magnetic fields only impact electron current collection when the collector radius is larger than the electron gyroradius [108]. As is discussed in section 6.2, probe radii are ideally a fraction of a centimeter, such that they are smaller than, or at worst equal to, the plasma's Debye length. As a result, the probe collector radius is smaller than the electron gyroradius in the Earth's magnetic field in LEO, so the impact on LP current collection due to the ambient magnetic field will be minimal for steady state conditions. In the second case, the spacecraft is larger than the electron gyroradius, and the ambient magnetic field will likely impact electron current collection to the spacecraft [109]. However, in this scenario, the spacecraft is very close to its floating potential because its potential is minimally shifted when the LP collects net ion current (see section 1.3.2). Therefore, the electron current that reaches the spacecraft body is typically one to two orders of magnitude smaller than the electron thermal current, and the change in electron current collection due to the magnetic field is small. As a result, the first case is of greater interest in this dissertation, as it is the balance between ion current to the spacecraft and electron current to the LP that dictates the magnitude of the induced negative spacecraft potential (see section 1.3.2). Thus, to maintain the simplicity of current collection models and focus solely on the relationship between area ratio and spacecraft charging, the effects of the Earth's magnetic field are not considered when modeling current collection to conductive surfaces.

2.1.2 Venus' Ionosphere

Unlike Earth, Venus has no strong, intrinsic magnetic field. Therefore, Venus' ionosphere and atmosphere directly interact with the Sun's solar wind. This creates interesting dynamics that are very different from what is observed in the Earth's ionosphere. One of these differences is a distinct tangential discontinuity at the Venusian ionosphere's edge called the ionopause. In this pause, the kinetic pressure from the ionosphere's plasma is equal to the solar wind pressure [78]. Some key phenomena that are observed at the ionopause include: a sharp drop off in plasma density across the ionopause, the altitude of the ionopause being directly related to solar activity, and fluctuations in plasma density on the night side ionosphere lending to the idea of the existence of holes in the ionosphere [85, 78, 80]. A diagram of Venus' ionosphere can be found in *Schunk et. al.* [78, p. 33]).

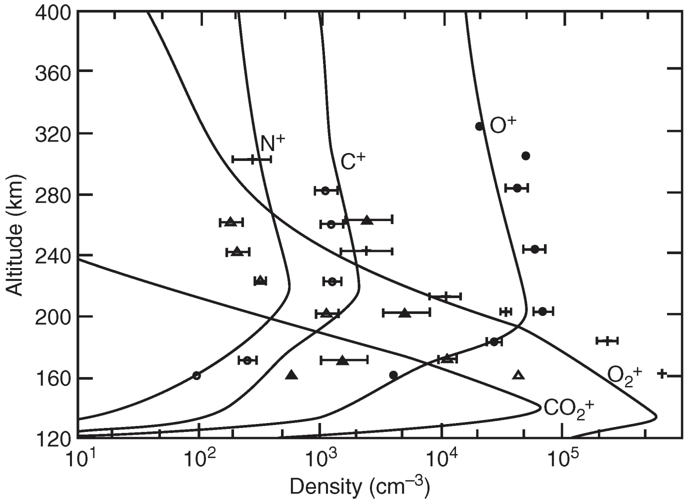

Figure 2.4: Daytime ion densities at Venus. Figure from *Schunk et. al.* [78, p. 484].

Venus' ionosphere has been heavily studied through the 12 year PVO satellite mission. Its ionosphere extends from about 120 km to 600 km above the surface. At roughly 135 km to 140 km, the electron density peaks at $5 \times 10^{11}\ m^{-3}$. In this peak region the dominant neutral species is CO_2. Photoionization produces CO_2^+ that reacts with O to produce the dominant ion in the region O_2^+ [85]. Above the lower region of the ionosphere, O^+ is the dominant ion species while O and CO become the main neutral species. At the highest level of the ionosphere, H and He become the main constituents of the neutral population. The charged particle density and electron temperature as a function of altitude is shown in figs. 2.4 and 2.5, respectively.

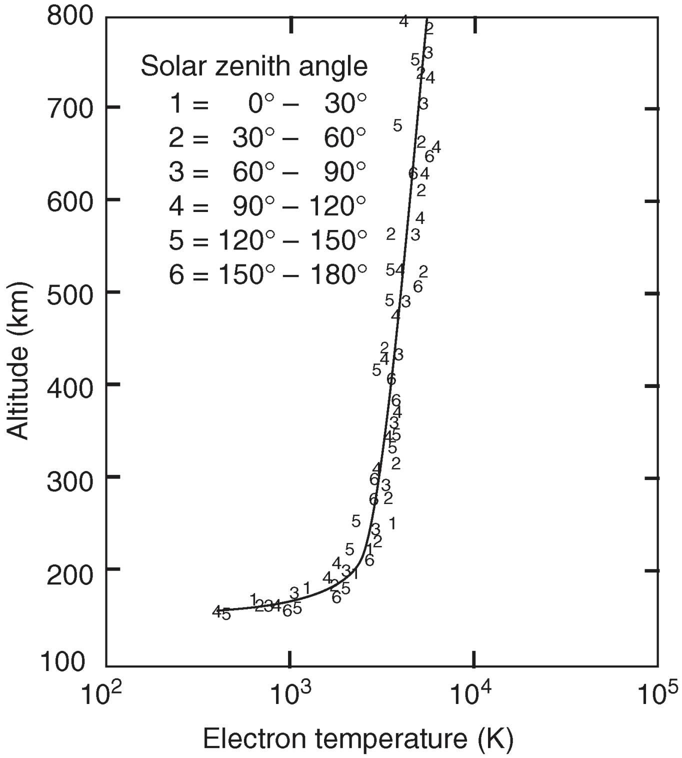

Figure 2.5: Electron temperature measurements of Venus at solar cycle maximum electron temperatures as a function of zenith angle and altitude. Figure from *Schunk et. al.* [78, p. 490].

2.1.3 Mars' Ionosphere

The Martian ionosphere is thought to be very similar to that of Venus in terms of composition, intrinsic magnetic fields, and densities [85]. For instance, fig. 2.6 diagrams the interactions and chemical reactions that are applicable to both Venus' and Mars' ionospheres. Due to limited observations relative to those performed at Venus, not as much is definitively known about Mars' ionosphere. Its ionosphere extends from roughly 100 km to 500 km with a density peak of $1 \times 10^{11}\,\mathrm{m}^{-3}$ occurring between 120 km and 140 km [80]. This density peak corresponds with the main ionization layer where the driving ionizing reaction is due to ultraviolet solar photons [85]. The lower ionosphere is dominated by neutral CO_2, but CO and O will dominate at higher latitudes. While not the main neutral constituent, the dominating ion species is O_2^+ with the exception in the upper ionosphere where O_2^+ and O^+ appear in equal numbers (see fig. 2.7)[78]. Finally, like Venus, the Martian ionosphere does stop at the ionopause where plasma densities drop significantly. However, the exact behavior and altitude of the drop is still being studied with measurements indicating that it exists at an altitude between 300 km and 500 km [78].

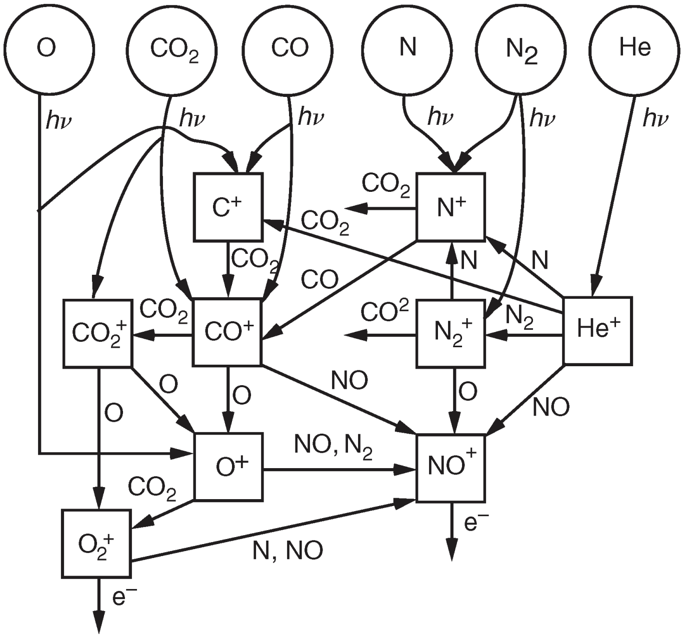

Figure 2.6: Chemistry of ions in both the Venusian and Martian ionospheres Venusian ionosphere. Figure from *Schunk et. al.* [78, p. 483].

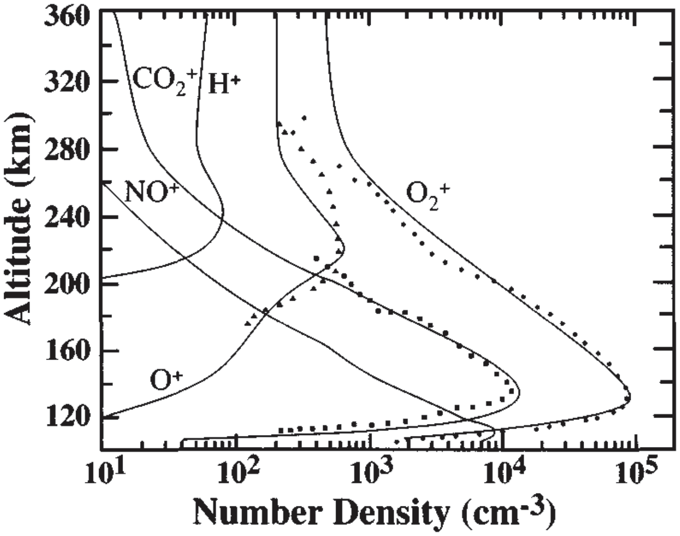

Figure 2.7: Calculated and measured day side ion density profiles at Mars. Figure from *Schunk et. al.* [78, p. 36].

2.2 Plasma Current Collection to a Planar Surface

Before developing the equations for a cylindrical LP (see section 2.3), the simpler case of current collection by a planar surface is first discussed. These models are useful in predicting the currents collected by a planar satellite face and are at best conservative estimates. The effect of an accelerating bias will not be considered for these derivations. Furthermore, it is assumed that the surface is sufficiently large to ignore edge effects; that is, the surface's length is much larger than the plasma Debye length.

Using fig. 2.8 as a pictorial reference, let v and w be particle velocities parallel to the planar surface, u the particle velocity perpendicular to the surface, and v_i is the ion drift velocity perpendicular to the planar surface. Following the work presented by *Hoegy et. al.* [110], the currents to a planar probe are calculated by integrating the distribution function over all velocities parallel to the plane and over velocities perpendicular to the plane such that

$$I = qA_p n_s \int_{0,\sqrt{-\frac{2q\phi}{m_s}}}^{\infty} \int_{\infty}^{\infty} \int_{\infty}^{\infty} u f(u,v,w) dw dv du \tag{2.1}$$

where the lower limit of u is 0 for accelerating potentials and $\sqrt{-2q\phi/m_s}$ for retarding potentials, n_s corresponds to the density of the charged particle species (either electrons or ions), m_s corresponds to the charge particle mass, and A_p is the probe area.

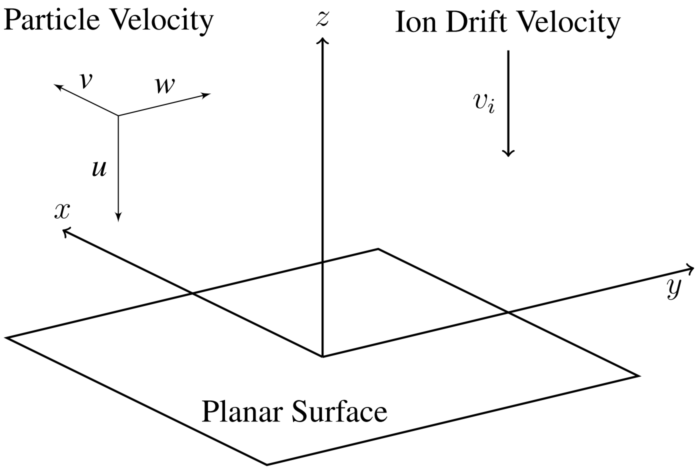

Figure 2.8: Components of particle velocity relative to planar surface.

Following the assumptions in section 2.1.1, the electron population is described by the following three dimensional Maxwellian distribution:

$$f(u,v,w) = \left(\frac{m_e}{2\pi k_B T_e}\right)^{\frac{3}{2}} \exp\left(-\frac{m_e}{2k_B T_e}\left[u^2 + v^2 + w^2\right]\right).$$

Integrating the Maxwellian over any accelerating potential using eq. 2.1 gives

$$\begin{aligned} I_e\left(\phi>0\right) &= qA_pN_e\left(\frac{m_e}{2\pi k_BT_e}\right)^{\frac{3}{2}}\int_0^\infty\int_\infty^\infty\int_\infty^\infty u\exp\left(-\frac{m_e}{2k_BT_e}\left[u^2+v^2+w^2\right]\right)dwdvdu \\ &= qA_pN_e\sqrt{\frac{k_BT_e}{2\pi m_e}}. \end{aligned} \tag{2.2}$$

Equation 2.2 provides a useful normalization constant for the electron current, the electron thermal current. When the accelerated electron current is normalized by the thermal current, it becomes unity. Additionally, the retarding current is

$$\begin{aligned} I_e\left(\phi\leq 0\right) &= qA_pN_e\left(\frac{m_e}{2\pi k_BT_e}\right)^{\frac{3}{2}}\int_{\sqrt{-\frac{2q\phi}{m_e}}}^\infty\int_\infty^\infty\int_\infty^\infty u\exp\left(-\frac{m_e}{2k_BT_e}\left[u^2+v^2+w^2\right]\right)dwdvdu \\ &= qA_pN_e\sqrt{\frac{k_BT_e}{2\pi m_e}}\exp\left(\frac{q\phi}{k_BT_e}\right). \end{aligned} \tag{2.3}$$

Without considering the effects of an accelerating potential or the size of the sheath, the current collection to a planar probe is simply exponential decaying for all retarding biases and the thermal current for any attractive potentials (see fig. 2.9).

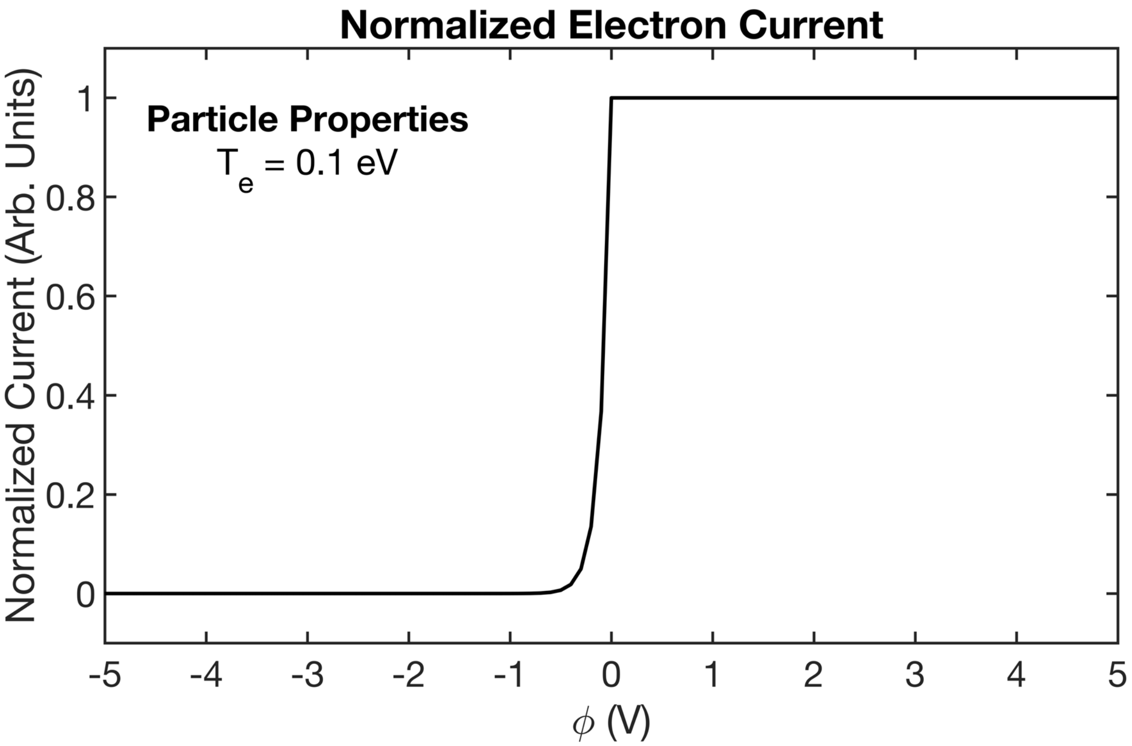

Figure 2.9: Normalized electron currents collected by a planar surface as a function of potential relative to the ambient plasma.

The ions can be treated identically using a drifting Maxwellian distribution

$$f(u,v,w) = \left(\frac{m_i}{2\pi k_B T_i}\right)^{\frac{3}{2}} \exp\left(-\frac{m_i}{2k_B T_i}\left[(u-v_i)^2 + v^2 + w^2\right]\right).$$

To simplify the calculations, normalize the bias and velocities using the ion temperature such that

$$\eta = \frac{q\phi}{k_B T_i} \quad u_n = u\sqrt{\frac{m_i}{2k_B T_i}} \quad v_n = v\sqrt{\frac{m_i}{2k_B T_i}} \quad w_n = w\sqrt{\frac{m_i}{2k_B T_i}} \quad s = v_i\sqrt{\frac{m_i}{2k_B T_i}}$$

and the ion current is normalized using the ion thermal current,

$$I_{i_{therm}} = qA_p N_i \sqrt{\frac{k_B T_i}{2\pi m_i}}.$$

Now, assuming the probe is oriented perpendicular to the drift velocity, the normalized accelerated ion current is

$$\begin{aligned} I_{i_n}(-\phi > 0) &= \frac{2}{\pi}\int_0^{\infty}\int_{\infty}^{\infty}\int_{\infty}^{\infty} u_n \exp\left(-\left[(u_n - s)^2 + v_n^2 + w_n^2\right]\right) du_n dv_n dw_n \\ &= \exp\left(-s^2\right) + \sqrt{\pi} s \operatorname{erfc}(-s), \end{aligned} \tag{2.4}$$

and the full current expression is

$$I_i(-\phi > 0) = qA_p N_i \sqrt{\frac{k_B T_i}{2\pi m_i}}\left[\exp\left(-s^2\right) + \sqrt{\pi} s \operatorname{erfc}(-s)\right] \tag{2.5}$$

Similarly, the normalized retarding ion current is

$$\begin{aligned} I_{i_n}(-\phi \leq 0) &= \frac{2}{\pi}\int_{\sqrt{-\eta}}^{\infty}\int_{\infty}^{\infty}\int_{\infty}^{\infty} u_n \exp\left(-\left[(u_n - s)^2 + v_n^2 + w_n^2\right]\right) du_n dv_n dw_n \\ &= \exp\left[-\left(\sqrt{-\eta} - s\right)^2\right] + \sqrt{\pi} s \operatorname{erfc}\left(\sqrt{-\eta} - s\right), \end{aligned} \tag{2.6}$$

and the full current expression is

$$I_i(-\phi \leq 0) = qA_p N_i \sqrt{\frac{k_B T_i}{2\pi m_i}}\left[\exp\left[-\left(\sqrt{-\eta} - s\right)^2\right] + \sqrt{\pi} s \operatorname{erfc}\left(\sqrt{-\eta} - s\right)\right] \tag{2.7}$$

Figure 2.10 provides an example of the I-V curved produced by eqs. 2.4 and 2.6. Should the planar probe be oriented parallel to the ion drift velocity, the collected ion currents would be identical to the thermal current collection behavior that describes electron current collection.

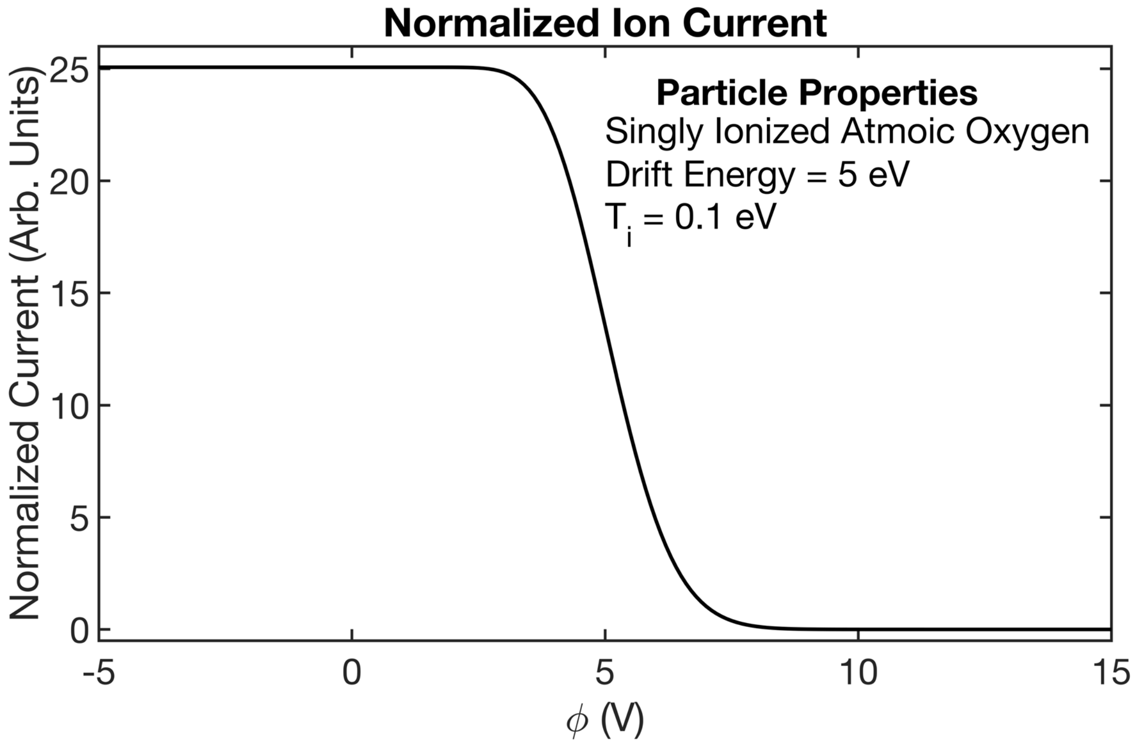

Figure 2.10: Normalized ion currents collected by a planar probe as a function of potential relative to the ambient plasma.

2.3 Cylindrical Probe Current Collection

For the case of a cylindrical Langmuir probe, the following assumptions are made to simplify the calculations. The probe's length, l, is assumed to be much longer than its radius, r_p, or the probe is assumed to be guarded, such that probe end effects can be ignored. A guarded Langmuir probe has a cylindrical conductor on one, or both, ends that is biased at the same potential as the LP to extend uniformity of the electric field surrounding the probe. Furthermore, the shape of the probe's sheath is assumed to be unchanged by high drift velocity of the spacecraft. The combination of these assumptions idealizes the sheath surrounding the probe such that it is perfectly cylindrical and coaxial with the probe and end effects can be ignored. Accounting for the errors associated with these assumptions are detailed in section 2.4.

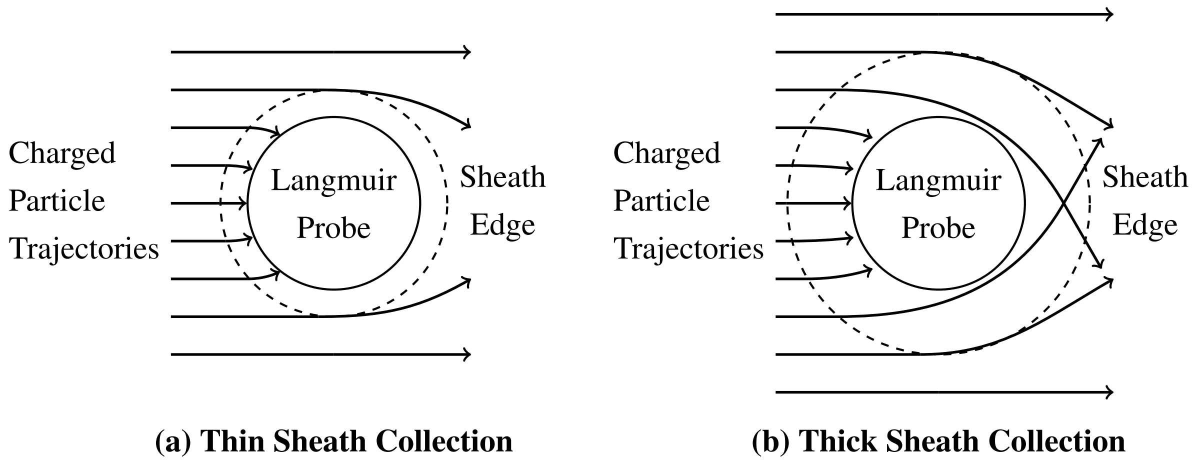

Figure 2.11: Approximate charged particle trajectories for: (a) thin sheath collection and (b) thick sheath collection.

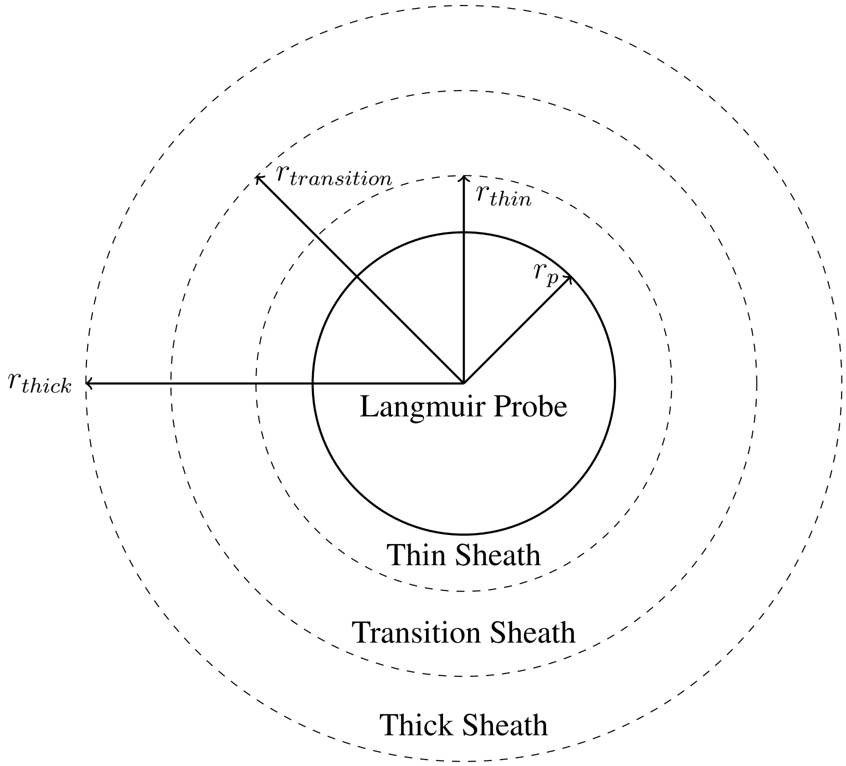

Figure 2.12: Varying coaxial sheaths sizes surrounding a cylindrical Langmuir probe of constant size. There are 3 sheath categories (denoted by dotted lines) considered based on the ratio of sheath radius to probe radius: thin sheath, transitional sheath, thick sheath. Relative sheath sizes are not to scale.

While the sheath is unaffected by orbital velocities, its size is dependent on electron density and temperature. For ionospheric conditions in the F-region, typical Debye lengths range from a fraction of a centimeter to a few centimeters [103]. The size of the sheath relative to the probe radius also dictates the current collection behavior of the probe. For thin sheath current collection, the ratio of the sheath radius to probe radius, r_s/r_p, is approximately one ($r_s/r_p \approx 1$), and all particles that cross the sheath boundary are collected at the probe surface [111] (see left-most diagram of fig. 2.11 for approximate particle trajectories). For thick sheath current collection, the sheath radius-to-probe radius ratio is much greater than 1 ($r_s/r_p >> 1$), and most of the particles that enter the sheath boundary are not collected by the probe [55] (see right-most diagram of fig. 2.11 for approximate particle trajectories). A transition sheath thickness that exists between what is considered thick or thin sheath does exist and has been summarized by *Lobbia et. al.* [112], but will not be considered in this discussion. Refer to fig. 2.12 for a visual representation of various sheath to probe thickness ratios.

For sections 2.3.1 and 2.3.2, fig. 2.13 can be used as a reference to understand the polar coordinates of the charge particle's velocity. u is the velocity component radial to the sheath edge, v is the velocity component tangential to the sheath edge, and v_i is the velocity component of the ion drift velocity (antiparallel to the spacecraft orbital velocity). u is positive when directed towards the origin.

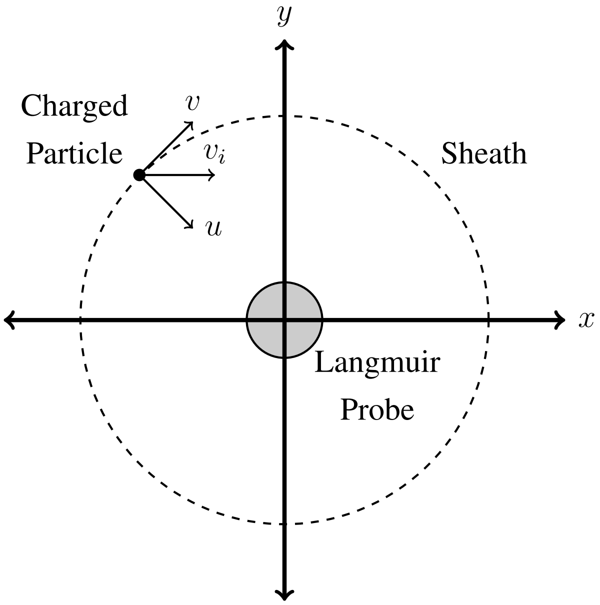

Figure 2.13: Components of particle velocity in cylindrical coordinates.

2.3.1 Electron Current Collection

Using the assumptions described in section 2.1.1, the Maxwellian distribution function for electrons, $f\left(u,v\right)$, can be written as [113]

$$f\left(u,v\right)=\frac{m_e}{2\pi k_B T_e}\exp\left[-\frac{m_e}{2k_B T}\left(u^2+v^2\right)\right]. \tag{2.8}$$

The current density through the sheath can then be expressed as

$$j=Nq\int_{0,u_1}^{\infty}\int_{v_1}^{v_2}uf\left(u,v\right)dvdu \tag{2.9}$$

where the lower limit of u is 0 for accelerating potentials and u_1 for retarding potentials. Substituting the Maxwellan distribution into eq. 2.9 and integrating over all tangential velocities and all velocities towards the probe provides the thermal electron current density

$$j_{e_{therm}}=qN_e\sqrt{\frac{k_B T_e}{2\pi m_e}}. \tag{2.10}$$

To model the current collection due to a biased probe using eq. 2.9, first normalize the probe bias by the electron temperature

$$\eta=\frac{q\phi}{k_B T_e}$$

and the electron velocities by the most probable speed as follows

$$u_n=u\sqrt{\frac{m_e}{2k_B T_e}} \qquad v_n=v\sqrt{\frac{m_e}{2k_B T_e}}.$$

Then the total accelerating current will be

$$\begin{aligned}I_e\left(\phi>0\right)&=8\sqrt{\pi}r_s l j_{e_{therm}}\int_0^{\infty}\int_0^{r_p\sqrt{u_n^2+\eta}/\sqrt{r_s^2-r_p^2}}u_n e^{-\left(u_n^2+v_n^2\right)}dv_n du_n\\&=2\pi r_p l j_{e_{therm}}\left(\frac{r_s}{r_p}\operatorname{erfc}\sqrt{\frac{r_p^2\eta}{r_s^2-r_p^2}}+\operatorname{erf}\sqrt{\frac{r_s^2\eta}{r_s^2-r_p^2}}\right)\end{aligned} \tag{2.11}$$

In the thin sheath limit where $r_s\approx r_p$, eq. 2.11 is rewritten as

$$I_{e_{thinsheath}}=r_p l j_{e_{therm}}.$$

The thin sheath limit is effectively equivalent to the electron thermal current collected by the LP. In the thick sheath limit where $r_s/r_p \to \infty$,

$$I_{e_{thicksheath}} = r_p l j_{e_{therm}} \left(\frac{2}{\sqrt{\pi}} \sqrt{\eta} + e^{\eta} \operatorname{erf} \sqrt{\eta} \right)$$

which can be further simplified for values of η greater than 2 to be

$$I_{e_{thicksheath}} = r_p l j_{e_{therm}} \frac{2}{\sqrt{\pi}} \sqrt{1+\eta}. \tag{2.12}$$

This final, simplified form of the thick sheath electron current is the orbit motion limited electron current for cylindrical probes [3]. The retardation current is calculated using eq. 2.9 such that

$$\begin{aligned} I_e\left(\phi \leq 0\right) &= 8\sqrt{\pi} r_s l j_{e_{therm}} \int_{\sqrt{-\eta}}^{\infty} \int_0^{r_p\sqrt{x^2+\eta}/\sqrt{r_s^2-r_p^2}} x e^{-\left(x^2+y^2\right)} dy dx \\ &= 2\pi r_p l j_{e_{therm}} e^{\eta}. \end{aligned} \tag{2.13}$$

As shown in fig. 2.14, the electron retardation current is independent of sheath radius, unlike the accelerated current.

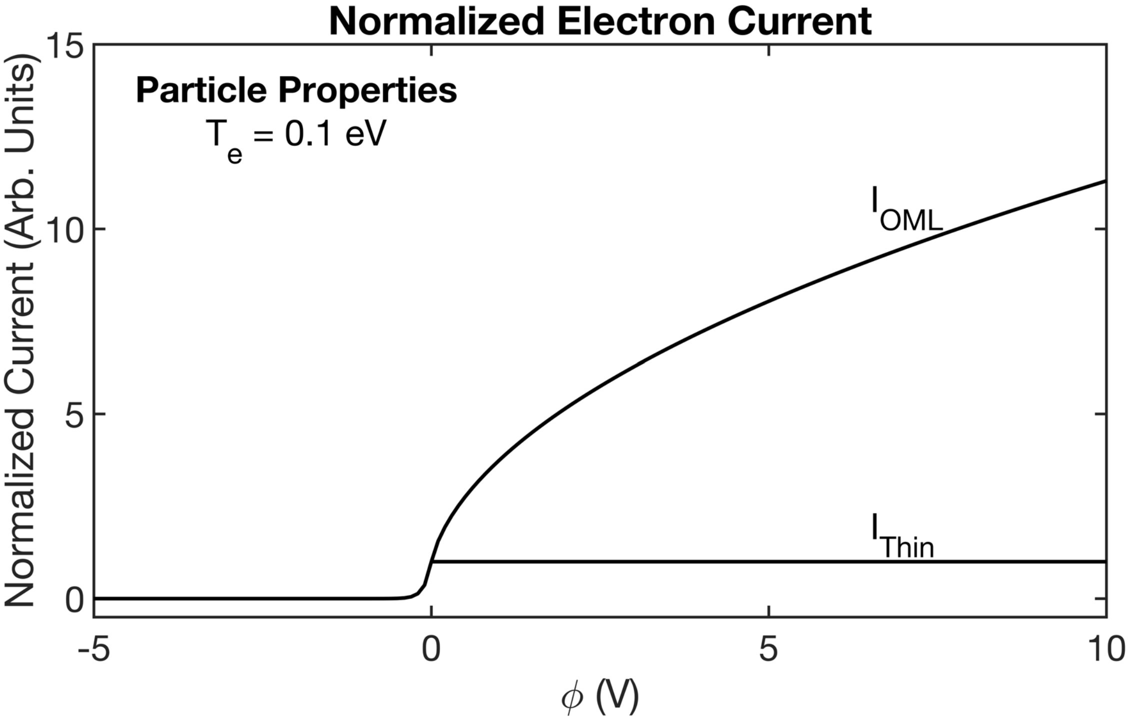

Figure 2.14: Normalize electron current collected by a cylindrical probe as a function of potential relative to the ambient plasma.

2.3.2 Ion Current Collection

Due to the orbital velocity of the spacecraft, the ion population is described by a drifting Maxwellian distribution function, $f(u, v)$, which can be written as [113].

$$f(u,v) = \frac{m_i}{2\pi k_B T_i} \exp\left[-\frac{m_e}{2k_B T}\left((u - v_i)^2 + v^2\right)\right] \tag{2.14}$$

where v_i is the ion drift speed and is equivalent to the orbital speed of the spacecraft. To obtain the ion currents, the normalization is as follows: the probe potential is normalized by the ion temperature,

$$\eta = \frac{q\phi}{k_B T_i},$$

and the radial, tangential, and ion drift speeds are normalized by the most probable ion thermal speeds

$$u_n = u\sqrt{\frac{m_i}{2k_B T_i}} \qquad v_n = v\sqrt{\frac{m_i}{2k_B T_i}} \qquad s = v_i\sqrt{\frac{m_i}{2k_B T_i}}.$$

However, as demonstrated by *Langmuir et. al.* [113] and later in greater detail by *Hoegy et. al.* [114], the introduction of a drift term greatly complicates the calculations, and so the results from *Hoegy et. al.* will be presented without derivation. The general calculations will be done in their normalized form for simplicity but the final results will not be normalized. The normalized ion retardation current is estimated using

$$I_{i_n}(-\phi \leq 0) = \frac{4}{\sqrt{\pi}} \int_{\sqrt{-\eta}}^{\infty} \sqrt{u_n^2 - \eta} \exp\left[-\left(u_n^2 + s^2\right)\right] I_0(2su_n)\, u_n du_n \tag{2.15}$$

where $I_0(2su_n)$ is a modified Bessel function of the first kind. An important distinction in the retardation current is the relationship between probe bias and ion drift speed. When the drift energy is smaller than the probe bias, the retarding current decreases exponentially with bias. However, the current's exponential behavior is overshadowed by the drift energy, approximating the form $I_i \propto \sqrt{s^2 - \eta}$ for large drift energies greater than the retarding bias [114].

For accelerating currents, the full normalized expression is

$$I_{i_n}\left(-\phi>0\right)=\frac{4}{\sqrt{\pi}}\int_{\sqrt{\eta\left(\frac{r_s^2}{r_p^2}-1\right)^{-1}}}^{\infty}\sqrt{u_n^2+\eta}\exp\left[-\left(u_n^2+s^2\right)\right]I_0\left(2su_n\right)u_n du_n+$$
$$\frac{4}{\sqrt{\pi}}\frac{r_s}{r_p}\int_0^{\sqrt{\eta\left(\frac{r_s^2}{r_p^2}-1\right)^{-1}}}\exp\left[-\left(u_n^2+s^2\right)\right]I_0\left(2su_n\right)u_n^2 du_n \tag{2.16}$$

Again, two approximations can be made: 1) the thin sheath approximation and 2) the thick sheath approximation. For the thin sheath approximation, the ion current simplifies to

$$I_{i_{thinsheath}}=qA_pN_i\sqrt{\frac{k_BT_i}{2\pi m_i}}\frac{r_s}{r_p}e^{-\frac{1}{2}s^2}\left[\left(1+s^2\right)I_0\left(\frac{1}{2}s^2\right)+s^2I_1\left(\frac{1}{2}s^2\right)\right]$$

where $I_1\left(s^2/2\right)$ is a modified Bessel function of the first kind.

For thick sheath conditions, there are various approximations based on the magnitude of the ion drift speed and accelerating potential, as well as their ratio relative to each other. The full expression is given as

$$I_{i_{thicksheath}}=qA_pN_i\sqrt{\frac{k_BT_i}{2\pi m_i}}\sum_{n=0}^{\infty}\sum_{m=0}^{\infty}\frac{\left(-s^2\right)^n\eta^m}{n!m!}\left(\frac{\Gamma\left(n+m-\frac{1}{2}\right)}{\Gamma\left(m-\frac{1}{2}\right)\Gamma\left(n+1\right)}-\right.$$
$$\left.\frac{V^{\frac{3}{2}}\Gamma\left(n+m+1\right)}{\Gamma\left(m+\frac{5}{2}\right)\Gamma\left(n+1\right)}\right), \tag{2.17}$$

where $\Gamma()$ are gamma functions. From eq. 2.17, multiple approximations arise depending on the operating region. As $s\rightarrow 0$, the normalized ion current collection approaches the classical orbit motion limited formula to zeroth order

$$I_{i_{thicksheath}}\approx qA_pN_i\sqrt{\frac{k_BT_i}{2\pi m_i}}\left[\frac{2}{\sqrt{\pi}}\sqrt{\eta}+e^{\eta}erf\sqrt{\eta}\right]$$

which, for large values of η, further simplifies to

$$I_{i_{thicksheath}}\approx qA_pN_i\sqrt{\frac{k_BT_i}{2\pi m_i}}\frac{2}{\sqrt{\pi}}\sqrt{1+\eta}. \tag{2.18}$$

For small attractive potentials but very large drift speeds, the accelerated current is nearly identical to the retarding current such that

$$I_{i_{thicksheath}}\approx I_{ret}\left(-\eta\right).$$

Finally, the approximation that is most applicable to the plasmas considered in this work occurs for the case where $\eta + s^2 > 1$. Under these conditions,

$$I_{i_{thicksheath}} \approx qA_pN_i\sqrt{\frac{k_BT_i}{2\pi m_i}}\frac{2}{\sqrt{\pi}}\left(\eta + s^2 + \frac{\frac{1}{2}s^2+\eta}{s^2+\eta}\right)^{\frac{1}{2}}. \tag{2.19}$$

eq. 2.19 simplifies again to the classical OML expression for $s \to 0$ and for $s^2 > \phi$, it becomes the generalized Mott-Smith and Langmuir equation for high drift velocity [113, 114],

$$I_{i_{thicksheath}} \approx qA_pN_i\sqrt{\frac{k_BT_i}{2\pi m_i}}\frac{2}{\sqrt{\pi}}\left(\eta + s^2 + \frac{1}{2}\right)^{\frac{1}{2}} \tag{2.20}$$

$$\approx qA_pN_iv_i\pi^{-1}\left(1+\frac{k_BT_i}{m_iv_i^2}+\frac{2q\phi}{m_iv_i^2}\right)^{\frac{1}{2}}. \tag{2.21}$$

Figure 2.15 shows the differences in normalized ion current collection for drifting and non-drifting ions in both the thin sheath and thick sheath limits. Most notably, the current immediately decays exponentially when the probe bias repels ions in the non-drifting scenario, while the drifting case has non-negligible current collection up until the repelling bias approaches the ion drift energy. Understandably, the thick sheath conditions collect more current than their thin sheath counterparts due to the differences in sheath sizes. Additionally, the drifting scenario collects more current than the non-drifting case due to the additional flux of the drifting component.

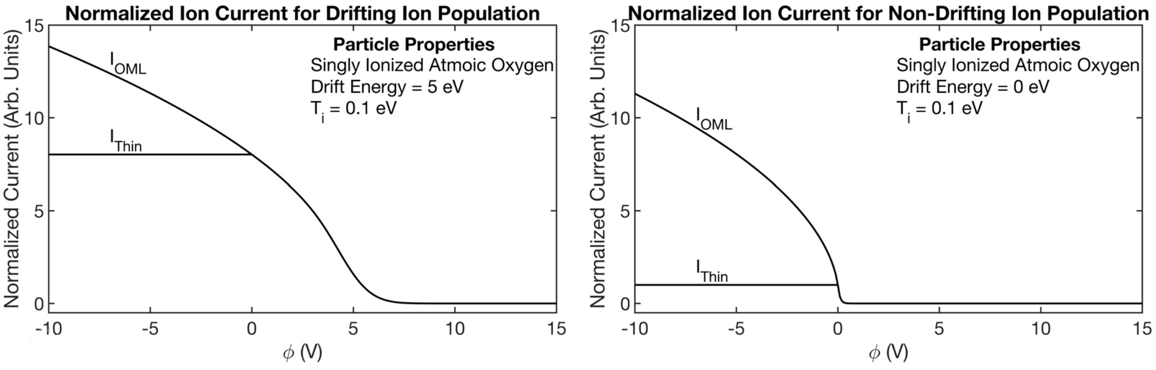

(a) Collected currents for an oxygen ion species drifting at 5 eV.

(b) Collected currents for an oxygen ion species with no drift.

Figure 2.15: Normalized ion current collected by a cylindrical probe as a function of potential relative to the ambient plasma.

2.4 Sources of Error

Up until now, all currents to a probe are due to either ions or electrons sourced by the plasma. Factors that alter this current collection behavior are treated as sources of error. There are two sources of error that are considered: 1) additional sources of current and 2) physical characteristics that affect the probe's current collecting surface. These sources of error must be accounted for in order to fully understand the uncertainties in individual probe operation. These external current sources can also change the probe and spacecraft potentials relative to the plasma and each other. Here we will briefly detail the error terms that spacecraft in orbit may encounter. Calibration methods for many of these uncertainties are possible when carrying multiple probes and are detailed in section 3.3. For a more in depth look at these various charging effects, refer to Hank Garrett's review or Shu T. Lai's book on the subject [115, 89].

2.4.1 Photoelectrons

Photoelectron current is the electron current due to the photoelectric effect caused by solar photons interacting with a conducting surface. For probe biases more negative than the plasma potential, all photoelectron current leaves the surface. However, when the probe is biased above the plasma potential, photoelectrons emitted with energies less than the attractive potential return to the probe's surface. When the probe is biased sufficiently positive relative to the plasma, all photoelectron current returns to the probe. If photoelectron current is substantial, but not accounted for during analysis, the most likely effect is an overestimation of the ion density [116].

Electrons leaving the spacecraft or probes are regarded as negative current to the spacecraft system and will therefore drive the spacecraft potential and probe potentials positive relative to the ambient plasma [118] (see fig. 2.16 for a pictorial representation). For instance, *Brace et. al.* noted that LP measurements of the probes photoelectron emission may have sometimes been impacted due to positive spacecraft potentials [116]. Additionally, if a large enough potential difference exists between the probes and spacecraft (or their sheaths overlap), it is possible for the probes and spacecraft to exchange photoelectrons, further complicating current estimates and data analysis. The full photoelectron current can be estimated using the solar intensity, solar spectrum in the region, the angle between the probe or spacecraft and the sun, and the material emitting photoelectrons [115, 119, 120].

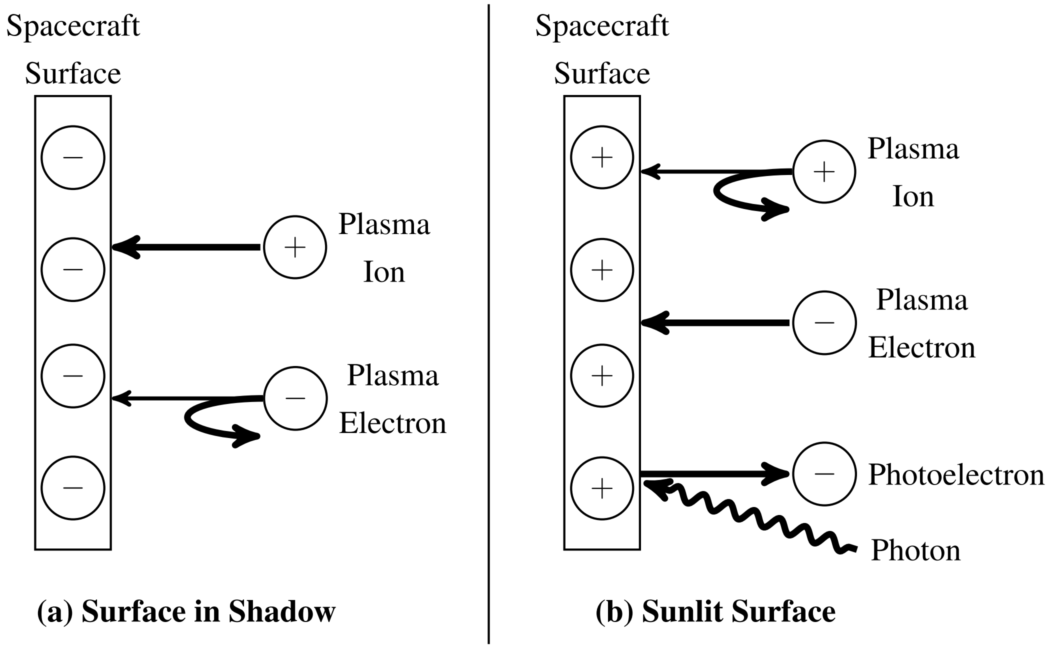

Figure 2.16: Illustration of charge effects due to photoelectrons. Side (a) presents a negatively charged conductor without the presence of solar photons. Side (b) presents a positively charged conductor due to solar radiation. Figure adapted from *Grard et. al.* [117, p. 292]

2.4.2 Secondary Electrons

Secondary electron emission has the same effect as photoelectron emission through a different mechanism. Secondary electron emissions occur when an energetic particle, either an ion or an electron, strikes the surface of a solid with enough energy to eject secondary electrons [121, 122]. Typically, secondary electrons are considered low energy ($<50\,\mathrm{eV}$) [123]. Secondary electron emission is dependent on the energy of the charged particle striking the conductor, referred to as the primary particle, and the solid's stopping power [123, 124]. Figure 2.17 provides an example of the secondary electron yield (SEY) as a function of primary particle energy. SEY (on the y-axis) is expressed as a number representing the ratio between the number of secondary electrons, and the number of incident electrons. SEY curves have a single peak and decay as the primary particle energy increases. Therefore, secondary electron emission occurs within a band of energies, typically between a few eV and up to $50\,\mathrm{keV}$ [125, 126]. If the primary particle energy is too low, not enough energy is deposited to eject an electron from the solid. For very large primary particle energies, the primary particle penetrates the material too deeply for secondary electron emission to occur. When secondary electron emission does occur, the ejected electron will be accelerated away from the surface if the probe or spacecraft is negative relative to the plasma, or be recollected if the probe/spacecraft is positive of the plasma and the electron does not have the energy required to overcome the potential barrier [115, 127].

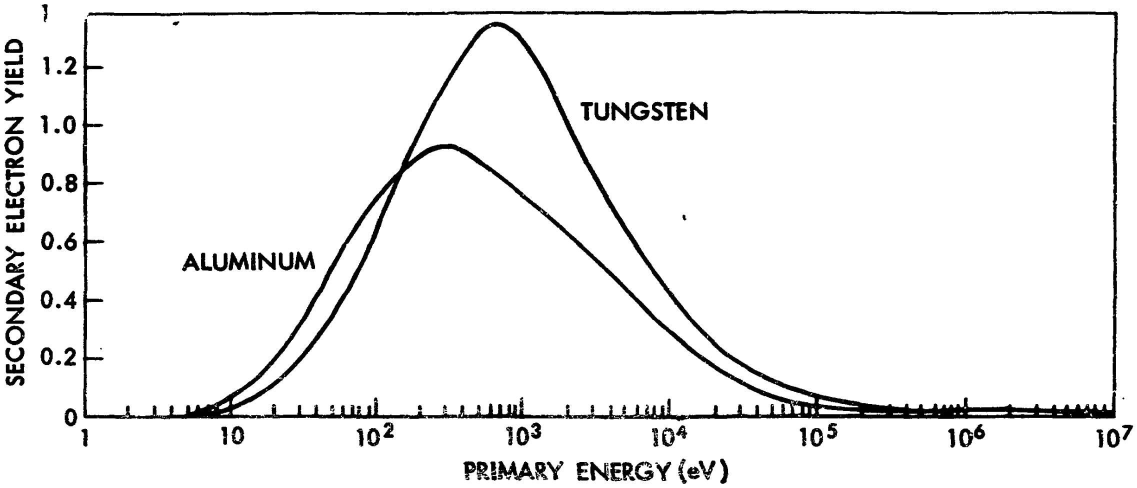

Figure 2.17: SEY curves from electron impact. Image from *Whipple* [128].

While secondary electron emission will raise the potential of the probe or spacecraft, it will typically be much smaller than photoelectron current [120]. Therefore, in regions where secondary electrons emission occurs, it can play a dominant role when photoelectrons are negligible, such as when the spacecraft is shadowed. Moreover, in situations where a significant population of highly energetic charged particles exists, such as the plasma surrounding Saturn, secondary electron emission can produce multiple floating potential biases, affect the slope of the ion saturation regime, and provide insight as to whether the probe is enveloped in its spacecraft's sheath [129, 130, 131].

2.4.3 Auroral Precipitation

For spacecraft stationed in polar orbits, auroral precipitation must be considered as an additional current term when the spacecraft passes through the auroral region (see fig. 2.18). In this region, electrons with energies greater than a kilo-electron volt (sometimes orders of magnitude greater) can be injected into the region due to either a reconnection of the magnetic fields lines in the Earth's magneto-tail or wave-particle interactions [89, 133]. When these energetic electrons interact with a passing spacecraft, the spacecraft potential can experience severe negative charging, disrupting spacecraft functions, and an increase in secondary electron emission current. Defense Meteorological Satellite Program (DMSP) satellites have shown charging levels that exceed -100V, and the DMSP F13 spacecraft

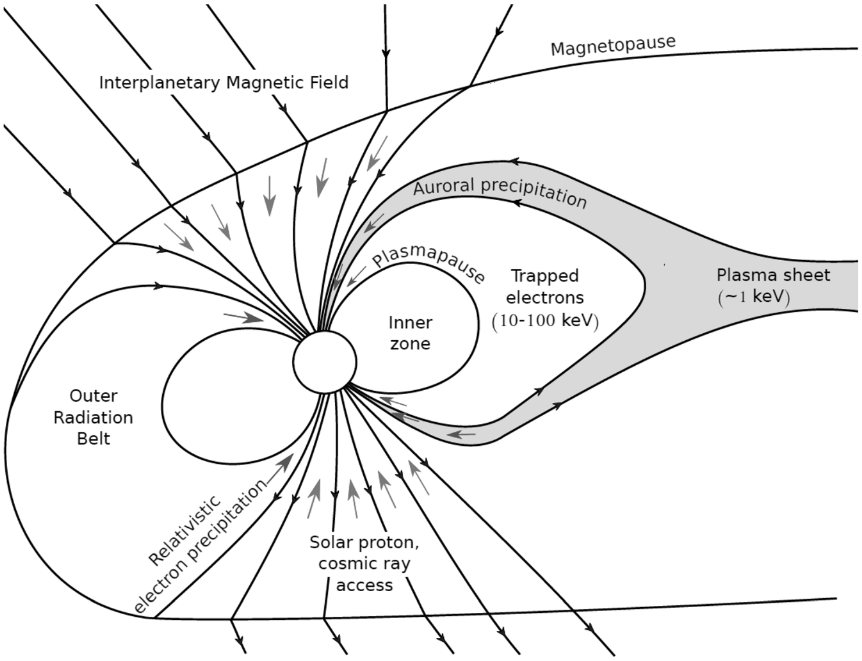

Figure 2.18: Particle precipitation from the Earth's magnetosphere. Auroral precipitation originates from magnetic reconnection. Figure from *Tyssøy* [132, p. 13].

experienced a lockup of its microprocessor unit as an indirect result of a precipitation event [134, 135, 136]. When passing through auroral precipitation, spacecraft charge mitigation is accomplished with a combination of two processes: ensure the charge can move as freely as possible along the spacecraft surface and dissipate the charge from the spacecraft body. When the surface area of the satellite is composed of as many conductive surfaces as possible, charge can equally balance itself along the surface, thus avoid differential charging. To dissipate charge from the spacecraft, a hollow cathode plasma contactor can be used to emit electrons from the spacecraft and collect ions to the more negative sections of the spacecraft [137]. As an example, the ISS uses a plasma contactor to discharge excess electrons, which is engaged when interacting with auroral precipitation [138].

2.4.4 Electromotive Force

Due to the Earth's magnetic field, an electromotive force (emf) is generated between the probe tips and spacecraft as they orbit the Earth. This electromotive force is given as

$$V_{EMF} = -\int_0^l \left(\vec{v}(l) \times \vec{B}(l)\right) \cdot d\vec{l} \tag{2.22}$$

where V_{EMF} is the induced voltage, $\vec{v}$ is the spacecraft velocity, and $\vec{B}$ is the magnetic field along the line probe mast [139]. While this effect is non-negligible for booms and tethers that are longer than a meter or in very strong magnetic fields, it should be considered when designing probes and masts for low density measurements. The simplest way to mitigate the induced emf is to design the booms to be as short as possible or to orient the booms along the ambient magnetic field. However, even with these mitigation techniques, the satellite position along its orbit, its attitude, and the boom orientation should be tracked during instrument operation. Induced emf plays can affect high-impedance probe measurements as was seen on the ISS as more solar arrays and segments were added [140]. Furthermore, variations in the induced voltage can be on the order of the ambient plasma's electron temperature, introducing large errors into electron temperature measurements. For instance, the Freja Cold Plasma Analyzer measured induced emf variations of $\pm 0.5\,\mathrm{V}$, which modulated the collected current of a fixed potential probe with a sinusoidal waveform whose amplitude was roughly $1\,\mu\mathrm{A}$[141]. Using the spacecraft and probe attitudes, in conjunction with either direct measurements of the local magnetic field or models of the magnetic field, such as the International Geomagnetic Reference Field (IGRF) model [142], the induced emf can be calculated and used to adjust the measured high-impedance measurements and the applied potentials of a swept Langmuir probe [141, 143].

2.4.5 Work Function

The work function of a material (measured in eV) is the energy required to remove an electron from the Fermi level of a material to the external vacuum level. This energy difference is highly governed by both bulk and surface conditions [144]. Variability in the work function is due to either contamination of the probe or inhomogeneity of the crystalline structure of the probe's surface [145]. Work function variation inevitably leads to altered I-V characteristics resulting in hotter measured electron temperatures and increased uncertainties for plasma potential measurements (see fig. 2.19) [145, 146]. While there may be variations of the work function along different atomic planes within a single material, as well as anisotropy of its crystal structure, the use of a material with a homogeneous surface work function (variations are small in comparison to the lowest expected electron temperature) is necessary to ensure reliable measurements [147]. To deal with contaminants, periodic cleaning by either ion bombardment or electron heating can be performed [148, 149].

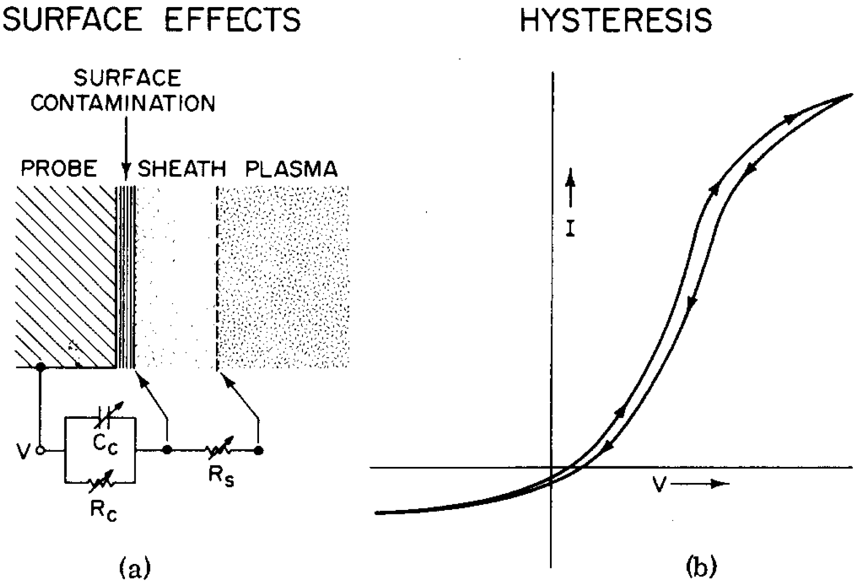

Figure 2.19: a) Effective circuit for work function variation due to surface contaminants. b) Hysteresis effects on I-V curve due to contaminants. Figure from *Szuszczewicz et. al.* [148, p. 5134].

2.4.6 Transient Effects

Transient effects that affect I-V characteristics are numerous and complex. As described by *Lobbia et. al.* [150] and *Schott* [55], the plasma's response to changing probe potentials are limited by : 1) sheath transit time, 2) sheath formation time, 3) plasma resonance, 4) polarization drift, 5) sheath capacitance, 6) stray capacitance. Using the equations provided in *Lobbia et. al.*, some of the minimum elapsed times necessary to avoid transient effects are highlighted in tables 2.1 to 2.3.

The simplest way to overcome the distortions introduced by the first 4 transient effects is to slow the slew rate of the LP sweep to dwell on each voltage step at least three times longer than the various response times that are all governed by the ion plasma period (the inverse of ion plasma frequency). Resolving issues with sheath and stray capacitances requires a combination of managing slew rate, voltage step size, and physical hardware design. Larger voltage step sizes increase the RC time constant of capacitive effects, slowing the slew rate, and so a balance between voltage step size and bias sweep slew rate is required to minimize these effects. Additionally, stray capacitances can be minimized by employing Langmuir probes affixed to triaxial booms, allowing the central conductor and inner shield to be held at the same potential, nearly eliminating stray capacitances [150, 151].

Density (m^{-3})	Sheath Transit (ms)	Sheath Formation (ms)	Resonance (ms)
4.1×10^9	3.1×10^{-2}	3.1×10^{-2}	1.1×10^{-4}
1×10^{10}	2.0×10^{-2}	2.0×10^{-2}	7.2×10^{-5}
1×10^{11}	6.3×10^{-3}	7.6×10^{-3}	2.5×10^{-5}
7×10^{11}	2.4×10^{-3}	4.0×10^{-3}	1.1×10^{-5}

Table 2.1: Temporal limits of LP slew rates based on ion sheath transit, ion sheath formation in a flowing plasma, and the resonance between probe potential and plasma oscillations for a range of possible densities found in the Earth's ionosphere.

	Settle Time (ms)		
Density (m^{-3})	ΔV_{A_1} =$0.001\,\mathrm{V}$	ΔV_{A_2} =$10\,\mathrm{V}$	ΔV_{A_3} =$20\,\mathrm{V}$
4.1×10^9	7.1×10^{-4}	0.73	1.5
1×10^{10}	4.6×10^{-4}	0.47	0.93
1×10^{11}	1.4×10^{-4}	0.15	0.30
7×10^{11}	5.4×10^{-5}	0.06	0.11

Table 2.2: Temporal limits of LP slew rates, in milliseconds, based on sheath capacitance for 3 voltage step sizes and a range of possible densities found in the Earth's ionosphere.

	Settle Time (ms)		
Density (m^{-3})	ΔV_{A_1} =$0.001\,\mathrm{V}$	ΔV_{A_2} =$10\,\mathrm{V}$	ΔV_{A_3} =$20\,\mathrm{V}$
4.1×10^9	8.2×10^{-3}	8.4	16.8
1×10^{10}	3.4×10^{-3}	3.45	6.9
1×10^{11}	3.4×10^{-4}	0.35	0.69
7×10^{11}	4.8×10^{-5}	0.05	0.10

Table 2.3: Temporal limits of LP slew rates, in milliseconds, based on stray capacitance for 3 voltage step sizes, and a range of possible densities found in the Earth's ionosphere, and a stray capacitance of $1\,\mathrm{pF}$.

2.4.7 Probe End Effects

While cylindrical LP theory assumes infinitely long probes to ignore end effects, spacecraft missions and additional development of theory has demonstrated that end effects can enhance ion current collection when the probe is aligned, or nearly aligned, with the ion flow direction, depending on drift velocity, ion-ion collisions, and Debye length to probe radius ratio [152, 153, 154]. Ignoring these end effects greatly impacts the accuracy of ion density measurements, which are typically considered more accurate than electron density measurements [3, 153]. Maintaining probe lengths that are much greater than their diameter and guarding one end of the probe helps minimize these effects, but will not make them vanish. However, probes oriented transverse to the ion flow are unaffected by end effect issues [155, 156, 3].

CHAPTER 3

The Twin-Probe Method

The twin-probe method is a multi-purpose Langmuir probe instrument technique that improves the accuracy of LP measurements under restrictive probe-to-spacecraft surface area ratio conditions. The chief application is to correct the effects of induced spacecraft charging by tracking the spacecraft potential while an LP is being swept across various biases relative to the spacecraft. A secondary benefit is the calibration capabilities due to the virtue of having two physically identical probes aboard the spacecraft.

3.1 Formulation of the Twin-Probe Method

As a short summary of the discussion in chapter 1, during Langmuir probe operation, as the LP collects ion or electron current under different bias conditions, the electric potential reference of the probe must collect an equal but opposite current to achieve net-zero current collection in the probe-spacecraft system. It is thus essential to think of the LP on a spacecraft as half of a double probe configuration. On very large spacecraft, this current balance requirement is non-restrictive, as the spacecraft's conductive surface area can be made much larger than the probe's surface area, and currents can be balanced by very small changes to the spacecraft potential [56]. However, on small satellites, the current collection area ratio is not sufficiently large, and the I-V curve is impacted by the spacecraft's charging behavior as the probe is swept. This is primarily an issue when the LP is biased positive relative to spacecraft electrical common and collects net electron current. In this situation, the satellite must collect equal current from the ambient ion population whose thermal flux is a factor of 100 less than the electron thermal flux for the same density and temperature. As a result, the spacecraft charges negatively to collect enough ion current to balance the electron current collected by the LP [3, 61]. By adjusting the Langmuir probe sweeps using a tracked spacecraft potential, corrected I-V curves are produced imitating LP sweeps from a stable reference, thus improving in-situ measurements. The twin-probe method is an effective technique to use the spacecraft potential to correct the I-V curves.

The twin-probe method requires a Langmuir probe and an instrument capable of tracking the spacecraft potential relative to the ambient plasma during LP operation. As discussed in section 1.3, the applied voltage between the LP and spacecraft is given by

$$V_A = \phi_{LP} - \phi_{SC}$$

By measuring ϕ_{SC}, ϕ_{LP} can be calculated by adding ϕ_{SC} to the known applied voltage. Since ϕ_{LP} is unaffected by the spacecraft potential, it is possible to plot the collected current as a function of ϕ_{LP} and produce a current-voltage graph devoid of spacecraft charging effects. The corrected I-V curve can then be used to obtain more accurate electron density and temperature measurements.

Figure 3.1 provides an example of multiple LP sweeps referenced against a CubeSat and their twin-probe corrected I-V curves for the same plasma conditions (experiment conditions can be found in section 5.1). Interestingly, while the uncorrected sweeps have a wide spread, after twin-probe corrections the resultant I-V characteristics have a considerably smaller spread and are nearly aligned with a control sweep referenced against the vacuum chamber.

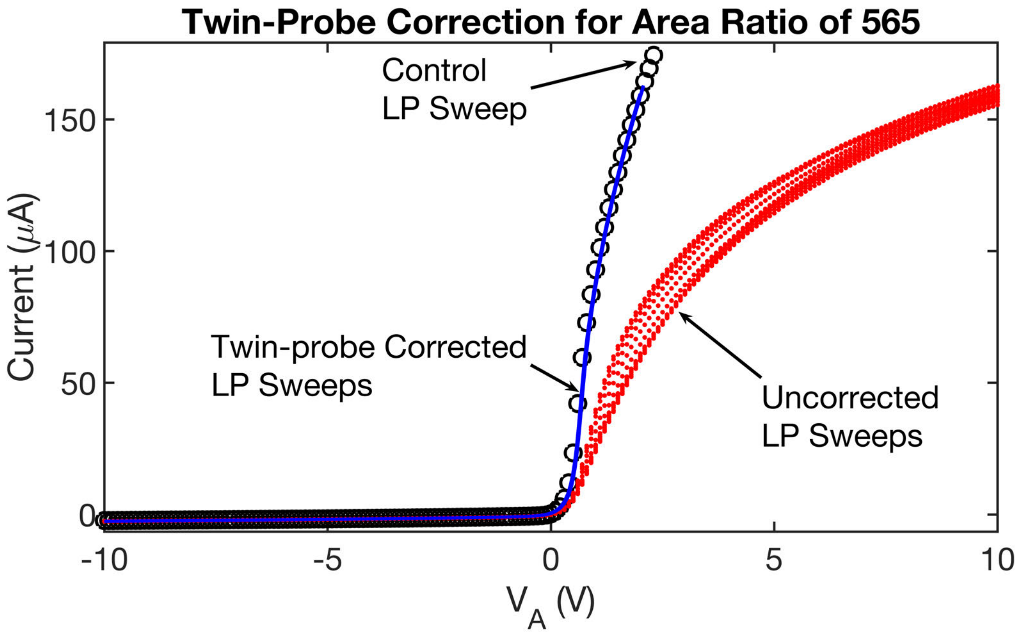

Figure 3.1: Example of measured I-V curve correction using the twin-probe method. The red bundle of solid dots corresponds to sweeps referenced against the spacecraft. The blue bundle of solid lines are sweeps corrected using the twin-probe method, and the single black line of circles is a control sweep referenced against the chamber.

One way to track the spacecraft potential is to use a high-impedance probe, an instrument which consists of an LP kept electrically isolated from spacecraft common using a sufficiently large resistance (discussed in section 4.4.4 and shown in fig. 4.19) that is placed well outside of a disturbance sheath around the charged spacecraft. The high-impedance probe will be close to its natural floating potential, while the spacecraft will either be at its floating potential or in a charged state. As shown in fig. 3.2, the input impedance, R_{in}, electrically isolates the high-impedance probe from the spacecraft and allows for accurate measurements to changes in the spacecraft potential. R_{in} must be large enough such that $I_{LP} >> I_{HI}$ to ensure the current to the high-impedance probe does not affect the spacecraft potential. However, R_{in} has an upper bound based on the current sense circuitry because I_{HI} must be above the noise floor of the circuitry.

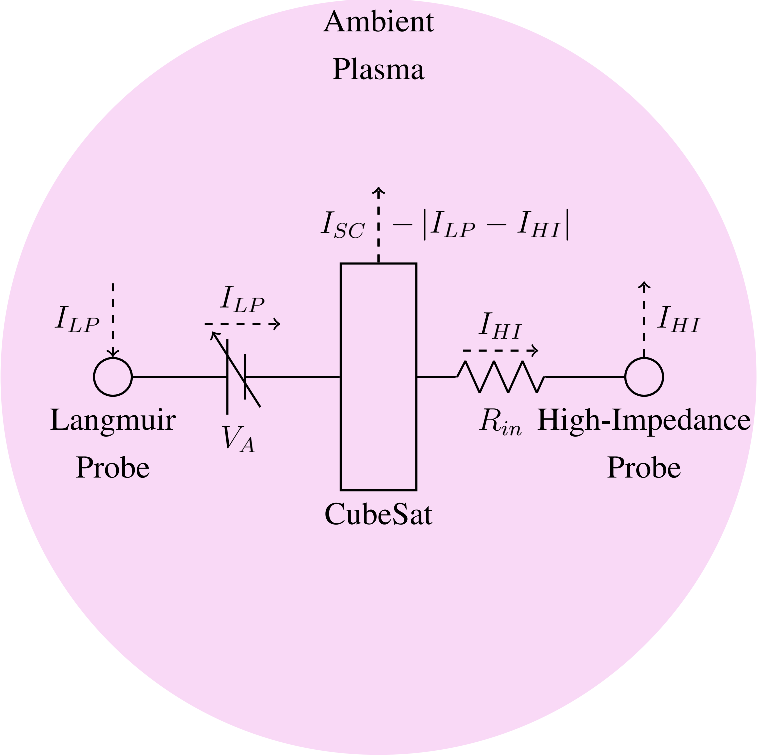

Figure 3.2: General schematic of depicting current flow between the LP, spacecraft, high-impedance probe, and the ambient plasma.

As noted by *Mozer* [157], the potential difference between the probe and spacecraft is given by

$$\Delta V = I_{HI} R_{in} = \frac{\phi_{HI} - \phi_{SC} + \vec{E}_T \cdot \vec{d}_{HI} + WF_{HI} - WF_{SC}}{\gamma} \tag{3.1}$$

where γ is

$$\gamma = 1 + \frac{R_{HI}}{R_{in}} + \frac{R_{SC}}{R_{in}}, \tag{3.2}$$

and $\vec{E}_T$ is

$$\vec{E}_T = \vec{E} + \vec{v} \times \vec{B}; \tag{3.3}$$

ϕ_{HI} is the high-impedance probe's potential relative to the ambient plasma; $WF_{HI} - WF_{SC}$ is the difference in work functions of the high-impedance probe and spacecraft, or their contact potential difference (in units of V); R_{in} is the input impedance between the spacecraft and probe; R_{HI} and R_{SC} are the sheath resistance of the high-impedance probe and spacecraft; $\vec{E}_T$ is the total electric field given by the ambient electric field, $\vec{E}$, the magnetic field, $\vec{B}$, and the probe's orbital velocity, $\vec{v}$; and $\vec{d}_{HI}$ is the vector separation between the high-impedance probe and spacecraft.

The contact potential difference and the potential difference induced by the ambient electric and magnetic fields are sources of error for high-impedance instrument measurements. A discussion of the sources of error for the twin-probe method and ways to calibrate for them is found in section 3.3. Additionally, the measured potential difference is attenuated by γ, which is a natural resistance divider composed of the high-impedance probe's input resistance and sheath resistances. The effect of the magnitude of the input resistance, and by extension γ, is shown in fig. 4.19 and discussed in its accompanying text. To mitigate this attenuation, the probe input resistance must be sufficiently larger than either sheath resistance terms (demonstrated in fig. 4.19). However, as will be discussed in section 3.2.2, the settle time of the measurement will increase with decreasing plasma density even when using a sufficiently large input impedance.

Using the diagrams in fig. 3.3, the potential terms can be summed to give

$$V_A = \phi_{LP} - \phi_{SC} + \vec{E}_T \cdot \vec{d}_{LP} + WF_{LP} - WF_{SC} \tag{3.4}$$

where $WF_{LP} - WF_{SC}$ is the difference in work functions of the LP probe and spacecraft, and $\vec{d}_{LP}$ is the vector separation between the Langmuir probe and spacecraft. Similarly to eq. 3.1, two error terms have appeared when operating only the swept LP: 1) the induced potential difference from the total ambient electric field and 2) the difference in work function between LP and SC.

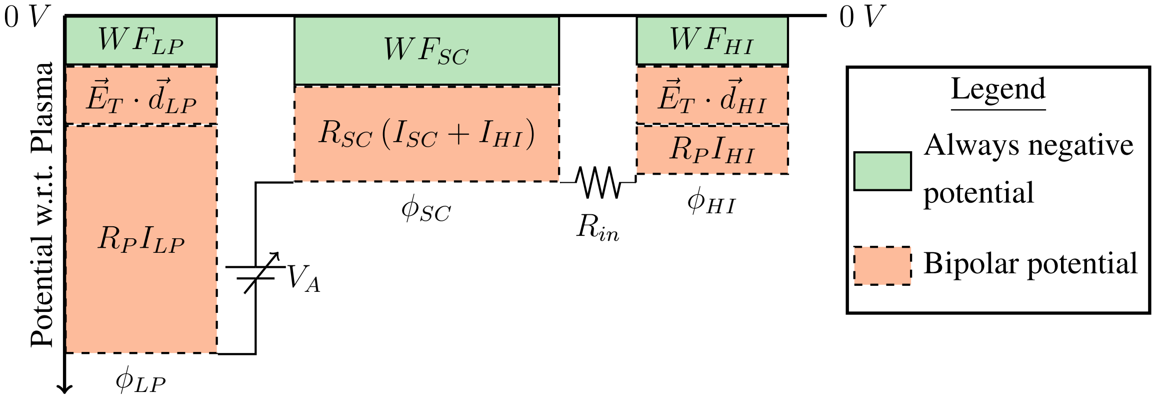

(a) Potential diagram of the LP, high-impedance probe, and S/C relative to the ambient plasma for a negative applied bias to the LP.

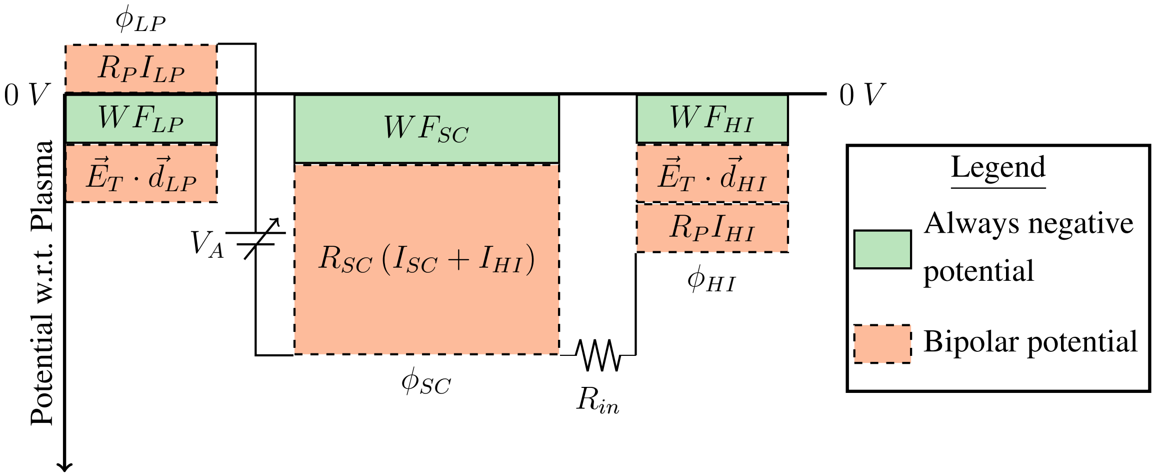

(b) Potential diagram of the LP (ϕ_{LP}), high-impedance probe (ϕ_{HI}), and spacecraft relative (ϕ_{HI}) to the ambient plasma for a positive applied bias to the LP, such that its in the electron saturation region.

Figure 3.3: Diagrams of spacecraft's charging response to positive and negative applied biases to an LP.

When operated independently, the high-impedance probe and swept LP will have uncertainties associated with differing work functions relative to the spacecraft and ambient electric fields as previously stated. However, the uncertainties due to differing work functions can be mitigated by using two physically identical probes. The work functions of the two such probes can be assumed to be roughly the same by ensuring surface probe cleanliness and equivalent manufacturing. By combining eqs. 3.1 and 3.4, we obtain

$$\phi_{LP} = V_A + (\phi_{HI} - \gamma \Delta V) + \vec{E}_T \cdot \left(\vec{d}_{HI} - \vec{d}_{LP}\right) + WF_{HI} - WF_{LP} \tag{3.5}$$

Equation 3.5 gives a more complete correction for the changing spacecraft potential than eq. 1.5 or eq. 3.4 in terms of measurable parameters. The change in potential due to the ambient electric field can be managed using a two-pronged method by: 1) measuring and/or modeling the ambient electric and magnetic fields, and 2) tracking the attitude of spacecraft and probes with respect to the ambient environment (e.g. plasma, magnetic field, electric field). Finally, ϕ_{HI} cannot be directly measured but can be approximated as outlined in section 3.3.2.

Equation 3.5 can be understood pictorially using fig. 3.3 and the discussion in section 1.3.2. In the case when the Langmuir probe is biased negatively of the spacecraft, as shown in fig. 3.3a, the spacecraft potential remains relatively steady. When the probe is biased sufficiently positive of the spacecraft, as shown in fig. 3.3b, the spacecraft charges negatively, limiting the probe potential relative to the plasma. However, while the spacecraft potential varies between the two cases, the high-impedance probe's floating potential remains stable. Therefore, by tracking the changing potential difference between the high-impedance probe and spacecraft, ΔV, the Langmuir probe's reference can be shifted from the spacecraft to the high-impedance probe. In order to achieve this, a sufficiently large impedance is necessary to minimize I_{HI}, such that it is much smaller than I_{LP}, ensuring a stable high-impedance probe potential (refer to fig. 3.2). Discussions on the criteria of the minimum impedance are given in sections 3.2.2 and 4.4.4.

3.2 Implementation Considerations

To successfully implement the twin-probe method, two design parameters must be considered: the position of both probes and the bias slew of the swept probe. Probe position must be considered to ensure that the ambient, unperturbed plasma environment is properly sampled and referenced. Considering the bias slew rate of the swept probe ensures that the high-impedance probe has enough time to obtain accurate measurements of the spacecraft potential.

3.2.1 Sheath Expansion

Both the high-impedance probe and LP must be adequately located outside the spacecraft sheath to sample the unperturbed ambient plasma environment. The local electrostatic potential grows exponentially when approaching the spacecraft body through its sheath. Thus when the high-impedance probe is too close to the spacecraft (i.e. in the sheath), this perturbed potential is measured in place of the ambient plasma potential, reducing the accuracy of the measured spacecraft potential. These local potential structures are further complicated in the wake of the spacecraft, where the ion and electron depletion region distorts both LP sweeps and spacecraft potential measurements [105, 158]. Therefore, it is important to calculate the spacecraft sheath size when designing the probes' deployable boom structures. The booms are coated in an insulating material (e.g. Kapton) to collapse the boom's sheath and ensure the LP remains in the unperturbed plasma environment [159]. Sheath estimates for a range of negative spacecraft potentials are especially critical, since Langmuir probe operation generally causes negative spacecraft charging and significant sheath expansion. Typically, positive spacecraft potentials will produce a smaller sheath, since the repelled ions are more massive, and sheath shape is dominated by phenomena like ram/wake effects [160].

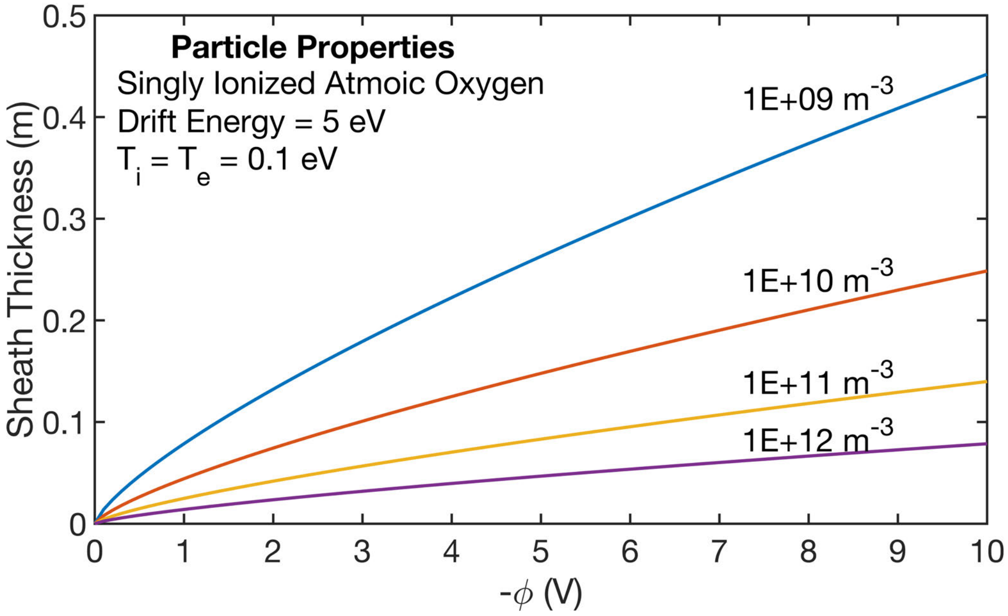

Figure 3.4: Sheath thickness as a function of negative spacecraft voltage and plasma density. The sheath thickness becomes increasingly large with decreasing plasma density.

To estimate the sheath expansion, the collected ion current to a spacecraft surface can be compared to the space-charge limited electron current collection [159]. These calculations are a conservative estimates since the collected currents are affected by both spacecraft geometry and the asymmetric, spacecraft potential dependent sheath [161, 162, 163, 164]. As an example, consider the sheath of the $0.1\,\mathrm{m}\times 0.3\,\mathrm{m}$ face of a 3U CubeSat in low-Earth orbit. The current collected on the planar surface due to the drifting ions was shown to be eq. 2.5 in section 2.2. From the Child-Langmuir Law [165], the maximum current between a sharp sheath edge and the surface of the planar probe is

$$I_i = \frac{4A_p\epsilon_0}{9}\sqrt{\frac{2q}{m_e}}\frac{\phi^{\frac{3}{2}}}{d^2} \tag{3.6}$$

where d is the sheath thickness. After equating eqs. 2.5 and 3.6, the sheath thickness as a function of plasma density and negative spacecraft voltage can be estimated (see fig. 3.4). Therefore, one can estimate that when operating in plasma densities of at least $1 \times 10^{10}\,\mathrm{m}^{-3}$ of Earth's ionosphere, for instance, a $0.3\,\mathrm{m}$ long boom will be sufficiently long to keep the probes outside of the spacecraft sheath for applied probe biases up to $10\,\mathrm{V}$.

3.2.2 RC Time Constant

Similar to the problem of sheath expansion, ensuring that the high-impedance probe can settle before making a measurement is a high priority to guarantee accurate measurements. As seen in fig. 3.5, the Langmuir probe in a representative high-impedance configuration will form a low pass filter from the boom capacitance and the plasma resistance in parallel with the input resistance of the high-impedance probe. Therefore, to calculate the RC time constant, or settle time, of the high-impedance probe, two characteristics of the system must be known: 1) the total resistance of the plasma and input resistances; and 2) the boom capacitance. Examples of tabulated settle times and high-impedance measurement accuracy may be found in table 3.1.

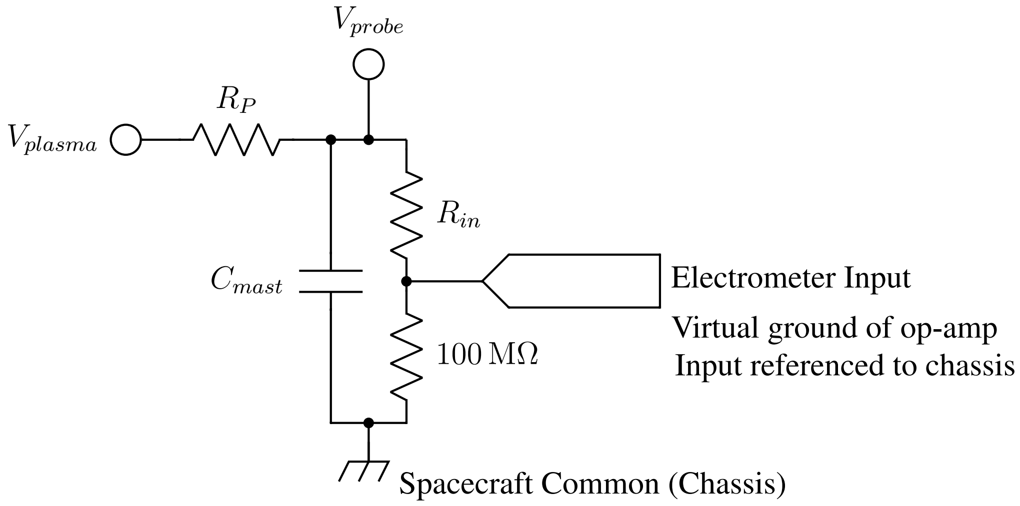

Figure 3.5: General circuit for a high-impedance probe; adapted from *Gilchrist* [159]. The RC time constant ultimately determines the spacecraft potential measurement cadence.

Calculating the total resistance of the system first requires a calculation of the plasma's resistance, R_P. R_P is obtained by linearizing the inverse of the net current to the LP around the floating potential [157] (see eq. 3.7). Therefore, the ion and electron currents must be known to determine both the floating potential and the net current's dependence on voltage. Since the velocity of spacecraft in LEO will be greater than the ion thermal speed, the current collection to a cylindrical probe can be described using eqs. 2.13 and 2.21 for any potential below the plasma potential [3].

$$R_P = \left(\frac{dI}{dV}\right)^{-1}\Bigg|_{V=V_{Floating}} \tag{3.7}$$

With a known plasma resistance, the probe's settling time and accuracy can both be estimated. From fig. 3.5, the input impedance, R_{in}, forms a voltage divider circuit with the plasma resistance. Therefore, the error in potential measurements (in units of volts) is related to the voltage divider circuit, and can be calculated using

$$\sigma_{Meas} = \Delta V \left[1 - \frac{R_{in}}{R_P + R_{in}}\right] \tag{3.8}$$

where the input impedance is $1\,\mathrm{G\Omega}$ in table 3.1, and ΔV is the measured potential difference between the high-impedance probe and spacecraft. There is an inverse relationship between the plasma density and plasma resistance. As a result, the error in the tracked spacecraft potential will be non-negligible for lower plasma densities, effectively making the twin probe method more inaccurate and more difficult to properly implement. Assuming all other sources of error are accounted for, when applying the twin-probe correction, the uncertainty in the applied bias is given by

$$\sigma_V = \sqrt{\sigma_{V_{inst}}^2 + \left(\sigma_{meas}\right)^2} \tag{3.9}$$

where σ_V is the uncertainty of corrected voltage, in units of volts, and $\sigma_{V_{inst}}$ is the instrumental uncertainty of the applied bias between the LP and SC.

To calculate the settle times, the boom capacitance, C_{Boom}, must also be known. Assuming a guarded Langmuir probe is used with an external shield in a triaxial configuration, a conservative estimate for the capacitance is $50\,\mathrm{pF\,m^{-1}}$. To determine the length of cable and mast needed, further assume that $0.15\,\mathrm{m}$ of cable is needed within the notional CubeSat, and the boom length is just long enough to remain out of the sheath, using the estimates shown in fig. 3.4. With a calculated plasma resistance and capacitance, and known input resistance, the settle time of the high-impedance probe can be determined using eq. 3.10 where the settling time is assumed to be three times larger than the RC-time constant of the high-impedance probe. As shown in table 3.1, the plasma resistance will dominate for sufficiently large plasma densities; however, at low densities, the plasma resistance approaches the same order of magnitude as the input resistance, and so the total resistance is split between the two impedances. When compared to the settling times calculated in section 2.4.6, the limit of the impedance probe is comparable to, and in some cases, are more restrictive than the limits imposed by sheath and stray capacitive effects.

$$\tau = 3C_{Boom}\left(\frac{1}{R_{in}} + \frac{1}{R_P}\right)^{-1} \tag{3.10}$$

$N_i\,(\mathrm{m}^{-3})$	$R_p\,(\Omega)$	$R_{Total}\,(\Omega)$	$\sigma_{Meas}/\Delta V\,(\%)$	$C_{Boom}\,(\mathrm{pF})$	$\tau\,(\mathrm{ms})$
1×10^{9}	3.49×10^{8}	2.56×10^{8}	26	30	29.4
1×10^{10}	3.49×10^{7}	3.38×10^{7}	3.4	20	2.08
1×10^{11}	3.49×10^{6}	3.49×10^{6}	0.35	15	0.16
1×10^{12}	3.49×10^{5}	3.49×10^{5}	0.03	10	0.01

Table 3.1: Impedance probe potential errors and settling time constants relative to plasma density.

3.3 Calibrating for Additional Current Sources

As discussed in section 3.1, the twin-probe method is instrumental in correcting the I-V curves of swept LPs affected by unstable spacecraft potentials. The additional benefits of carrying two identical Langmuir probes cannot be understated. The currents collected by each probe can be directly compared, when in similar plasma environments, to calibrate for the additional sources of current described in section 2.4, and provide internal consistency checks. In this section, the methods of calibrating for various sources of error are discussed.

3.3.1 Photoelectrons

As discussed in section 2.4.1, photoelectrons can raise the potentials of conductors relative to the ambient plasma environment and produce currents in the ion saturation regime of I-V curves that are larger than they would be in the absense of solar photons. Figure 3.6 provides a comparison between two I-V curves for plasma conditions found in Earth's ionosphere: one that includes photoelectron current (sunlit) and one that collects only plasma currents (shadowed). For this example, the LP is assumed to be rhenium coated and orthogonal to the solar photons, such that the area of photoelectron emission is maximized. The photoelectron emission flux, Γ_{pe}, was determined from the maximum photoelectron current ($11.7\,\mathrm{nA}$) and emission area ($2.14 \times 10^{-4}\,\mathrm{m}^2$) quoted by *Brace et. al.* from solar EUV measurements made at Venus by the PVO Langmuir probe [116]. Γ_{pe} is adjusted to account for the decreased solar photon flux that reaches Earth. The photoelectron current was estimated using the characterization determined by *Pederson* [166],

$$\begin{aligned} I_{pe}(\phi > 0) &= I_{pe_0}\left[\exp\left(-\frac{\phi}{2}\right) + 0.0375\exp\left(-\frac{\phi}{7.5}\right)\right] \\ I_{pe}(\phi <= 0) &= I_{pe_0} \end{aligned} \tag{3.11}$$

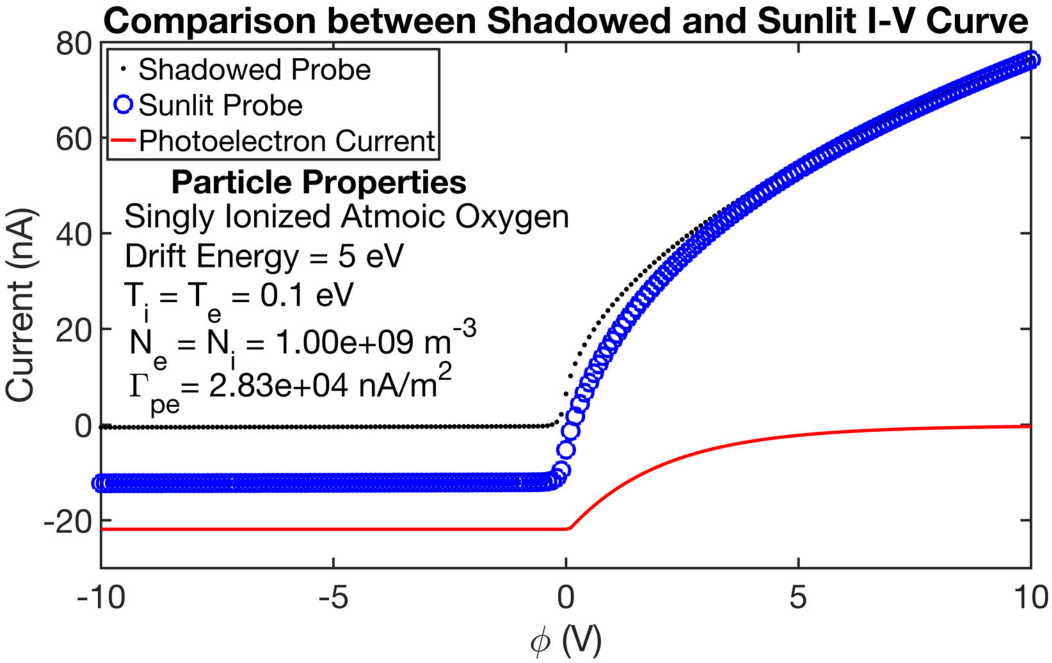

Figure 3.6: Comparing current collection difference between a sunlit and shadowed probe in a low-density plasma.

Photoelectron current is a significant source of error for ion density estimates when the plasma density is low ($<1 \times 10^{10}\,\mathrm{m}^{-3}$) [3]. To calibrate for photoelectrons in orbit, the spacecraft must be oriented such that both Langmuir probes are oriented perpendicular to the orbital velocity while one probe is in shadow. While in this orientation, both probes can be set to a constant, negative bias with respect to the spacecraft so they collect exclusively ion current. If the photoelectron current is significant, there will be a discrepancy between the sunlit probe and the shadowed probe due to photoelectron emission (see fig. 3.6). This current can then be used during data analysis to adjust the I-V measurement of the swept Langmuir probe.

3.3.2 High Impedance Probe Floating Potential

Ideally, it is assumed that the high-impedance probe is at the same potential as the ambient plasma. However, the higher mobility of the electrons when compared to the ions will cause the probe's floating potential to be slightly negative of the plasma. The potential difference between the ambient plasma and the floating potential is an offset in the tracked spacecraft potential measurements that shifts with changes in the plasma environment. To correct for the floating potential of the high-impedance probe, eq. 3.5 must be considered with a few assumptions. First, let the input resistance be sufficiently high such that the voltage division factor (eq. 3.2), γ, approaches unity. A discussion on the necessary minimum impedance is given in section 4.4.4. Furthermore, assume that the ambient total electric field is perfectly accounted and the work functions of the swept probe and high-impedance probe are identical. Finally, assume the probe is in a quiescent plasma, and its orientation relative to the flow does not change. Under these conditions, the high-impedance probe's floating potential can be estimated when the swept probe is at the plasma potential as shown in eq. 3.12. Equation 3.12 can then be used to estimate the high-impedance probe potential relative to the plasma using eq. 1.5, or, for higher accuracy estimates eq. 3.4,

$$\phi_{HI} = (\Delta V - V_A)|_{V_A = V_P} \tag{3.12}$$

where V_P is the plasma potential.

3.3.3 High-Impedance Measured with Variable Angle of Attack

Should any of the above assumptions break down, the uncertainties of the measured spacecraft potential and high-impedance probe floating potential increase. The most difficult assumptions to maintain are the constant orientation relative to the plasma flow and the condition of a quasi-steady plasma. By modeling the net current to a probe, using eqs. 2.13 and 2.16, it is possible to estimate the variation in the high-impedance probe's floating potential as the probe's orientation relative to the plasma flow changes. Figure 3.7 shows that the floating potential is estimated to change by about $0.1\,\mathrm{V}$ as the probe transitions from being parallel to being perpendicular to the plasma flow. If this transition occurs during a Langmuir probe sweep, when the twin-probe technique is being implemented, then the tracked spacecraft potential may be modulated by the rotation of the spacecraft. If the rotation rate is significant enough to modulate the measured spacecraft potential, high-impedance measurements should be performed, without operating the Langmuir probe, to calibrate tracked spacecraft potential measurements during Langmuir probe operations. A general approach to this method is to first make successive high-impedance measurements for at least one full rotation of the satellite, to serve as calibration data. Then, before and after operating the Langmuir probe in conjunction with the high-impedance probe, the attitude of the spacecraft is measured. Using knowledge of the satellite attitude, its rotation rate, and calibrated data, each measurement of the tracked spacecraft potential is adjusted to provide more accurate values.

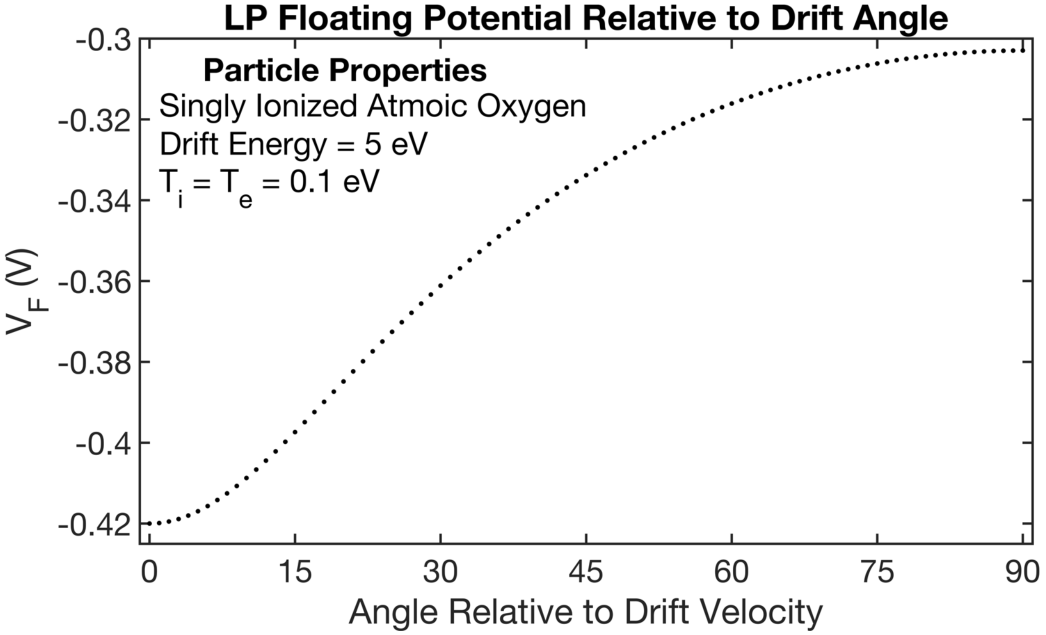

Figure 3.7: Modeled floating potential of a cylindrical probe for various angles relative to the plasma flow. 0° corresponds to a probe oriented parallel to the plasma flow and 90° represents a probe oriented perpendicular to the plasma flow.

3.3.4 Work Function

As the work function can be highly variant, even within a single material, it could be a significant source of error in high-impedance measurements. Since the collection of electrons and ions have a dependency on the work function as a potential barrier [27], any difference in work function between the probes will manifest as an error term in the measurement [167, 168, 157]. To mitigate error in the measured spacecraft potential, both probes' work functions must be accounted for. The first step to reducing the uncertainty due to the work function difference of the probes is to minimize the material differences between the two Langmuir probes and periodically clean the probes during flight. While a portion of the spacecraft potential measurement's error is due to the difference between the high-impedance probe's work function and the satellites's work function, as shown in eq. 3.5, operating identical probes eliminates the uncertainties due to this work function difference. This is because the work function difference between a probe and its satellite affects both the swept probe and the high-impedance probe. This difference cancels out when both probes are used in tandem.

CHAPTER 4

Plasma Spacecraft Interaction Codes for Low Earth Orbit: Twin-Probe Method Modeling using Analytic Methods

Understandably, performing in-chamber and in-orbit experiments for all possible spacecraft and instrument configurations is infeasible and prohibitively expensive. To predict the spacecraft's charging behavior, *NASA/Air Force Spacecraft Charging Analyzer Program (Nascap-2K)* models and MATLAB codes, called the Plasma Spacecraft Interaction Codes for Low Earth Orbit (PSIC-LEO), were developed independently. The *Nascap-2K* program allowed for various types of calculations (e.g particle-in-cell (PIC) and analytic expressions) under different spacecraft orientations, orbital speeds, and material components and is detailed in appendix A. This PSIC-LEO codes allow for faster calculations, relative to *Nascap-2K*, and iterative spacecraft design modeling.

The PSIC-LEO program was created by Dr. Walter R. Hoegy and Omar Leon at the University of Michigan. The PSIC-LEO codes perform "back of the envelope" calculations to estimate spacecraft charging behavior and understand how Langmuir probe measurements are impacted by an unstable spacecraft platform. The discussion of the PSIC-LEO program covers

- Spacecraft charging for different area ratios.
- The impact of spacecraft charging on uncorrected and corrected measurements of electron temperature and density.
- Estimates on the smallest possible allowed area ratio between the swept Langmuir probe and referenced satellite.

The PSIC-LEO codes calculate the spacecraft potential that balances the currents between the spacecraft and a Langmuir probe for a given applied LP potential. In its current state, the PSIC-LEO models current collection to small, cuboid shaped spacecraft that do not have large deployable surfaces (e.g. solar panels). For simplicity, this section focuses on the CubeSat, a subset of these small cuboid spacecraft. To properly discuss the results of the codes, this section will first cover its assumptions and the models used to estimate current collection to a CubeSat and LP. Then, the results of the simulations are discussed. The full code can be found in appendix B.

4.1 General Procedure and Assumptions

The specific current models used to determine the current balance are detailed in section 4.2, but the codes estimate the spacecraft potential using the following procedure:

1. Simulation parameters are given to the codes. Examples of simulation parameters are:
    - Plasma properties such as density, ion drift speed, and electron temperature.
    - CubeSat and cylindrical Langmuir probe dimensions.
    - Start and stop applied potential values, and the number of voltage steps between the start and stop potentials.
2. The LP area, the electron current collection area of the CubeSat, and the ion current collection areas of each side of the CubeSat are calculated. The CubeSat's electron current collection area is the total area of the CubeSat. Its ion current collection area is divided into three sections: a ram-facing area, a wake-facing area, and "drift parallel" faces.
3. Normalization constants such as ion and electron thermal speeds are calculated.
4. The thermal ion and electrons currents for the spacecraft and Langmuir probe are calculated using their respective areas and simulation parameters.
5. For each applied bias, the *fzero* MATLAB function [169] numerically determines the spacecraft potential such that

$$I_{e_{LP}}(V_A + \phi_{SC}) - I_{i_{LP}}(V_A + \phi_{SC}) - [I_{e_{SC}}(\phi_{SC}) - I_{i_{SC}}(\phi_{SC})] = 0$$

   where V_A is the applied voltage, and ϕ_{SC} is the spacecraft potential relative to the plasma. As shown in eq. 3.5, the LP potential, relative to the plasma, is the sum of the applied voltage and the spacecraft potential.

6. The spacecraft potential, applied voltage, probe potential, net LP current, net spacecraft current, and area ratio between the spacecraft and probe are given as outputs of the calculations for further analysis.

The outputs of the PSIC-LEO program are used to make conservative estimates of near maximum spacecraft charging behavior, understand the effects of spacecraft charging on the LP I-V curves, and develop new analysis techniques. The goal is to perform fast, iterative changes to satellite and Langmuir probe sizes under various plasma properties to determine which conditions should be tested using the *Nascap-2K* program. In its current state, the PSIC-LEO codes best simulate the steady-state plasma conditions found in the Earth's ionosphere for spacecraft in LEO. To expedite the calculations performed by the PSIC-LEO codes, the following assumptions on the nature of the ambient plasma and the spacecraft/instrument system were made:

- The ion population is composed only of singly ionized atomic oxygen whose distribution is described by a drifting Maxwellian distribution.
- The electron population is Maxwellian.
- The CubeSat surface area is entirely conductive.
- The CubeSat size is constant, but the probe dimensions can change to vary the area ratio.
- The wake region of the satellite collects negligible ion current. Table A.1 demonstrates that ion current collection in the wake region is small enough to be ignored when atomic oxygen is the only ion species. Furthermore, *Bowen et. al.* noted the depletion of positive ions and significant decrease in ion current in the wake of the Ariel I satellite [63].
- The satellite's sheath is small relative to the satellite's size, such that the currents collected by the spacecraft are in the "thin" sheath regime. The sheath size is shown to change with potential and Debye length in appendices A.2.1 and A.2.2; thus, this simplification will produce smaller ion currents than what would be seen in space.
- The ambient ion drift velocity does not change the sheath shape significantly.
- For any simulated density and temperature, the probe radius was set to assure that ion and electron currents collected by the cylindrical Langmuir probe satisfy the thick sheath criteria.

- The plasma density is sufficiently large enough to dominate the effects of photoelectron current and can be safely ignored. See discussion in section 3.3.1.
- The work functions of the two probes are identical and the probes are oriented perpendicular to one another.
- The high-impedance probe orientation relative to the ion drift velocity is constant.
- The ambient plasma is assumed to be non-magnetic.
- Probe boom lengths are assumed to be short enough to ignore motional emf effects but long enough to remain outside the spacecraft sheath.
- The high-impedance probe's input resistance is infinitely large such that the voltage divider between the input resistance and the sheaths surrounding the satellite and LP described in eq. 3.2 approaches unity.

4.2 Object Current Collection

In this section, the currents collected by the Langmuir probe and CubeSat are detailed. Each conducting object has a series of assumptions based on its geometry and size relative to the ambient plasma's Debye length.

4.2.1 Langmuir Probe Current Collection

The cylindrical Langmuir probe current collection, for ions and electrons, is calculated using the equations detailed in sections 2.3.1 and 2.3.2. Specifically, the ion accelerating current is described using

$$I_i\left(-\phi > 0\right) = qA_pN_i\sqrt{\frac{k_BT_i}{2\pi m_i}}\frac{4}{\sqrt{\pi}}\int_{\sqrt{\eta\left(\frac{r_s^2}{r_p^2}-1\right)^{-1}}}^{\infty}\sqrt{x^2+\eta}\exp\left[-\left(x^2+s^2\right)\right]I_0\left(2sx\right)xdx+$$
$$qA_pN_i\sqrt{\frac{k_BT_i}{2\pi m_i}}\frac{4}{\sqrt{\pi}}\frac{r_s}{r_p}\int_0^{\sqrt{\eta\left(\frac{r_s^2}{r_p^2}-1\right)^{-1}}}\exp\left[-\left(x^2+s^2\right)\right]I_0\left(2sx\right)x^2dx$$

and the ion retardation current is

$$I_i\left(-\phi \leq 0\right) = qA_pN_i\sqrt{\frac{k_BT_i}{2\pi m_i}}\frac{4}{\sqrt{\pi}}\int_{\sqrt{-\eta}}^{\infty}\sqrt{x^2-\eta}\exp\left[-\left(x^2+s^2\right)\right]I_0\left(2sx\right)xdx.$$

While not specifically studied in this thesis, the ion current is affected by probe's orientation relative to the ion drift velocity. For instance, when the probe is parallel to the drift velocity (equivalent to $s = 0$), the collected ion current resembles thermal current collection. The maximum ion current is collected when the LP is perpendicular to the ion drift velocity, assuming end effects are negligible (discussed in section 2.4.7).

The electron currents are not dependent on the spacecraft's orbital velocity due to the mesothermal nature of the spacecraft's orbital speed. Therefore, as long as the probe is outside of the satellite's sheath, the collected electron current is assumed to be independent of the probe's orientation. The accelerated electron current is given by

$$I_e\left(\phi > 0\right) = 8\sqrt{\pi} r_s l j_{e_{therm}} \int_0^{\infty} \int_0^{r_p \sqrt{x^2+\eta} / \sqrt{r_s^2 - r_p^2}} x e^{-\left(x^2+y^2\right)} dy dx$$

while the retarded electron current is

$$I_e\left(\phi \leq 0\right) = 2\pi r_p l j_{e_{therm}} e^{\eta}.$$

4.2.2 CubeSat Current Collection

The CubeSat currents are estimated assuming that the satellite is composed of 6 planar conductors oriented perpendicular to each other. Therefore, one side will be ram-facing, another is wake-facing, and the remainder are parallel to the ion drift velocity. However, the CubeSat electron current and ion current have their own sets of assumptions.

For electron current collection, it is well understood that it is affected by ram/wake effects, just like the drifting ions. Electron currents decrease in the wake region [170] and increase in the ram region [105]. The electron's sensibility to a satellite's ram/wake effects are closely tied to ion motion and is generally complicated by the existence of multiple ion species at different energy levels. However, as a simplifying assumption, the collected electron current is assumed to be independent of ram/wake effects, is collected equally on all sides, and is estimated using

$$\begin{aligned} I_e\left(\phi > 0\right) &= q A_p N_e \sqrt{\frac{k_B T_e}{2\pi m_e}} \\ I_e\left(\phi \leq 0\right) &= q A_p N_e \sqrt{\frac{k_B T_e}{2\pi m_e}} \exp\left(\frac{\phi}{T_e}\right) \end{aligned}$$

where A_p is the total area of the CubeSat.

The collected ion currents are dependent on the orientation of the side of the CubeSat.

Unlike electron current collection, the ion current collection cannot be assumed to be independent of ram/wake effects, because the satellite travels faster than the ion thermal speed. Therefore, ion currents are greater in the ram region and are typically smaller by a factor of ten in the wake region [164, 171]. The ion currents in the wake are assumed to be negligible when compared to the remaining sides of the CubeSat, and so it is estimated to be 0 regardless of the magnitude of the potential (following the numerical results in appendix A.2.4). In contrast, the ram currents are estimated as

$$\begin{aligned} I_i\left(-\phi > 0\right) &= qA_pN_i\sqrt{\frac{k_BT_i}{2\pi m_i}}\left(\exp\left(-s^2\right)+\sqrt{\pi}s\,\mathrm{erfc}\left(-s\right)\right) \\ I_i\left(-\phi \leq 0\right) &= qA_pN_i\sqrt{\frac{k_BT_i}{2\pi m_i}}\left(\exp\left[-\left(\sqrt{-\eta}-s\right)^2\right]+\sqrt{\pi}s\,\mathrm{erfc}\left(\sqrt{-\eta}-s\right)\right) \end{aligned}$$

where s is the ion drift speed normalized by the most probable ion thermal speed, η is the satellite potential normalized by the ion temperature, and A_P is the ram-facing side's surface area. Finally, the ion current for the remaining sides, those parallel to the ion drift speed, are

$$\begin{aligned} I_i\left(-\phi > 0\right) &= qA_pN_i\sqrt{\frac{k_BT_i}{2\pi m_i}} \\ I_i\left(-\phi \leq 0\right) &= qA_pN_i\sqrt{\frac{k_BT_i}{2\pi m_i}}\exp\left(-\eta^2\right) \end{aligned}$$

where A_P is the total area of the satellite excluding the ram and wake sides. This model for CubeSat current collection represents the minimum ion current collection possible by a cuboid in a drifting plasma, since neither the effects of an attractive potential nor current collection in the wake are considered.

4.3 Spacecraft Charging Behavior and its Effects on Langmuir Probe I-V Curves

In this section and the next, the notional CubeSat is modeled as a 3U satellite with a total collection area of $0.14\,\mathrm{m}^2$; the plasma parameters are: a plasma density of $1\times10^{11}\,\mathrm{m}^{-3}$, an electron temperature of $0.25\,\mathrm{eV}$, and an ion drift speed of $7.8\,\mathrm{km\,s}^{-1}$; and the LP sweeps ranged from an applied bias of $-10\,\mathrm{V}$ to $10\,\mathrm{V}$ with a voltage step size of $2\times10^{-4}\,\mathrm{V}$. The electron temperature was purposefully chosen near the upper limit of electron temperatures observed in the ionosphere (see fig. 2.3) to have increased electron current to the LP and study the more severe charging cases that may be observed.

To begin, fig. 4.1 demonstrates the calculated spacecraft potential relative to the plasma, ϕ_{SC}, as a function of applied bias between the LP and the CubeSat, V_A. The LP potential relative to the plasma, ϕ_{LP}, is calculated by adding the spacecraft potential to the applied bias. As expected, the spacecraft potential is most negative for small area ratios, and the effects of sweeping the LP decreases as the area ratio increases. At the smallest area ratios, the negative spacecraft potential is large enough to bar the LP potential from reaching the plasma potential.

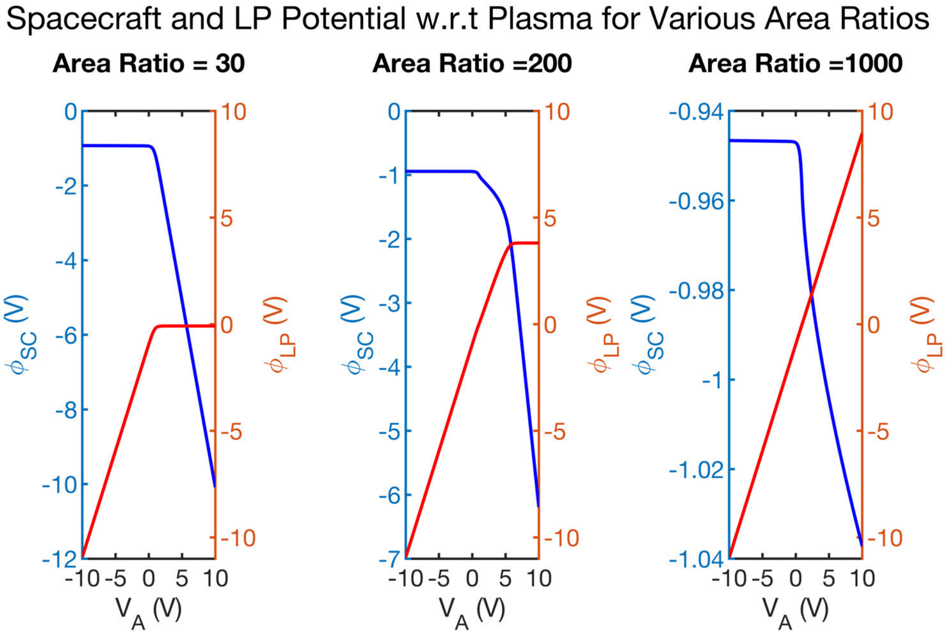

Figure 4.1: Spacecraft potential (blue) and LP potential (red) with respect to the ambient plasma. For small enough area ratios, the LP potential does not reach the plasma potential.

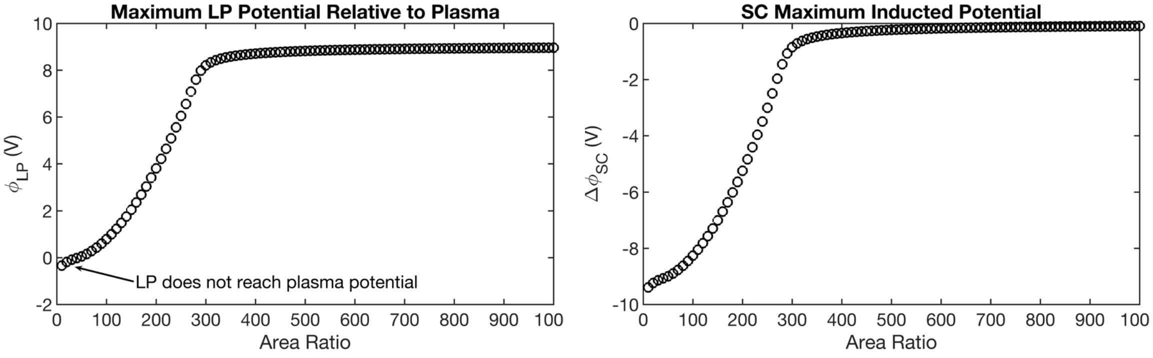

(a) The maximum Langmuir probe potential with respect to the ambient plasma.

(b) The potential difference between the spacecraft floating potential and its maximum negative charge (applied bias to LP is 10 V).

Figure 4.2: Calculated potentials with respect to the plasma.

As shown in fig. 4.2a (see arrow), for any area ratio below 50, the Langmuir probe does not reach the plasma potential. Furthermore, while the probe can reach the plasma potential when the area ratio is 50, it does not sufficiently probe the potential region above the plasma potential, the electron saturation region, prohibiting a proper analysis of the I-V curve to estimate the electron density. For accurate electron density measurements, the ability to sample the plasma at least 2 electron temperatures above the plasma potential is necessary (see appendix C.6.2). A soft lower bound for the maximum LP potential should be about $2\,\mathrm{V}$ above the plasma potential; so to sufficiently probe the electron saturation regime, the area ratio between the satellite and LP should be at least 150.

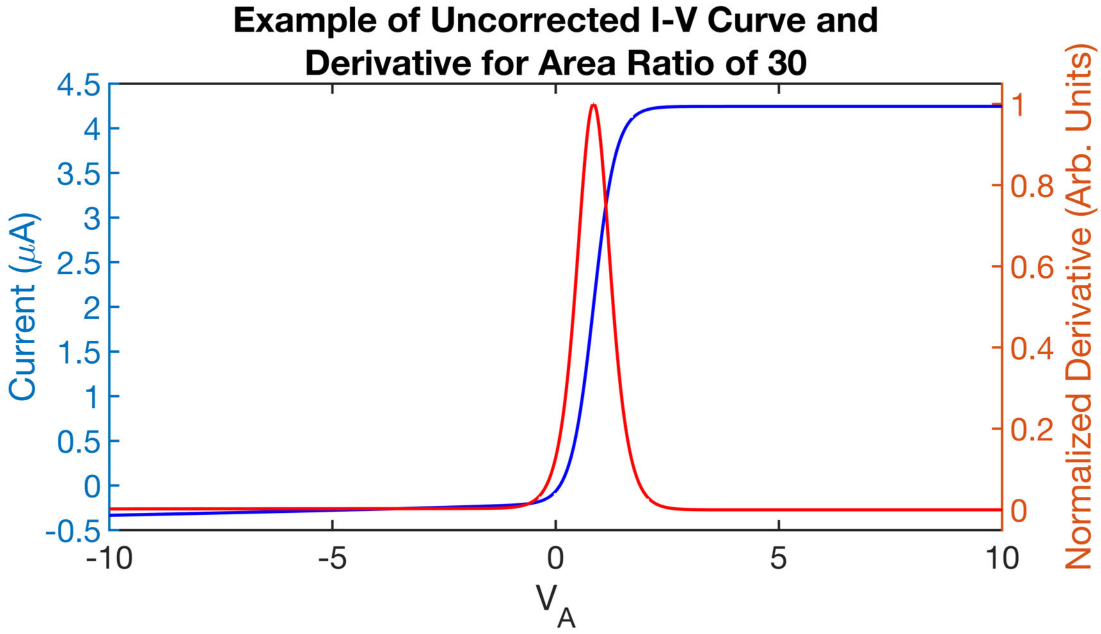

Figure 4.3: Example I-V curve and derivative for a Langmuir probe that does not reach the plasma potential. The x-axis is the applied potential between the LP and spacecraft and so the LP potential relative to the plasma is not shown (this is similar to LP operations without a twin-probe system).

Interestingly, even when the LP does not reach the plasma potential, there is still a distinct peak in the first derivative of the I-V curve. As an example, consider the I-V curve and derivative shown in fig. 4.3. The peak in the first derivative is normally due to the LP reaching the plasma potential (demarcated by a change in concavity of the I-V curve). However, when the LP does not reach the plasma potential, the first derivative peak is caused by the limiting ion current to the spacecraft chassis. Since the plasma potential is determined using the peak of the I-V curve's derivative, incorrect identification of the plasma potential, in the form of false peaks, can be introduced when the area ratio is small [56]. Indeed, fig. 4.4 shows that the plasma potential is incorrectly determined due to the spacecraft's impact on the I-V curve for area ratios of 60 and below. As a reminder, when the LP is at the plasma potential, the applied voltage is equal to the negative of the spacecraft potential relative to the plasma. Thus, for area ratios of 70 and above, the plasma potential measurement correctly estimates the spacecraft potential, even when the spacecraft is in a charged state. Therefore, for this discussion, only area ratios greater than or equal to 70 are discussed, as any measurements of temperature and density will be impacted more by the improper identification of the plasma potential than spacecraft charging.

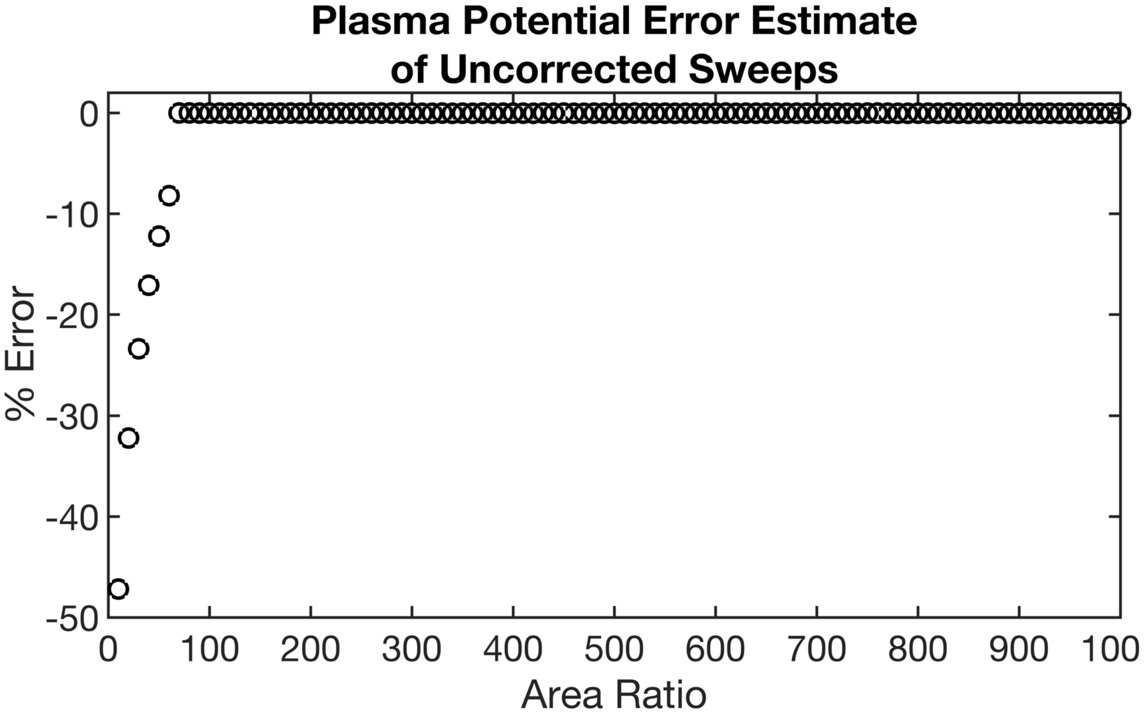

Figure 4.4: Plasma potential percent error estimates of uncorrected I-V sweeps. For area ratios of 60 and below, the spacecraft greatly impacts the I-V curve leading to incorrect identification of the plasma potential.

Regardless of area ratio, when the applied voltage is negative, the spacecraft potential is relatively constant. As shown in the bottom figure of fig. 4.5, when the applied bias, V_A, is $-10\,\mathrm{V}$ the spacecraft is slightly ($<2\,\%$) more positive than its floating potential. This is because the electron current to the spacecraft is much greater than the ion current collected by the probe at the applied biases considered. As the electron current begins to increase, the spacecraft potential charges slightly negatively. From the bottom figure of fig. 4.5, when the applied bias is $0\,\mathrm{V}$, the LP current collection is still dominated by ion current collection and so the spacecraft is near its floating potential. When the LP is at its floating potential, V_F, it collects a net 0 current and the spacecraft is at its own floating potential, depicted by the LP V_F case in the bottom figure of fig. 4.5. Above the LP's floating potential, electron current collection dominates and the induced spacecraft potential increases, where eventually the charging is nearly linear. At the plasma potential point, shown in the top figure of fig. 4.5 for the case LP V_P, the spacecraft charges more negatively at smaller area ratios. For the largest area ratios, the spacecraft potential barely charges, even at the most positive applied biases considered (see fig. 4.2b), resulting in nearly one-to-one correlations between ϕ_{LP} and the applied voltage. This behavior agrees well with *Nascap-2K* simulations (see appendix A.2.5) and chamber measurements (discussed in section 5.4).

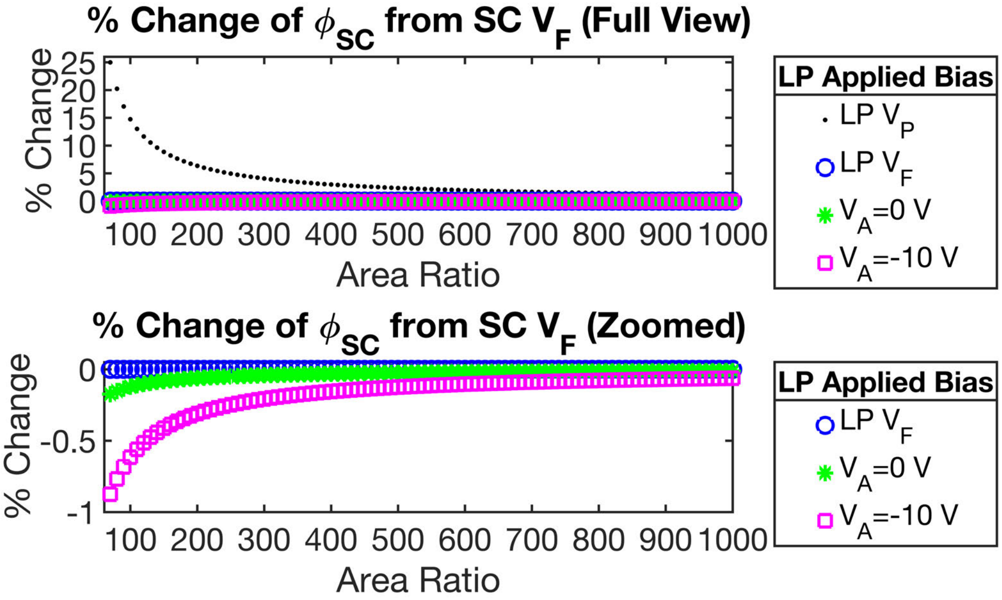

Figure 4.5: Percent change between spacecraft potential relative to the plasma at different applied biases to the LP and the spacecraft's floating potential. LP V_F corresponds to the applied bias when the LP is at its floating potential, LP V_P is the applied bias when the LP is at the plasma potential, $V_A = 0V$ corresponds to an applied bias of $0\,\mathrm{V}$, and $V_A = 10V$ corresponds to an applied bias of $10\,\mathrm{V}$. The top figure has all four biases and the bottom figure considers all of the biases except LP V_P.

Assuming a twin-probe correction scheme is not available to the spacecraft system, it is to be expected that plasma property measurements, such as electron temperature and electron density, are impacted. To begin, ion density and floating potential measurements are minimally impacted. These plasma property measurements occur when electron currents are negligible or equal to the ion current, and so the spacecraft potential is not shifted significantly from its floating potential. The greatest impact would occur from overestimating the plasma potential due to a charged spacecraft; however, it will be shown that the most severe spacecraft charging occurs when the probe applied voltage is pushed into the electron saturation regime. To understand how these electron temperature and density measurements were impacted, two electron temperature analysis techniques are implemented:

- The integral method: electron temperature is estimated by integrating the electron retardation current (described in appendix C.5.2).
- The log-linear method: electron temperature is estimated by the inverse slope of the linearized electron retardation regime (described in appendix C.5.3).

and three electron density analysis techniques are used:

- Thermal current method: electron density is estimated using the electron current at the plasma potential (see appendix C.6.1)
- Ideal OML Fit: electron density is estimated by fitting a power law function to the electron saturation current assuming the current behaves like the ideal OML theory shown in eq. 2.12 (see appendix C.6.2 with the assumption that $\gamma = 0.5$ and $\beta = 2/\sqrt{\pi}$)
- Single Point OML: electron density is estimated assuming the electron saturation current behaves like ideal OML cylindrical probe theory and that the potential is much greater than the electron temperature (refer to eq. C.41 in appendix C.6.2)

4.3.1 Spacecraft Charging Impact on Electron Temperature Measurements

For electron temperature measurements, only area ratios where the LP could reach the plasma potential are considered. Figures 4.6a and 4.6b present the percent errors of the integral and log-linear methods respectively. The percent error in this case refers to the deviation between the ”measured” electron temperature and the modeled electron temperature. Regardless of the method used, *uncorrected electron temperatures always overestimated the actual electron temperature*. The error in temperature measurements is greatest at an area ratio around 70 with a percent error of $50\,\%$ for the integral method and $20\,\%$ for the log-linear method. As shown in fig. 4.4 and discussed in its accompanying text, below an area ratio of 70, the plasma potential is incorrectly identified skewing the predicted error. Since both of the methods used for obtaining electron temperature rely on the plasma potential, there is no way to untangling the effects of spacecraft charging and the improperly identified plasma potential. As the area ratio approaches 1000, the percent error in both methods approach approximately $1\,\%$. This result is similar to the findings presented by *Szuszczewicz* [56] who performed similar studies for a cylindrical Langmuir probe referenced against both spherical and cylindrical conductors and found a deviation of $2\,\%$ at an area ratio of 1×10^4.

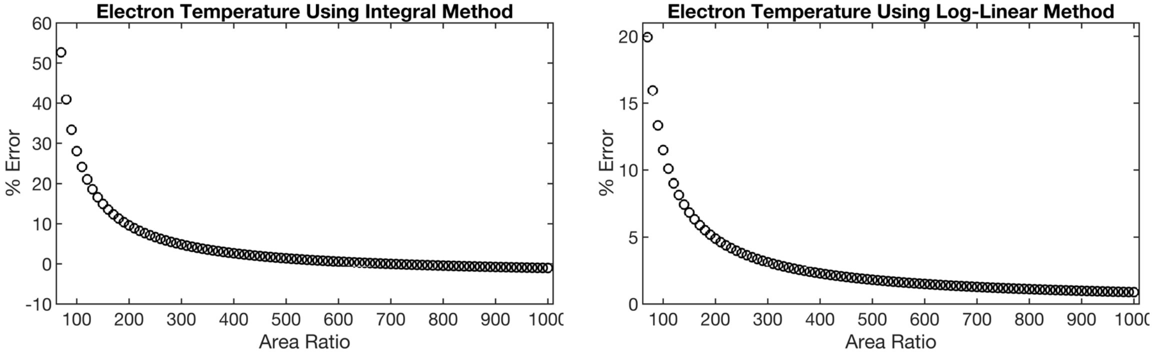

(a) Percent error of electron temperature estimates using the integral method.

(b) Percent error of electron temperature estimates using the log-linear method.

Figure 4.6: Deviation of uncorrected measurements from modeled electron temperature.

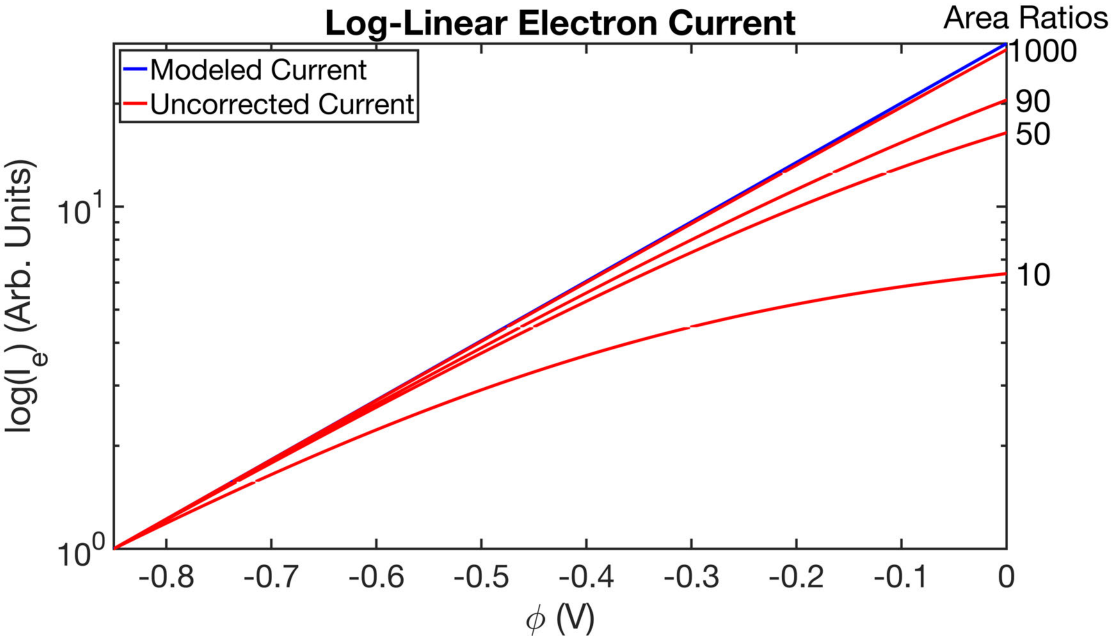

Figure 4.7: Semilog linearization of the electron current at different area ratios. The electron currents were individually normalized by their respective minimum value and the potentials of the uncorrected current were shifted to start at the same position as the modeled current.

Additionally, the log-linear method highlights how the spacecraft's charging behavior impacts the current's exponentially decaying behavior in the electron retardation regime as shown in fig. 4.7. For small area ratios, it is clear that the electron currents deviate strongly from an exponential form, leading to the large percent errors shown in fig. 4.6b. Even at an area ratio of 1000, there is a slight discrepancy between the uncorrected and modeled current, even though the two currents are linear.

4.3.2 Spacecraft Charging Impact on Electron Density Measurements

Electron density measurements tell a similar story; however, instead of overestimating the electron temperature, the *electron density is consistently underestimated for uncorrected measurements*. The single measurement methods, the electron thermal current method and the single point OML method, were applied for all area ratios. For area ratios above 70, the OML fit method was also applied. Figures 4.8a and 4.8b demonstrates the percent error of the thermal current method and single point OML method, respectively, due to spacecraft charging effects. Unsurprisingly, the lowest area ratios displayed the largest underestimations of electron density, with the smallest area ratios (area ratio less than 100) estimating a density that was one to two orders of magnitude smaller than the true density.

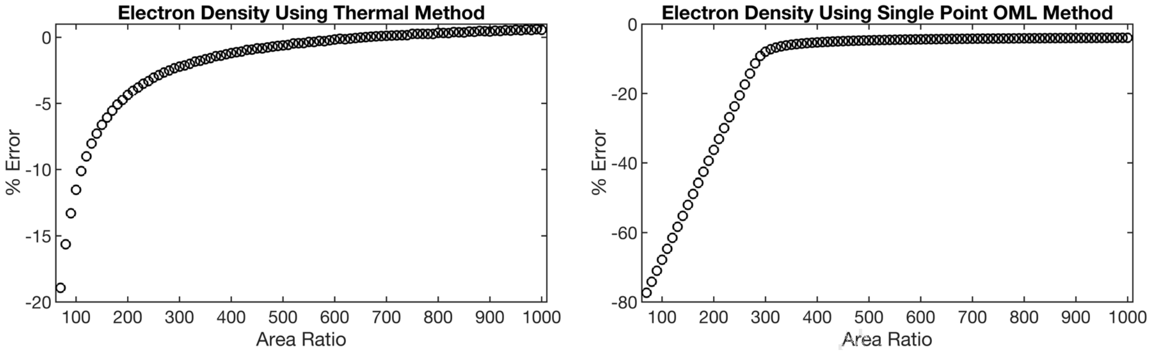

(a) Percent error of electron density estimated using electron thermal current.

(b) Percent error of electron density estimated using the single point OML method.

Figure 4.8: Percent error of single point methods for estimating of the electron density. The negative percent error indicates an underestimation.

Since the single point OML method estimates electron density using the current at the greatest positive applied bias, it will consistently underestimate the electron density until the asymptotic behavior of ϕ_{LP} is no longer present (see leftmost plot of fig. 4.1 for examples of asymptotic behavior). Asymptotic behavior tends to no longer affect probe potentials at around an area ratio of 290.

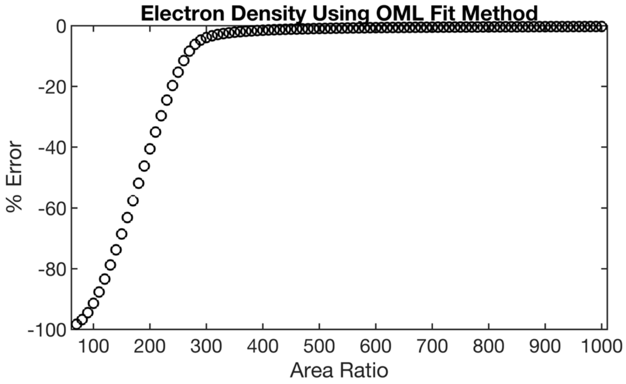

Figure 4.9: Percent error of electron density calculated using the OML fit method.

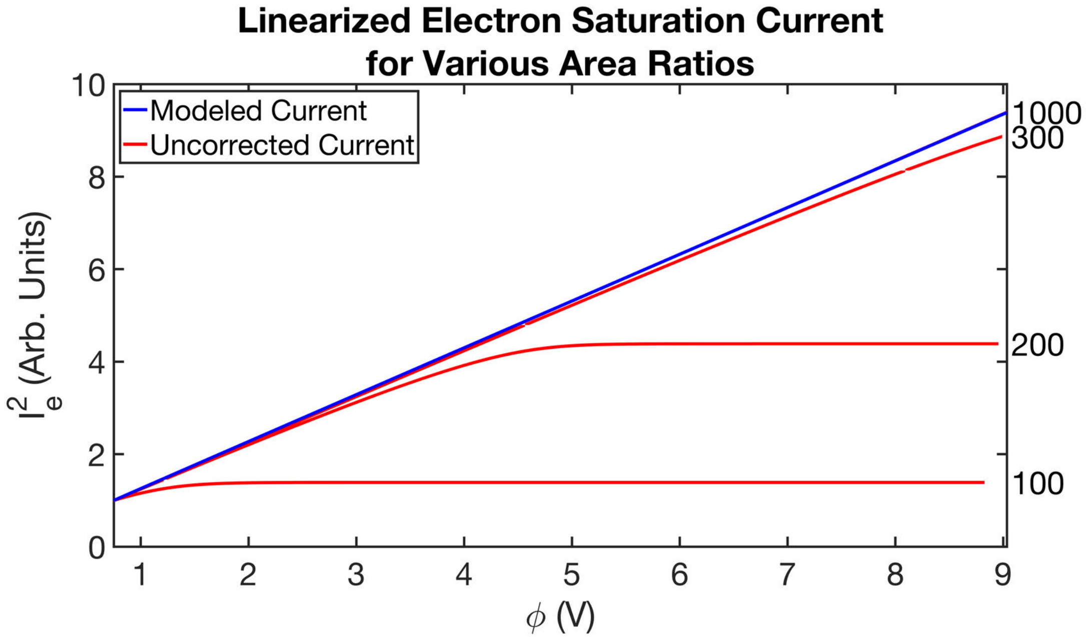

Figure 4.10: Linearized electron saturation regime by squaring the currents. The electron currents were individually normalized by their respective minimum value and the potentials of the uncorrected current were shifted to start at the same position as the modeled current.

A similar result is seen in the OML fit method, even though the method was only applied to area ratios that allowed the LP to reach at least one T_e above the plasma potential (shown in fig. 4.9). Figure 4.10 demonstrates the underlying cause of the underestimated electron densities more clearly using an attempted normalization of the electron saturation current for modeled and uncorrected currents. Since PSIC-LEO calculates OML current collection to the LP, the square of the currents should be linear with potential. However, for the area ratios of 100 and 200, the LP electron current reaches the SC ion current and the LP current flat lines; in contrast, for area ratios larger than 290, the LP electron current never reaches the maximum ion current collected by the CubeSat and so this ”flat lining” never occurs. The uncorrected line for an area ratio of 1000 and the modeled current align nearly perfectly. As a result, electron density measurements from uncorrected modeled sweeps provide limited insight into how drastic the underestimation of the electron density would be for in-chamber or in-orbit measurements due to the strict upper bound on available ion current.

For all cases, it is apparent that the induced spacecraft potential forces the electron current to deviate from ideal OML theory ($I_e \propto \sqrt{\phi_{LP}/T_e + 1}$). Accelerated OML electron currents, like the ones modeled in these examples, are proportional to the square root of the attractive potential. Therefore, if the collected currents are squared (to linearize the square root relationship), the resulting plot should be linear with applied voltage (see fig. 4.10). However there is a noticeable deviation for a true linear relationship in the uncorrected plots, even for the largest test area ratios, implying that *both an unstable reference and the ratio between the probe's sheath radius and probe radius affects LP I-V curve in the electron saturation regime*. A discussion on the relationship between the probe's sheath radius and probe radius and classical OML theory is given in appendix C.6.2.2.

4.4 Twin-Probe Correction Analysis

The key to the twin-probe correction is its ability to produce an I-V curve unperturbed by variations in spacecraft potential. As is shown in fig. 4.11, for smaller area ratios (where the LP potential doesn't reach the plasma potential) the twin-probe corrected sweeps do not sample the plasma above the plasma potential. Therefore, while the twin-probe method can correct the I-V curves, *if the uncorrected sweeps did not probe a particular region of the I-V sweep, such as the electron saturation region, the twin-probe corrections will be devoid of the same regions*.

Taking this limitation into consideration, this section analyzes two characteristics of the twin-probe method. First, the accuracy of the twin-probe method when determining electron density, electron temperature, and plasma potential is detailed. It is important to verify the effectiveness of correction LP sweeps using the twin-probe correction, and to identify any limits in their application. Second, once the efficacy of the twin-probe method is verified, the twin-probe corrected measurements are compared to uncorrected measurements to understand the maximum possible level of correction attainable using the twin-probe method.

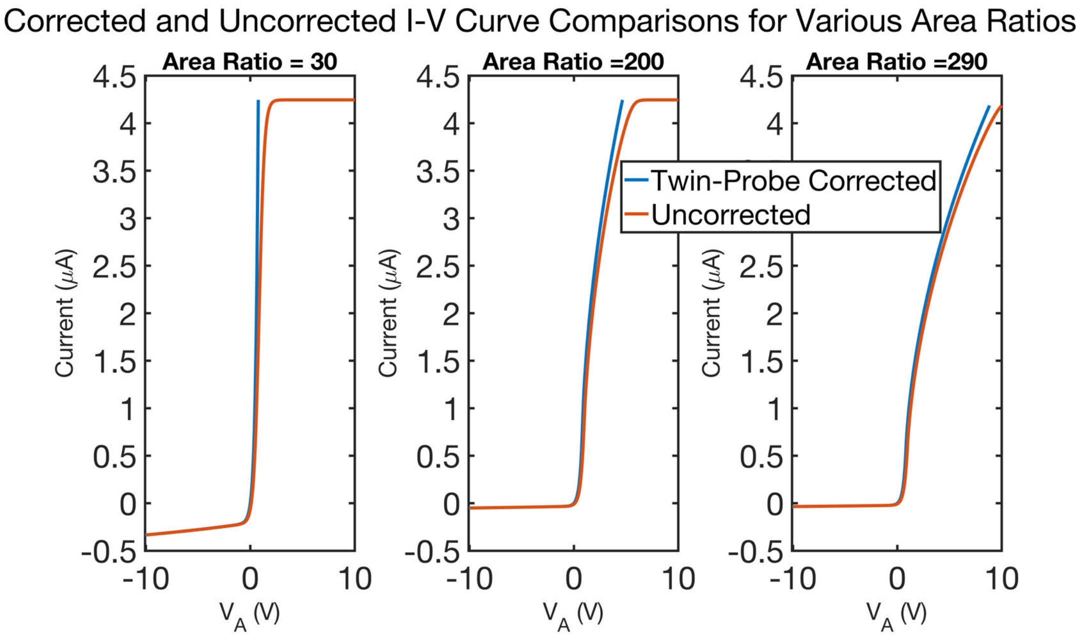

Figure 4.11: Modeled twin-probe corrected Langmuir probe sweeps.

4.4.1 Accuracy of Twin-Probe Correction for Electron Temperature Measurements

Beginning with electron temperature estimates, the same two methods, the log-linear and integral methods, are used to calculate electron temperature. Both estimates have variations across all area ratios several orders of magnitude smaller than the measurement. The percent error of the log-linear method has a standard deviation of 4.9×10^{-13} with an average of 8.4×10^{-14} (see fig. 4.12b). This estimate is on the noise floor of numerical computation, insinuating that there is no discernible difference between twin-probe corrected electron retardation current and currents modeled from theory. Caution should be taken here, as the analytic models do not mimic effects that introduce error into the log-linear method, such as the log-linearized currents rounding at the plasma potential (see appendix C.5.3.2). Similarly, the integral method is also at its noise floor. The percent error of integral method has a standard deviation of 9.3×10^{-4} with an average value of $3.3\,\%$ (fig. 4.12a). The step size of $2 \times 10^{-4}\,\mathrm{V}$ ensures that the method is at its noise floor (see appendix C.5.2.2 for more details). Therefore, when calculating the electron temperature with twin-probe corrected currents, the spacecraft charging effects are fully mitigated and only numerical noise remains. The log-linear method should be used whenever possible as it tends to be the more precise and less error-prone of the two methods.

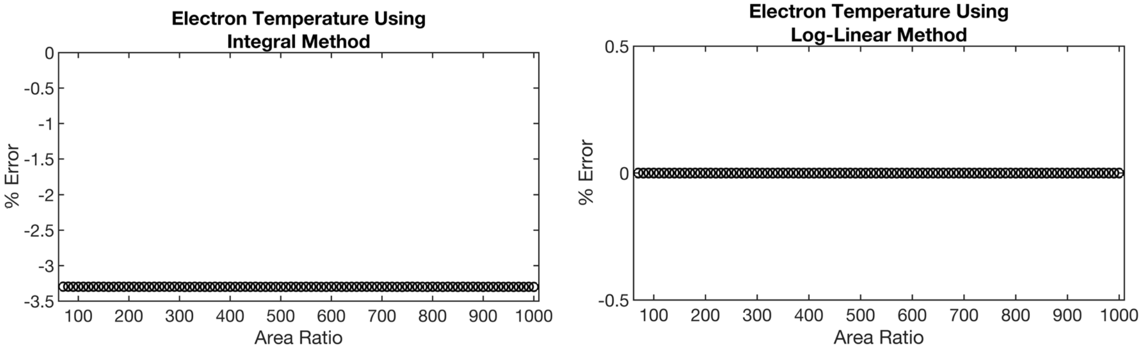

(a) Electron temperature percent error estimates of twin-probe corrected I-V sweeps using the integral method.

(b) Electron temperature percent error estimates of twin-probe corrected I-V sweeps using the log-linear method.

Figure 4.12: Electron temperature percent error estimates of twin-probe corrected sweeps.

4.4.2 Accuracy of Twin-Probe Correction for Electron Density Measurements

The electron density estimates of corrected sweeps were also studied for the thermal current method, the OML fit method, and the single point OML method. The thermal current method will be the first studied method, with a more careful investigation of the OML methods due to the asymptotic behavior of the electron saturation current for area ratios smaller than 300. Beginning with the percent error of the thermal current method, its standard deviation is 0.03 with an average of $1.79\,\%$ (see fig. 4.13). This method is useful for fast estimates of the electron density, but more accurate methods for calculating electron density or the ion density should ultimately be used due to the thermal method's sensitivity to other plasma properties.

Before discussing the efficacy of the OML methods for determining electron density, it is first necessary to understand how much of the electron saturation regime is available for analysis after implementing the twin-probe technique. Figure 4.14a displays the maximum Langmuir probe potential relative to plasma normalized by the electron temperature. The maximum LP potential governs how deep into the electron saturation regime the LP can probe, affecting the OML single point and fit methods. Referencing fig. C.16b in appendix C.6.2, the maximum LP potential must be greater than a few T_e for acceptable accuracies of the single point OML method. The maximum potential reaches a soft lower boundary of $5T_e$ at an area ratio of roughly 130, and the ideal maximum potential of $20T_e$ is reached at an area ratio between 230 and 240. Additionally, fig. 4.14b displays the range of potentials that the LP probes in the electron saturation regime. The potential range is calculated by taking the difference between the maximum LP potential and a potential

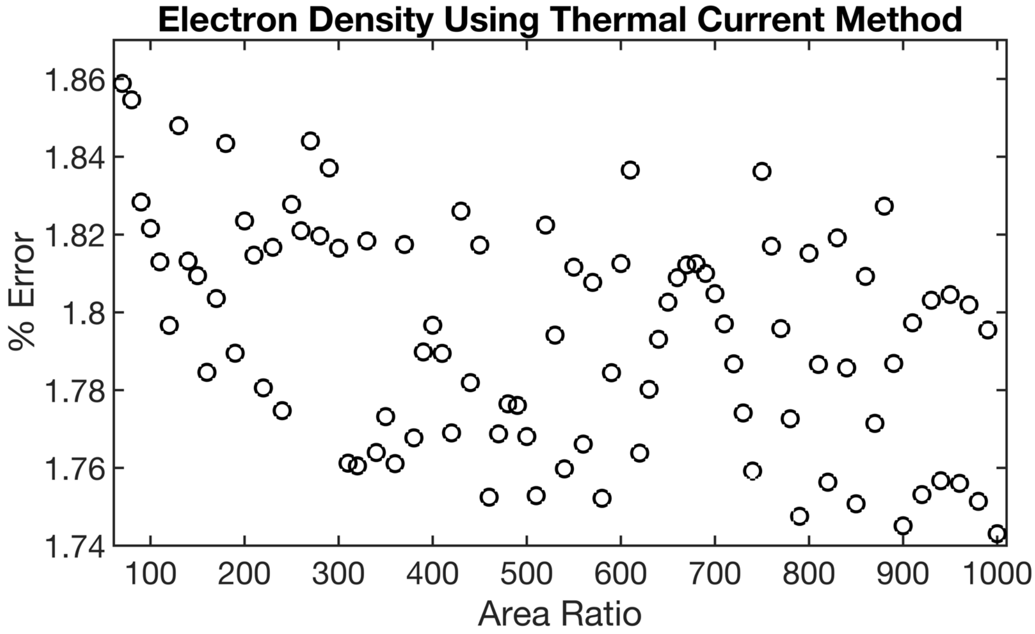

Figure 4.13: Electron density percent error estimates of twin-probe corrected I-V sweeps using the thermal current method.

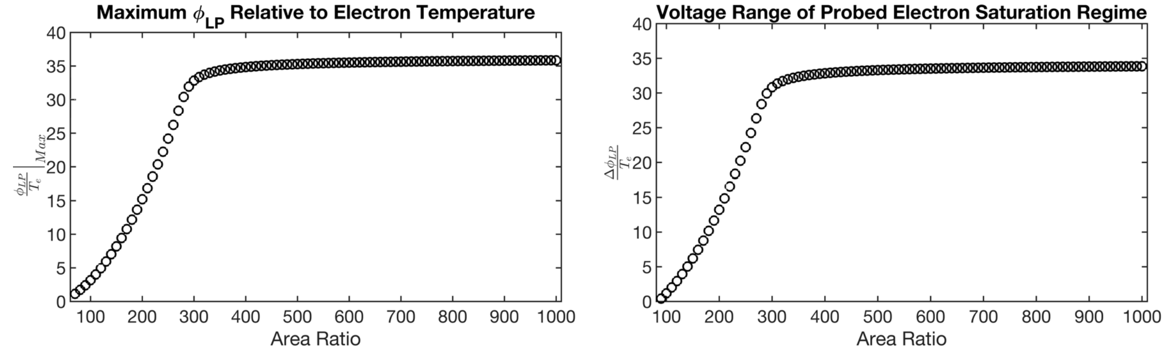

(a) The maximum LP potential relative to the plasma normalized by the electron temperature.

(b) The range of potentials in the electron saturation region probed by the LP normalized by the electron temperature.

Figure 4.14: Details on the electron saturation regime probed by corrected sweeps.

that is $2T_e$ above the measurement's plasma potential. This is the same range over which the OML fit method is employed. The voltage ranges are similar to those seen for the maximum potential, where the soft lower bound of a range of $5T_e$ is reached at an area ratio of between 140 and 150.

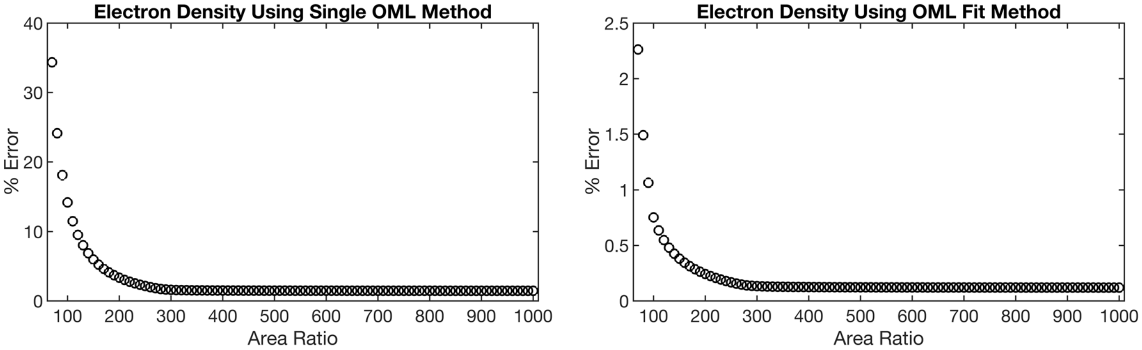

(a) Percent error of twin-probe corrected electron density measurements using the OML single point method.

(b) Percent error of twin-probe corrected electron density measurements using the OML fit method.

Figure 4.15: Percent error of twin-probe corrected electron density measurements using the OML methods.

Figure 4.15 highlights the percent error estimates of the electron density measurements using the OML methods. As expected, the percent error for the single point OML method is larger for smaller area ratios (see fig. 4.15a). However, these percent error estimates agree with the minimum uncertainty of the method in appendix C.6.2, implying that the twin-probe corrections successfully corrected the I-V curve, and the error is more closely related to the limitation of the most positive potential of ϕ_{LP}. This once again highlights that while the twin-probe method can correct for spacecraft charging, it can not extend the range of the biases sampled by uncorrected sweeps. The percent errors of the OML fit methods converge to roughly $0.1\,\%$ (shown in fig. 4.15b). Finally, for all area ratios greater than or equal to 100, the number of measurements included in the fit ranged from 400 to 437, such that the regions within the fit were well sampled.

4.4.3 Magnitude of Twin-Probe Correction

The previous subsection showed that the twin-probe method is capable of correcting the I-V curves such that the methods estimate the electron density and temperature near or at their respective method's minimum uncertainty. However, when studying plasma properties in-orbit or in a vacuum chamber, the exact electron temperature and density are not known. Therefore, it is important to understand the percent change between the uncorrected and twin-probe corrected measurements; that is, the percentage of improvement the twin-probe method provides without prior knowledge of the ”true” values of the plasma properties. All percent change values are therefore given as

$$\text{Percent Change} = 100\frac{F_{corrected} - F_{uncorrected}}{F_{uncorrected}} \tag{4.1}$$

where $F_{corrected}$ correspond to twin-probe corrected measurements and $F_{uncorrected}$ refers to uncorrected measurements.

Starting again with electron temperature, fig. 4.16 demonstrates the percent change between twin-probe corrected electron temperature measurements and uncorrected measurements using the log-linear and integral methods. The maximum correction occurs for the smallest area ratio considered (70) between $15\,\%$ to $30\,\%$, and asymptotically approaches $1\,\%$ for the log-linear method and $3\,\%$ for the integral method. As expected, *the amount of correction possible from the twin-probe method decreases with increasing area ratio, since the effects of LP operation on the spacecraft potential diminishes as the area ratio grows.*

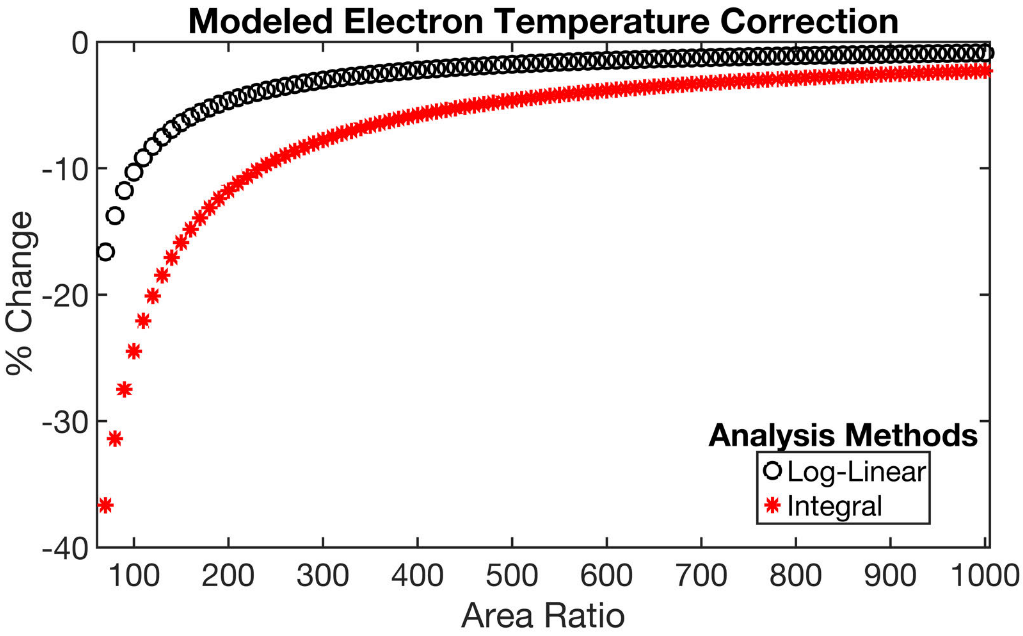

Figure 4.16: Magnitude of twin-probe correction of electron temperature when compared to uncorrected measurements.

When comparing electron temperature measurements, greater care must be taken due to the unphysical, asymptotic behavior of the electron saturation current collection due to the limited CubeSat ion current correction. To ensure this asymptotic behavior is avoided, the only method that is looked at is the electron thermal current method for area ratios greater than or equal to 70. Similar to the electron temperature corrections, the magnitude of twin-probe correction for electron density also decreases as the area ratio increases. At

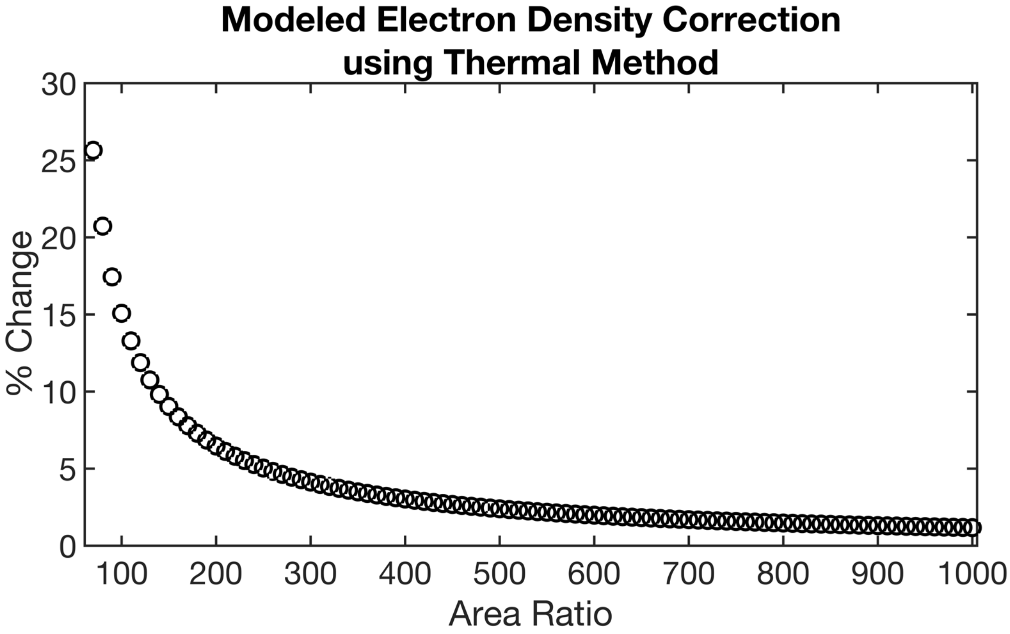

Figure 4.17: Magnitude of twin-probe correction of electron density measurements when compared to uncorrected measurements.

the smallest considered area ratio, the percent change between the twin-probe corrected and uncorrected electron density measurements are roughly $25\,\%$, and reach $1\,\%$ when the area ratio grows to 1000.

4.4.4 Importance of Proper Input Resistance for Accurate Tracking of Spacecraft Potential

While the PSIC-LEO codes are capable of calculating the exact spacecraft potential, it is also possible to estimate the spacecraft potential measured by a high-impedance probe using eqs. 3.1 and 3.2. Since the twin-probe method shifts the reference potential of the LP from the spacecraft to the electrically isolated high-impedance probe, the plasma potential from twin-probe corrected sweeps is the negative of the high-impedance probe's floating potential. Indeed, for an infinitely large input resistance, the plasma potential of the corrected I-V sweeps estimates the floating potential of the high-impedance measurements to within $0.1\,\%$ for area ratios of 70 and greater (see fig. 4.18), supporting the discussion in section 3.3.2. Therefore, *as long as all additional error terms are accounted for, the spacecraft potential can be estimated by calculating the floating potential of the high-impedance probe and shifting the measured spacecraft potential by this floating potential*.

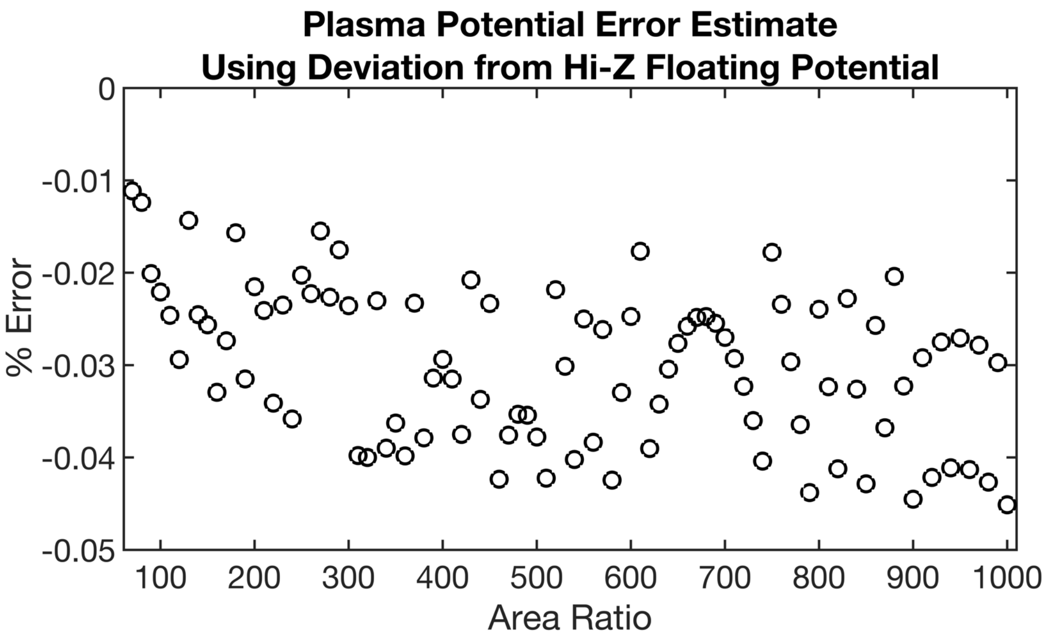

Figure 4.18: Percent error estimates of twin-probe corrected I-V sweeps when the correction is accomplished using the modeled ”measured” spacecraft potential instead of the calculated spacecraft potential.

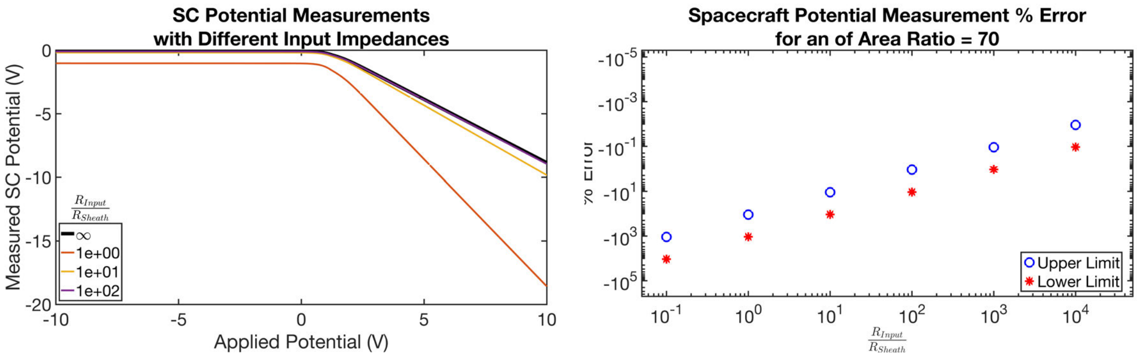

(a) Measured spacecraft potential using various input resistances relative to the plasma sheath resistance.

(b) Percent error of measured spacecraft potential relative to ideal measurement at the maximum and minimum applied voltages.

Figure 4.19: Effect of high-impedance input resistance on measured spacecraft potential.

An assumption in the section 3.3.2 discussion is that the input resistance used to track the spacecraft potential is large enough to minimize the effects of the voltage divider caused by the plasma sheath resistance and the input resistance. Indeed, fig. 4.19a demonstrates the effects of the input impedance on the overall form of the measured spacecraft potential. When the input resistance is on the order of or below the plasma’s sheath resistance, the measured spacecraft potential is overestimated, skewing the overall spacecraft potential behavior. To ensure spacecraft potential measurements have a minimum uncertainty of $10\,\%$, and properly spacecraft potential tracked, the input resistance for the high-impedance probe must be at least a factor of 100 greater than the sheath resistance, as shown in fig. 4.19b.

CHAPTER 5

Experiments

Experiments performed at NASA MSFC were used to determine the feasibility and effectiveness of the twin-probe method. The twin-probe method was employed to track spacecraft potential, understand the magnitude of electron density and temperature measurement corrections, and identify limitations. All of the experiments studying the twin-probe technique were performed in the low Earth orbit simulation chamber at NASA MSFC [172]. In this chapter, the instruments, chamber, and plasma source are detailed before presenting the results of the experiment.

5.1 Experiment Description

The experiment's setup is divided into 3 subsections: 1) the chamber and plasma source; 2) the notional CubeSat and instrumentation; and 3) the twin-probe method circuitry.

5.1.1 Chamber and Plasma Source

A cylindrical vacuum chamber approximately $2.4\,\mathrm{m}$ long and $1.2\,\mathrm{m}$ in diameter was used during this experiment (diagram shown in fig. 5.1a). A base pressure of $6.5 \times 10^{-7}\,\mathrm{Torr}$ was achieved when using three cryopumps and a turbomolecular pump, and $7.7 \times 10^{-7}\,\mathrm{Torr}$ was achieved when using only two cryopumps and a turbomolecular pump. One cryopump malfunctioned during the final weeks of the campaign, necessitating the switch from three to two pumps.

The plasma source uses a magnetic filter (shown in fig. 5.2a) to produce a low-electron-temperature plasma with a streaming ion population. Briefly, gas is flown through a heated tube, referred to as the cathode, and ionized using a DC electric field in a region between the tube's exit orifice and a flat, toroidal plate, called the keeper. Once the plasma discharge is initiated, the plasma is accelerated towards the anode exit

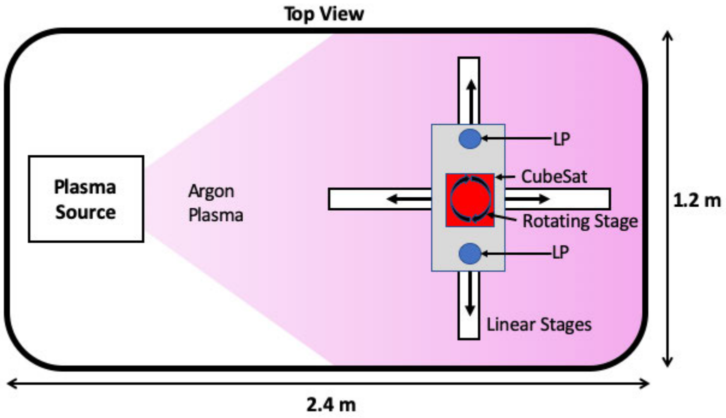

(a) Diagram depicting a top view of the vacuum chamber. The CubeSat is mounted on a rotation stage; this rotation stage and two LPs are all attached to a platform mounted on two linear stages.

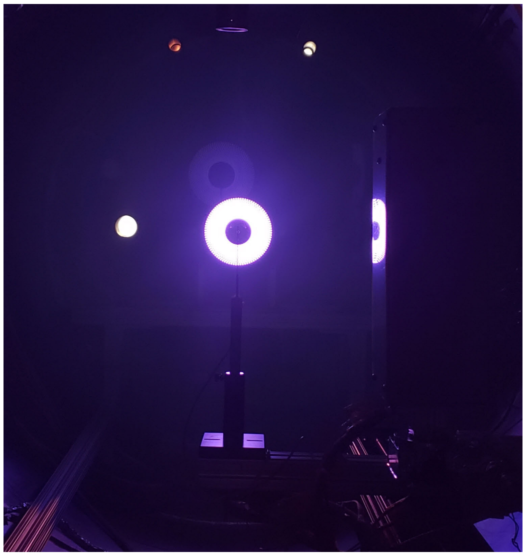

(b) Example of the argon plasma created by the plasma source as viewed from the chamber's view port near the LPs and CubeSat.

Figure 5.1: NASA MSFC chamber description.

orifice using a positive bias between the anode and cathode. An electrical schematic is detailed in fig. 5.2b.

The plasma source was chosen for its ability to approximate the plasma environment found in LEO. It is capable of producing densities in the range of $1.4 \times 10^{12}\,\mathrm{m}^{-3}$ to $4.4 \times 10^{13}\,\mathrm{m}^{-3}$; electron temperatures between $0.17\,\mathrm{eV}$ to $0.35\,\mathrm{eV}$, and argon ion drift energies between $2\,\mathrm{eV}$ to $5\,\mathrm{eV}$. In comparison to the LEO environment, the lowest density

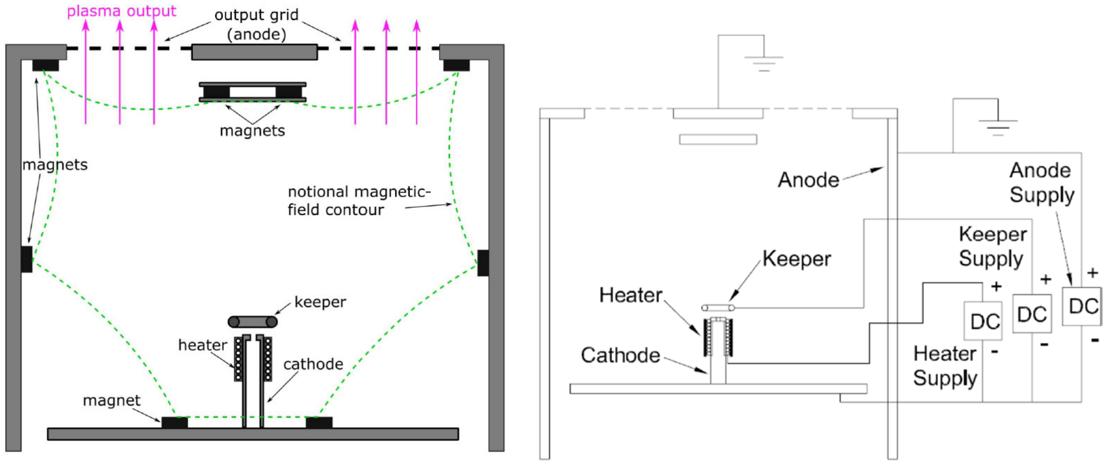

(a) Schematic of plasma source used to approximate LEO environment. Image taken from *Jesse et. al.* [173].

(b) Electrical schematic of plasma source. Image adapted from *Rubin et. al* [174].

Figure 5.2: NASA MSFC chamber plasma source mechanical drawings and electrical schematic.

produced by the source is roughly a factor of 2 to 100 greater than the typical, quiescent LEO density range; the lowest generated electron temperature is roughly a factor of 3 greater than the lowest observed LEO electron temperature, and the argon drift speed is about 1.4 to 3.6 times slower than a spacecraft's orbital velocity. A detailed study of the plasma source used during these experiments is discussed by *Rubin et. al* [174] (shown operating in fig. 5.1b). While the ideal operating conditions of the plasma source were not always met, due to degradation and maintenance, the range of plasma properties measured during the experiment are not very different from their ideal values (measured values shown in table 5.1).

Argon was used for the ionized expellant gas, and was delivered through a Matheson ultrahigh-purity regulator. The gas flow rate was controlled with a manual valve and measured by a Hastings flowmeter. The flow rate was kept constant during each set of measurements, but varied from $4.6\,\mathrm{sccm}$ to $13.2\,\mathrm{sccm}$ between sets, which yielded operating pressures ranging from $5.3 \times 10^{-5}\,\mathrm{Torr}$ to $1.3 \times 10^{-4}\,\mathrm{Torr}$ over the total set of experiments. The flow rate was changed between measurement sets to achieve different ion temperatures and ion drift velocities as the flow rate proved to be inversely proportional to both drift speed and ion temperature. For these experiments, the ion population was composed of either a single drifting Maxwellian ion distribution, or a main drifting Maxwellian ion population and a slower Maxwellian charge exchange population (representative measurements are shown in section 5.3.2.1).

Electron temperature	$0.15\,\mathrm{eV}$ to $0.78\,\mathrm{eV}$
Plasma density	$1.8\times10^{12}\,\mathrm{m^{-3}}$ to $2.8\times10^{13}\,\mathrm{m^{-3}}$
Main ion drift velocity	$2.4\,\mathrm{km\,s^{-1}}$ to $10.6\,\mathrm{km\,s^{-1}}$
Charge exchange ion drift velocity	$0.5\,\mathrm{km\,s^{-1}}$ to $0.8\,\mathrm{km\,s^{-1}}$

Table 5.1: Range of plasma parameters measured during the experiment.

5.1.2 Notional CubeSat and Instrumentation

During the experiment campaign, a CubeSat was simulated using a $0.109\,\mathrm{m}\times0.109\,\mathrm{m}$ $\times0.311\,\mathrm{m}$, 316-stainless-steel cuboid. The dimensions of the cuboid were specifically chosen to represent a 3U CubeSat, where 1U is a $0.1\,\mathrm{m}\times0.1\,\mathrm{m}\times0.1\,\mathrm{m}$ structure. Stainless steel was chosen as a conductive building material to reduce any potential experiment error in the current collection due to oxidation on the surface over time. To isolate the individual faces, the faces were joined at the corners using non-conducting Teflon cubes and the inner faces were covered in $2\,\mathrm{mil}$ non-conducting Kapton. This led to an average isolation of $10\,\mathrm{G\Omega}$ between any pair of faces, limiting the leakage currents between isolated conductors to tenths of a nanoamp. The CubeSat itself was mounted on a rotation stage to rotate around either its Z-axis or Y-axis (perpendicular to both its Z-axis and the ion drift velocity), depending on how the CubeSat was mounted (see different CubeSat mounting schemes in fig. 5.4).

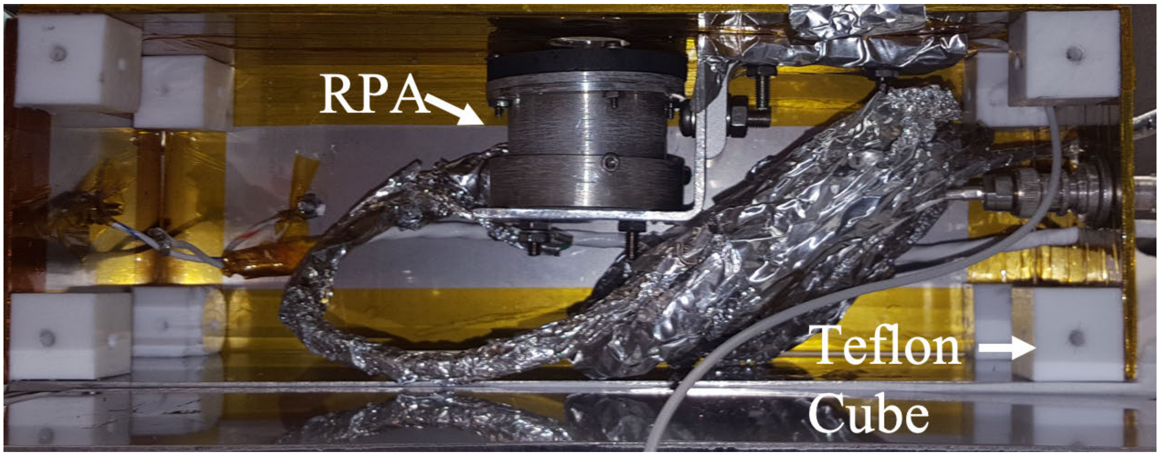

Figure 5.3: Internal structure of the CubeSat. The Teflon cubes in the corners and Kapton layers isolate the individual faces from each other. The RPA is mounted in the center of the CubeSat (top of the image).

To measure the ion energy distribution function, a retarding potential analyzer (RPA) was mounted within the CubeSat (displayed in fig. 5.3). The RPA is described in detail by *McTernan et. al* [173], but is summarized as follows. The RPA is a planar, circular-aperture sensor composed of four grids and a collector plate [175]. In order from closest to the instrument opening, the grids are: ground, electron repelling, ion discriminator, and secondary electron suppression. The grids are equally spaced with a $5.7 \times 10^{-3}\,\mathrm{m}$ gap and the diameter of the opening is $1.6 \times 10^{-2}\,\mathrm{m}$. Each grid is composed of a fine nickel mesh with a combined transparency of $70\,\%$. The inner structure of the CubeSat is shown in fig. 5.3. The analysis technique used to determine the ion energy distribution function from RPA operations is detailed in appendix D.

Multiple Langmuir probes were used in this experiment to study the effects of the current collection area on plasma property measurements and spacecraft charging behavior. The largest LP had a surface area of $8.25 \times 10^{-4}\,\mathrm{m}^2$ (area ratio ~ 160) whereas the smallest LP had a surface area of $2.3 \times 10^{-4}\,\mathrm{m}^2$ (area ratio ~ 565). The largest probe was a guarded, rhenium-coated titanium cylinder that was originally designed for the ProSEDS mission [159]. The remaining LPs were made of stainless steel and varied in length to achieve different area ratios. These smaller probes used an eye loop at the end, so that a screw and nut could be used to mount it to either a Teflon block or garolite tube. Furthermore, the stainless steel LPs were not guarded; however, their length was very long relative to their radius, such that end-effects were minimized. Moreover, their measurements (plasma density and temperature) were checked against each other and the ProSEDS LP (when available) to ensure accuracy and self-consistency. An example of both kinds of Langmuir probes is shown in fig. 5.4. The various analysis techniques used to determine plasma properties from LP operations are detailed in appendix C.

5.1.3 Twin-Probe Method Setup

Implementing the twin-probe method in the chamber required the CubeSat to be electrically isolated from the chamber and for both Langmuir probes to be referenced relative to the CubeSat. The measured isolation impedance between the CubeSat and ground was greater than $20\,\mathrm{G\Omega}$ at $100\,\mathrm{V}$ without a plasma present, using the isolation measures described in the previous section. Only the CubeSat face connected to the rotation stage was grounded (through the rotation stage itself). This isolation scheme allows for leakage current on the order of a tenth of a nanoamp between the CubeSat and the chamber; however, it is minimal compared to the ion ($\sim 10\,\mu\mathrm{A}$) and electron ($\sim 1\,\mathrm{mA}$) current collected by the CubeSat.

Referencing the Langmuir probes relative to the CubeSat was accomplished using electronics outside the chamber in order to test the twin-probe method for various probe sizes and orientations without breaking vacuum. The high-impedance probe used a $1\,\mathrm{G\Omega}$ sense resistor and a Keithley 6430 sourcemeter to track the spacecraft potential, while the

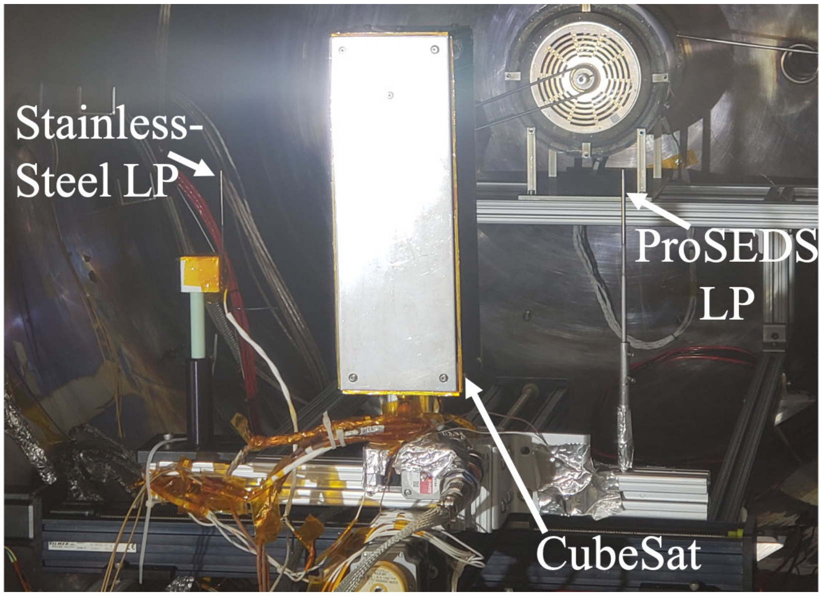

(a) Image displays the LPs mounted next to the CubeSat while the CubeSat is configured to rotate around its Z-axis. The ProSEDS LP is mounted on the right of the CubeSat and the stainless steel LP is mounted on the left.

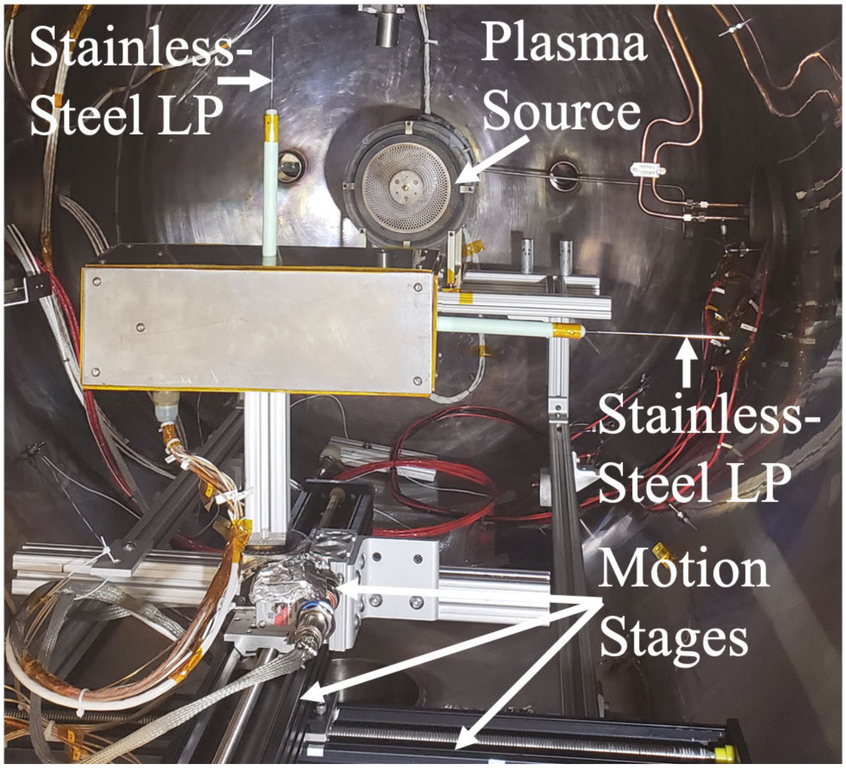

(b) Image displays the stainless steel LPs mounted onto the CubeSat while the CubeSat rotates perpendicular to both the Z-axis and the ion drift velocity.

Figure 5.4: The two configurations of the experiment are shown: a) an unmounted LP setup and b) a mounted LP setup.

swept probe was biased using a Keithley 2400. The full experiment system displaying the source; translation and rotation stages; the CubeSat in both orientations; and the LPs is shown in fig. 5.4, and a schematic of the twin-probe circuitry is shown in fig. 5.5.

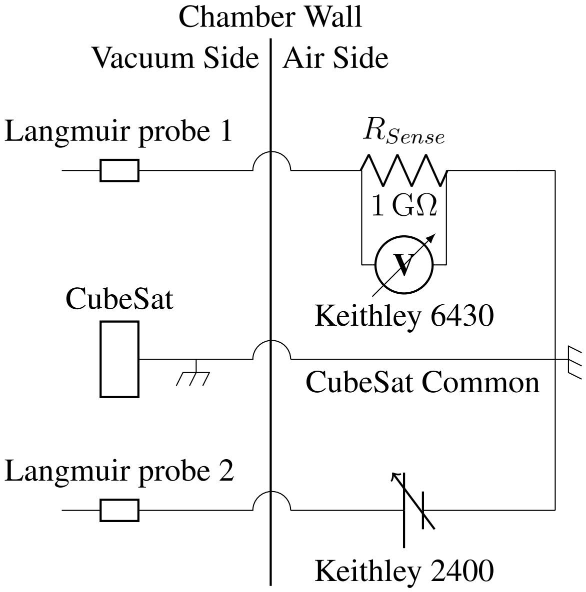

Figure 5.5: Twin-probe circuitry for unmounted and mounted probe configurations. The high-impedance probe was isolated from the CubeSat using a $1\,\text{G}\Omega$ sense resistor, Langmuir probe 1 in this configuration.

5.2 Hollow Cathode Plume Homogeneity and Controls

Before any experiments studying the twin-probe method were performed, the plasma plume was probed to understand its homogeneity and determine the best regions for performing twin-probe measurements. In particular, three plasma properties of interest were studied:

1. An ion density nearly equal to the electron density. This equivalence ensures the probes would be in the quasi-neutral portion of the plume and would minimize the risk of having measurements impacted by chamber wall effects such as the wall's plasma sheath.

2. Electron temperatures and densities that are spatially symmetric along the axis of the source. This ensures the measurements of each probe can be compared against the other both with and without twin-probe method corrections.

3. A drift energy greater than 1 eV. A drifting plasma better approximates the plasma environment found in LEO.

As shown in this section, each constraint was met with varying degrees of success. The exhibited representative plume was produced from a source operating at a flow rate of $13.1\,\mathrm{sccm}$ and an anode current of $10\,\mathrm{A}$. All plumes flow from east to west (top to bottom in the figures below) and the source is always outside of the boundary of the plots shown. The contour plots all demonstrate a measured or calculated plasma property, centered along the source's centerline, with a spatial resolution of approximately $5 \times 10^{-2}\,\mathrm{m}$.

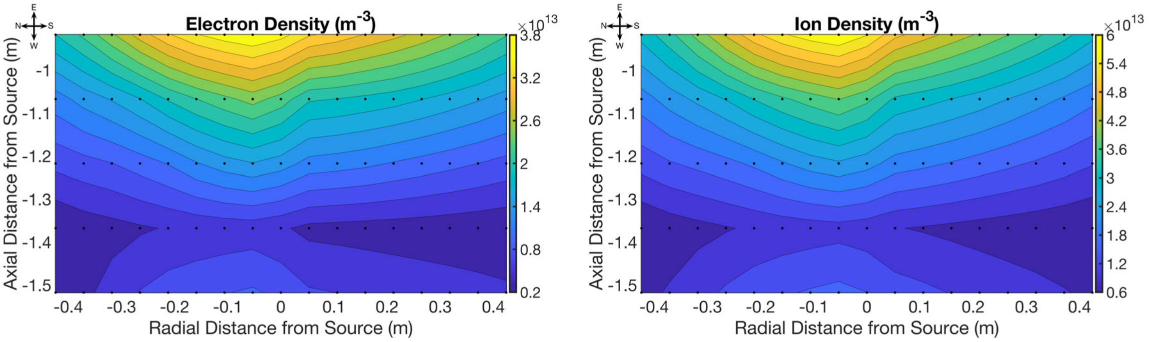

(a) Representative electron density of plasma plume.

(b) Representative ion density of plume.

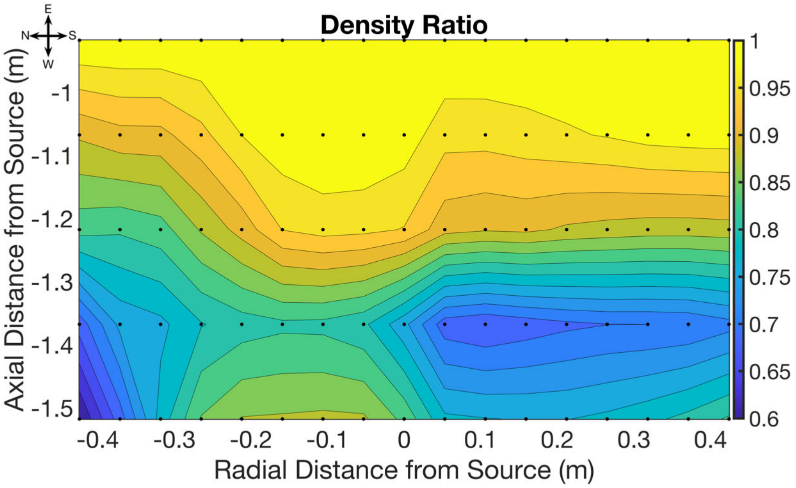

(c) Representative electron density to ion density ratio of plasma plume.

Figure 5.6: Ion and electron densities measured in representative plasma plume.

Beginning with density measurements, the density is typically greater near the source's centerline, and decreases with distance away from the source (see figs. 5.6a and 5.6b). A ratio of the electron density to the ion density demonstrates that the majority of the plasma plume is quasineutral (see fig. 5.6c). Typically quasineutrality is broken at the farthest corners of the mapping region where this ratio approaches 0.6, as the region becomes ion rich near the walls of the chamber. Furthermore, there is a slight bias of greater densities towards the northern side of the chamber. However, this bias is not enough to warrant drastic changes in the experiment's design. The difference in densities between the north and south side are within a factor of two, which is within the error of the measurements, and so the plume is symmetric enough with regards to density. It should be noted that fig. 5.6c is normalized by the largest ratio, such that the maximum value of the density ratio is always 1. The electron temperature exhibits a similar behavior to that of the density. There is a skew for hotter electron temperatures towards the north side of the plume. Finally, the ion drift velocity is always measured to be at least $1\,\mathrm{eV}$, and typically increases with increased distance from the plasma source due to the potential drop between the source and the chamber walls (see fig. 5.8b).

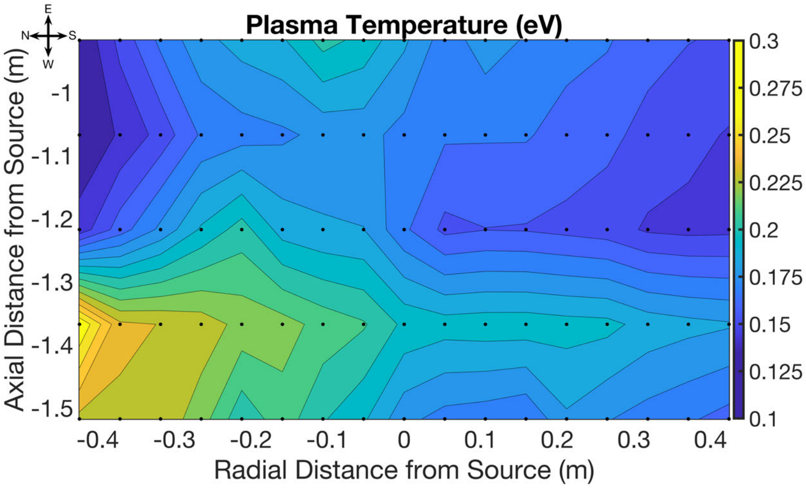

Figure 5.7: Representative electron temperature of plasma plume. Slight bias towards the north side of the plume.

It is not fully understood why the north side of the plasma plume has higher densities and electron temperatures. As shown in fig. 5.2a, the cathode and keeper are housed in a conducting drum lined with $\mathrm{Sm-Co}$ magnets. Measurements of all magnets along the drum and near the center of the plasma output orifice verified that the magnetic field was axially symmetric. Furthermore, adjustments made to the magnetic field strength at the output orifice, by adding or removing magnets from the cluster at the center of the output, yielded no noticeable difference in the skew. Private correspondences with Dr. Jesse McTernan confirmed that the ion drift velocity is not symmetric along the centerline of the plasma source, as measured by the maximum current to a planar retarding potential analyzer [176] (see fig. 5.8a). A possible theory is that the magnetic filter positioned at the center of the source's plasma output shadows the flow in such a way that produces the skew, but this is mostly conjecture.

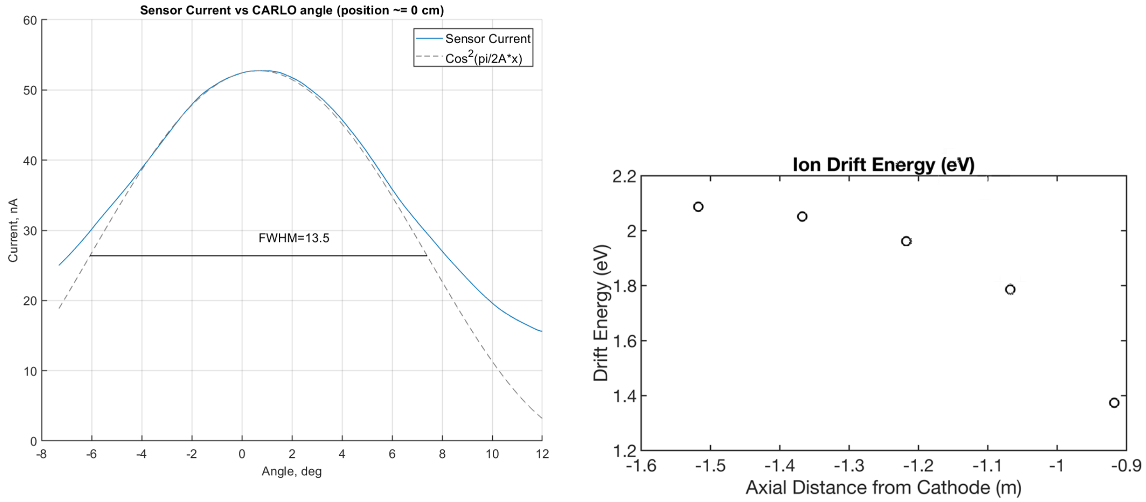

(a) Maximum radial ion current as measured by the planar retarding potential analyzer, CARLO. Image from *McTernan* [176].

(b) Axial ion drift energy as measured by an RPA.

Figure 5.8: Radial and axial ion velocities from hollow cathode source.

A fix for the skew is to float the cathode and keeper, and remove the anode from the plasma source circuit. In this new electrical configuration, the cathode can be biased positive relative to the chamber, guiding the plasma with a highly directional DC electric field (see fig. 5.9). While this technique is effective, it introduces several additional problems that make it difficult to analyze the results of these experiments. Chief amongst these issues is the ability to drive the cathode potential by biasing the LPs or the CubeSat with a large enough bias relative to the chamber and a noticeable increase in electron temperature because the magnetic filter is no longer effective.

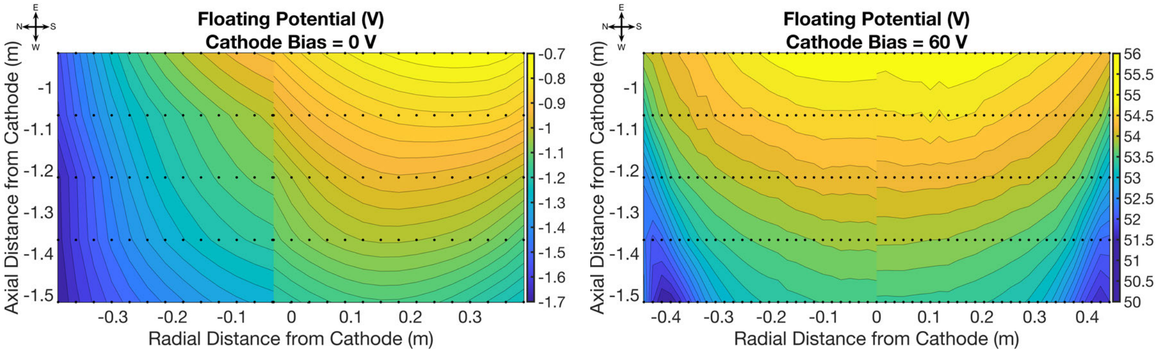

(a) Floating potential map with a floating, unbiased cathode.

(b) Floating potential map with a cathode biased at 60 V above the chamber wall.

Figure 5.9: Floating potential map of the plasma plume for an unbiased and biased cathode.

5.3 Results

The results and analysis section will focus on two distinct measurements that the twin-probe method can improve using the tracked spacecraft potential: the electron temperature and the electron density. The examples shown in sections $5.3.2.4$, $5.3.4.1$ and $5.3.5.1$ correspond to the same measurement set for an area ratio of 565. Its plasma and chamber properties can be found in table 5.2. The voltage step size is also roughly $0.25T_e$, allowing for more accurate determination of the plasma properties. If the experiment properties are different, they are explicitly stated.

Electron temperature	$0.16\,\mathrm{eV}$
Plasma density	$2.8 \times 10^{13}\,\mathrm{m}^{-3}$
Main ion drift velocity	$1.8\,\mathrm{km\,s^{-1}}$
Charge exchange ion drift velocity	N/A
Background pressure	$2.1 \times 10^{-4}\,\mathrm{Torr}$

Table 5.2: Range of plasma parameters for example measurement set.

Generally when studying the twin-probe method's effect on a LP's plasma property measurements, there are three different types of measurements based on the LP's electrical reference:

1. Control measurements: Plasma properties corresponding to measurements where the LP was referenced relative to the chamber. Analogous to a probe referenced against a reference electrode at least 1×10^4 times greater than the probe.
2. Uncorrected measurements: Plasma properties corresponding to measurements where the LP was referenced relative to the notional 3U CubeSat.
3. Twin-probe corrected measurements: Plasma properties corresponding to measurements where the LP was referenced relative to the notional 3U CubeSat, but the applied voltage is corrected by the tracked spacecraft potential.

All probes were cleaned using electron heating and confirmed to have no hysteresis before each experiment was conducted. However, the CubeSat's current collection had noticeable hysteresis and electron heating alone was not sufficient to fully remove it. One possibility for the persistent hysteresis behavior is that the CubeSat was not rotated during the cleaning process, and so the CubeSat faces may not have received equal treatment, possibly requiring longer treatment, larger biases, or slow rotation during cleaning.

5.3.1 Spacecraft Charging

The spacecraft charging behavior was successfully tracked during Langmuir probe operation and the measured behavior was in agreement with modeling predictions. The potential of the CubeSat was tracked using a high-impedance probe electrically isolated from the CubeSat by a $1\,\mathrm{G\Omega}$ sense resistor. As shown in fig. 5.10, the spacecraft potential remains relatively constant as the LP is biased negative of the spacecraft. In this configuration, the LP collects net ion current, and so the SC does not significantly charge positive or negative, as it can collect sufficient electron current to compensate for the current to the LP. As predicted by *Nascap-2K* (appendix A.2.5) and PSIC-LEO (section 4.3), the potential will become increasingly negative with positive applied bias to the LP, as the CubeSat tries to balance the electron current collected by the probe with ion current collected by the CubeSat surface.

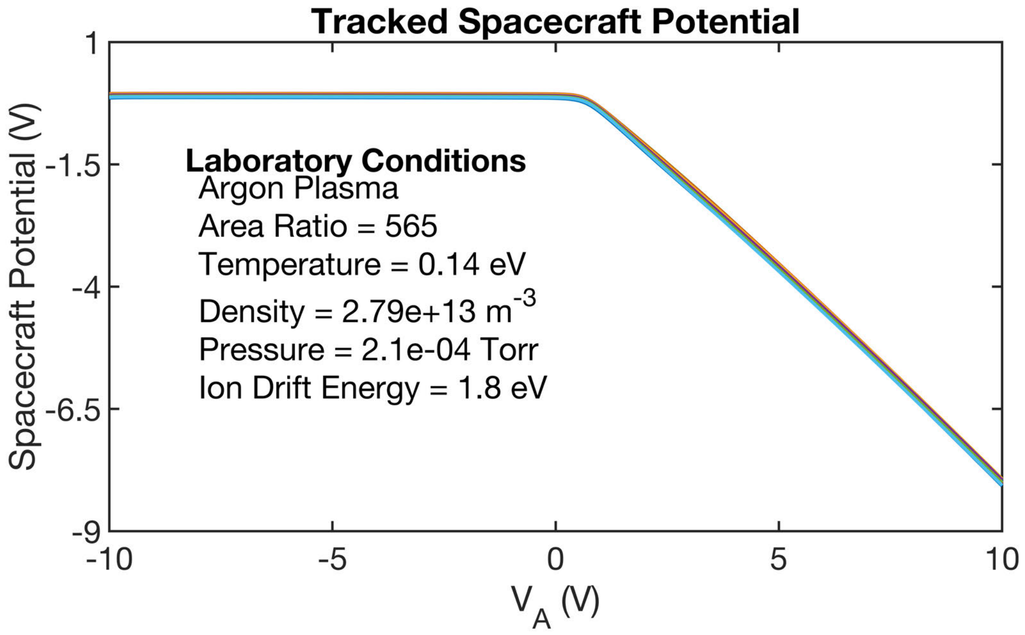

Figure 5.10: This plot is an example of a properly implemented high-impedance measurement where all sweeps lie very close to one another.

5.3.1.1 Maximum Charging as a Function of Area Ratio

The area ratio has a clear relationship with the maximum negative spacecraft charging levels that the CubeSat reaches. Generally, the greater the area ratio, the more stable the spacecraft potential during the Langmuir probe sweep, and the less negatively charged the spacecraft becomes, as shown in fig. 5.11. Therefore, as the area ratio increases, the magnitude of the correction due to the twin-probe method in density and temperature measurements decreases. Indeed, fig. 5.37 indicates that the percent change between the corrected and uncorrected density will decrease with increasing area ratio, regardless of the employed method (discussed in section 5.3.5). This same relationship is observed for electron temperature measurements, as discussed in section 5.3.4 (see fig. 5.32). Cases where the percent difference between single and twin-probe measurements are low (below about 20) correspond to cases with a combination of low plasma densities (low $1 \times 10^{12}\,\mathrm{m}^{-3}$) and high area ratios (around 565). This is an expected result, as low plasma densities (allowing for higher ion drift speeds, as shown in fig. 6.1a) and high area ratios both lead to reduced spacecraft charging and less need for the twin-probe method.

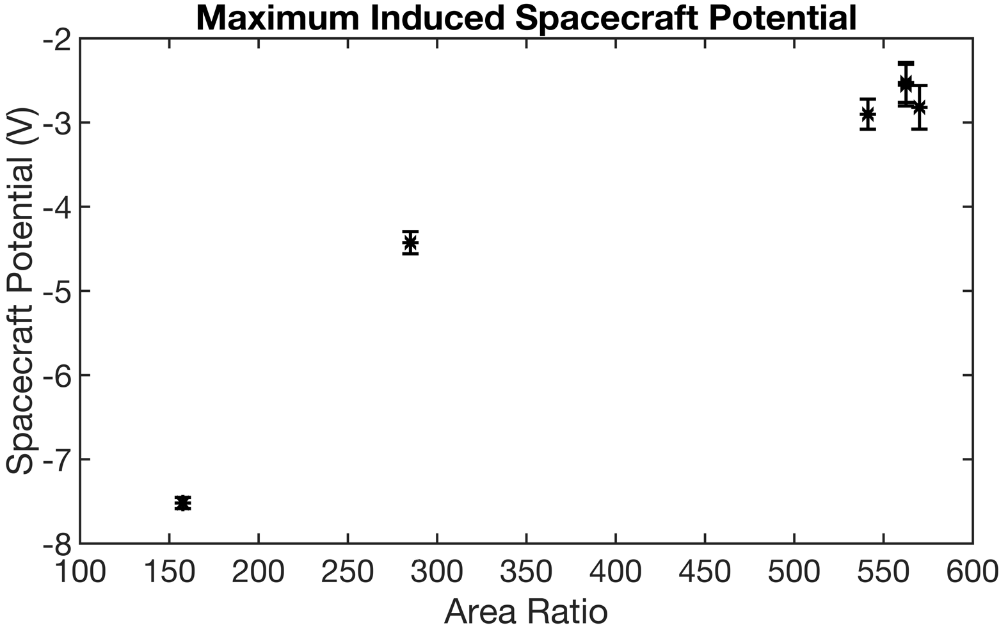

Figure 5.11: The points represent the maximum negative potential for densities below $1 \times 10^{13}\,\mathrm{m}^{-3}$ where the SC potential becomes more positive as the area ratio increases.

When studying the maximum charge as a function of area ratio, the case where densities are greater than $1 \times 10^{13}\,\mathrm{m}^{3}$ is excluded. This is because density and drift energy were inversely proportional leading to significantly lower drifts speeds and greater negative charging. Further, discussion on the correlation between drift energy and plasma density, as well as drift energy and spacecraft charging can be found in section 6.1 (accompanied by fig. 6.1). The range of plasma parameters accompanying fig. 5.11 is shown in table 5.3.

Electron temperature	$0.22\,\mathrm{eV}$ to $0.78\,\mathrm{eV}$
Plasma density	$1.8 \times 10^{12}\,\mathrm{m^{-3}}$ to $3 \times 10^{12}\,\mathrm{m^{-3}}$
Main ion drift velocity	$3.8\,\mathrm{km\,s^{-1}}$ to $11\,\mathrm{km\,s^{-1}}$
Charge exchange ion drift velocity	$0.47\,\mathrm{km\,s^{-1}}$ to $0.8\,\mathrm{km\,s^{-1}}$

Table 5.3: Range of plasma parameters for measurement sets in fig. 5.11.

5.3.1.2 Issues with Settling Time

As mentioned in section 3.2.2, considering the settling time is key to making proper high-impedance measurements for the twin-probe method. For any set of measurements, the Langmuir probe was swept with a sawtooth waveform from $-10\,\mathrm{V}$ to $10\,\mathrm{V}$. Between each sweep, the bias to the probe was shut off, and there was some elapsed time that ranged from a couple of seconds to tens of minutes. Thus, a large voltage step occurred between the last measurement of one sweep (spacecraft at maximum negative potential) and the first measurement of the subsequent sweep. Figure 5.12a is an example of capacitive effects that can be experienced during a twin-probe measurement. In this particular set of measurements, 4 seconds elapsed between Langmuir probe sweeps. The very first sweep shows little to no transient effects, since the entire system was in equilibrium (i.e. all conductors were at their floating potential). For subsequent sweeps, there is clear transient behavior, and it will be shown that *this transience is due to the CubeSat discharging, and not the temporal limit of high-impedance measurements*. These transient effects severely impact uncorrected ion density measurements. In the first measurement of Figure 5.12b, the ion densities between corrected and uncorrected measurements show little difference (similar behavior is seen in section 5.3.2.4 for ion density measurements that are not impacted by transient effects). However, for all subsequent measurements in fig. 5.12b, there is a clear difference between uncorrected and corrected measurements. A sharp increase in uncorrected ion density estimates, between the first sweep and subsequent sweeps, is observed in Figure 5.12b. This increase is directly attributed to the negative charging of the CubeSat, as uncorrected sweeps do not take the actual spacecraft potential into account. As discussed in section 1.3, for stable spacecraft potentials, the measured plasma potential is an estimate of the spacecraft floating potential. The uncorrected sweeps for this measurement set consistently estimate a spacecraft floating potential of $-1\,\mathrm{V}$, while the high-impedance probe measures spacecraft potentials of at least $-1.5\,\mathrm{V}$ (see measured potential for most negative applied bias of fig. 5.12a) . Since the uncorrected sweeps could not account for the more negative spacecraft potential, the ion densities are overestimated. However, the twin-probe corrected ion density estimates are noticeably smaller than their uncorrected counterparts suggesting some level of correction occurred.

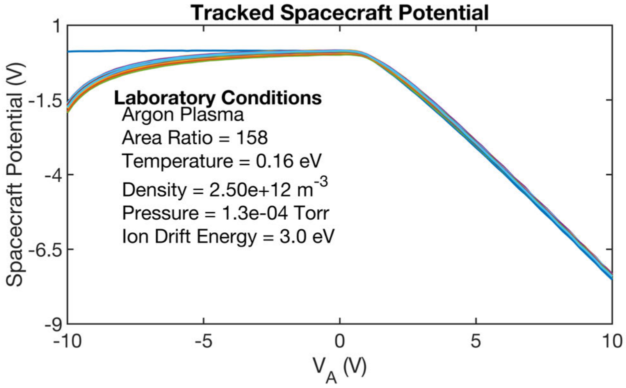

(a) This plot shows high-impedance measurements affected by system capacitance, as the system settling time was not satisfied between sweeps.

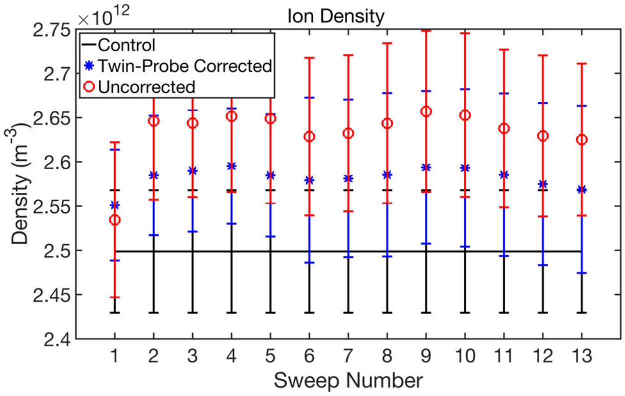

(b) Discrepancies between uncorrected and corrected ion density estimates due to settling time issues.

Figure 5.12: Transient effects on spacecraft charging and ion density measurements.

Further studies into these capacitive effects verify that the settling times between biases in any given sweep aren't the source of capacitive effects. As shown in table 3.1, the settling time of the high-impedance probe for the densities in these experiments is orders of magnitude smaller than a millisecond, and does not hinder the LP bias slew. The Keithley sourcemeters averaged measurements between 1 to 10 power line cycles to reduce the effects of AC noise. As a result, they would take between $16\,\mathrm{ms}$ to $160\,\mathrm{ms}$ to integrate over the DC signal when making current or voltage measurements [177]. However, the settling time due to sheath capacitance for large voltage steps is considerably larger. Figure 5.13 demonstrates that if the elapsed time between LP sweeps is on the order of seconds, the measured spacecraft potential displays transient behavior, after the initial sweep. The source of the increased negative potential cannot be verified; however, one explanation is that the spacecraft had not fully dissipated its induced negative charge from balancing

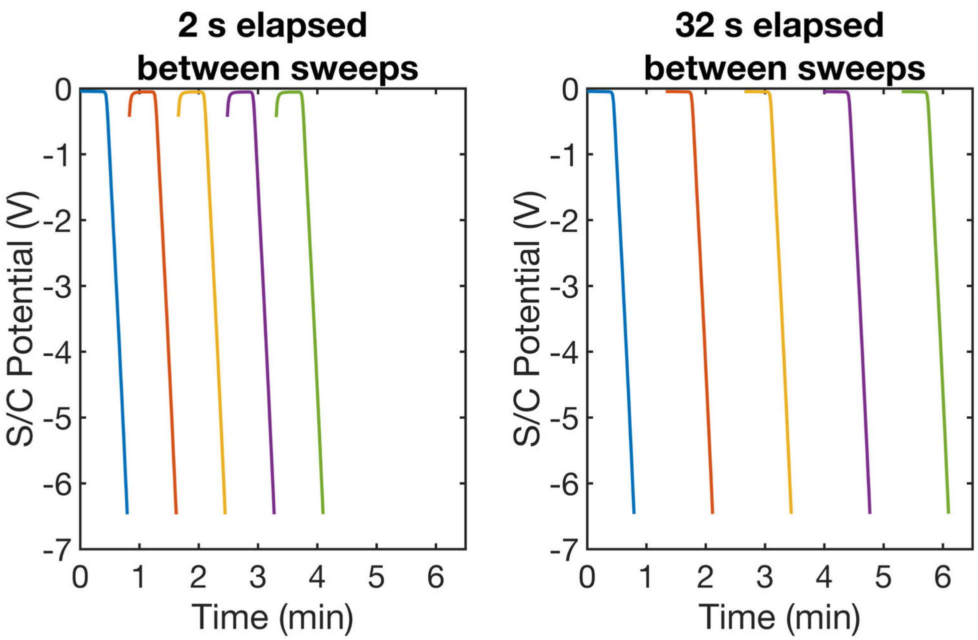

Figure 5.13: Spacecraft charging behavior for two different elapsed times between sweeps.

electron current to the probe by the time the next sweep began. Additionally, facility effects, such as longer cables and greater capacitances due to operating in the vacuum chamber, contributed to longer than expected settling times.

Moreover, we can qualitatively compare transient times for different densities using fig. 5.14 as an example. Figure 5.14a corresponds to measured transients for a high-density case. Since these measurements were made with the nominal spacecraft system in a mounted state, like the one shown in fig. 5.4b, the recorded plasma properties are off center-line plasma properties, and the ion drift velocities are a rough approximation, since plasma potential measurements at the same position as the RPA were not made. For fig. 5.14b, the nominal spacecraft system was configured in an unmounted state, like the one shown in fig. 5.4a, and more accurate measurements were made. While the area ratio of the higher density case is greater than the lower density case, the higher density case also had a slower ion drift speed, and thus, produced similar charging magnitudes to the lower density case. Between the two cases, there is a noticeably shorter transient time when the plasma density is greater, likely due to the nearly ten-fold increase in available charge to dissipate charge buildup from the CubeSat. This suggests that in situations of sparse plasmas with no additional methods of removing negative charge build up, such as photoelectron current or an active electron beam emission, operators should be wary of long transient times related to CubeSat discharge rates.

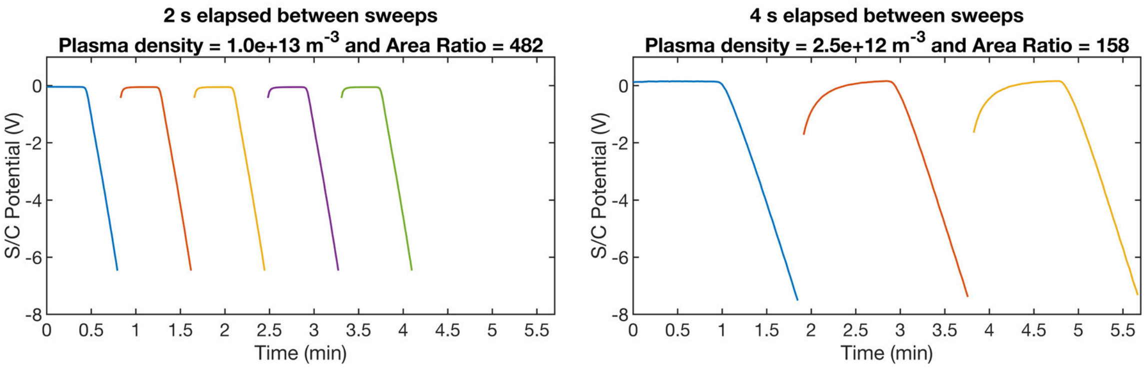

(a) Transient effects observed for a plasma density above $1 \times 10^{13}\,\mathrm{m}^{-3}$.

(b) Transient effects observed for an approximate plasma density of $1 \times 10^{12}\,\mathrm{m}^{-3}$.

Figure 5.14: Transient effects observed at different plasma densities and area ratios.

	Figure 5.14a	Figure 5.14b
Electron temperature	$0.26\,\mathrm{eV}$	$0.22\,\mathrm{eV}$
Plasma density	$>1 \times 10^{13}\,\mathrm{m}^{-3}$	$2.5 \times 10^{12}\,\mathrm{m}^{-3}$
Main ion drift velocity	$\sim 2\,\mathrm{km\,s}^{-1}$	$3.8\,\mathrm{km\,s}^{-1}$
Charge exchange ion drift velocity	N/A	$0.5\,\mathrm{km\,s}^{-1}$
Area Ratio	482	158
Number of Biases in a Sweep	51	101
Elapsed Time between Biases	$0.9\,\mathrm{s}$ to $1\,\mathrm{s}$	$1.1\,\mathrm{s}$ to $1.2\,\mathrm{s}$

Table 5.4: Range of parameters for measurement sets in fig. 5.14.

5.3.1.3 Tracking Spacecraft Potential for Different Probe Orientations

As will be shown below, *the twin-probe method is able to correct impacted I-V curves, regardless of orientation relative to the ion drift speed and spacecraft.* To demonstrate this capability, the CubeSat is rotated along its Y-axis (refer to fig. 5.15) such that one probe changes its angle of attack relative to the ion drift velocity, and the other probe maintains a nearly constant orientation relative to the plasma flow. A visual of the spacecraft configuration is shown in fig. 5.4b. In this manner, a swept probe rotates around the spacecraft to study how Langmuir probe orientation may affect spacecraft charging, or the high-impedance probe can rotate to understand if its orientation affects the accuracy of the twin-probe method.

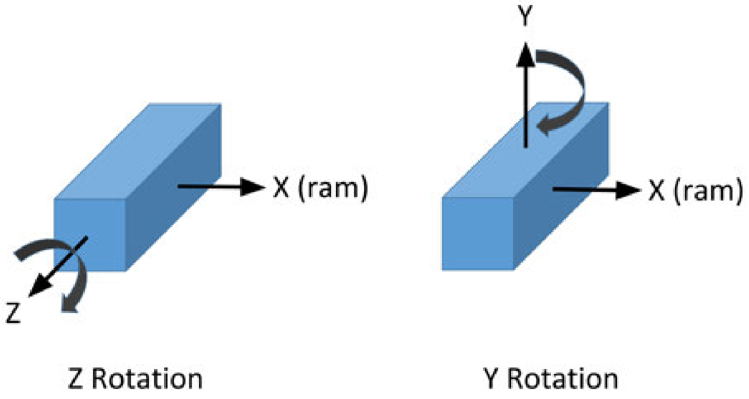

Figure 5.15: Rotation about the CubeSat's Z-axis and Y-axis.

Consider a Y-axis rotation where the high-impedance probe changes attack angle as the SC rotates and the sweeping probe remains stationary. Using fig. 5.4b as a reference, the swept Langmuir probe is mounted vertically and the high-impedance probe is horizontal. There were four high-impedance probe orientations: two orientations where the high-impedance probe was perpendicular to the drift velocity, one orientation where the probe was parallel to the ion drift velocity and in the ram direction, and a final orientation where the probe was in the wake region and parallel to the ion drift velocity. When twin-probe corrections are applied, the resulting I-V curves are in closer agreement (i.e. curve trends were more similar) than uncorrected sweeps. However, there is a clear offset between the corrected I-V curves (shown in fig. 5.16). As mentioned in section 3.1, the twin-probe method shifts the reference of the LP to the high-impedance probe. Since the plasma potential of the I-V curve is a measure of the floating potential of the reference electrode (discussed in section 1.3), the plasma potential as a function of probe orientation can be studied to determine the root of the offset. Indeed, fig. 5.17 shows that the plasma potential changes with high-impedance probe orientation, even though the swept probe has not changed orientation. The discrepancy between the two perpendicular cases is likely due to the electron temperature being consistently hotter on the northern side of the chamber relative to the southern side of the chamber (see fig. 5.7 for an example). When perpendicular to the plasma flow, the high-impedance probe would be roughly $0.3\,\mathrm{m}$ from center-line, and so the difference in temperature between one perpendicular orientation and the other could vary by $0.05\,\mathrm{eV}$ to $0.08\,\mathrm{eV}$, producing a noticeable difference in high-impedance probe floating potential. If the corrected sweeps are shifted by their individual plasma potentials, as depicted in fig. 5.18, it is clear that the corrected sweeps are grouped more tightly than their uncorrected counterparts in fig. 5.16.

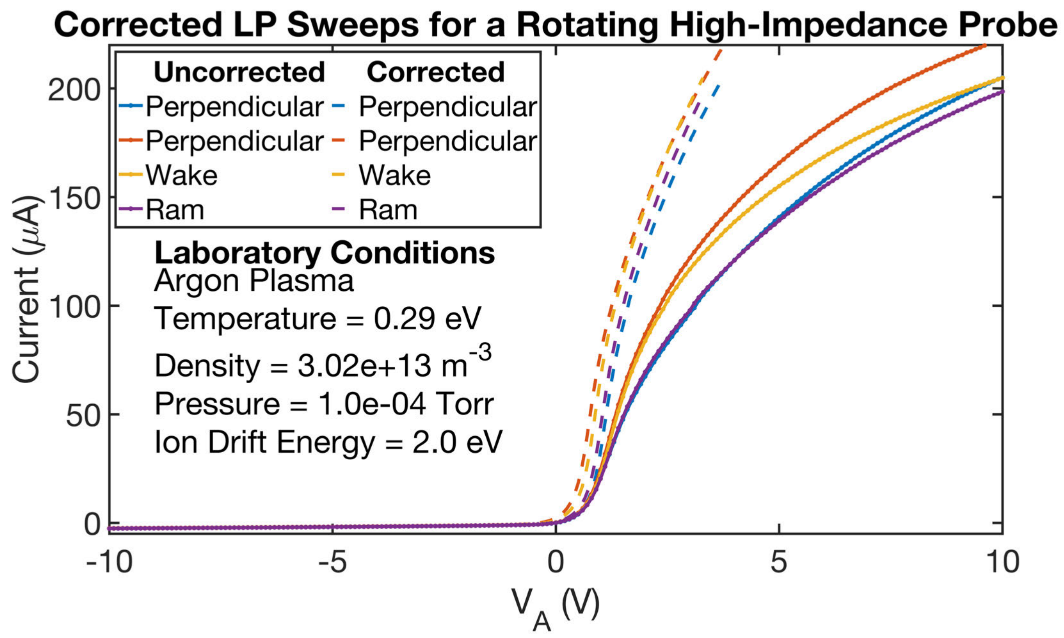

Figure 5.16: Twin-probe LP corrections as the CubeSat rotates about its Y-axis. The high-impedance probe changes its angle of attack relative to the ion drift velocity as the CubeSat rotates (sweeping probe remains in the same location and orientation).

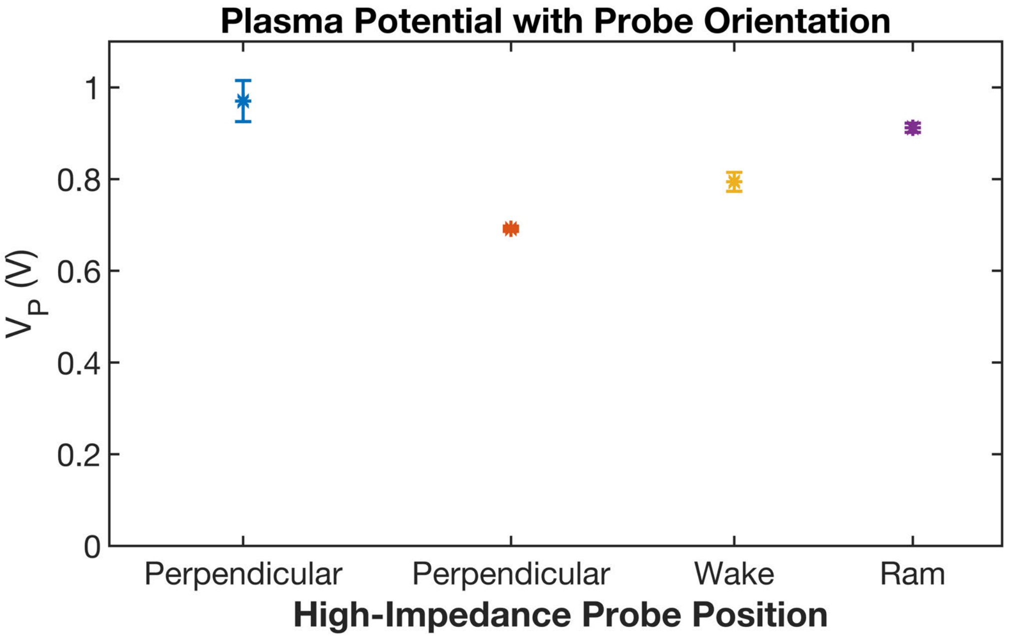

Figure 5.17: Plasma potential of twin-probe corrected I-V curves indicate that the high-impedance probe's floating potential varies as the CubeSat rotates around its Y-axis.

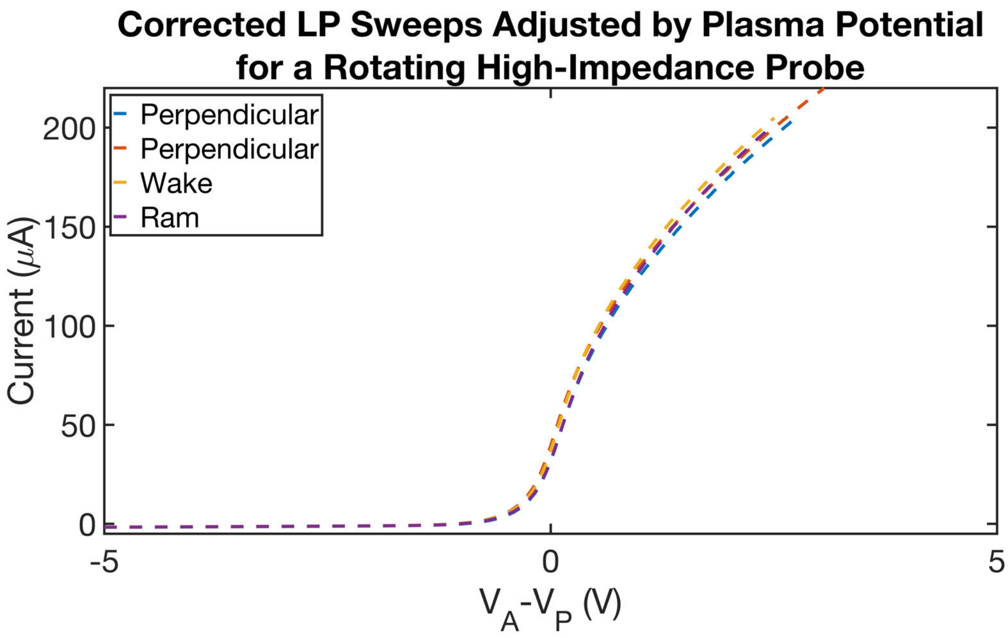

Figure 5.18: Twin-probe LP corrections for a rotating CubeSat adjusted by their individual plasma potentials. The high-impedance probe changes its angle of attack relative to the ion drift velocity as the CubeSat rotates (sweeping probe remains in the same location and orientation).

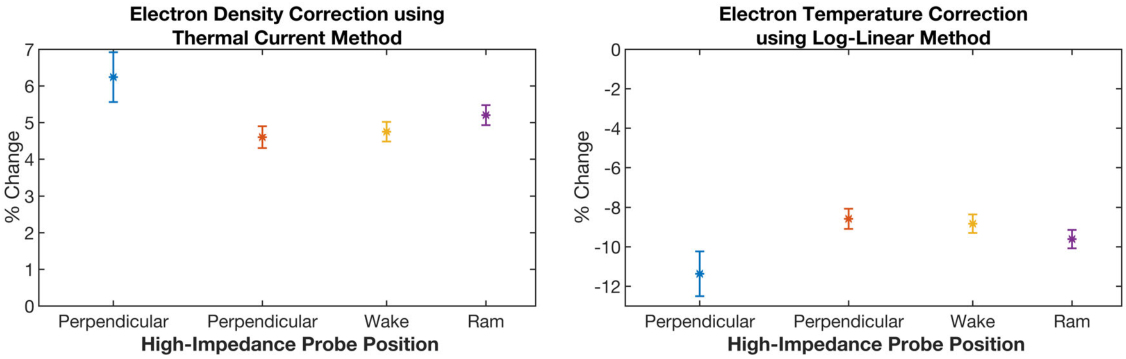

(a) Percent change of electron density estimates using thermal current method.

(b) Percent change of electron temperature estimates using log-linear method.

Figure 5.19: Percent change between corrected and uncorrected plasma property estimates for a high-impedance probe that is perpendicular to the plasma flow, parallel to the flow in the spacecraft ram, and parallel to the plasma flow in the spacecraft wake. The area ratio is 482.

Next, the percent change between twin-probe corrected and uncorrected electron temperature estimates (using the log-linear method discussed in appendix C.5.3) and electron density estimates (using the thermal current method discussed in appendix C.6.1) were studied. A comparison of the different methods for determining electron temperature is given in section 5.3.4, and a similar comparison for electron density estimates is presented in section 5.3.5. Three sweeps were performed at the four high-impedance probe orientations, each with a different elapsed time between sweeps to account for settling time issues ($0.13\,\mathrm{min}$, $2.13\,\mathrm{min}$, $30.15\,\mathrm{min}$). The results shown in fig. 5.19 represent the average density (fig. 5.19a), or temperature (fig. 5.19b), and the corresponding standard deviations. From fig. 5.19, it can be determined that the twin-probe method is not strongly impacted by the high-impedance probe's position. The largest discrepancy occurs at the left-most perpendicular case where the percent change is a few percent greater compared to the other orientations.

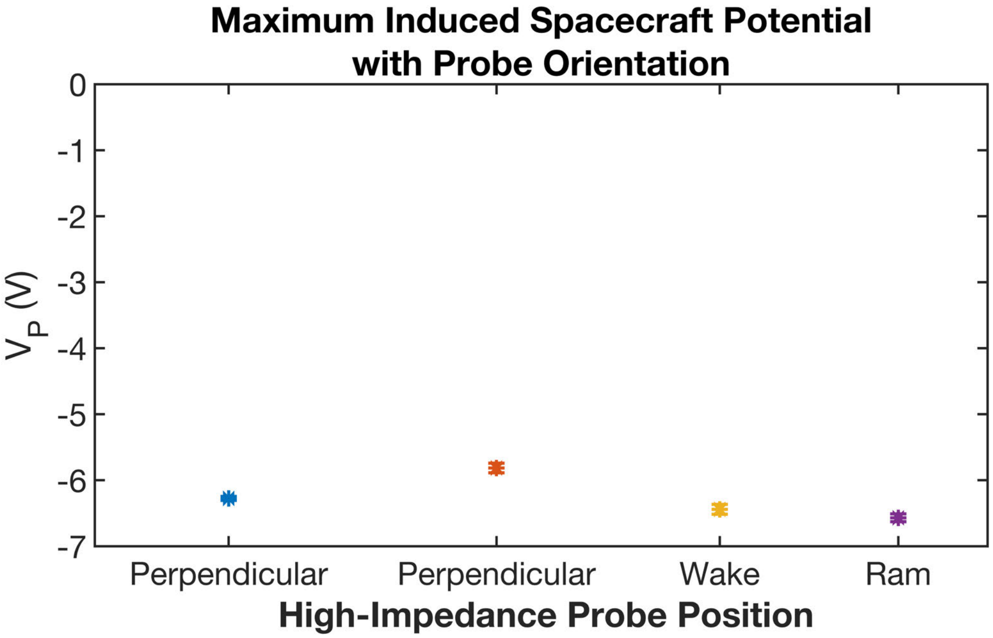

Figure 5.20: Maximum spacecraft potential induced by LP operation as the CubeSat rotates the high-impedance probe around its Y-axis. The high-impedance probe changes its angle of attack relative to the ion drift velocity as the CubeSat rotates (sweeping probe remains in the same location and orientation).

It is assumed that the variations are due to changes in the spacecraft's current collection behavior. Even though the swept LP remained roughly in the same position and orientation as the SC was rotated, it is likely that the CubeSat's own orientation relative to the plasma flow and facility effects (e.g. contamination of CubeSat surfaces and skew in plasma properties discussed in section 5.2) affected the I-V characteristics. For instance, when inspecting the maximum induced spacecraft potential (as was done in section 5.3.1.1), it is clear that there is a difference in charge between the two perpendicular orientations (see fig. 5.20). Additionally, the orientation with the smallest induced potential also had the smallest magnitude of correction.

As a word of caution, while chamber results do not show any strong impact on twin-probe corrections due to high-impedance probe orientation, the same may not be true in the wake region of satellites in space. When deep in the satellite's wake, plasma densities have been known to fall significantly [171], which can produce plasma resistances that are too low for proper high-impedance measurements (see table 3.1 for the relationship between plasma density and resistance).

Similarly, a Y-rotation of the CubeSat can be considered with probe roles reversed (the swept probe rotates with the SC and the high-impedance probe remains stationary). In this configuration, the swept probe will have the same orientations relative to the plasma that the high-impedance probe had in the previous case. For the following discussion, figs. 5.21 and 5.22 can be used as references. As a point of clarity, all LP sweeps in fig. 5.21 are shifted such that each sweep's plasma potential aligns with $0\,\mathrm{V}$ for ease of comparison between control, uncorrected, and twin-probe corrected sweeps. The measured plasma properties are not specifically detailed, since all comparisons will be made within a measurement set; thus, only the tracked spacecraft potential and grouping of the corrected probes are analyzed.

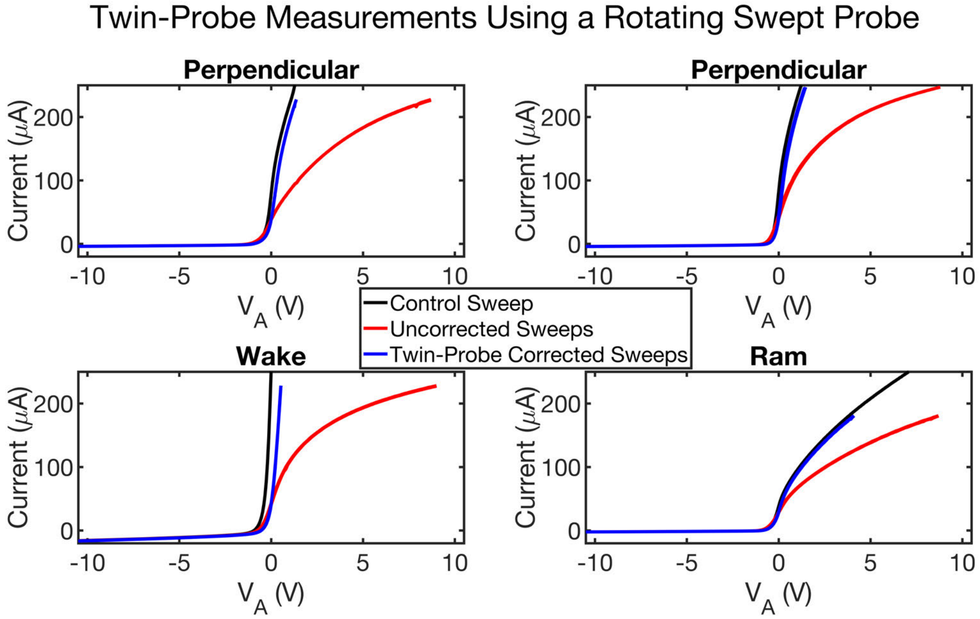

Figure 5.21: Twin-probe LP corrections as the CubeSat sweeping probe rotates around its Y-axis (high-impedance probe remains in the same location and orientation). All sweeps have been adjusted by their respective plasma potential; thus, $0\,\mathrm{V}$ corresponds to the measured plasma potential.

As expected, in the two orientations where the swept probe was perpendicular to the ion drift velocity, the spacecraft charge induced from probe operation is roughly equivalent. When the probe is oriented parallel to the drift velocity and in the ram direction, it only collected thermal electrons and ions, leading to significantly less current collection; and as a result, less spacecraft charging. Finally, when the LP was in the wake of the spacecraft, the probe collected significantly more current, resulting in the most negatively-induced spacecraft potentials. The dependence of probe orientation relative to ion drift speed is discussed in section 5.3.2.2, but in terms of its effects on the charging behavior of the satellite, it is clear that *when the probe collects greater electron current, the spacecraft charges to a more negative potentia*l, as shown in fig. 5.22. When comparing the twin-probe corrected LP sweeps to the control sweeps, in fig. 5.21, they both exhibit the similar current characteristics, but are offset by a constant value, the floating potential of the high-impedance probe. The variable offset between twin-probe corrected and control values is likely due to the changing satellite and high-impedance probe floating potentials at each orientation.

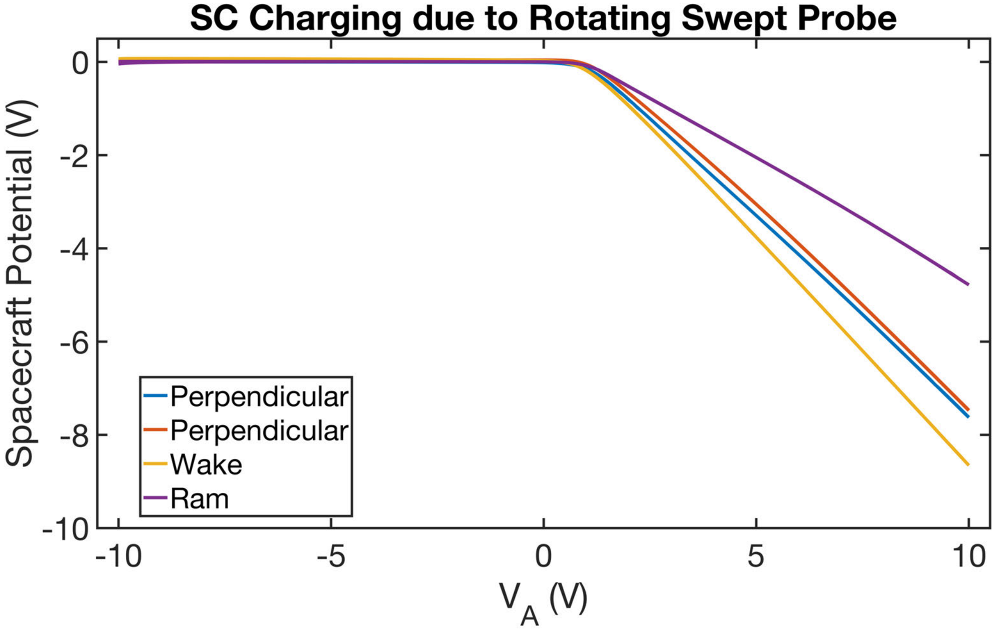

Figure 5.22: High-impedance measurements of spacecraft potentials as the CubeSat rotates around its Y-axis. The swept probe rotates with the CubeSat.

5.3.2 Plasma Plume Ions

The first plasma property that is analyzed from LP current-voltage characteristics is the ion density. For accurate ion density measurements, understanding the ion energy distribution function (IEDF), the number of distinct ion populations, and their respective characteristics (temperature, drift speed, prevalence in the IEDF), which are parameters obtained from RPA measurements, is invaluable. Ion densities are a useful plasma property for determining the accuracy of electron density measurements, so reducing their uncertainties is key in making reasonable comparisons.

5.3.2.1 Ion Energy Distribution Functions

Ion energy distribution functions were all measured using a retarding potential analyzer. All measured IEDFs were smoothed using a SavitskY-Golay filter with a fourth order polynomial and a window size that is $15\,\%$ of the total number of points. The aggressive filtering was necessary to sufficiently smooth the peaks of the first derivative of the current, but the window size will shift the peaks of the distribution slightly. Furthermore, as shown in fig. 5.23a, there was clear ohmic leakage current at high biases relative to the plasma potential. Since it is expected that the measured current approaches zero, this leakage current should be removed from the measured current before analyzing its first derivative. The following process was taken for every RPA measurement set to remove the ohmic behavior:

1. A first order polynomial was fit to the final $25\,\%$ of the data. This is referred to as ”Ohmic Fit” in fig. 5.23a.
2. The Ohmic Fit is extended over the full range of biases that the RPA was operated over, and subtracted from the measured currents.

As shown in figs. 5.23b and 5.23c, removing the ohmic current does not affect the IEDF’s peak amplitudes, peak position, or the full width half maximum of each peak. However, the high-energy tail of the distributions were slightly modified. Since this region is not considered when fitting a Maxwellian to the individual peaks, the ion characteristics remain unaffected by the Ohmic Fit. Generally speaking, there will always be one drifting Maxwellian population and a CEX population that varies in prominence [178]. As noted by *Rubin et. al.* [174], the charge exchange population is more prominent in regions with greater neutral flow, since the charge exchange collision frequency increases with neutral particle density and background pressure. Furthermore, the probability that a drifting ion has a charge exchange collision increases the farther it travels from the plasma source. Thus, the fraction of the ion population composed of CEX ions increases further from the source.

CEX ions typically have no initial drift velocity; however, the complicated potential structure near and downstream of a hollow cathode can provide the energy to accelerate

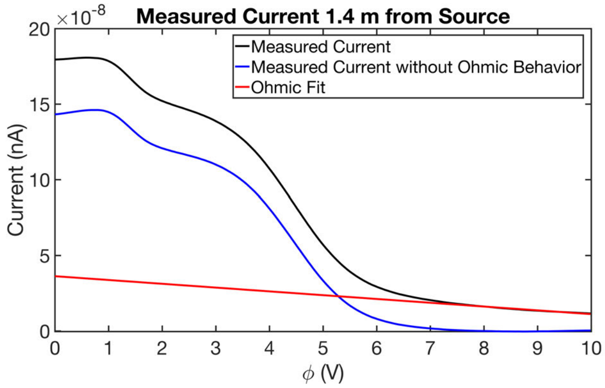

(a) Measured current from RPA positioned $1.4\,\mathrm{m}$ from plasma source.

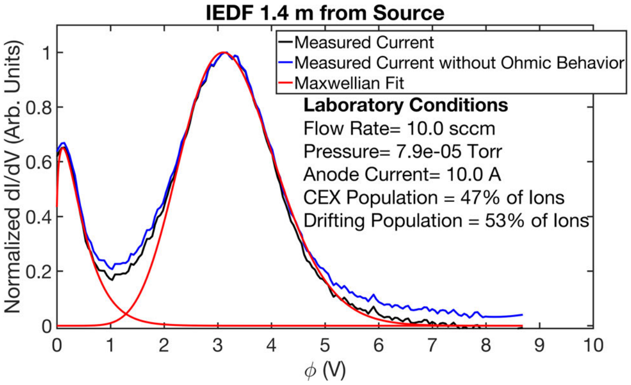

(b) Double peaked IEDF with small CEX ion population $1.4\,\mathrm{m}$ from plasma source.

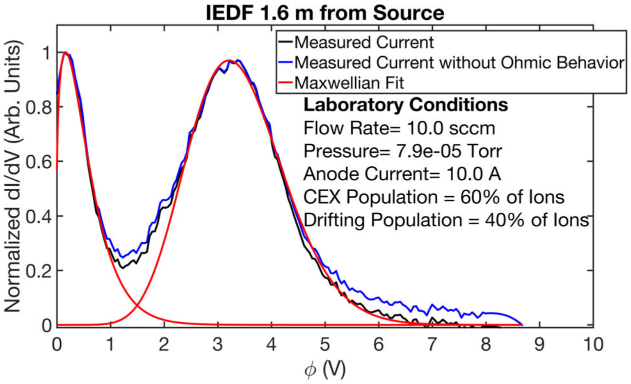

(c) Double peaked IEDF with more significant CEX ion population $1.6\,\mathrm{m}$ from plasma source.

Figure 5.23: Ion energy distribution functions representing plasma plumes with no charge exchange ions and a significant charge exchange ion population.

CEX ions. There is a potential drop across the plasma plume that accelerates CEX ions towards the chamber wall where CEX ions produced near the source experience the greatest gain in kinetic energy. Figure 5.9 provides an example of this potential drop (note the potential drop of an LP's floating potential is similar to the drop seen in the plasma potential across the plume). Additionally, it is possible for a CEX ion to be created with a non-negligible drift velocity. To understand this *Goebel et. al.* notes that the potential structure immediately down stream of the hollow cathode accelerates ions towards center line where they undergo charge exchange collisions with the neutrals. The neutralized ions keep their kinetic energy and are eventually reionized, producing ions that carry the sum of their thermal energy, the energy due to their initial acceleration, and the energy from the plasma potential where they were reionized [179]. Thus, CEX ions produced at the plasma source or throughout the plasma plume will gain kinetic energy as they travel to the edge of the plasma plume (towards the chamber wall or the RPA). Refer to fig. 5.23c or IEDF plots provided by *Rubin et. al.* [174] for examples of CEX ions with a non-zero drift produced by the hollow cathode used in the experiments of this dissertation (section 5.1.1). Since the exact relationship between flow rate, distance from plasma source, and CEX ion population isn't known, RPA measurements are taken in conjunction with each twin-probe measurement set to estimate the ion population properties (examples shown in figs. 5.23b and 5.23c). An in-depth description of the analysis methods employed to extract ion temperature, drift speed, and the ion population's prominence in the total ion distribution is given in appendix D.

5.3.2.2 Ion Current Collection as a Function of Angle of Attack

Taking advantage of the fact that LPs were mounted on a rotating spacecraft, the ion current as a function of angle of attack relative to the ion drift speed was measured for full $360°$ rotations of the satellite. Figure 5.24a shows the result of several such rotations where a LP was biased to $-10\,\mathrm{V}$, and measurements were taken every $0.5\,\mathrm{s}$ as the spacecraft rotated clockwise and counterclockwise at a rate of $22.5\,°\,\mathrm{s}^{-1}$. The angles of $\pi/2$ and $3\pi/2$ correspond to probes that are perpendicular to the ion drift velocity, an angle of 0 corresponds to the probe being parallel to the drift velocity, and π corresponds to the probe in the wake.

When compared to similar ion current measurements made by the AE missions (see fig. 5.24b), there are some stark differences when the probe is pointed parallel to the ion drift speed and when the probe is in the wake. For the AE measurements, probe end effects enhanced ion current collection while angles $\pm15°$ from a $0°$ angle of attack are at a local minimum for ion current collection. This local minimum more closely resembles the local minimum seen in the chamber measurements (see current collection for parallel probe orientation fig. 5.24a), where the probe current more closely resembles orbit motion limited (OML) current collection for thermal ions instead of drifting ions. The wake region

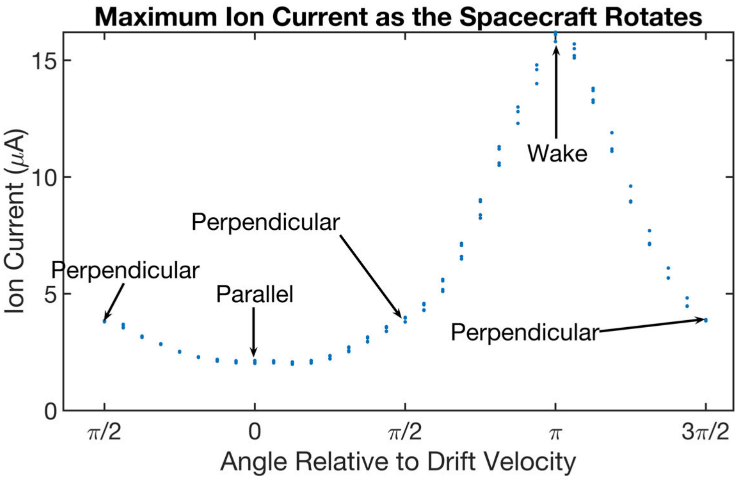

(a) Maximum ion current measured by LP at different angles of attack relative to ion drift speed in the chamber.

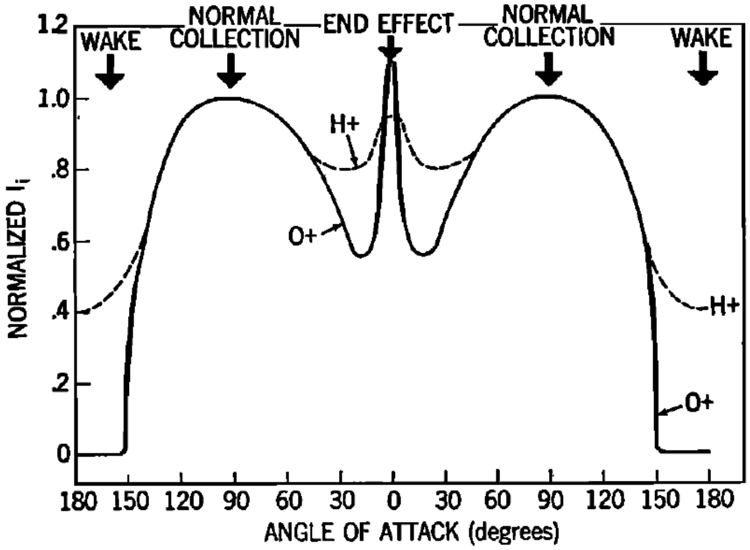

(b) Ion current as a function of angle relative to drift velocity from Atmospheric Explorer -C, -D, and -E missions. Figure from *Brace et. al.* [153]

Figure 5.24: Comparing chamber and satellite measurements ion current relative to angle of attack.

has the largest discrepancies between in-orbit and in-chamber measurements. Where the ion current collected in the wake was near zero for in-orbit measurements, the wake ion current was a global maximum in the chamber. This discrepancy is due to a combination of factors but two major contributors at play are: 1) significant CEX ion population and 2) the probe may be near a region of the wake where ions and electrons are focused by the CubeSat potential profile. The larger population of CEX ions in the chamber decreases the size of the satellite's wake region, as they are less energetic and can fill the wake region more easily (discussed in section 5.3.2.3). Furthermore, higher background pressures in the chamber can further distort the wake region due to an increase of charge-neutral collision frequencies. Finally, *Albarran et. al.* [171] demonstrated that a CubeSat is capable of focusing ions and electrons at the tail of its wake region where the densities increase by an order of magnitude greater relative to the quasi-neutral region of the plasma. This ratio roughly agrees with the ratio between the ion currents seen when the probe is parallel to the ion drift speed and in the wake.

5.3.2.3 CubeSat Surface Ion Current Collection

Since each side of the CubeSat is isolated from the rest of the structure, the currents to each face can be measured while the total structure is biased relative to the plasma. During each sweep of notional CubeSat, the side that is initially in the ram direction and the current to the rest of the structure were measured as a function of the attack angle between the ram-facing side and the ion drift velocity, and bias relative to the plasma plume. As described in section 5.1.2, the only face of the CubeSat that could not be biased relative to the plasma was the face of the CubeSat grounded to the chamber, as it was physically connected to the rotation stage. Thus, there are two total surface areas for the CubeSat based on the axis of rotation. When the CubeSat was rotated along its Z-axis, a small face of the CubeSat was mounted on the rotation stage, and so the total area is approximately $0.13\,\mathrm{m}^2$. Similarly, the total area of the CubeSat was approximately $0.11\,\mathrm{m}^2$ when it was rotated about its Y-axis. Figures 5.25 and 5.26 exhibit the ion currents collected by the nominal CubeSat surfaces for both axes of rotation. There is a factor of ten difference in ion density between the case where the CubeSat rotates along its Z-axis and when the CubeSat rotates along its Y-axis (see table 5.5 for a comparison of plasma properties). The denser plasma for the Y-axis of rotation case results in significantly more ion current collection by the CubeSat, when compared to the current collection in the Z-axis of rotation case.

Figure 5.25 compares the ram ion current to the total ion current collected by the CubeSat for different ram-facing surface areas. Near the floating potential of the CubeSat, it is difficult to determine the percent of the total current that is comprised of ram ion current. This is because the floating potential of the ram-facing side and the total collected current differ slightly, and so an accurate ratio is difficult to establish. As an example, fig. 5.25a shows the large ram face and full CubeSat currents intersecting while still collecting net negative current. In this situation, the floating potential of the whole CubeSat is slightly more negative than the floating potential of the ram-facing side. At attractive potentials several ion temperatures greater than the ion drift energy, the large face approaches $40\,\%$

to $50\,\%$ (see fig. 5.25c). Therefore, as the attractive potential reaches and surpasses the ion drift energy, the non-ram-facing sides of the SC and its large ram-facing side will equally comprise the total collected ion current. This behavior agrees with the modeled oxygen ion ram and wake currents in *Nascap-2K* simulations, where ram ion currents would represent close to $70\,\%$ of the total collected currents at low attractive potentials, but would represent just $44\,\%$ of the total current when the attractive potential was twice as large as the ion drift energy (refer to table A.1). Additionally, when the smaller side of the 3U CubeSat is ram-facing, the small face is never as pronounced as the large side's ram-facing current collection. Even at the most attractive potentials, the small face's current collection represented roughly $10\,\%$ of the CubeSat's total current collection (see fig. A.19). Therefore, it should be expected that larger ram-facing areas will be a more significant source of the total current collection of the CubeSat, as modeled by *Nascap-2K* (see fig. A.19).

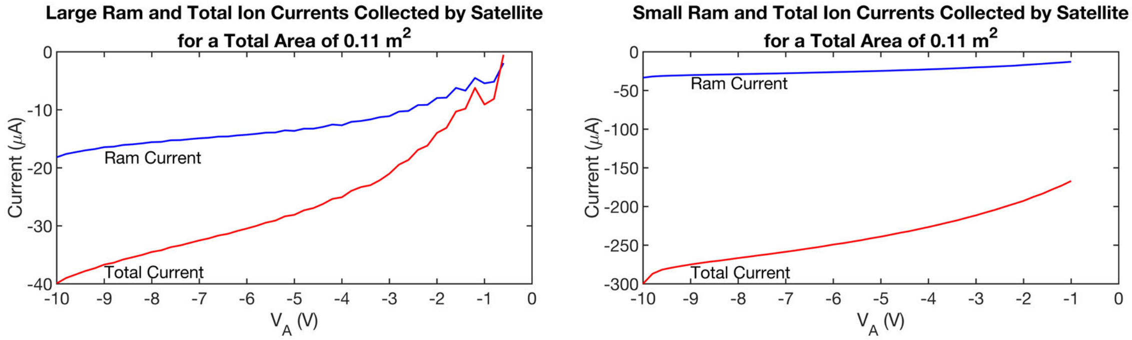

(a) Ion current collection when a $0.3\,\mathrm{m}^2$ face is in the ram direction.

(b) Ion current collection when a $0.1\,\mathrm{m}^2$ face is in the ram direction.

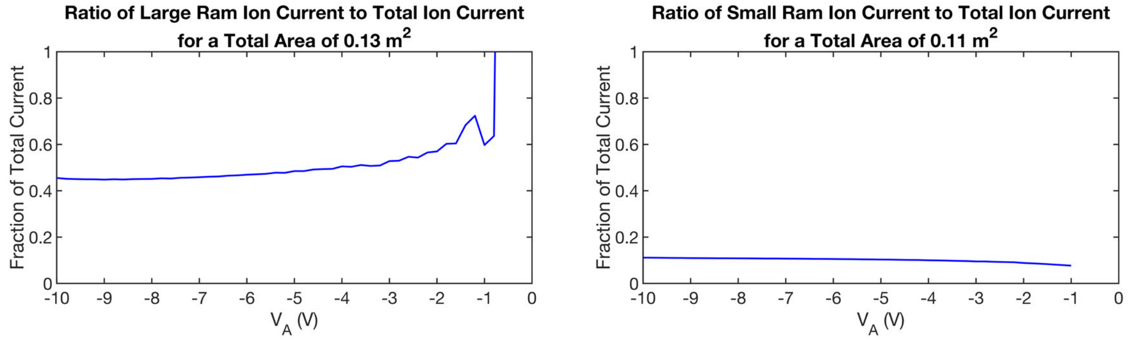

(c) Percentage of ram ion current collection as a function of applied bias for a $0.3\,\mathrm{m}^2$ ram-facing side.

(d) Percentage of ram ion current collection as a function of applied bias for a $0.1\,\mathrm{m}^2$ ram-facing side.

Figure 5.25: Ram and total ion current collection for differently sized ram direction areas for Z-axis ($0.13\,\mathrm{m}^2$ surface area) and Y-axis rotations ($0.11\,\mathrm{m}^2$ surface area).

Beyond the ratio between the ram ion current collection and the total ion current collection, the wake ion currents were also studied. As shown in table A.1 of appendix A.2.3, there should be negligible ion current collected in the wake region when the satellite's attractive potential is below the ion drift energy, unless there is a significant presence of low energy ions. In the *Nascap-2K* simulations, the low energy ions were light hydrogen ions, but in the chamber, these low energy ions are CEX ions. Indeed, fig. 5.26 demonstrates non-negligible ion current collection in the wake region of the CubeSat, even at low attractive potentials. This higher-than-expected wake ion current collection is likely due to the presence of CEX ions and high neutral background pressures helping to validate the theories presented in section 5.3.2.2. Additionally, the presence of CEX ions increases the current collected by the sides of the CubeSat that are not ram-facing, reducing the fraction of the total current that is attributed to the ram-facing area presented in figs. 5.25c and 5.25d.

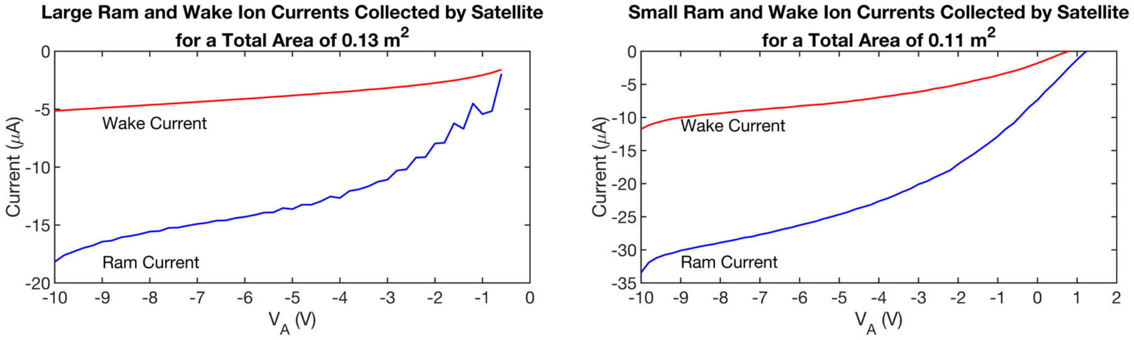

(a) Ion current collection when a $0.3\,\mathrm{m}^2$ face is in the ram direction.

(b) Ion current collection when a $0.1\,\mathrm{m}^2$ face is in the ram direction.

Figure 5.26: Ram and wake current collection for differently sized ram direction areas for Z-axis ($0.13\,\mathrm{m}^2$ surface area) and Y-axis rotations ($0.11\,\mathrm{m}^2$ surface area).

	Total Area $0.13\,\mathrm{m}^2$	Total Area $0.11\,\mathrm{m}^2$
Rotation	Z-Axis	Y-Axis
Ram-Facing Area	$0.3\,\mathrm{m}^2$	$0.1\,\mathrm{m}^2$
Electron temperature	$0.20\,\mathrm{eV}$	$0.25\,\mathrm{eV}$
Plasma density	$2.9 \times 10^{12}\,\mathrm{m}^{-3}$	$3.1 \times 10^{13}\,\mathrm{m}^{-3}$
Main ion drift velocity	$3.9\,\mathrm{km\,s}^{-1}$ ($3.15\,\mathrm{eV}$)	$3.7\,\mathrm{km\,s}^{-1}$ ($2.85\,\mathrm{eV}$)
CEX ion drift velocity	$0.80\,\mathrm{km\,s}^{-1}$ ($0.13\,\mathrm{eV}$)	$1.5\,\mathrm{km\,s}^{-1}$ ($0.47\,\mathrm{eV}$)

Table 5.5: Range of parameters for measurement sets in figs. 5.25 and 5.26.

5.3.2.4 Ion Density

As seen in section 5.3.1, the spacecraft charge remains relatively unchanged when the LP is biased negative of the spacecraft and collects net negative current (mainly ion current). Therefore, it is not as critical to employ twin-probe corrections to the I-V curve when analyzing the ion saturation regime. However, since the ion population can be composed of both CEX and drifting ion populations, the analysis techniques detailed in section C.3 must be extended to include the situation where the ion density is composed of multiple species.

To begin, when only the drifting Maxwellian population is present, the ion density is calculated using the fitting algorithm that accompanies the full expression (eq. C.13),

$$I_{i_{Drift}} = \frac{qA_pN_{i_{Drift}}v_i}{\pi}\sqrt{1+\frac{k_BT_i}{m_iv_i^2}+\frac{2q\left(V_P-V_A\right)}{m_iv_i^2}}.$$

In the situation where Maxwellian CEX ions (sometimes also drifting) are present alongside the drifting ion population, the ion current is broadly estimated as the sum of the currents due to both populations, without taking into account any current modifications due to interactions between the two populations such as ion-ion collisions. Assuming the CEX ion current can be estimated as OML current (eq. 2.18), the total ion current is then

$$\begin{aligned} I_{i_{OML}} &= qA_pN_{i_{CEX}}\sqrt{\frac{2k_BT_{i_{CEX}}}{\pi^2m_i}}\sqrt{1+\frac{\phi}{T_{i_{CEX}}}} \\ N_{i_{CEX}} &= \eta_{CEX}N_i \\ N_{i_{Drift}} &= \eta_{Drift}N_i \\ \therefore I_i &= \frac{qA_pN_i}{\pi}\left(\eta_{CEX}\frac{\pi I_{OML}}{qA_pN_i}+\eta_{Drift}\frac{\pi I_{i_{Drift}}}{qA_pN_i}\right) \end{aligned} \tag{5.1}$$

where η_{CEX} and η_{Drift} are the fraction of the total density that is comprised of CEX ions and drifting ions, respectively. Since eq. 5.1 cannot be linearized by squaring the current, as was done in section C.3, a non-linear fit of the current must be performed. The total ion density is then given by

$$N_i = \frac{\pi\alpha}{qA_p} \tag{5.2}$$

where α is the fit parameter. The uncertainty of the calculation of density is affected by the non-linearity of the model, and so a Monte Carlo scheme is utilized to estimate the error [180]. This is accomplished by calculating the density while varying the plasma potential, measured current, sourced voltage, ion temperatures, and the fractions of the total density within their respective uncertainties. The density is then the average of all of the calculated densities from the Monte Carlo scheme. The total error is the square root of the sum of squares of the standard deviations of the calculated density due to variations in each variable. This is effectively numerically calculating a first order approximation of the standard error

$$\sigma_F = \sqrt{\sum_{i=1}^{N} \left(\frac{\partial F}{\partial x_i} \sigma_{x_i} \right)^2} \tag{5.3}$$

where N is the number of independent variables, x_i is a distinct independent variable (e.g. plasma potential, ion temperature, etc.), and F is the function of interest (in this case it is ion density).

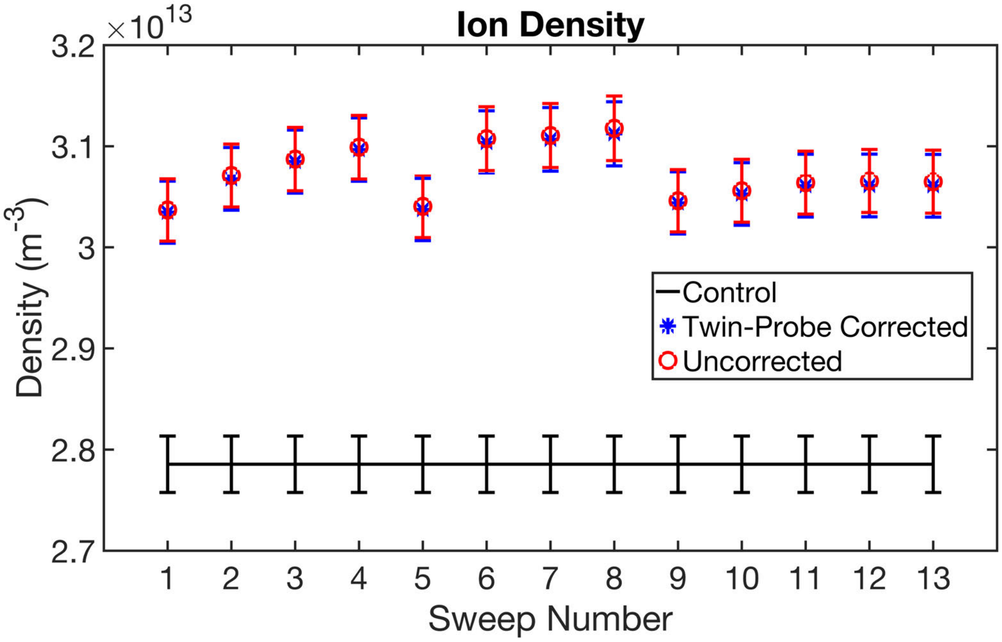

Figure 5.27: Ion density measurements where only a single drifting ion population was present at the location of measurements.

Figure 5.27 provides an example of ion density measurements using the twin-probe method when compared to control and uncorrected sweeps. As expected, *the discrepancy between uncorrected and twin-probe corrected measurements is nearly negligible as the spacecraft potential is constant when the LP collects ions*. Since the correction is effectively shifting the applied bias by a constant value, the I-V characteristics in the ion saturation regime are identical between the two types of measurements. Discrepancies between the control measurements and twin-probe corrected measurements are less than $10\,\%$ and can be largely attributed to variations in the plasma source during the experiment and errors in the plasma potential and ion population properties (i.e. drift speed and temperature).

5.3.3 Electron Energy Distribution Function

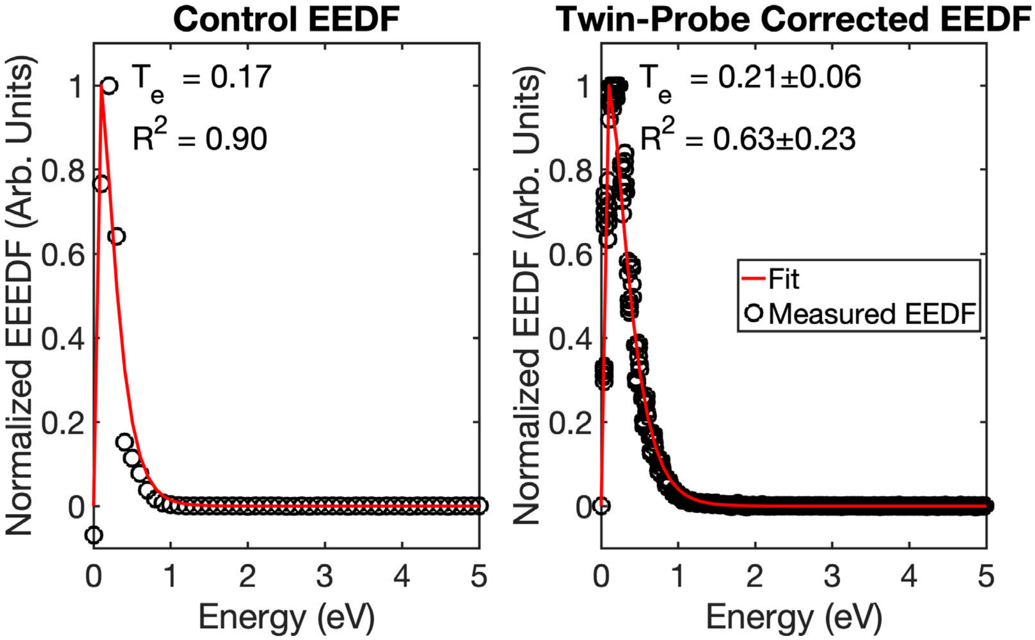

Figure 5.28: Example electron energy distribution measurement of the plasma source at NASA MSFC.

Many of the analysis techniques employed below in sections 5.3.4 and 5.3.5 assume that the EEDF is Maxwellian. Just as section 5.3.2.1 verified that the ion populations are either Maxwellian or drifting Maxwellian, the same care should be taken to ensure the electron population is Maxwellian. Figure 5.28 presents an example EEDF composed of the control (left-most plot) and twin-probe corrected (right-most plot) sweeps for a single measurement set. While the EEDF from the control sweep shows good agreement with a Maxwellian distribution (the R^2 is 0.9), the small sample size makes it difficult to argue that the plasma is Maxwellian. To further provide evidence of the Maxwellian nature of the hollow cathodes plasma, all twin-probe corrected sweeps for one measurement set (plasma properties of this set are detailed in table 5.2) were analyzed for their respective EEDF. The electron temperature and goodness of fit (GoF) quoted in the right most plot is the average temperature and GoF and the standard error is simply the standard deviation of the measurement set.

Changes in the plasma source will cause slight deviations in the plasma properties over the course of a measurement set; however, the Maxwellian fit is generally in good agreement with the measured EEDF. Furthermore, fig. 5.31b presents a fairly linear example semi-log plot of the electron retardation regime which is indicative of a Maxwellian electron population. Therefore, for this work, it is assumed that neither the magnetic filtering of the plasma source nor external facility effects cause the EEDF to deviate from a Maxwellian distribution.

5.3.4 Electron Temperature

There are multiple ways of determining the electron temperature from the I-V characteristics of a Langmuir probe. The reader is encouraged to review section C.5 as background for electron temperature estimates. This section specifically focuses on the following methods:

- The non-drifting potential difference method: electron temperature is estimated using the potential difference between the plasma and floating potential (described in appendix C.5.1).
- The integral method: electron temperature is estimated by integrating the electron retardation current (described in appendix C.5.2).
- The log-linear method: electron temperature is estimated by the inverse slope of the linearized electron retardation regime (described in appendix C.5.3).

The potential difference method that uses the ion drift speed is not used due to the fact that the method is not any more accurate than the non-drifting method and the non-drifting method appears more stable (discussed in appendix C.5.1.2). Regardless of which method was used, the calculated *electron temperature when using the twin-probe correction was always colder and closer to the control measurements than the uncorrected electron temperature measurements*. This is because the I-V characteristic of an uncorrected sweep is always shallower due to the increasingly negative charge on the spacecraft during LP operation.

5.3.4.1 Example Analysis Methods

As expected, each method varies in accuracy based on its assumptions and necessary inputs. With the exception of the single point method, all methods generally agree with an electron temperature of roughly $0.2\,\mathrm{eV}$.

The potential difference method is a candidate for measuring the electron temperature with relatively high accuracy (fig. 5.29). A statistical analysis of all relative uncertainties for control and twin-probe corrected measurements determined the percent error is $22{\pm}20\,\%$ and uncorrected sweeps have a percent error of $26{\pm}20\,\%$. This method relies heavily on the floating and plasma potentials and so its uncertainty is directly related to the uncertainties of the two measured potentials. A discussion on the uncertainties of this method is given in appendix C.5.1.2 and appendix C.5.1.1.

The integral method closely agrees with the results of the log-linear and potential difference methods; however, it is much more inaccurate. The greater uncertainty is apparent when comparing error bars in fig. 5.30 to those of figs. 5.29 and 5.31a. The uncertainty of the integral method is inversely proportional to the number of measurements included in the integral. Therefore, the voltage step size relative to the electron temperature should be smaller than a quarter of the electron temperature. Furthermore, accurately known floating and plasma potentials are required, as they define the lower and upper bounds of the integral. This range affects both the number of measurements that are included in the numerical integration and the percentage of the retardation regime sampled during integration. Due to an insufficient sampling of the retardation regime, the relative uncertainties are $52{\pm}39\,\%$ for the control and twin-probe corrected measurements, and $61{\pm}40\,\%$ for uncorrected measurements. A detailed description of the uncertainties for the integral method are given in appendices C.5.2.1 and C.5.2.2.

The most accurate method is the log-linear method, which is typically the standard analysis for determining electron temperature in a Maxwellian plasma (fig. 5.31a). It should be noted that the error in the log-linear method is calculated using a Monte Carlo scheme instead of an analytic equation, so it is possible that the uncertainty is underestimated (see discussion of uncertainty in appendices C.5.3.1 and C.5.3.2). However, it is unlikely that the uncertainty is grossly underestimated due to the linear form of the semi-log plot (example shown in fig. 5.31b). The percent error for control and twin-probe corrected measurements is $25{\pm}12\,\%$, while uncorrected sweeps have a percent error of $26{\pm}13\,\%$. The slightly greater uncertainty for the uncorrected sweeps is likely due to the small non-linear effects that spacecraft charging has on the IV characteristics in the electron retardation regime.

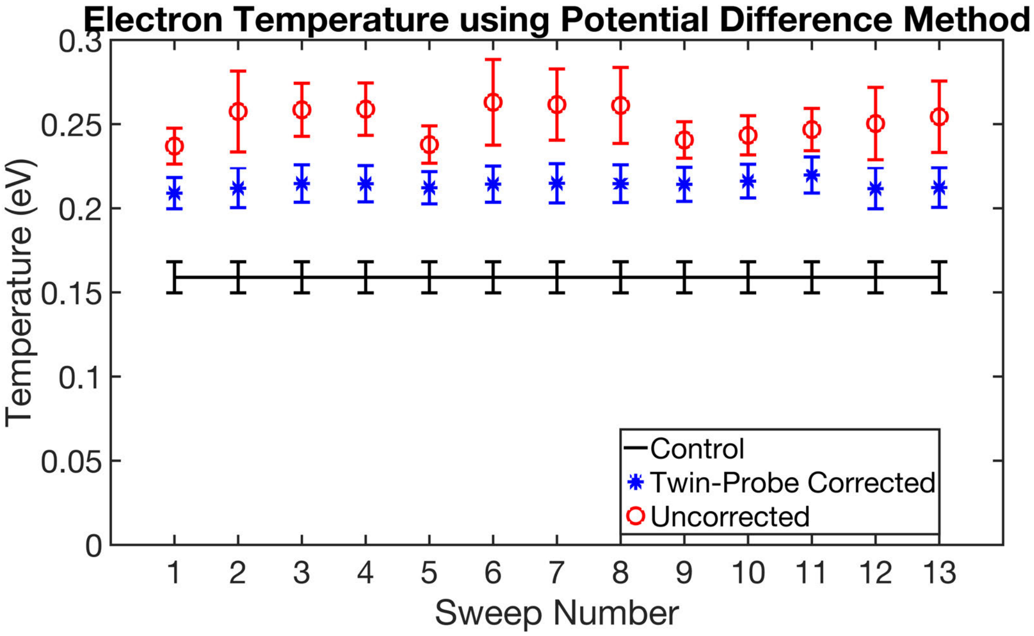

Figure 5.29: The potential difference method uses the difference between the plasma and floating potential to estimate the electron temperature.

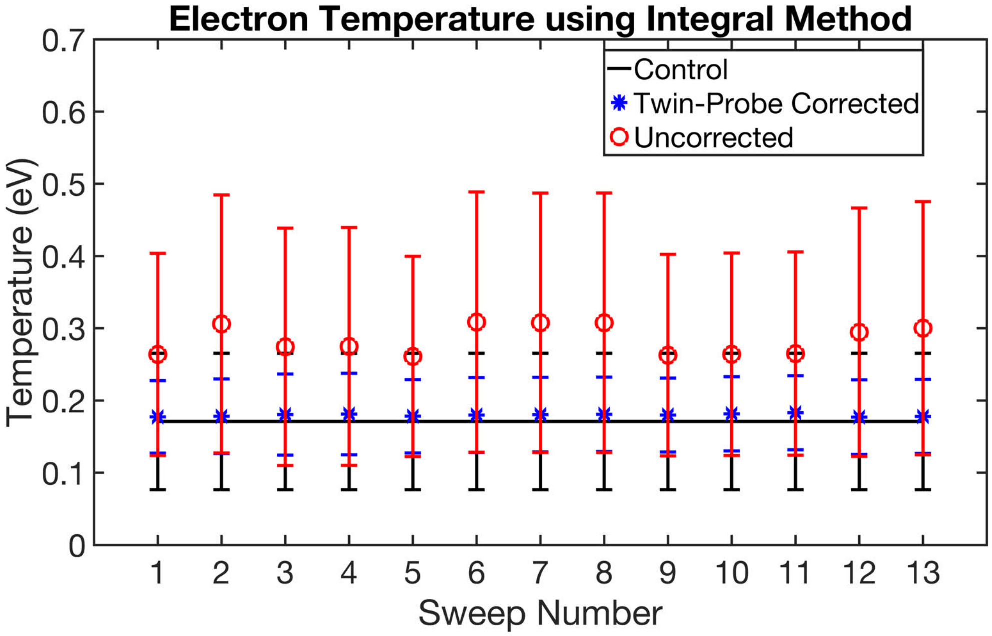

Figure 5.30: The integral method integrates the electron current between the floating and plasma potential.

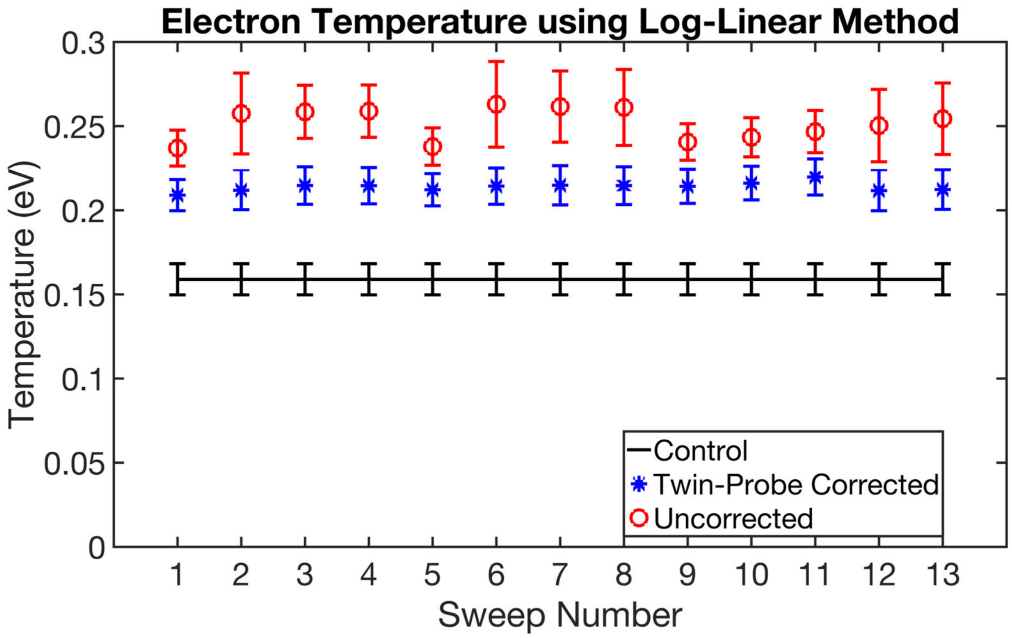

(a) The log-linear method fits a first order polynomial to the log of the electron current.

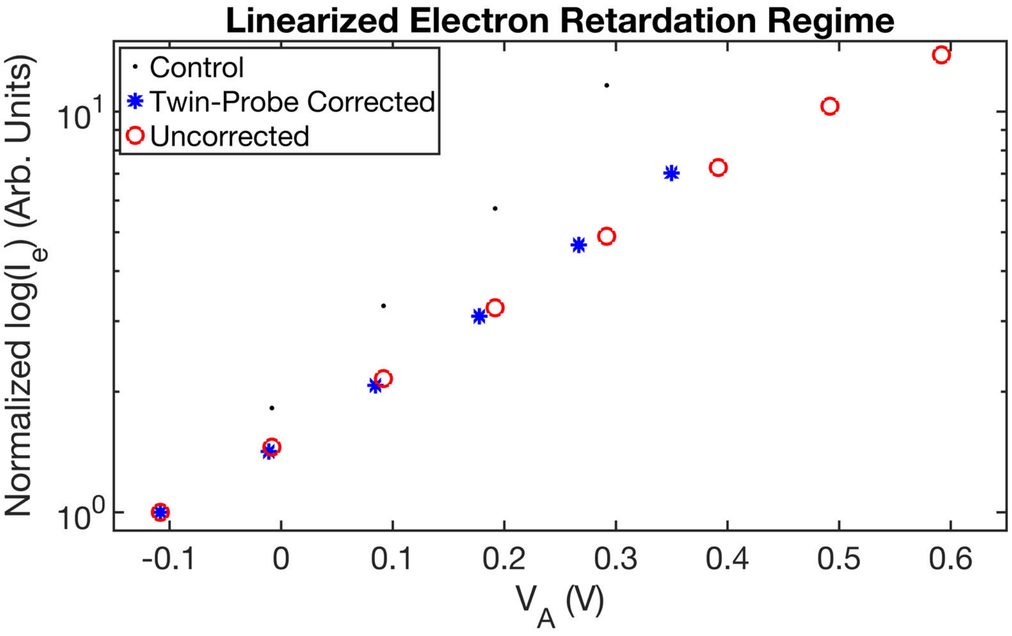

(b) Semi-log plot of the electron current between each sweep's respective floating and plasma potentials. Each sweep has been normalized by their respective sweep's minimum current, and the biases have been adjusted so they all begin at the same potential.

Figure 5.31: Examples of log-linear analysis methods and results.

5.3.4.2 Magnitude of Electron Temperature Corrections

To determine the magnitude of the correction due to implementing the twin-probe method, the percent change between the uncorrected and corrected electron temperature of each sweep is determined. The reported value of the correction (percent change) is the average of all calculated percent changes in a measurement set, where the error is the standard deviation of the array of percent changes. Since the most accurate methods were the log-linear fit and potential difference methods, they will be the focus of discussion in this section (the integral method is included for completeness). As shown in fig. 5.32, using these methods in conjunction with the twin-probe techniques will lead to corrections as great as $20\,\%$ for the lowest area ratios, dropping to about $7\,\%$ when the area ratio approaches 600. As discussed in section 5.3.2.3, it is likely that the satellite would collect less current collection in a space environment than in the chamber due to the lack of CEX ions and larger wake regions. As a result, these calculated magnitudes should be considered the best-case scenarios for correction. For clarity, the range of plasma properties captured in fig. 5.32 is given in table 5.3.

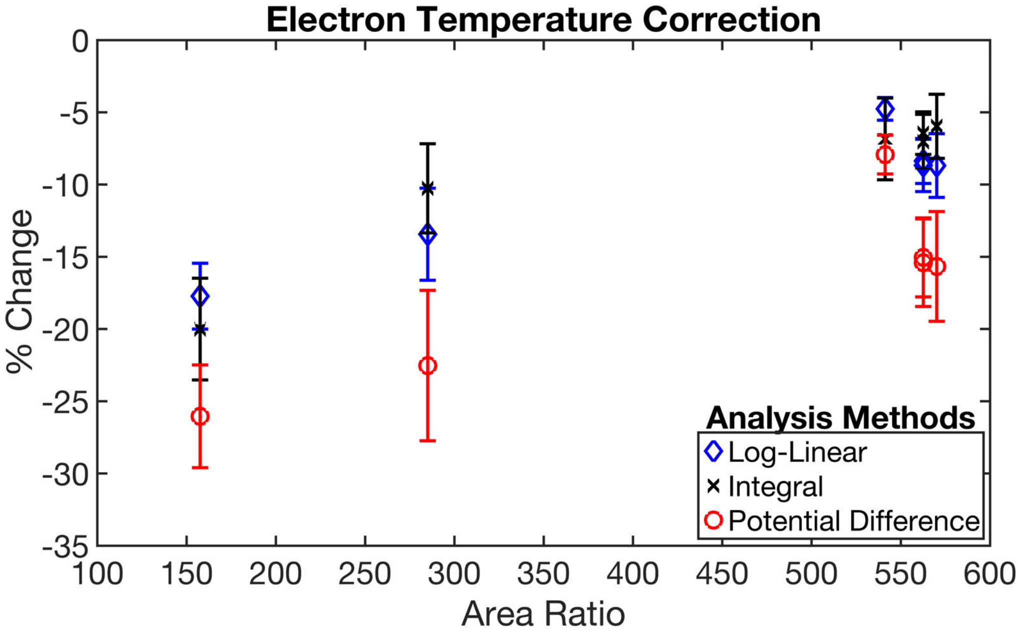

Figure 5.32: The plot presents the percent change in correction of temperature measurements as the area ratio is changed for densities between $1 \times 10^{12}\,\mathrm{m}^{-3}$ to $1 \times 10^{13}\,\mathrm{m}^{-3}$.

5.3.5 Electron Density

There are multiple distinct methods of calculating the electron density from the I-V characteristics of a Langmuir probe. The reader is encouraged to review section C.6 as background for electron density estimates. This section specifically focuses on the following methods:

- Thermal current method: electron density is estimated using the electron current at the plasma potential (see appendix C.6.1)
- Ideal OML Fit: electron density is estimated by fitting a power law function to the electron saturation current assuming the current behaves like the ideal OML theory shown in eq. 2.12 (see appendix C.6.2 with the assumption that $\gamma = 0.5$ and $\beta = 2/\sqrt{\pi}$)
- Single Point OML: electron density is estimated assuming the electron saturation current behaves like ideal OML cylindrical probe theory and that the potential is much greater than the electron temperature (refer to eq. C.41 in appendix C.6.2)

Before discussing the twin-probe method's ability to improve electron density estimates, it is important to determine whether or not OML theory applies when analyzing the electron saturation regime by determining the probe's sheath radius-to-probe radius ratio. A soft minimum ratio of 30 is required to be considered OML current collection as detailed in appendix C.6.2.2. The sheath radius-to-probe radius ratio can be calculated as follows

$$\frac{r_s}{r_p} = \frac{r_p + d_{sh}}{r_p} = \frac{r_p + 3\lambda_D}{r_p} \tag{5.4}$$

where d_{sh} is the sheath thickness (assumed to be at least 3 Debye lengths thick). The resulting sheath-to-radius ratios range from 4 to 20 for this experiment, placing them in a transition region between thin sheath and thick sheath current collection.

This is further verified by attempting to linearize the electron saturation regime (lowest and highest ratio examples shown in fig. 5.33). In appendix C.6.2, an OML fitting algorithm is detailed that assumes the electron saturation regime can be described using a power law function. The first step of the algorithm requires a linear fit of the logarithm of the electron current as a function of the logarithm of the probe bias, relative to the plasma, that is normalized by the electron temperature ($\log(\phi/T_e + 1)$). For sufficiently large sheath-to-radius ratios, the resulting line's slope provides the appropriate scaling exponent of the power law function. However, as can be seen by the control lines (representing

LP sweeps referenced against the chamber wall) in fig. 5.33, a sufficiently straight line that can be used to obtain the scaling exponent does not exist. Moreover, uncorrected sweeps are further impacted by the induced spacecraft potential, as predicted by the PSIC-LEO simulations in section 4.3.2 and fig. 4.10. The additional non-linearity makes it infeasible to linearize the uncorrected curves and apply the fitting algorithm, even for sufficiently large sheath-to-radius ratios. Unfortunately, while twin-probe corrected I-V curves were closer to the control curves, the magnitude of the correction was sometimes limited. For instance, in the left-most plot of fig. 5.33, the twin-probe corrected and control curves are in good agreement, but the right-most plot shows the twin-probe corrected curve to be somewhere between the uncorrected and control curves. At this time, there is no satisfactory answer that explains why some twin-probe corrections agree with their control counterparts and some don't. While OML theory does not strictly apply to these electron saturation curves, to ensure the same fitting method is compared between control, uncorrected, and twin-probe corrected measurements, the electron saturation current is assumed to be proportional to the square root of the applied bias (equivalent to eq. 2.12). Greater uncertainties are assumed when estimating electron density to account for the less than ideal conditions.

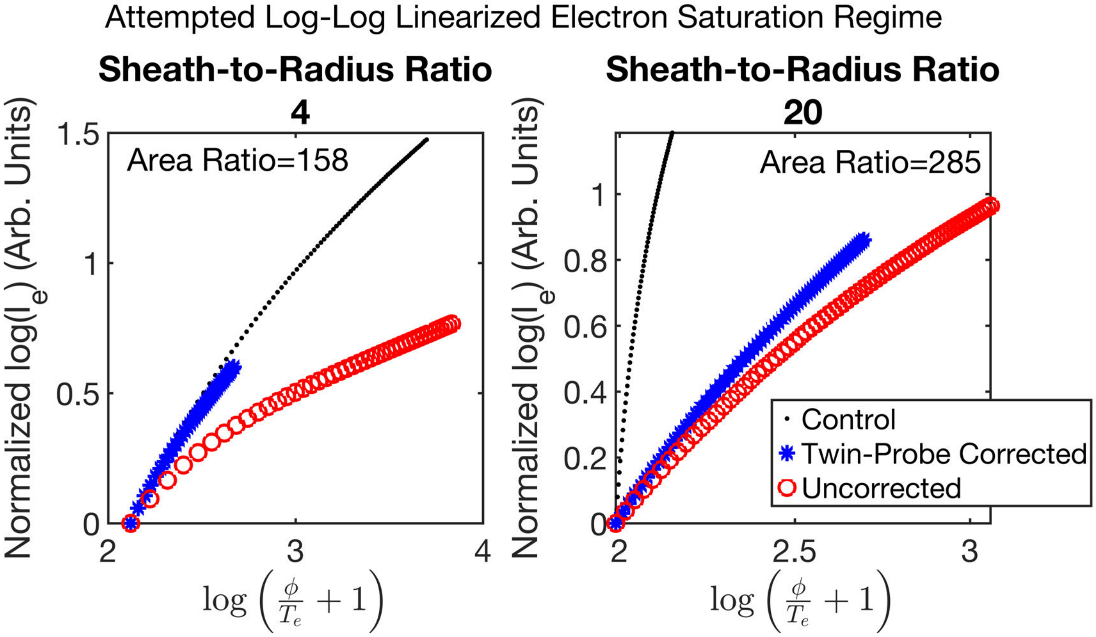

Figure 5.33: Plot of failed linearization of the electron current between each sweep's respective electron saturation regime due to small sheath-to-probe radius ratio. Each sweep has been normalized and the biases have been adjusted so they all begin at the same potential and the same arbitrary unit.

For the employed methods, *the calculated electron density, when using the twin-probe* *correction, was always greater and closer to the control measurements than the uncorrected electron density estimates.* This is because the I-V characteristic of an uncorrected sweep is always shallower, due to the increasingly negative charge on the spacecraft during LP operation. Therefore, the same effect that produces hotter electron temperatures in uncorrected sweeps will skew the calculated electron density to be lower than the actual plasma property. Finally, as mentioned in section 2.4.7, ion density estimates are typically more accurate than electron density estimates. Historically, estimated electron densities are corrected using ion density measurements [3, 153]. While such correction schemes aren't used in this discussion, the example electron density estimates provided in this subsection will be compared to ion densities measured by the control sweep.

5.3.5.1 Individual Example Measurement Sets

Just as was seen for the electron temperature, each method for determining electron density varies in accuracy based on its assumptions. The calculated electron densities all generally agree with each other and the control estimates of electron density are within a factor of two or three below the estimated ion density.

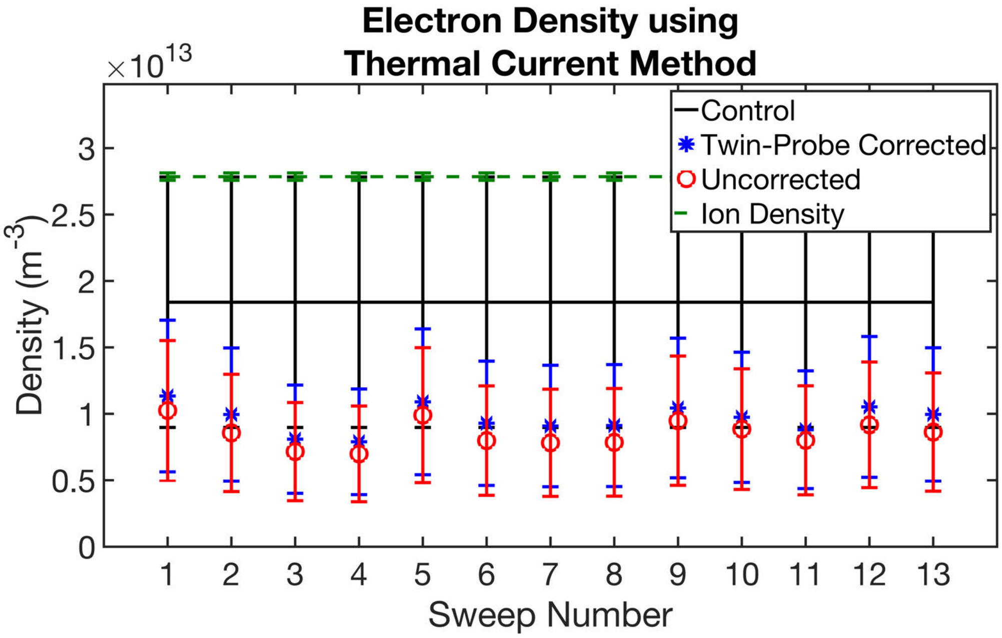

Figure 5.34: The thermal current method estimates the electron density from the current measured at the plasma potential.

The thermal current method has the smallest shift between the uncorrected and twin-probe corrected sweeps. Furthermore, the twin-probe corrected electron densities deviate the greatest from control measurements for the four considered methods. Part of this small shift is due to the small negative charging induced on the spacecraft between the spacecraft's floating potential and when the probe is near the plasma potential. As a result, the small current difference between the two sweeps causes a density difference that is roughly $1 \times 10^9\,\mathrm{m}^{-3}$, in this case. It is likely, that for more severe charging conditions, such as a smaller area ratio or a smaller CEX ion population, the corrected density shift would be greater. As noted in appendices C.6.1.1 and C.6.1.2, this method is naturally uncertain, and so the measurement's uncertainty ranges from $50\,\%$ to $60\,\%$ regardless of the sweep type considered.

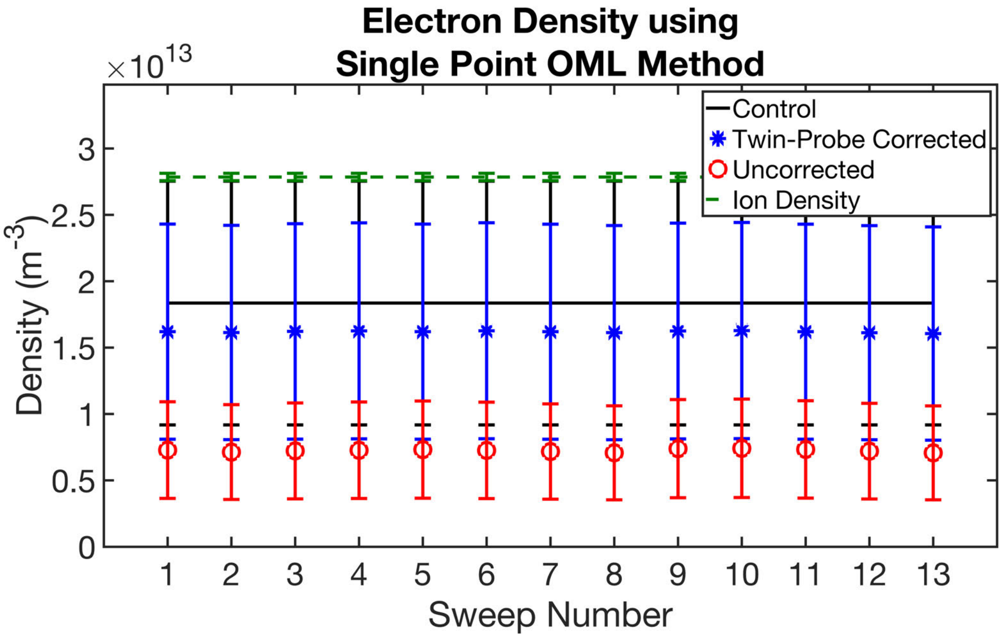

Figure 5.35: The single point OML method estimates the electron density assuming the attractive potential dominates random thermal motion. The ion density is a constant value in this example.

Since the probe sheath to radius ratio was not guaranteed to be outside of the transition region between thick and thin sheath current collection, the full algorithm described in appendix C.6.1 was not used. Instead, it was assumed that all attracted electron currents are proportional to the square root of the attractive potential and can be linearized by squaring the currents. This assumption was made for the single point OML method (fig. 5.35) and the ideal OML fit method (fig. 5.36a). It is clear from the twin-probe corrected sweeps that LP sweeps referenced against the notional satellite do not probe the ambient plasma well above the plasma potential. As a result, the minimum uncertainty of the single point OML method is unlikely to have reached its asymptotic limit from fig. C.16b. Since the linearization is not always successful (fig. 5.36c) and only one measurement is considered to calculate the electron density, the density's uncertainty is estimated to be $50\,\%$ at a minimum. The uncertainty estimates are provided in eq. C.42 and appendix C.6.2.2.

For the OML fit method, the electron density was determined from the slope of the squared currents (see appendix C.6.1). Figures 5.36b and 5.36c demonstrate that this linearization scheme is not always successful and so all calculated electron densities are assumed to have a minimum uncertainty of $25\,\%$ combined with any additional systematic uncertainties (as described in appendices C.6.2.1 and C.6.2.2). In the case of successful linearization of control and twin-probe corrected sweeps (fig. 5.36b), it is clear that the uncorrected sweep's collected current was not proportional to the square root of the accelerating potential, due to the spacecraft's charging behavior (see fig. 4.10).

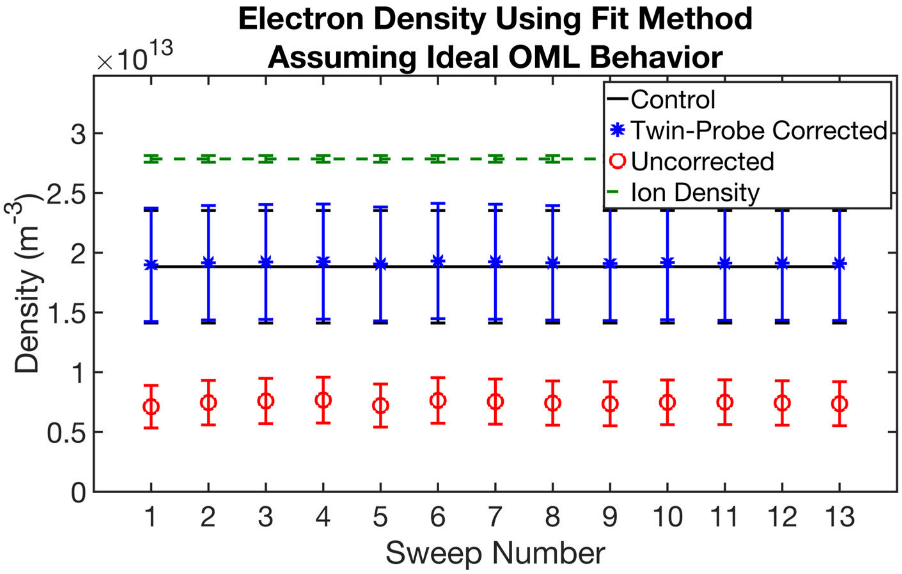

(a) The ideal OML fit method assumes the electron saturation regime follows ideal cylindrical thick sheath electron current collection. The ion density is a constant value in this example.

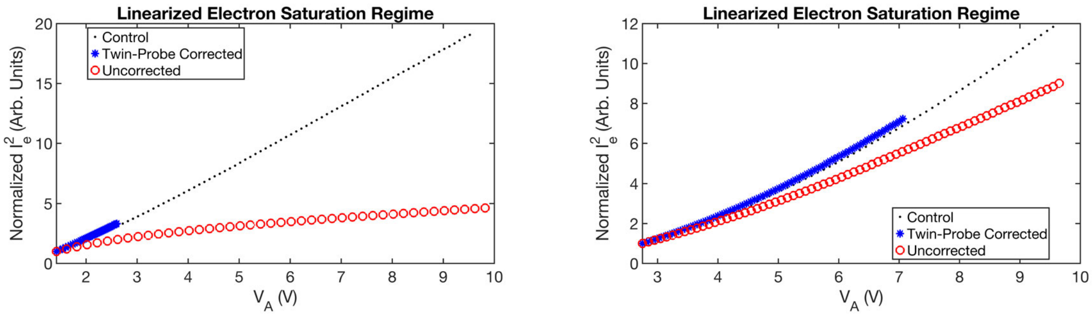

(b) Successful linearization example where the electron saturation current behaves close to a square root function.

(c) Unsuccessful linearization example where the electron saturation current behaves far from a square root function.

Figure 5.36: Example of idea OML fit results and linearization.

5.3.5.2 Magnitude of Electron Density Corrections

To determine the magnitude of the correction due to implementing the twin-probe method, the percent change between uncorrected and corrected calculated electron densities of each sweep is determined. The reported value of the correction is the average of all calculated percent changes in a measurement set where the error is the standard deviation of the array of percent changes. As shown in fig. 5.37, using these methods in conjunction with the twin-probe techniques will lead to greater corrections at low area ratios that diminish with increasing area ratio. For completeness, the range of plasma properties captured in fig. 5.37 is given in table 5.3.

The smallest correction at a low area ratio occurred when applying the thermal current method. Its maximum correction was $20\,\%$, dropping to just below $10\,\%$ when the area ratio approaches 565. The OML methods, both the fit and single point schemes, resulted in the highest corrections and the measurements consistently closest to the density estimates made by control sweeps.

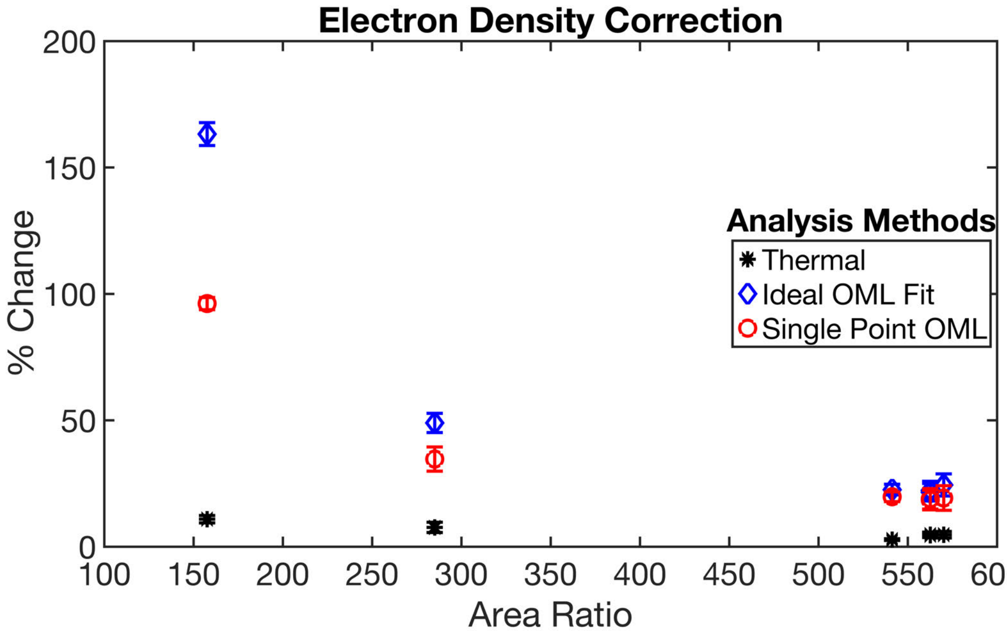

Figure 5.37: The plot presents the percent change in correction of density measurements as the area ratio is changed for densities between $1 \times 10^{12}\,\mathrm{m}^{-3}$ to $1 \times 10^{13}\,\mathrm{m}^{-3}$.

5.4 Comparing PSIC-LEO Model to Experiment Results

The PSIC-LEO codes were developed to quickly estimate the measured spacecraft potential using the twin-probe method, understand the effects of induced spacecraft charging on

LP I-V characteristics, and develop new analytic techniques. Therefore, efforts should be made to at least validate the charging behavior modeled by PSIC-LEO. Direct comparisons between in-chamber measurements and the models are not possible due to three major barriers: 1) a lack of exact analytic equations for current collections to a cuboid structure to use in the model; 2) an asymmetric potential structure around the physical CubeSat in the chamber because one side was grounded; and 3) the presence of CEX ions and high background pressures altering the wake region. Even though the direct comparisons cannot be made, the behavior between the model and in-chamber measurements can be compared (qualitative comparisons are made using fig. 5.38). Experimental measurements are shown in the left-most column and PSIC-LEO model results are shown on the right-most column. In these comparisons, the modeled accelerated electron current is orbit motion limited.

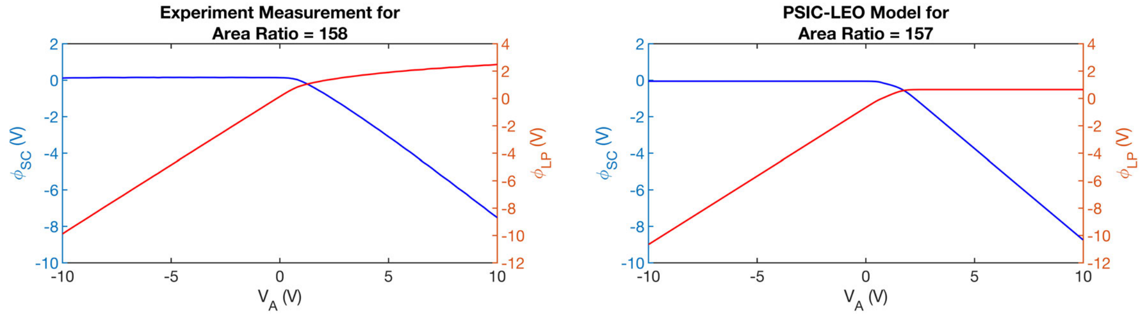

(a) Chamber measurements for the smallest area ratio.

(b) Predicted spacecraft charging behavior for smallest area ratio used in the chamber.

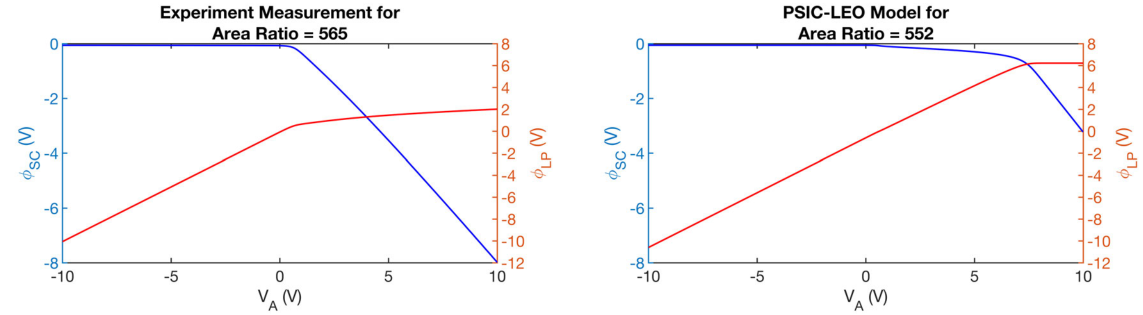

(c) Chamber measurements for the largest area ratio.

(d) Predicted spacecraft charging behavior for largest area ratio used in the chamber.

Figure 5.38: Measured spacecraft potential and Langmuir probe potential. The red line corresponds to Langmuir probe potentials and blue lines correspond to the spacecraft potential.

To begin, both the chamber measurements and the model predict a measured spacecraft potential near 0 as the floating potentials of the high-impedance probe and spacecraft would be very similar when the swept LP is collecting a net ion current or it is at its floating potential. As the LP is biased positive of its floating potential, the electron current begins to dominate over the ion current slowly inducing a negative charge on the satellite. This is typically observed as the curved portion of the measured spacecraft potential and initial negative charging. This limited charging behavior explains why the electron temperature measurements have limited corrections relative to electron density corrections. As the LP surpasses the plasma potential, the spacecraft potential becomes increasingly negative at a near linear rate. The slope of the line is dependent on the area ratio and the magnitude of the satellite's ram-facing conductive surface area, but an exact expression has not been developed at this time. Both the PSIC-LEO codes and chamber measurements exhibit the same behavior but will predict different negative potentials at the most positive applied biases to the LP.

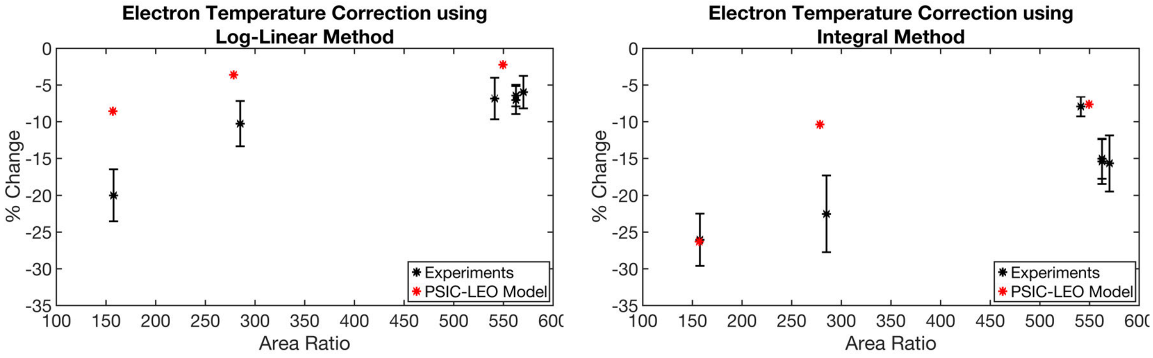

(a) Comparison between experiment results and PSIC-LEO model predictions of twin-probe correction for electron temperature using the log-linear method.

(b) Comparison between experiment results and PSIC-LEO model predictions of twin-probe correction for electron temperature using the integral method.

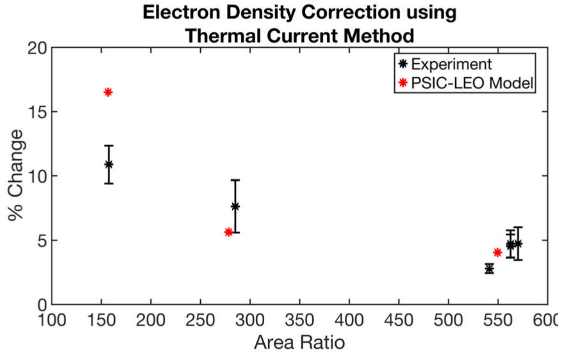

(c) Comparison between experiment results and PSIC-LEO model predictions of twin-probe correction for electron density using the thermal current method.

Figure 5.39: Measured spacecraft potential and Langmuir probe potential. The red line corresponds to Langmuir probe potentials and blue lines correspond to the spacecraft potential.

While their exact potentials cannot be compared, the predicted magnitude of the twin-probe corrections for electron temperature and density made by the PSIC-LEO codes can be compared by running the simulations with the plasma properties measured in the experiment. The corrections predicted by the model the have the same trend and are generally close to experiment results. For comparisons of temperature corrections, the PSIC-LEO codes generally underpredict the magnitude of twin-probe corrections when using the log-linear method (see fig. 5.39a). Similarly, when determining electron temperature using the integral method (see fig. 5.39b), PSIC-LEO model predictions agree with the experiment, with the exception of the area ratio of 280 where the model and experiment differ greatly (about $12\,\%$). Finally, corrections of electron density using the thermal current method determined by the PSIC-LEO model and seen in the chamber closely agree (see fig. 5.39c). The largest discrepancy occurs at the smallest area ratio and is roughly $5\,\%$. Again, the reported experiment value of the correction is the average of the measurement set and the error bars are the standard deviation of the measurement set for a given area ratio. The PSIC-LEO model results do not have error bars since the results are analytic and would yield the same result regardless of how many times the simulation is ran. This general agreement in the trends between the model predictions and experiment lends credibility to the PSIC-LEO codes as a tool to understanding the effects of spacecraft charging on LP measurements when designing future CubeSat missions.

CHAPTER 6

Applications and System Level Design

A very small satellite, which is the most likely to have issues of restrictive area ratios, is any satellite lighter than $100\,\mathrm{kg}$ [181]. Implementing twin-probe correction may require adding additional hardware to the satellite, so that it has spacecraft potential tracking capabilities. As a result, there may not be enough mass or volume budget available for the extra equipment, especially after accounting for more massive subsystems related to power generation (solar panels), power supplies, and communications (radio and antenna). Therefore, it is imperative to know under what conditions the twin-probe method is most effective and what system level design choices can be made to maximize its impact. In this chapter, the results from simulations and experiments are first interpreted. Then, recommendations for general system level designs are detailed, including probe dimensions and suggested analysis methods. Finally, possible future missions with twin-probe method capabilities are highlighted and implementations to improve the versatility of the twin-probe method are proposed.

6.1 Interpretation of Simulation and Experiment Results

To begin, the spacecraft charging results are most applicable for plasma environments that are either devoid of sunlight, such as being in eclipse, or for plasma densities greater than $1 \times 10^{11}\,\mathrm{m}^{-3}$ where the effect of photoelectron and secondary electron emission is minimal. Since neither the simulations nor the experiment campaign studied the impact of photoelectron or secondary electron emission on spacecraft charging, no parametric data can be presented to discuss these effects. However, in very low density environments ($N_e \sim 1 \times 10^{9}\,\mathrm{m}^{-3}$), such as the Martian environment, photoelectron current has been demonstrated to be sufficient in compensating for the limited ion current to the spacecraft during probe operation. For instance, the Maven spacecraft did not exhibit significant charging when operating a swept Langmuir probe [74, 75]. This suggests that in low-density situations, the effect of probe operation on small spacecraft may be mitigated, as long as additional current sources to the spacecraft, such as photoelectron current, are sufficiently large.

In the chamber experiments, the notional CubeSat charged between $-7.5\,\mathrm{V}$ to $-2.5\,\mathrm{V}$ for area ratios ranging from 160 to 565, and so the percent difference between twin-probe corrected measurements and uncorrected measurements changed accordingly. Also, slight changes in ion drift speed affect the total charge on the spacecraft (see fig. 6.1b). Typically, smaller drift speeds result in more severe charging. In turn, these charging differences result in slight variations for the magnitude of twin-probe correction of both electron temperature and density measurements (see highest area ratio twin-probe corrections of figs. 5.32 and 5.37). Ion drift speed was correlated to the plasma density, as shown in fig. 6.1a. Lower densities allowed for higher ion drift speeds, and a measurement set from the NASA MSFC experiment campaign is not included in sections 5.3.1.1, 5.3.4.2 and 5.3.5.2 due to densities being too large to allow for nominal drift speeds.

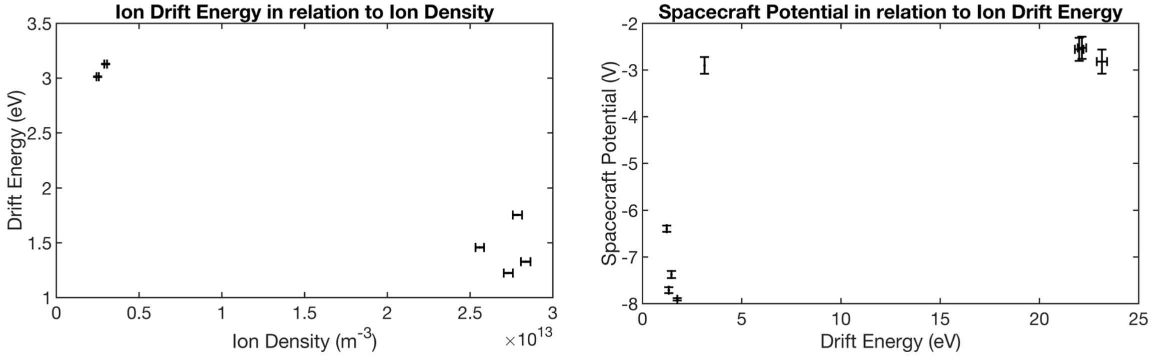

(a) Ion energy decreases with ion density.

(b) Spacecraft charging for similar area ratios but different drift speeds.

Figure 6.1: Ion energy in relation to ion density and spacecraft charging.

Fortunately, the largest electron densities were encountered when the largest area ratios were being tested. As a result, it is possible to study the effects of ion drift energy on spacecraft charging for similar, large area ratios (i.e. those ranging from 540 to 570). For instance, for drift energies above $3\,\mathrm{eV}$, the measured spacecraft charging ranged between negative $2\,\mathrm{V}$ to $3\,\mathrm{V}$; however, when the ion drift speeds were below $1.75\,\mathrm{eV}$, the charging was comparable to area ratios below 200 ($-6\,\mathrm{V}$ to $-8\,\mathrm{V}$). While these low drifting conditions exemplify the importance of the ion drift speed on improving the CubeSat's current balance capabilities, they do not provide good comparisons for the expected spacecraft charging levels seen in LEO. Interestingly, there appears to be some asymptotic behavior for drift energy as there is not as drastic a change in maximal spacecraft charging between the $3\,\mathrm{eV}$ and $22\,\mathrm{eV}$ ion drift energies, when compared to the charging difference seen between the sub-$1.75\,\mathrm{eV}$ and $3\,\mathrm{eV}$ ion drift energies. At this time the cause if this asymptotic behavior is not well understood and is only noted.

For transparency, fig. 6.1a only includes data when the hollow cathode used the grounded anode to accelerate the ions. When the cathode is biased above the chamber and the anode is not in use, the ion drift energies could be forced above $20\,\mathrm{eV}$, but this is not the intended use of the plasma source as it can not filter higher temperature electron populations. Therefore, it can not be used to analyze the relationship between ion density and ion drift energy when the anode is in use. Additionally, fig. 6.1b only contains data for area ratios above 540, regardless of plasma source configuration, to isolate the effects of ion drift energy .

Focusing specifically on the log-linear method of electron temperature determination, the twin-probe method corrected temperatures by $20\,\%$ to $7\,\%$, depending on the area ratio. Notably, independent modeling by *Shkarofsky* and *Szuszczewicz* report similar percent errors in temperature for area ratios below 1000 using different assumptions on spacecraft geometry and charged particle current collection [182, 56]. At the larger area ratios, corresponding to the least amount of charging and correction, the percent error in the measurements overlap considerably with the corrections between the twin-probe corrected and uncorrected measurements. As a result, correction factors in this regime cannot be definitively confirmed, and more accurate measurements are required to validate correction factors in these regions of minimal charging. Possible improvements to these measurements focus on decreasing the voltage step size to increase the number of measurements in the electron retardation regime, and performing more sweeps under the same conditions to provide a larger sample size of measured currents for a given applied bias. Comparing the experiment results to PSIC-LEO estimates of correction, modeling estimates differ with experiment results by about $5\,\%$ to $10\,\%$ at the area ratios considered (comparison shown in fig. 5.39a). However, more definitive statements are made for correction factors in the area ratio regime below 300. In this region, the correction factors are greater than the percent error of the individual measurements, and so it is clear that uncorrected measurements overestimate the electron temperature by a significant margin. At the smallest area ratios considered in the experiment, 165, uncorrected log-linear measurements can be expected to deviate between $15\,\%$ to $20\,\%$ from the true temperature measurements. Therefore, twin-probe corrections would be vital in ensuring more accurate measurements of the electron temperature.

Similarly, using the thermal current method for electron density determination, one could expect a $20\,\%$ to $10\,\%$ correction factor for uncorrected sweeps. However, due to the intrinsic and systematic uncertainties of the method, it is very difficult to obtain highly accurate electron densities using this method. For these experiments, the uncertainty ranges between $50\,\%$ to $60\,\%$, and so conclusive statements on the correction factor using the twin-probe method cannot be made, as the uncertainties in the measurements overlap with the correction factor. Using the PSIC-LEO model predictions, the experimental estimates of the correction factor are typically $5\,\%$ greater than model predictions, but both the model and experiment show the same general trend (comparison in fig. 5.39c). Additionally, the single point OML method demonstrated corrections ranging between just below $100\,\%$ for the smallest area ratio to $20\,\%$ for the largest area ratio. The significantly greater correction factor of the single point OML method, when compared to the thermal current method, is due mostly to the region of the LP IV curve used for the respective measurements (pictorial representation in fig. 6.2). The thermal current method studies the current near the plasma potential where the spacecraft potential has minimally changed. In contrast, the OML single point method uses the largest applied potential of the LP, corresponding to the greatest amount of spacecraft charging. As a reminder, the single point OML method estimates the electron density as follows

$$N_e \approx \frac{\pi I_e\left(\phi\right)}{A_p}\sqrt{\frac{m_e}{2q^3\phi}}$$

where ϕ is the probe potential relative to the plasma potential. Therefore, the difference between uncorrected and twin-probe corrected electron density determination is the probe potential. For uncorrected sweeps, the maximum probe potential relative to the plasma potential ranges between $8.8\,\mathrm{V}$ to $9\,\mathrm{V}$. For corrected curves, the maximum potential ranges from approximately $1.5\,\mathrm{V}$ to $6.3\,\mathrm{V}$, where the smaller maximum potential corresponds to the smaller area ratio. The percent change between twin-probe corrected and uncorrected measurements would then be

$$\%Change = 100\frac{\sqrt{\frac{1}{\phi_{Corrected}}}-\sqrt{\frac{1}{\phi_{Uncorrected}}}}{\sqrt{\frac{1}{\phi_{Uncorrected}}}}$$

where $\phi_{Corrected}$ is the corrected probe potential and $\phi_{Uncorrected}$ is the uncorrected probe potential. Substituting for the probe potentials above, the percent change would be broadly estimated to be $143\,\%$ for the smallest area ratio considered in the experiment, and $19\,\%$ for the largest ratio, which is close to the experimental percent change values. With a combination of larger than expected electron densities and, at times, thicker than optimal Langmuir probes, the electron saturation current did not behave like ideal OML current collection; thus, the uncertainties in density estimates using the OML single point method were $50\,\%$. To improve these estimates and further verify correction factors for area ratios above 300, thinner probes should be employed at the lowest possible plasma densities that can be generated in order to better approximate OML electron current behavior. Ultimately, if the probe geometry allows for it, the electron saturation regime and OML theory should be used to estimate electron density. The thermal current method should only be used if other schemes are not available due to its small correction factors and intrinsic inaccuracies.

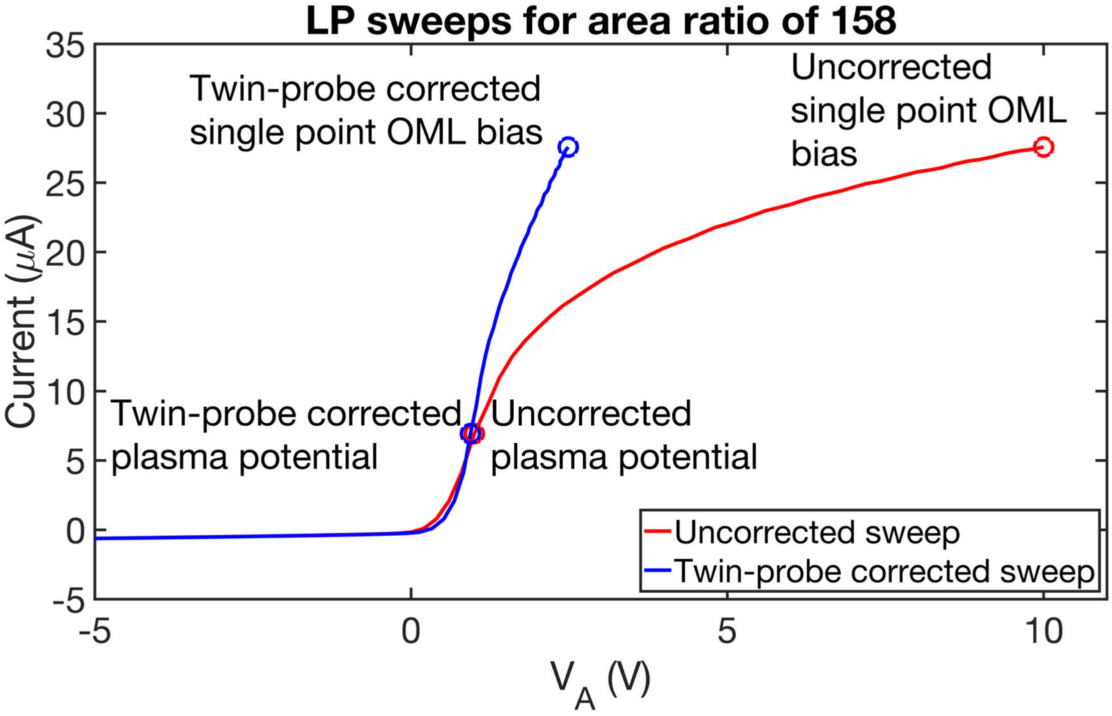

Figure 6.2: Example of the location of measurements used for thermal current and single point OML methods of determining electron density.

6.2 Optimal System Design for Small Spacecraft

Using the information gleaned from simulations and experiments, we can begin to outline optimal system level designs for small spacecraft. To begin, area ratios below 300 stand to benefit the most from twin-probe operations. These are the regions where uncorrected sweeps can be improved by the largest margins. Generally, the spacecraft should be designed to have the largest amount of conductive surface area as possible to aide in ion current collection. Furthermore, while the entire satellite can be available for current balance, having a sizeable ram current collection area can further minimize the magnitude of negative charging. Maximizing the surface area ratio can be accomplished through several methods, including fixing the CubeSat orientation such that the largest surface area is ram-facing; or ensuring large, deployable structures are always ram-facing, such as solar panels with ITO coated cover glass or conductive drag panels. However, maximizing the ram-facing surface area also maximizes the drag on the spacecraft. While this may not be an issue at higher altitudes, for altitudes below $600\,\mathrm{km}$, drag effects play a significant role in satellite orbital dynamics, and increasing the drag will inadvertently decrease orbital lifetimes [183]. A trade study between ram ion current collection and orbital lifetime should be conducted for small satellites that plan on implementing the twin-probe method.

Equally important to balancing the satellite drag and ram-facing surface area is determining proper Langmuir probe dimensions for the expected electron densities and temperatures. For instance, consider the probe dimensions for a mission, carrying twin cylindrical Langmuir probes, in the F-region of Earth's ionosphere. It will be made quickly apparent that reaching proper OML dimensions is not feasible, and some compromises must be made. In the Earth's F-region, we can consider the typical electron temperature to be $0.1\,\mathrm{eV}$ and the electron density to range from $1 \times 10^{10}\,\mathrm{m}^{-3}$ to $5 \times 10^{11}\,\mathrm{m}^{-3}$. The corresponding Debye lengths are then between $2.34 \times 10^{-2}\,\mathrm{m}$ to $3.3 \times 10^{-3}\,\mathrm{m}$, with the longer Debye length corresponding to the sparser plasma. The diameter of the Langmuir probe should be thin enough such that the sheath radius is at least 50 times greater than the probe radius for all expected densities to approximate OML current collection. The ratio can be calculated using

$$ratio = \frac{r_s}{r_p} = \frac{r_p + d_{sh}}{r_p}$$

where r_p is the probe radius and d_{sh} is the sheath thickness measured from the surface of the probe. In this example, the probe diameter should be $4 \times 10^{-4}\,\mathrm{m}$, assuming the sheath is 3 Debye lengths thick, which is prohibitively thin when considering mechanical strength, and limiting to the magnitude of expected charged particle current collections. An attempt to reconcile this can be made by relaxing the ratio requirement of 50 to one where the ratio must be 5 or greater, so that it is still outside of the thin sheath regime. With this new requirement, the probe can be as thick as $5 \times 10^{-3}\,\mathrm{m}$, which is still thin but much more manageable. For comparison, the diameter of previous flight probes are those in the m-NLP system at $5 \times 10^{-3}\,\mathrm{m}$ [184, 73]; the probe that would have flown on ProSEDS had a diameter of $4 \times 10^{-3}\,\mathrm{m}$ [159]; and the Langmuir probe on the AE mission was $2 \times 10^{-3}\,\mathrm{m}$ [153].

Once the probe diameter is determined, the probe length can be decided based on constraints due to the spacecraft and ambient plasma. Selecting the proper probe length, to ensure end effects are minimized, is typically a function of both the probe potential and the Debye length. As the probe potential increases, the sheath structure around the probe will expand around the probe tip, and consequently, the current collection is increasingly affected by probe end effects. Agreement on the appropriate probe length-to-Debye length ratio for the applied potential range considered, $-10\,\mathrm{V}$ to $10\,\mathrm{V}$, varies due to limited, tested, plasma parameters and probe lengths, and can range between 5 to 600 [185, 186, 187]. In this case, the limiting factor is not the smallest Debye length, but rather the longest. Assuming the smallest ratio is sufficient, the expected minimum probe length is $1.17 \times 10^{-1}\,\mathrm{m}$. Understandably, this is prohibitively long for small satellites when also taking into account the fact that the probe should be located outside the spacecraft sheath, as discussed in section $3.2.1$. Alternatively, a different criteria for a sufficiently long probe can be considered, where the probe length-to-probe diameter ratio is considered. Jakubowski estimates that a ratio of 40 was sufficient in the presence of a collisional plasma [156], while *Marholm et. al.* found that a ratio of 10 was insufficient and a larger ratio closer to 20 was more applicable in a collisionless plasma [188]. By utilizing these ranges, for a $5 \times 10^{-3}\,\mathrm{m}$ diameter probe, the expected length would range from $0.1\,\mathrm{m}$ to $0.1\,\mathrm{m}$. This is again prohibitively long.

At this point, it can be appreciated that attempting to satisfy the ”infinitely long” probe condition of most Langmuir probe theory is infeasible for small spacecraft. The purpose of the ”infinitely long” assumption is to ignore end effects. Another method of eliminating probe end effects is to use a guard. A guard can be used at one or both ends of a cylindrical probe, but it is usually simpler to utilize a guard on only one end. The guard element is a conductor of similar diameter to the Langmuir probe that precedes the probe along the boom structure, but is electrically insulated from the probe. It has the same conductive surface as the Langmuir probe, and is driven at the same potential; but, its current collection does not have to be measured [153]. While the guard can be a few centimeters long, care has to be taken to include the surface area of the guard into calculations when determining the spacecraft-to-probe area ratio [3]. Effectively, a guard element allows for a probe whose length is less than ideal by extending the uniformity of the electric field surrounding the probe; however, the probe should still be made as long as possible to further reduce end effects [187]. Some guard lengths that have been used for LEO missions and systems include $1.5 \times 10^{-2}\,\mathrm{m}$ on the m-NLP system [188]; and $2.5 \times 10^{-2}\,\mathrm{m}$ for both the ProSEDS LP and the AE LP [159, 153]. Assuming the notional probe is now guarded, let the allowed probe length-to-diameter ratio decrease to 10, such that the probe length is $5 \times 10^{-2}\,\mathrm{m}$, which is much more achievable. It should be noted, that this smaller length-to-diameter ratio will still experience end-effects, but a guard eliminates such effects on one end of the probe [188, 187]. Again for comparison, the probe length-to-diameter ratios for the three LEO cases are 5 for the m-NLP system, 12.5 for ProSEDS, and 37.5 for the AE mission. Notably, the Atmospheric Explorer missions allowed for much longer boom and probe structures due to the satellite's larger size.

Another consideration for determining the probe length, once a diameter has been chosen, is the area ratio between the spacecraft and probe. As mentioned earlier, because the notional probe is guarded, the surface area of the guard must be taken into account as well, given as

$$AreaRatio = \frac{A_{SC}}{A_p + Ag}$$

where A_g is the guard area. Here, we will assume the guard and probe have the same radius, the guard length is $2.5 \times 10^{-2}\,\mathrm{m}$, and the reference satellite is perfectly conducting 3U CubeSat, area of $0.14\,\mathrm{m}^2$. PSIC-LEO simulations demonstrated that the area ratio between a spacecraft and LP should be greater than 70 to ensure spacecraft potential and electron temperature measurements are unaffected after making twin-probe corrections (refer to fig. 4.4). More stringently, to sample at least $5T_e$ above the plasma potential, for LEO-like conditions, the minimum area ratio is roughly 130. Therefore, the maximum probe length would be $8.6 \times 10^{-2}\,\mathrm{m}$ for an area ratio of 80 and $4.4 \times 10^{-2}\,\mathrm{m}$ for an area ratio of 130. As expected, if the guard is made longer, or shorter, the maximum length of the LP will decrease, or increase, respectively; however, the area ratio will not change. In this instance, the probe length calculated for a guarded LP, with a probe length-to-diameter ratio of 10, is long enough to ensure an area ratio above 80, but is just short of the 130 area ratio mark and may run into limitations when analyzing the twin-probe corrected electron saturation regime. If studying the electron density is necessary for the mission, the probe and guard can be made thinner, as was shown to be possible for the ProSEDS and AE Langmuir probes, in order to increase the area ratio. For instance, if the probe has the thickness of the AE probe, the maximum probe length for an area ratio of 130 is then $0.146\,\mathrm{m}$. Similarly, for the thickness of the ProSEDS LP, which was slightly thinner than the maximum diameter of $5 \times 10^{-1}\,\mathrm{m}$, the maximum probe length would be $5.5 \times 10^{-2}\,\mathrm{m}$.

Once the probe dimensions have been determined, it is important to ensure the probe is large enough to collect currents above the noise floor of the sensing circuitry. Assume the design team decides to use a Lanmguir probe mounted on a triaxial boom that is stored along a $0.30\,\mathrm{m}$ long side of the 3U CubeSat. Based on the expected charging levels, a $0.20\,\mathrm{m}$ boom is deemed sufficient to remain outside the spacecraft sheath (see fig. 3.4), a $2.5 \times 10^{-2}\,\mathrm{m}$ guard is used, and the length of the LP should be no more than

$6 \times 10^{-2}\,\mathrm{m}$. This would allow for a $1.5 \times 10^{-2}\,\mathrm{m}$ gap between the probe tip and the end of the spacecraft, in case adjustments are necessary. Using the calculations above, the team settles on 3 possible probe dimensions and opts to keep the guard and probe diameters as similar as possible; the choices are given in table 6.1.

Option	Length (m)	Diameter (m)	Probe Area (m^2)	Area Ratio
1	4.4×10^{-2}	5×10^{-3}	6.9×10^{-4}	130
2	5.5×10^{-2}	4.3×10^{-3}	7.4×10^{-4}	130
3	6×10^{-2}	2×10^{-3}	3.75×10^{-4}	260

Table 6.1: Example of various probe dimensions for a notional 3U CubeSat platform. Guard dimensions are included in the area ratio calculation; the guard length is $2.5 \times 10^{-2}\,\mathrm{m}$, and the guard diameter is equal to the probe diameter.

Considering the options, it seems like option 2 and 3 are the best candidates. Options 1 and 2 have the same area ratio, but option 2 has a larger surface area, which equates to greater current collection; a smaller diameter, so it is more likely to approximate OML current collection; and a greater probe length-to-diameter ratio that should produce slightly smaller probe end effects. Option 3 has the smallest diameter and greatest probe length-to-diameter ratio. However, it also has the smallest probe area; and, while this would result in reduced spacecraft charging, it also means less current collection. So the next step would be to compare expected ion and electron currents to determine what the requirements of the probe circuitry would need to be; expected current collection shown in table 6.2.

Option	Electron Thermal Current ($\mu\mathrm{A}$)	Ion Drift Current ($\mu\mathrm{A}$)
2	0.06 to 3.1	0.003 to 0.15
3	0.03 to 1.6	0.002 to 0.08

Table 6.2: Estimated ion and electron currents to various LP dimensions and densities for notional 3U CubeSat system. Electron thermal current was calculated using eq. 2.10 and minimum ion drift current was calculated using eq. 2.19 for oxygen with $5\,\mathrm{eV}$ drift energy.

Comparing the ranges in expected electron and ion currents, it is clear that regardless of which probe option is used, the probe circuitry must accurately sense ion currents in the nanoampere regime. Notably, this is the minimum expected ion current, as it is the ion current collected without an accelerating potential. Furthermore, the electron thermal current is the electron current at the plasma potential, and should be expected to rise with increased attractive potential. This implies that the probe circuitry should also be capable of measuring currents in the tens of microamps, but should not be expected to measure currents greater than one hundred microamps. Experimental measurements for densities roughly an order of magnitude greater in density could approach $200\,\mu\mathrm{A}$ at applied potentials of $10\,\mathrm{V}$ (see examples in figs. 3.1 and 5.16); and since current is linear with density, a factor of 10 decrease in density corresponds to an order of magnitude decrease in current. Therefore, the requirements for the LP circuitry should be to reliably sense current between $1\,\mathrm{nA}$ and $100\,\mu\mathrm{A}$, regardless of the considered dimensions. As a result, option 3 should be the primary option unless other circumstances prohibit its use, such as cost of manufacturing, difficulty in ensuring homogeneous surface work function, or insufficient mechanical strength.

Assuming the appropriately-sized probe is chosen, many avenues for analysis are available when using the twin-probe method. First, ensure the high-impedance probe has a sufficiently large input impedance. As shown in fig. 4.19b, the input resistance should be at least two orders of magnitude greater than the largest expected plasma resistance. Since the plasma resistance is inversely proportional to its density, an input impedance of $5\,\mathrm{G\Omega}$ should be sufficient (see table 3.1 for expected plasma resistances). As an example, the ProSEDS LP carried a $5\,\mathrm{G\Omega}$ input resistance for its high-impedance probe [159] and the ISS's Floating Potential Monitor Unit (FPMU) uses an input resistance of $100\,\mathrm{G\Omega}$ [189].

To determine ion density, the spacecraft's mesothermal state is advantageous in ensuring the dominant oxygen ion population is drifting at approximately $5\,\mathrm{eV}$. Assuming the probe is oriented perpendicular to the ion drift velocity, the ion density can then be determined using the orbit motion limited theory (detailed in section C.3). Electron temperature properties should be obtained by performing the log-linear method (detailed in appendix C.5.3) on twin-probe corrected data. To help ensure the electron retardation regime is properly sampled for the log-linear method, the voltage step size should be no larger than $0.25T_e$. There are multiple schemes that can be used to accomplish this resolution. These approaches include simply oversampling the LP sweeps based on expected plasma temperatures from models and previous missions; a framing algorithm that adjusts sweep parameters using a series of Langmuir probe, as was done on PVO and was planned for ProSEDs [151, 159]; or a semi-logarithmic method where voltage step sizes decrease near the zero applied potential point, as is executed on MAVEN [74]. Electron density approximations should be derived from the electron saturation regime; however, true OML current collection behavior should not be expected. Instead, the electron saturation current can be assumed to follow a power law function and steps can be taken to determine the power of the function, as detailed in appendix C.6.2. Bear in mind that this approach can only be applied on twin-probe corrected measurements. At these restrictive area ratios, spacecraft charging behavior will cause the electron saturation current collection of uncorrected sweeps to deviate from the power law approximation, as was discussed in section 5.3.5.

6.3 Applications for Future Missions

So far, discussion on the twin-probe method has centered around correcting Langmuir probe sweeps by utilizing two identical probes. However, this method is flexible enough to fit other roles and can be performed by systems that do not necessarily carry two Langmuir probes. First, we will detail how to employ twin-probes to induce negative charge on a spacecraft for wider ion sensing analysis by highlighting a proposed mission, the Composition and Dynamics Experiment in the Topside Ionosphere (CODEX). Then, the possibility of tracking the spacecraft potential by using a tethered end body is discussed in the context of a series of tethered CubeSat missions called the Miniature Tether Electrodynamics Experiment (MiTEE).

6.3.1 CODEX

The proposed CODEX mission focuses on studying mass resolved bulk properties and non-thermal ion distribution functions associated with ion outflows near the polar regions of the Earth's ionosphere. To analyze the cold ion populations, CODEX carries an ion composition and three-dimensional velocity analyzer, the 3-Dimensional ion velocity and mass Imager (3DI) [190]. The 3DI instrument is optimized to separate H^+, He^+, O^+, and heavy ions (NO^+, O_2^+, and N_2^+). However, light ions such as H^+ and He^+ can be difficult to measure since the spacecraft potential can charge positive, repelling the ions that are of interest [191]. To counteract this positive charging, the CODEX satellite implements twin Langmuir probes with a scheme to purposefully induce a negative charge on the spacecraft in order to sample the full spectrum of available ions.

The CODEX satellite is a 6U CubeSat with two deployable solar panels, covered with ITO coated cover glass, that are each roughly $0.3\,\mathrm{m}\times0.3\,\mathrm{m}$ (see fig. 6.3). The area ratio between the Langmuir probes and the total conductive surface area of the satellite (main body and solar panels) is 360. As expected, the spacecraft will charge negatively when operating the Langmuir probe. Simple *Nascap-2K* models of the CODEX satellite estimate that the most severe charging reach $-4.75\,\mathrm{V}$ with stowed solar panels and $-3.5\,\mathrm{V}$ with deployed panels. As an aside, the potential difference between deployed and stowed panels highlights how effective additional, deployable, conductive structures can be in reducing the effects of probe operation on the spacecraft's potential. As long as the satellite floating potential is not greater than the magnitude of the maximum negative charge that the LP can induce on the satellite—due to a combination of energetic outflowing ions, photoelectron emission, and secondary electron emission—one of the Langmuir probes can drive the spacecraft potential below the plasma potential. The remaining probe would be operated as a high-impedance probe to track changes in the spacecraft potential. If the satellite floating potential rises above the most negative potential the LPSP can induce, operating the probe in this constant bias system would still help increase the range of the ion population that can be sampled, but the full distribution would remain unavailable. Depending on how positive the spacecraft floats relative to the plasma, this could be problematic for sampling the H^+ and He^+, since they are the first ions to be repelled due to positive spacecraft potentials. Finally, the twin Langmuir probes, denoted as LPSP in fig. 6.3, are positioned relative to spacecraft such that one probe can be shadowed while the other is sunlit to calibrate for photoelectron current (as discussed in section 3.3.1).

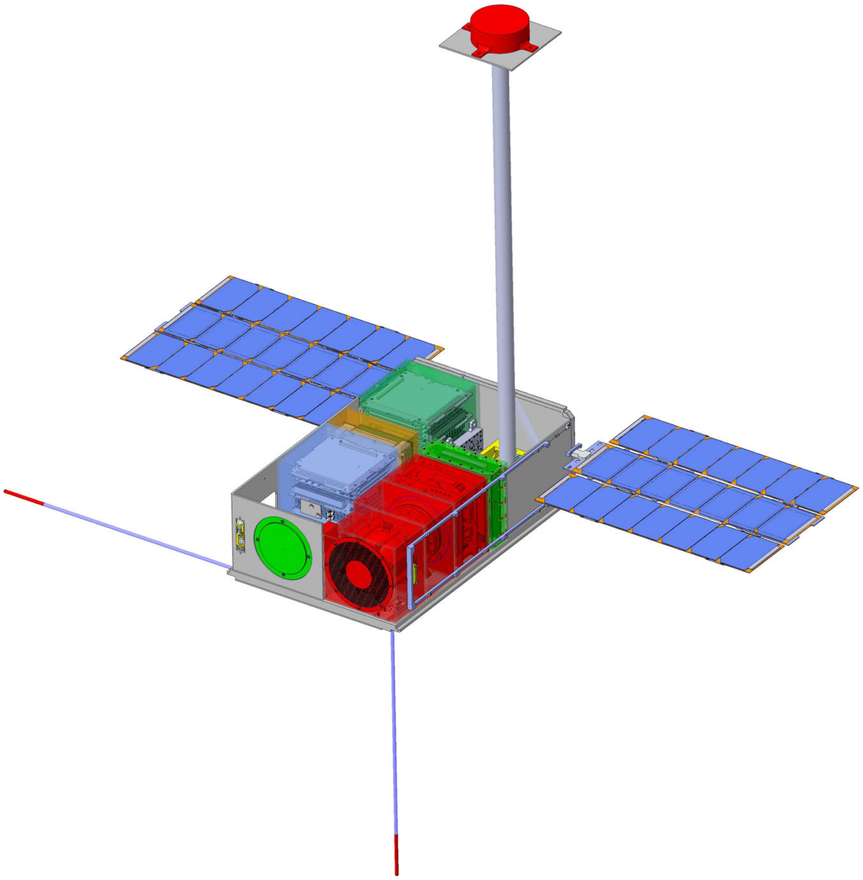

Figure 6.3: CAD representation of fully deployed CODEX satellite. From personal communication with *Dr. Keiichi Ogasawara* [192].

6.3.2 MiTEE-I and MiTEE-II

MiTEE is a series of technology demonstration missions to demonstrate the capability of short electrodynamic tethers (EDTs) for drag make-up and orbital maneuvers on picosatellites and femtosatellites [193]. MiTEE-I focuses on validating current collection models to a picosatellite-sized end body, and MiTEE-II will study the thrust capabilities of a $10\,\mathrm{m}$ to $20\,\mathrm{m}$ EDT [194, 109]. Each MiTEE satellite will carry at least one Langmuir probe, but the small area ratio guarantees that the spacecraft will charge negatively during probe operation. Due to limited volume, carrying two Langmuir probes may be infeasible for MiTEE-II. Instead, the MiTEE-II satellite team will study the feasibility of operating the tethered end body as a high-impedance probe to track the spacecraft potential during LP operation. With a tether length of $10\,\mathrm{m}$ to $20\,\mathrm{m}$, this end body will be outside of the main body's sheath regardless of how negative the spacecraft charges. However, this method is not without issues that are not necessarily dealt with for twin-probe corrections using identical probes. As a reminder, the twin-probe correction is given by eq. 3.5, shown here for convenience as

$$\begin{aligned}\phi_{LP} &= V_A + (\phi_{HI} - \gamma\Delta V) + \vec{E}_T \cdot \left(\vec{d}_{HI} - \vec{d}_{LP}\right) + WF_{HI} - WF_{LP},\\ \gamma &= 1 + \frac{R_{HI}}{R_{in}} + \frac{R_{SC}}{R_{in}}.\end{aligned}$$

The three major issues are as follows: 1) estimate the motional emf to correct tracked spacecraft potential; 2) determine how the work functions would play a role in twin-probe corrections; and 3) ensure the capacitance of the tether doesn't produce unreasonably long RC time constants.

Motional emf has to be considered for the lengths of the Langmuir probe boom structure and satellite tether that are considered, as discussed in section 2.4.4. However, where the boom masts are typically tens of centimeters long, a tether of $10\,\mathrm{m}$ should expect voltage drops that are two orders of magnitude greater for the same orientation relative to the ambient magnetic field and the satellite. Therefore, high-impedance measurements made from a tethered end body should expect significantly larger measurement errors, unless the motional emf term is accounted for. This would require that the satellite system has the capacity to, at a minimum, keep track of both the end body position relative to the main body and the position of the main body along its orbit. Further improvements to the accuracy of the tracked spacecraft potential can be made by ensuring a taught tether, since bends in the tether affect the total induced potential, and by directly measuring the ambient magnetic field strength and direction.

When implementing the twin-probe method with two Langmuir probes, the work function difference between the probes is usually ignored because the probes can be manufactured from the same material. However, this assumption fails for the case where the Langmuir probe is used in conjunction with the end body. Exact estimates are difficult to predict, as the work functions of the end body surface would be specific to the materials used. However, it should be expected that the magnitude of the difference in work functions is greater than 0. Therefore, ground experiments would likely be required to determine this work function difference in a series of calibration tests, which may be similar to measurements of contact potential difference [195].

For RC time constant estimates, the longer tether may introduce larger capacitances into the system, so it becomes necessary to estimate what the settling times would be to determine if they are prohibitively long. In this example, the same plasma resistances and densities from table 3.1 are used; however, the input impedance is now $5\,\mathrm{G\Omega}$ to give an estimate closer to design specifications. The capacitance per unit length of the tether can be estimated using the coaxial capacitor detailed by *Bilén* [196],

$$C_{sh} = \frac{2\pi\epsilon_0}{\ln\left(\frac{r_{sh}}{r_a}\right)} \tag{6.1}$$

where r_{sh} is the sheath radius and r_a is the tether radius. The sheath radius will change as a function of voltage across the sheath, and so the sheath radius is given by

$$r_{sh} \simeq \sqrt{3}\left(\frac{V_a\epsilon_0}{qn_0}\right)^{\frac{5}{12}} r_a^{\frac{1}{6}} \tag{6.2}$$

where V_a is magnitude of the applied bias and n_0 is the plasma density, as demonstrated by *Bilén* [196]. Assuming the tether geometry is identical to that of the Tethered Satellite System (TSS) missions, the tether radius is $0.43\,\mathrm{mm}$ [197]. Using eqs. 6.1 and 6.2, the settling times can be calculated for a $10\,\mathrm{m}$ tether with a potential difference across the sheath of either $1\,\mathrm{V}$ or $10\,\mathrm{V}$, corresponding to different levels of charging the tethered bodies can experience. The capacitance and settling time calculations are shown in table 6.3; for a $20\,\mathrm{m}$ tether, the capacitance and settling time would be twice as large as what is shown in the table.

In comparison to the shorter booms described in section section $3.2.2$, the estimated settling times of a tethered end body used as a high-impedance probe are considerably larger. To determine whether or not the settling times are prohibitively long, consider a 256-point LP sweep that is twin-probe corrected. At each LP applied bias, the system must be allowed to settle; so when the tether potential is $1\,\mathrm{V}$, the total time it would take for a single sweep ranges from $38.4\,\mathrm{ms}$ to $20.6\,\mathrm{s}$. Assuming an orbital velocity of $8\,\mathrm{km\,s^{-1}}$, a spacecraft would travel $0.31\,\mathrm{km}$ during the LP sweep, at the highest densities. This distance is short enough that the plasma can be considered homogeneous. At lower densities, the spacecraft would travel $165\,\mathrm{km}$ during the LP sweep, which is on the order of plasma instabilities, such as equatorial bubbles [198]. Therefore, the region of space where the tethered spacecraft will be operating is crucial in determining if the end body can satisfactorily be used as a high-impedance probe. The MiTEE missions will be operating in the F-region of the ionosphere, where ionospheric plasma densities are near their peak, so it will likely be implemented successfully in this region. However, for low flying spacecraft and rockets operating in the D and E regions of the ionosphere, this application of the twin-probe method should be avoided in favor of the twin probes; that is, two identical probes.

ΔV_{tether} =1 V				
$N\,(\mathrm{m}^{-3})$	$R_p\,(\Omega)$	$R_{Total}\,(\Omega)$	$C_{Tether}\,(\mathrm{pF})$	$\tau\,(\mathrm{ms})$
1×10^9	3.49×10^8	3.27×10^8	95.9	94.0
1×10^{10}	3.49×10^7	3.47×10^7	114.9	12.0
1×10^{11}	3.49×10^6	3.49×10^6	143.2	1.5
1×10^{12}	3.49×10^5	3.49×10^5	190.2	0.20
ΔV_{tether} =10 V				
$N\,(\mathrm{m}^{-3})$	$R_p\,(\Omega)$	$R_{Total}\,(\Omega)$	$C_{Tether}\,(\mathrm{pF})$	$\tau\,(\mathrm{ms})$
1×10^9	3.49×10^8	3.27×10^8	82.3	80.6
1×10^{10}	3.49×10^7	3.47×10^7	95.9	9.98
1×10^{11}	3.49×10^6	3.49×10^6	115	1.20
1×10^{12}	3.49×10^5	3.49×10^5	143	0.15

Table 6.3: Impedance probe settling time constants relative to plasma density for MiTEE mission with a $10\,\mathrm{m}$.

CHAPTER 7

Summary, Future Work, and Conclusion

After studying the results of simulations and experiments, enough evidence has been collected to answer the questions posed in section 1.3.4. First, work presented in this dissertation and any supplemental publication is used to answer as many of the queries as possible. Then, for the questions that aren't adequately answered, a plan for future work is presented. Finally, the dissertation is concluded.

To reiterate the questions asked at the beginning of this dissertation,

1. Can the spacecraft potential be tracked accurately enough during Langmuir probe operation to properly correct I-V curves?
    (a) What system level design choices limit the effectiveness of the twin-probe method?
    (b) Does probe orientation, size, or shape affect the efficacy of the twin-probe method?
    (c) What environmental effects limit accuracy?
2. Can spacecraft charging behavior during Langmuir probe operation be predicted by analytic expressions?
    (a) How does spacecraft charging affect the Langmuir probe's I-V characteristics in ways that cannot be resolved using the twin-probe method?
    (b) What is the impact of individual spacecraft conductive surface areas on spacecraft charging?
3. How can the twin-probe method be used synergistically with other space plasma instruments?

For this discussion, effectiveness refers to the magnitude of correction, or the percent difference, between uncorrected and twin-probe corrected estimates of plasma properties.

7.1 Summary of Research

To begin, tracked spacecraft potential measurements demonstrated the high-impedance probe's capability of tracking decreased spacecraft charging with increased area ratio (see section 5.3.1.1). Twin-probe corrections always produced electron temperature and electron density estimates that were closer to the control measurement, indicating at least some correction of the LP I-V sweeps (shown in sections 5.3.4 and 5.3.5). Additionally, regardless of the spread of uncorrected sweeps, the resultant twin-probe corrected sweeps were always more closely bundled, reducing variability in the measured plasma properties (see section 5.3.1.3 and fig. 3.1). Therefore, it is possible to track the spacecraft potential accurately enough to correct impacted Langmuir probe I-V curves, improving plasma property measurements; and the corrections were most effective for stable high-impedance probe floating potentials with area ratios less than 300, as shown in figs. 5.32 and 5.37.

Both settling time and area ratio have been shown to limit the twin-probe method's efficacy. Section 5.3.1.2 presented examples of transient effects impacting the tracked spacecraft potential measurement when the Langmuir probe's bias was mostly in the ion saturation regime. The resultant twin-probe corrected ion density provided some correction to the uncorrected measurements, in contrast to compared ion densities for tracked spacecraft potentials that were not affected by transients where no correction occurred. While these particular effects can be mitigated using twin-probe corrected data, ensuring that enough time elapses between LP sweeps to respect settling times is still good practice, as it is not always possible to distinguish where the transient effects end or what the cause of the transient is. Furthermore, the magnitude of twin-probe corrections decreased with larger area ratios. This is expected, as an increase in area ratio leads to a more stable spacecraft potential during Langmuir probe operations. However, due to the overlap between the magnitude of corrections and measurement uncertainties for area ratios greater than 300, it is not possible to clearly demarcate when the spacecraft potential is stable enough to minimally impact probe measurements (discussed in section 6.1). It is recommended that improved simulations (i.e. ones that better capture physical processes) should be performed to help inform the feasibility of a more focused experiment campaign to find the minimally stable area ratio.

High-impedance probe orientation relative to the plasma flow does not appear to impact its ability to track spacecraft charging (see section 5.3.1.3). However, care must be taken for probes operating in the wake of in-orbit spacecraft, as nominal spacecraft wakes in a chamber likely won't capture in-space wake dynamics nor size. Moreover, the Langmuir and high-impedance probes were never of equal size, but they were all cylindrical probes.

This suggests that neither probe orientation, size, nor shape greatly affects the efficacy of the twin-probe method. Instead, minimizing variations in the high-impedance probe's floating potential appears to be the dominant factor in properly correcting the Langmuir probe sweeps. Many environmental effects can vary the high-impedance probe's and satellite's floating potential, such as the local magnetic field, high energy charged particles, and sunlight. While the general environmental effects were discussed in sections 2.4 and 3.3, more simulation work is needed to carefully analyze how they impact the accuracy of the twin-probe method.

Multiple simulations, including those presented in this dissertation (see PSIC-LEO model in section 4.3, and comparison between experiment and simulations in section 5.4), have demonstrated that it is possible to model spacecraft potential behavior during Lanmguir probe operation [29, 56, 182, 199]. PSIC-LEO simulations have demonstrated that while the twin-probe method can correct spacecraft charging effects for area ratios below 50, at these very small ratios, the Langmuir probe potential will not reach an equipotential bias with the ambient plasma (see fig. 4.2a). As a result, only ion density and electron temperature, can be inferred from the Langmuir probe sweep. In situations where the area ratio is below 50, it is recommended that measures are taken to either increase the area ratio to a more acceptable level; or that design changes are made to control spacecraft charging by using active measures such as thermionic emitters, or more passive measures, like building the spacecraft from materials with high secondary emission coefficients [137].

In sections 5.3.1.3 and 5.3.2.3, it was shown that satellite bias and orientation dictated whether the satellite's conductive ram area or total conductive area was more important. For the biases considered, up to $-10\,\mathrm{V}$, the larger ram-facing area ($\sim 0.3\,\mathrm{m}^2$) always dominated the total current collection of the CubeSat; however, the non-ram-facing sides of the CubeSat played a non-negligible role at greater biases (see fig. 5.25a). Additionally, the smaller ram-facing side ($\sim 0.1\,\mathrm{m}^2$) only played a dominant role in ion current collection when the spacecraft bias was very close to the plasma potential, or slightly more positive of it (see fig. 5.25b). Therefore, while one should always consider maximizing the ram-facing area ratio, if the spacecraft potential is guaranteed to charge several volts negative relative to the plasma, during probe operation, the ram-facing area does not need to be maximized. Instead, a smaller drag coefficient and longer orbital lifetime can be favored. *Nascap-2K* demonstrated that the difference in the maximum negative potential of the spacecraft, when comparing a large and small ram face, was at most roughly $1\,\mathrm{V}$, with the smaller ram face having the more negative potential (see appendix A.2.5).

To answer the last question, it was noted in section 6.3 that there are two major synergistic opportunities for the twin-probe technique. Should the CODEX mission be accepted, it would provide an opportunity to demonstrate the ability of a Langmuir probe to enhance the capabilities of ion energy analyzers by holding the spacecraft negative of the ambient plasma, so the full local ion population can be sampled. Additionally, during the MiTEE-2 mission, the possibility exists to use a tethered end-body as a high-impedance probe to correct impacted Langmuir probe current voltage curves. While this technique would be more error-prone relative to a true twin-probe system, it may provide a method for maintaining the accuracy of Langmuir probes on tethered missions that may not have the space for two identical Langmuir probes.

7.2 Recommendations for Future Work

The results of simulations and experiments presented in this work have raised new questions. In this section, future work is proposed that can answer these questions to help make more informed decisions on how to implement the twin-probe method, under what conditions should it be implemented, and how to minimize its errors. These efforts will focus primarily on simulation campaigns and, like in chapter 4, the PSIC-LEO codes are used for iterative studies and developing new Langmuir probe analysis techniques, such as calibration methods. The questions of interest are:

1. How does satellite current collection change with angle relative to plasma flow?
2. How does a varying high-impedance probe floating potential affect the effectiveness of the twin-probe method and can they be accounted for? Processes that affect the probe's floating potential include:
    - Spacecraft rotation
    - Variable illumination
    - Variable ambient magnetic field
    - Variable orientation relative to a constant magnetic field
3. Is it possible to determine when it is no longer feasible to employ the twin-probe method, i.e. when does the cost and time required to employ a variant of the twin-probe method outweigh the improvements to plasma property estimates?

7.2.1 Improvements to PSIC-LEO Codes

The PSIC-LEO simulations have a nonphysical asymptotic response in the electron saturation regime of the modeled LP sweeps. The first step to produce more physically accurate curves is to model the current collection to a CubeSat with either the analytic equations used by *Nascap-2K*, shown in eq. A.1, or the derived equations from the parametric studies detailed in appendix A.2.6. Using the new models, the analysis performed in sections 4.3.2 and 4.4.2 should be redone with a focus on the electron saturation regime to better estimate the magnitude of twin-probe corrected electron density measurements. This may help identify if there exists an area ratio above 300 and below 1000 (the accepted lowest limit of spacecraft potential stability) for which the satellite potential's variability is sufficiently minimized, such that no correction nor charge control is necessary.

Once the currents to a CubeSat are satisfactorily modeled, new physical processes that vary the satellite and high-impedance probe's floating potential can be introduced. These processes include satellite rotation during LP sweeps, variable photoelectron current, and variable motional emf. The goal of adding these processes is two-fold. First, it is important to understand how a changing high-impedance probe and/or satellite floating potential affects the efficacy of the twin-probe method. Then, once the effects are understood, methods can be devised to account for them, and ensure the most accurate estimates of plasma properties possible, when using the twin-probe method. Finally, current collection models to a sphere can be added to determine how satellite and/or high-impedance probe shape affects the twin-probe method.

7.3 Conclusion

It has been shown that the twin-probe method can correct LP I-V curves that are impacted by spacecraft charging effects. Much has been achieved as a result of this research. A computational program, PSIC-LEO, has been created that can model spacecraft charging and its effects on LP sweeps. *Nascap-2K* simulations have been developed to predict how space environmental effects may impact the twin-probe method for spacecraft in LEO conditions. Earth-based chamber experiments were performed to provide invaluable data in understanding which LP analysis methods are most effective for in-space operation, and provide validity to numerical models. This work has extensively supported the MiTEE missions, and has informed decisions for proposed future spacecraft. The path forward involves improvements to current models, and may include further laboratory testing, to determine which conditions hamper the twin-probe method and how to account for them.

BIBLIOGRAPHY

[1] A Reifman and Wo Go Dow. Dynamic probe measurements in the ionosphere. *Physical Review*, 76(7):987, 1949.

[2] VI Krassovsk. Exploration of the upper atmosphere with the help of the third Soviet Sputnik. *Proceedings of the IRE*, 47(2):289–296, 1959.

[3] Larry H Brace. Langmuir probe measurements in the ionosphere. *Geophysical Monograph-American Geophysical Union*, 102:23–36, 1998.

[4] Dr. David R. Williams. Pioneer Venus project information. `https://nssdc.gsfc.nasa.gov/planetary/pioneer_venus.html`.

[5] Brian Dunbar. Pioneer Venus 1, orbiter and multiprobe spacecraft (included nasa ames partnership). `https://www.nasa.gov/centers/ames/missions/archive/pioneer-venus.html`, .

[6] Washito Sasamoto. Explorer program acquisition. `https://explorers.larc.nasa.gov/`, 2019.

[7] Anthony Freeman and Michael S. Saing. Nasa small mission explorer (smex) program: Past, present and future low costs. `https://www.nasa.gov/sites/default/files/atoms/files/19_nasa_smex_mission_explorer_program_past_present_and_future_low_costs_saing_and_freeman_jpl_final.pdf`, 2018.

[8] NASA CubeSat Launch Initiative et al. Cubesat 101: Basic concepts and processes for first-time cubesat developers. 2017.

[9] Armen Poghosyan and Alessandro Golkar. Cubesat evolution: Analyzing cubesat capabilities for conducting science missions. *Progress in Aerospace Sciences*, 88: 59–83, 2017.

[10] Jeremy Straub. Cubesats: A low-cost, very high-return space technology. In *Proceedings of the 2012 Reinventing Space Conference*, 2012.

[11] Michael A Swartwout. A brief history of rideshares (and attack of the cubesats). In *2011 Aerospace Conference*, pages 1–15. IEEE, 2011.

[12] Nanoracks. Faq: What is your price? `https://nanoracks.com/resources/faq/`.

[13] Spaceflight. Pricing information. `https://spaceflight.com/pricing/`.

[14] Alexander Chin, Roland Coelho, Lori Brooks, Ryan Nugent, and Jorgi Puig-Suari. Standardization promotes flexibility: a review of CubeSats' success. *Aerospace Engineering*, 805:756–5087, 2008.

[15] Kirk Woellert, Pascale Ehrenfreund, Antonio J Ricco, and Henry Hertzfeld. Cubesats: Cost-effective science and technology platforms for emerging and developing nations. *Advances in Space Research*, 47(4):663–684, 2011.

[16] Maurice Martin, Pete Klupar, Steve Kilberg, and James Winter. Techsat 21 and revolutionizing space missions using microsatellites. 2001.

[17] Sreeja Nag, Jacqueline LeMoigne, and Olivier de Weck. Cost and risk analysis of small satellite constellations for earth observation. In *2014 IEEE Aerospace Conference*, pages 1–16. IEEE, 2014.

[18] T Max Roberts, KA Lynch, RE Clayton, J Weiss, and DL Hampton. A small spacecraft for multipoint measurement of ionospheric plasma. *Review of Scientific Instruments*, 88(7):073507, 2017.

[19] H Hoang, Lasse Boy Novock Clausen, Ketil Røed, Tore Andre Bekkeng, Espen Trondsen, Bjørn Lybekk, Halvor Strøm, David Michael Bang-Hauge, Arne Pedersen, Andres Spicher, et al. The multi-needle Langmuir probe system on board NorSat-1. *Space Science Reviews*, 214(4):75, 2018.

[20] J-P Lebreton, S Stverak, P Travnicek, M Maksimovic, D Klinge, S Merikallio, D Lagoutte, B Poirier, P-L Blelly, ZMMS Kozacek, et al. The ISL Langmuir probe experiment processing onboard DEMETER: Scientific objectives, description and first results. *Planetary and Space Science*, 54(5):472–486, 2006.

[21] Francis F Chen et al. *Introduction to plasma physics and controlled fusion*, volume 1. Springer, 1984.

[22] Michael A Lieberman and Alan J Lichtenberg. *Principles of plasma discharges and materials processing*. John Wiley & Sons, 2005.

[23] José A Bittencourt. *Fundamentals of plasma physics*. Springer Science & Business Media, 2013.

[24] Grant Miars. *Spacecraft Charge Neutralization During Active Electron Emission*. PhD thesis, University of Michigan, 2020.

[25] Koichiro Oyama. DC Langmuir probe for measurement of space plasma: A brief review. *Journal of Astronomy and Space Sciences*, 32(3):167–180, 2015.

[26] Francis F Chen, John D Evans, and Wade Zawalski. Electric probes. In *In Plasma Diagnostic Techniques, edited by Huddlestone, RH and Leornard, SL*. Citeseer, 1965.

[27] U. Fahleson, C.-G. Fälthammar, and A. Pedersen. Ionospheric temperature and density measurements by means of spherical double probes. *Planetary and Space Science*, 22(1):41–66, January 1974. ISSN 00320633. doi: 10.1016/0032-0633(74)90122-6. URL `https://linkinghub.elsevier.com/retrieve/pii/0032063374901226`.

[28] David B Beard and Francis S Johnson. Ionospheric limitations on attainable satellite potential. *Journal of Geophysical Research*, 66(12):4113–4122, 1961.

[29] Richard T Bettinger. An in situ probe system for the measurement of ionospheric parameters. In *Interactions of Space Vehicles with an Ionized Atmosphere*, pages 163–270. Elsevier, 1965.

[30] Leslie Garrett Smith. Langmuir probes for measurements in the ionosphere. 1965.

[31] NASA Sounding Rockets User Handbook. Wallops. *VA: NASA Goddard Space Flight Center*, 2015.

[32] Koh-Ichiro Oyama and Kunio Hirao. Distortions of the energy distribution of ionospheric thermal electrons near the focus of sq current vortex. *Planetary and Space Science*, 27(2):183–192, 1979.

[33] A Dalgarno, WB Hanson, NW Spencer, and ER Schmerling. The atmosphere explorer mission. 1973.

[34] RA Hoffman, GD Hogan, and RC Maehl. Dynamics explorer spacecraft and ground operations systems. *Space Science Instrumentation*, 5(4):349–367, 1981.

[35] JS Lee, JP Doering, TA Potemra, and LH Brace. Measurements of the ambient photoelectron spectrum from Atmosphere Explorer: I. AE-E measurements below 300 km during solar minimum conditions. *Planetary and Space Science*, 28(10): 947–971, 1980.

[36] RA Heelis, JD Winningham, WB Hanson, and JL Burch. The relationships between high-latitude convection reversals and the energetic particle morphology observed by atmosphere explorer. *Journal of Geophysical Research: Space Physics*, 85(A7): 3315–3324, 1980.

[37] JL Burch, SA Fields, WB Hanson, RA Heelis, RA Hoffman, and RW Janetzke. Characteristics of auroral electron acceleration regions observed by Atmosphere Explorer C. *Journal of Geophysical Research*, 81(13):2223–2230, 1976.

[38] TL Killeen and RG Roble. Thermosphere dynamics: Contributions from the first 5 years of the Dynamics Explorer program. *Reviews of Geophysics*, 26(2):329–367, 1988.

[39] Charles R Chappell. The terrestrial plasma source: A new perspective in solar-terrestrial processes from Dynamics Explorer. *Reviews of Geophysics*, 26(2): 229–248, 1988.

[40] JL Burch. Energetic particles and currents: Results from Dynamics Explorer. *Reviews of Geophysics*, 26(2):215–228, 1988.

[41] Tatsuo Onishi, Michel Parrot, and Jean-Jacques Berthelier. The DEMETER mission, recent investigations on ionospheric effects associated with man-made activities and seismic phenomena. *Comptes Rendus Physique*, 12(2):160–170, 2011.

[42] Ames Research Center. Pioneer Venus, report of a study by the Science Steering Group. 1972.

[43] JG Luhmann, CT Russell, LH Brace, HA Taylor, WC Knudsen, FL Scarf, DS Colburn, and A Barnes. Pioneer Venus observations of plasma and field structure in the near wake of Venus. *Journal of Geophysical Research: Space Physics*, 87 (A11):9205–9210, 1982.

[44] LH Brace, RF Theis, HG Mayr, SA Curtis, and JG Luhmann. Holes in the nightside ionosphere of Venus. *Journal of Geophysical Research: Space Physics*, 87(A1): 199–211, 1982.

[45] LH Brace, RF Theis, JP Krehbiel, AF Nagy, TM Donahue, MB McElroy, and A Pedersen. Electron temperatures and densities in the Venus ionosphere: Pioneer Venus Orbiter electron temperature probe results. *Science*, 203(4382):763–765, 1979.

[46] Charles L Wolff and Walter R Hoegy. Solar irradiance observed from PVO and inferred solar rotation. 1990.

[47] JG Trotignon, R Boström, JL Burch, K-H Glassmeier, R Lundin, O Norberg, A Balogh, K Szegö, G Musmann, A Coates, et al. The Rosetta plasma consortium: Technical realization and scientific aims. *Advances in Space Research*, 24(9): 1149–1158, 1999.

[48] Elias Odelstad, Anders I Eriksson, Niklas JT Edberg, Fredrik Johansson, Erik Vigren, Mats André, C-Y Tzou, C Carr, and E Cupido. Evolution of the plasma environment of comet 67p from spacecraft potential measurements by the Rosetta Langmuir probe instrument. *Geophysical Research Letters*, 42(23):10–126, 2015.

[49] NJ Fox, MC Velli, SD Bale, R Decker, A Driesman, RA Howard, Justin C Kasper, J Kinnison, M Kusterer, D Lario, et al. The solar probe plus mission: humanity's first visit to our star. *Space Science Reviews*, 204(1-4):7–48, 2016.

[50] JR Szalay, P Pokornỳ, SD Bale, ER Christian, K Goetz, K Goodrich, ME Hill, M Kuchner, R Larsen, D Malaspina, et al. The near-sun dust environment: Initial observations from Parker Solar Probe. *The Astrophysical Journal Supplement Series*, 246(2):27, 2020.

[51] JS Halekas, P Whittlesey, DE Larson, D McGinnis, M Maksimovic, M Berthomier, JC Kasper, AW Case, KE Korreck, ML Stevens, et al. Electrons in the young solar wind: First results from the Parker Solar Probe. *The Astrophysical Journal Supplement Series*, 246(2):22, 2020.

[52] Richard T Bettinger. Offset voltages of Langmuir probes in the ionosphere. *Review of Scientific Instruments*, 36(5):630–634, 1965.

[53] Noah Hershkowitz. How Langmuir probes work. *Plasma diagnostics*, 1:113–183, 1989.

[54] EO Johnson and Louis Malter. A floating double probe method for measurements in gas discharges. *Physical Review*, 80(1):58, 1950.

[55] L Schott. Electrical probes. *Plasma diagnostics*, pages 668–731, 1968.

[56] Edward P Szuszczewicz. Area influences and floating potentials in Langmuir probe measurements. *Journal of Applied Physics*, 43(3):874–880, 1972.

[57] Charles M Swenson, Don Thompson, and Chad Fish. The ISS floating potential measurement unit. In *title 9th Spacecraft Charging Technology Conference 9th Spacecraft Charging Technology Conference*, page 722, 2005.

[58] M Carruth, Jr, Todd Schneider, Matt McCollum, Miria Finckenor, Rob Suggs, Dale Ferguson, Ira Katz, Ron Mikatarian, John Alred, and Courtney Pankop. ISS and space environment interactions without operating plasma contactor. In *39th aerospace sciences meeting and exhibit*, page 401, 2001.

[59] KS Jacobsen, J-E Wahlund, and A Pedersen. Cassini Langmuir probe measurements in the inner magnetosphere of Saturn. *Planetary and Space Science*, 57(1):48–52, 2009.

[60] Roger Gibbs. Cassini spacecraft design. In Linda Horn, editor, *Cassini/Huygens: A Mission to the Saturnian Systems*, volume 2803, pages 246 – 258. International Society for Optics and Photonics, SPIE, 1996. doi: 10.1117/12.253425. URL `https://doi.org/10.1117/12.253425`.

[61] Omar Leon, Walter Hoegy, Jesse McTernan, L Habash Krause, Grant Miars, and Brian E Gilchrist. Predicting spacecraft charging effects due to langmuir probe operation on a CubeSat using analytic equations. In *AGU Fall Meeting Abstracts*, 2018.

[62] François Buisson. The DEMETER program: a pathfinder to a high performance micro satellite line. 2003.

[63] PJ Bowen, Robert Lewis Fullarton Boyd, CL Henderson, AP Willmore, and Sir Harrie Massey. Measurement of electron temperature and concentration from a spacecraft. *Proceedings of the Royal Society of London. Series A. Mathematical and Physical Sciences*, 281(1387):514–525, 1964.

[64] LH Brace and PL Dyson. Documentation of Explorer 32 electron temperature measurements used in comparisons with backscatter measurements at jicamarca. 1968.

[65] Gunnar Hok, Nelson W Spencer, and Wo G Dow. Dynamic probe measurements in the ionosphere. *Journal of Geophysical Research*, 58(2):235–242, 1953.

[66] Walter R Hoegy and LH Brace. The dumbbell electrostatic ionosphere probe: theoretical aspects. Technical report, 1961.

[67] Larry H Brace. The dumbbell electrostatic ionosphere probe: ionosphere data. Technical report, 1962.

[68] Aroh Barjatya and Charles M Swenson. Observations of triboelectric charging effects on Langmuir-type probes in dusty plasma. *Journal of Geophysical Research: Space Physics*, 111(A10), 2006.

[69] Tore Andre Bekkeng, Aroh Barjatya, U-P Hoppe, Arne Pedersen, Jøran Idar Moen, Martin Friedrich, and Markus Rapp. Payload charging events in the mesosphere and their impact on langmuir type electric probes. 2013.

[70] Tore André Bekkeng, Espen Sørlie Helgeby, Arne Pedersen, Espen Trondsen, Torfinn Lindem, and Jøran Idar Moen. Multi-needle Langmuir probe system for electron density measurements and active spacecraft potential control on cubesats. *IEEE Transactions on Aerospace and Electronic Systems*, 55(6):2951–2964, 2019.

[71] CS Fish, CM Swenson, G Crowley, A Barjatya, T Neilsen, J Gunther, I Azeem, M Pilinski, R Wilder, D Allen, et al. Design, development, implementation, and on-orbit performance of the dynamic ionosphere cubesat experiment mission. *Space Science Reviews*, 181(1-4):61–120, 2014.

[72] M Shimoyama, KI Oyama, T Abe, and AW Yau. Effect of finite electrode area ratio on high-frequency Langmuir probe measurements. *Journal of Physics D: Applied Physics*, 45(7):075205, 2012.

[73] TA Bekkeng, KS Jacobsen, JK Bekkeng, A Pedersen, T Lindem, JP Lebreton, and JI Moen. Design of a multi-needle langmuir probe system. *Measurement science and technology*, 21(8):085903, 2010.

[74] L Andersson, RE Ergun, GT Delory, Anders Eriksson, J Westfall, H Reed, J McCauly, D Summers, and D Meyers. The Langmuir probe and waves (lpw) instrument for MAVEN. *Space Science Reviews*, 195(1-4):173–198, 2015.

[75] Bruce M Jakosky, RP Lin, JM Grebowsky, JG Luhmann, DF Mitchell, G Beutelschies, T Priser, M Acuna, L Andersson, D Baird, et al. The Mars atmosphere and volatile evolution (MAVEN) mission. *Space Science Reviews*, 195 (1-4):3–48, 2015.

[76] Andreas Waets, Fabrice Cipriani, and Sylvain Ranvier. LEO charging of the PICASSO cubesat and simulation of the Langmuir probes operation. *IEEE Transactions on Plasma Science*, 47(8):3689–3698, 2019.

[77] Arianespace. Launch kit june 2020: Vv16. `https://www.arianespace.com/wp-content/uploads/2020/06/VV16-launchkit-EN3.pdf`, 2020.

[78] Robert Schunk and Andrew Nagy. *Ionospheres: Physics, Plasma Physics, and Chemistry*. Cambridge university press, 2009.

[79] Andrew F Nagy, André Balogh, Thomas E Cravens, Michael Mendillo, and Ingo Mueller-Wodarg. *Comparative aeronomy*, volume 29. Springer Science & Business Media, 2008.

[80] O Witasse, T Cravens, M Mendillo, J Moses, A Kliore, AF Nagy, and T Breus. Solar system ionospheres. In *Comparative Aeronomy*, pages 235–265. Springer, 2008.

[81] Kazuo Takayanagi and Yukikazu Itikawa. Elementary processes involving electrons in the ionosphere. *Space Science Reviews*, 11(2-3):380–450, 1970.

[82] LH Brace, NW Spencer, and A Dalgarno. Detailed behaviour of the midlatitude ionosphere from the explorer xvii satellite. *Planetary and Space Science*, 13(7): 647–666, 1965.

[83] ER Schmerling. Advances in ionospheric physics in the rocket and satellite era. *Reviews of Geophysics*, 4(3):329–362, 1966.

[84] PJ Bowen, Robert Lewis Fullarton Boyd, WJ Raitt, AP Willmore, and Sir Harrie Massey. Ion composition of the upper f-region. *Proceedings of the Royal Society of London. Series A. Mathematical and Physical Sciences*, 281(1387):504–514, 1964.

[85] Antonio García Muñoz, Tommi T Koskinen, and Panayotis Lavvas. Upper atmospheres and ionospheres of planets and satellites. *Handbook of Exoplanets*, 2018.

[86] John G Lyon. The solar wind-magnetosphere-ionosphere system. *Science*, 288 (5473):1987–1991, 2000.

[87] Dave Anderson. *The ionosphere*. Space Environment Center, 1999.

[88] Southwest Research Institute. Ionosphere, 2000. URL `http://pluto.space.swri.edu/image/glossary/ionosphere.html`.

[89] Shu T. Lai. *Fundamentals of spacecraft charging: spacecraft interactions with space plasmas*. Princeton University Press, 2011.

[90] Tao Yu, Weixing Wan, Libo Liu, and Biqiang Zhao. Global scale annual and semi-annual variations of daytime nmf2 in the high solar activity years. *Journal of atmospheric and solar-terrestrial physics*, 66(18):1691–1701, 2004.

[91] Michael C Kelley. *The Earth's ionosphere: plasma physics and electrodynamics*. Academic press, 2009.

[92] JR Jasperse. Electron distribution function and ion concentrations in the earth's lower ionosphere from boltzmann-fokker-planck theory. *Planetary and Space Science*, 25(8):743–756, 1977.

[93] Oyama Koh-Ichiro and Hirao Kunio. Evidences of a distorted electron energy distribution in ionospheric plasma. *Planetary and Space Science*, 24(9):900–904, 1976.

[94] O Ashihara and K Takayanagi. Velocity distribution of ionospheric low-energy electrons. *Planetary and Space Science*, 22(8):1201–1217, 1974.

[95] Philip T Huang. Direct measurements of electron energy distributions in daytime ionosphere. 1969.

[96] M Yakovlev. The IADC space debris mitigation guidelines and supporting documents. In *4th European Conference on Space Debris*, volume 587, page 591, 2005.

[97] Peter M Banks and George J Lewak. Ion velocity distributions in a partially ionized plasma. *The Physics of Fluids*, 11(4):804–810, 1968.

[98] P Gaimard, C Lathuillere, and D Hubert. "Non-Maxwellian" studies in the auroral f region: a new analysis of incoherent scatter spectra. *Journal of Atmospheric and Terrestrial Physics*, 58(1-4):415–433, 1996.

[99] DR Moorcroft and K Schlegel. Evidence for non-Maxwellian ion velocity distributions in the f-region. *Journal of Atmospheric and Terrestrial Physics*, 50 (4-5):455–465, 1988.

[100] J-P St.-Maurice, WB Hanson, and JCG Walker. Retarding potential analyzer measurement of the effect of ion-neutral collisions on the ion velocity distribution in the auroral ionosphere. *Journal of Geophysical Research*, 81(31):5438–5446, 1976.

[101] K Suvanto, Mike Lockwood, and TJ Fuller-Rowell. The influence of anisotropic f region ion velocity distributions on ionospheric ion outflows into the magnetosphere. *Journal of Geophysical Research: Space Physics*, 94(A2):1347–1358, 1989.

[102] J-P St-Maurice and RW Schunk. Ion velocity distributions in the high-latitude ionosphere. *Reviews of Geophysics*, 17(1):99–134, 1979.

[103] VC Liu. Ionospheric gas dynamics of satellites and diagnostic probes. *Space Science Reviews*, 9(4):423–490, 1969.

[104] Daniel Hastings and Henry Garrett. *Spacecraft-environment interactions*. Cambridge university press, 2004.

[105] Dale C Ferguson. Ram-wake effects on plasma current collection of the PIX 2 Langmuir probe. 1985.

[106] JG Laframboise and LJ Sonmor. Current collection by probes and electrodes in space magnetoplasmas: A review. *Journal of Geophysical Research: Space Physics*, 98 (A1):337–357, 1993.

[107] JD Huba and Space Plasma Branch. Theoretical and simulation methods applied to high latitude, f region turbulence. In *World Ionosphere/Thermosphere Study*, volume 2, pages 399–428. SCOSTEP Secretariat Boulder, CO, 1989.

[108] JG Laframboise and J Rubinstein. Theory of a cylindrical probe in a collisionless magnetoplasma. *The Physics of Fluids*, 19(12):1900–1908, 1976.

[109] Iverson C Bell. *A System Concept Study and Experimental Evaluation of Miniaturized Electrodynamic Tethers to Enhance Picosatellite and Femtosatellite Capabilities.* PhD thesis, 2015.

[110] Walter R Hoegy and Larry H Brace. Use of langmuir probes in non-Maxwellian space plasmas. *Review of scientific instruments*, 70(7):3015–3024, 1999.

[111] Francis F Chen. Langmuir probe diagnostics. In *IEEE-ICOPS Meeting, Jeju, Korea*, volume 2, 2003.

[112] Robert B Lobbia and Brian E Beal. Recommended practice for use of Langmuir probes in electric propulsion testing. *Journal of Propulsion and Power*, 33(3): 566–581, 2017.

[113] Harold M. Mott-Smith and Irving Langmuir. The theory of collectors in gaseous discharges. *Physical review*, 28(4):727, 1926.

[114] WR Hoegy and Lawrence Ernest Wharton. Current to a moving cylindrical electrostatic probe. *Journal of Applied Physics*, 44(12):5365–5371, 1973.

[115] Henry Berry Garrett. The charging of spacecraft surfaces. *Reviews of Geophysics*, 19(4):577, 1981. ISSN 8755-1209. doi: 10.1029/RG019i004p00577. URL `http://doi.wiley.com/10.1029/RG019i004p00577`.

[116] LH Brace, WR Hoegy, and RF Theis. Solar EUV measurements at Venus based on photoelectron emission from the Pioneer Venus Langmuir probe. *Journal of Geophysical Research: Space Physics*, 93(A7):7282–7296, 1988.

[117] R Grard, K Knott, et al. Spacecraft charging effects. *Space Science Reviews*, 34(3): 289–304, 1983.

[118] Tomoko Nakagawa, Takuma Ishii, Koichiro Tsuruda, Hajime Hayakawa, and Toshifumi Mukai. Net current density of photoelectrons emitted from the surface of the geotail spacecraft. *Earth, planets and space*, 52(4):283–292, 2000.

[119] Jesse K. McTernan and Sven G Bilén. Plasma contacting methods for small-scale electrodynamic tether systems. Ann Arbor, MI, 2016.

[120] R Grard and K Knott. Spacecraft charging effects. *Space Science Reviews*, 34(3): 289–304, 1983.

[121] E. J. Sternglass. Theory of secondary electron emission by high-speed ions. *Physical Review*, 108(1):1–12, October 1957. ISSN 0031-899X. doi: 10.1103/PhysRev.108.1. URL `https://link.aps.org/doi/10.1103/PhysRev.108.1`.

[122] E. M. Baroody. A theory of secondary electron emission from metals. *Physical Review*, 78(6):780–787, June 1950. ISSN 0031-899X. doi: 10.1103/PhysRev.78.780. URL `https://link.aps.org/doi/10.1103/PhysRev.78.780`.

[123] AJ Dekker. Secondary electron emission. In *Solid state physics*, volume 6, pages 251–311. Elsevier, 1958.

[124] H Kanter. Energy dissipation and secondary electron emission in solids. *Physical Review*, 121(3):677, 1961.

[125] N Balcon, D Payan, M Belhaj, T Tondu, and V Inguimbert. Secondary electron emission on space materials: Evaluation of the total secondary electron yield from surface potential measurements. *IEEE Transactions on Plasma Science*, 40(2): 282–290, 2011.

[126] Ira Katz, Myron Mandell, Gary Jongeward, and MS Gussenhoven. The importance of accurate secondary electron yields in modeling spacecraft charging. *Journal of Geophysical Research: Space Physics*, 91(A12):13739–13744, 1986.

[127] Martin S. Leung, Michael B. Tueling, and Edwin R. Schnauss. Effects of secondary electron emission on charging.pdf. NASA STI/Recon Technical Report N, 1981.

[128] Elden Cole Whipple Jr. The equilibrium electric potential of a body in the upper atmosphere and in interplanetary space. 1965.

[129] Cheol-Hee Nam, Noah Hershkowitz, Moo-Hyun Cho, T Intrator, and D Diebold. Multiple valued floating potentials of Langmuir probes. *Journal of applied physics*, 63(12):5674–5677, 1988.

[130] Philippe Garnier, MKG Holmberg, J-E Wahlund, GR Lewis, S Rochel Grimald, MF Thomsen, DA Gurnett, Andrew J Coates, FJ Crary, and I Dandouras. The influence of the secondary electrons induced by energetic electrons impacting the Cassini Langmuir probe at Saturn. *Journal of Geophysical Research: Space Physics*, 118(11):7054–7073, 2013.

[131] X Wang, H-W Hsu, and M Horanyi. Identification of when a Langmuir probe is in the sheath of a spacecraft: The effects of secondary electron emission from the probe. *Journal of Geophysical Research: Space Physics*, 120(4):2428–2437, 2015.

[132] Hilde Nesse Tyssøy. The impact of particle precipitation on the atmosphere: A link between space and climate?, 2017. URL `https://www.physik.uni-heidelberg.de/c/image/d/highrr/NesseTyss%C3%B8y.pdf`.

[133] Daniel W. Swift. Mechanisms for auroral precipitation: A review. *Reviews of Geophysics*, 19(1):185, 1981. ISSN 8755-1209. doi: 10.1029/RG019i001p00185. URL `http://doi.wiley.com/10.1029/RG019i001p00185`.

[134] M. S. Gussenhoven, D. A. Hardy, F. Rich, W. J. Burke, and H.-C. Yeh. High-level spacecraft charging in the low-altitude polar auroral environment. *Journal of Geophysical Research*, 90(A11):11009, 1985. ISSN 0148-0227. doi: 10.1029/JA090iA11p11009. URL `http://doi.wiley.com/10.1029/JA090iA11p11009`.

[135] Phillip C. Anderson. Characteristics of spacecraft charging in low Earth orbit. *Journal of Geophysical Research: Space Physics*, 117(A7):n/a–n/a, July 2012. ISSN 01480227. doi: 10.1029/2011JA016875. URL `http://doi.wiley.com/10.1029/2011JA016875`.

[136] P. C. Anderson and H. C. Koons. Spacecraft charging anomaly on a low-altitude satellite in an aurora. *Journal of Spacecraft and Rockets*, 33(5):734–738, September 1996. ISSN 0022-4650, 1533-6794. doi: 10.2514/3.26828. URL `http://arc.aiaa.org/doi/10.2514/3.26828`.

[137] Shu T Lai. A critical overview on spacecraft charging mitigation methods. *IEEE Transactions on Plasma Science*, 31(6):1118–1124, 2003.

[138] Joseph I Minow, S Maurits, K Hwang, and RM Suggs. High latitude plasma electrodynamics and spacecraft charging in low Earth orbit. In *Spacecraft Charging Technology*, volume 476, page 241, 2001.

[139] Sven Bilen, Jesse McTernan, Brian Gilchrist, Iverson Bell, Nestor Voronka, and Robert Hoyt. Electrodynamic tethers for energy harvesting and propulsion on space platforms. In *AIAA SPACE 2010 Conference & Exposition*, Anaheim, California, August 2010. American Institute of Aeronautics and Astronautics. ISBN 978-1-60086-966-2. doi: 10.2514/6.2010-8844. URL `http://arc.aiaa.org/doi/10.2514/6.2010-8844`.

[140] Brandon Reddell, John Alred, Leonard Kramer, Ronald Mikatarian, Joe Minow, and Steve Koontz. Analysis of iss plasma interaction. In *44th AIAA Aerospace Sciences Meeting and Exhibit*, page 865, 2006.

[141] DJ Knudsen, TD Phan, MD Gladders, and MJ Greffen. Thermal electron temperature measurements from the Freja cold plasma analyzer. *GEOPHYSICAL MONOGRAPH-AMERICAN GEOPHYSICAL UNION*, 102:91–96, 1998.

[142] Erwan Thébault, Christopher C Finlay, Ciarán D Beggan, Patrick Alken, Julien Aubert, Olivier Barrois, Francois Bertrand, Tatiana Bondar, Axel Boness, Laura Brocco, et al. International Geomagnetic Reference Field: the 12th generation. *Earth, Planets and Space*, 67(1):79, 2015.

[143] Dale Ferguson, Thomas Morton, and G Hillard. First results from the floating potential probe (FPP) on the international space station. In *39th Aerospace Sciences Meeting and Exhibit*, page 402, 2001.

[144] Antoine Kahn. Fermi level, work function and vacuum level. *Materials Horizons*, 3(1):7–10, December 2015. ISSN 2051-6355. doi: 10.1039/C5MH00160A. URL `http://pubs.rsc.org/en/content/articlelanding/2016/mh/c5mh00160a`.

[145] Gottfried Wehner and Gustav Medicus. Reliability of probe measurements in hot cathode gas diodes. *Journal of Applied Physics*, 23(9):1035–1046, 1952.

[146] Robert Milton Howe. Probe studies of energy distributions and radial potential variations in a low pressure mercury arc. *Journal of Applied Physics*, 24(7):881–894, 1953.

[147] D. Smith. The application of Langmuir probes to the measurement of very low electron temperatures. *Planetary and Space Science*, 20(10):1717–1726, October 1972. ISSN 00320633. doi: 10.1016/0032-0633(72)90193-6. URL `http://linkinghub.elsevier.com/retrieve/pii/0032063372901936`.

[148] Edward P Szuszczewicz and Julian C Holmes. Surface contamination of active electrodes in plasmas: Distortion of conventional Langmuir probe measurements. *Journal of Applied Physics*, 46(12):5134–5139, 1975.

[149] John F Waymouth. Pulse technique for probe measurements in gas discharges. *Journal of Applied Physics*, 30(9):1404–1412, 1959.

[150] Robert B Lobbia and Alec D Gallimore. Temporal limits of a rapidly swept langmuir probe. *Physics of Plasmas*, 17(7):073502, 2010.

[151] JP Krehbiel, LH Brace, RF Theis, JR Cutler, WH Pinkus, and RB Kaplan. Pioneer Venus Orbiter electron temperature probe. *IEEE Transactions on Geoscience and Remote Sensing*, (1):49–54, 1980.

[152] Richard T Bettinger and A Anthony Chen. An end effect associated with cylindrical langmuir probes moving at satellite velocities. *Journal of Geophysical Research*, 73 (7):2513–2528, 1968.

[153] LH Brace, RF Theis, and A Dalgarno. The cylindrical electrostatic probes for Atmosphere Explorer-C,-D, and-E. *Radio Science*, 8(4):341–348, 1973.

[154] Sidney Dean Hester and Ain A Sonin. Ion temperature sensitive end effect in cylindrical Langmuir probe response at ionosphere satellite conditions. *The Physics of Fluids*, 13(5):1265–1274, 1970.

[155] Paul M Chung, Lawrence Talbot, and Kenell J Touryan. Electric probes in stationary and flowing plasmas: part 1. Collisionless and transitional probes. *AIAA Journal*, 12 (2):133–144, 1974.

[156] Antoni K Jakubowski. Effect of angle of incidence on the response of cylindrical electrostatic probes at supersonic speeds. *AIAA Journal*, 10(8):988–995, 1972.

[157] F. S. Mozer. Analyses of techniques for measuring DC and AC electric fields in the magnetosphere. *Space Science Reviews*, 14(2):272–313, February 1973. ISSN 0038-6308, 1572-9672. doi: 10.1007/BF02432099. URL `http://link.springer.com/10.1007/BF02432099`.

[158] Nagendra Singh, U Samir, KH Wright Jr, and NH Stone. A possible explanation of the electron temperature enhancement in the wake of a satellite. *Journal of Geophysical Research: Space Physics*, 92(A6):6100–6106, 1987.

[159] Brian Gilchrist and Leslie Curtis. Langmuir probe spacecraft potential end item specification document. 2001. URL `https://ntrs.nasa.gov/search.jsp?R=20010041079`.

[160] Binita Borgohain and H Bailung. Ion and electron sheath characteristics in a low density and low temperature plasma. *Physics of Plasmas*, 24(11):113512, 2017.

[161] WJ Miloch, J Trulsen, and HL Pécseli. Numerical studies of ion focusing behind macroscopic obstacles in a supersonic plasma flow. *Physical Review E*, 77(5): 056408, 2008.

[162] F Melandsø and J Goree. Polarized supersonic plasma flow simulation for charged bodies such as dust particles and spacecraft. *Physical Review E*, 52(5):5312, 1995.

[163] CL Henderson and U Samir. Observations of the disturbed region around an ionospheric spacecraft. *Planetary and Space Science*, 15(10):1499–1513, 1967.

[164] WJ Miloch, VV Yaroshenko, SV Vladimirov, HL Pécseli, and J Trulsen. Spacecraft charging in flowing plasmas; numerical simulations. In *Journal of Physics: Conference Series*, volume 370, page 012004. IOP Publishing, 2012.

[165] CD Child. Discharge from hot CaO. *Physical Review (Series I)*, 32(5):492, 1911.

[166] A Pedersen. Solar wind and magnetosphere plasma diagnostics by spacecraft electrostatic potential measurements. In *Annales Geophysicae*, volume 13, pages 118–129. Springer, 1995.

[167] U. Fahleson. Theory of electric field measurements conducted in the magnetosphere with electric probes. *Space Science Reviews*, 7(2-3):238–262, October 1967. ISSN 0038-6308, 1572-9672. doi: 10.1007/BF00215600. URL `http://link.springer.com/10.1007/BF00215600`.

[168] E. A. Bering, M. C. Kelley, F. S. Mozer, and U. V. Fahleson. Theory and operation of the split langmuir probe. *Planetary and Space Science*, 21(11): 1983–2001, November 1973. ISSN 0032-0633. doi: 10.1016/0032-0633(73)90128-1. URL `http://www.sciencedirect.com/science/article/pii/0032063373901281`.

[169] MATLAB. *9.7.0 (R2019b)*. The MathWorks Inc., Natick, Massachusetts, 2019.

[170] Uri Samir and Howard Jew. Comparison of theory with experiment for electron density distribution in the near wake of an ionospheric satellite. *Journal of Geophysical Research*, 77(34):6819–6827, 1972.

[171] Robert M Albarran and Aroh Barjatya. Plasma density analysis of cubesat wakes in the earth's ionosphere. *Journal of Spacecraft and Rockets*, pages 393–400, 2016.

[172] Mary Nehls, Jason Vaughn, Todd Schneider, Miria Finckenor, and Becky Farr. Did you know that marshall did that? space environmental effects. 2019.

[173] Jesse K McTernan, Omar J Leon, Sven G Bilén, John D Williams, Jason A Vaughn, Todd A Schneider, and Linda Habash Krause. Real-time density control of a plasma source used for simulating low-Earth-orbit plasma environment. *IEEE Transactions on Plasma Science*, 47(8):3891–3897, 2019.

[174] B Rubin, C Farnell, J Williams, J Vaughn, T Schneider, and D Ferguson. Magnetic filter type plasma source for ground-based simulation of low Earth orbit environment. *Plasma Sources Science and Technology*, 18(2):025015, 2009.

[175] RA Heelis and WB Hanson. Measurements of thermal ion drift velocity and temperature using planar sensors. *GEOPHYSICAL MONOGRAPH-AMERICAN GEOPHYSICAL UNION*, 102:61–72, 1998.

[176] Jesse K McTernan. personal communication.

[177] *Series 2400 SourceMeter SMU Instruments Datasheet*. Keithley: A Tektronix Company, 10 2018.

[178] Mark Crofton and Iain Boyd. The t6 hollow cathode: Measurements and modeling. In *34th AIAA Plasmadynamics and Lasers Conference*, page 4171, 2003.

[179] Dan M Goebel and Ira Katz. *Fundamentals of electric propulsion: ion and Hall thrusters*, volume 1. John Wiley & Sons, 2008.

[180] Christos E Papadopoulos and Hoi Yeung. Uncertainty estimation and Monte Carlo simulation method. *Flow Measurement and Instrumentation*, 12(4):291–298, 2001.

[181] Brian Dunbar. What are SmallSats and CubeSats? `https://www.nasa.gov/content/what-are-smallsats-and-cubesats`, .

[182] IP Shkarofsky. Accuracy of Langmuir probe measurements and skin potential on satellites. *Journal of Geophysical Research*, 76(16):3746–3754, 1971.

[183] Mark F Storz, Bruce R Bowman, Major James I Branson, Stephen J Casali, and W Kent Tobiska. High accuracy satellite drag model (HASDM). *Advances in Space Research*, 36(12):2497–2505, 2005.

[184] KS Jacobsen, A Pedersen, JI Moen, and TA Bekkeng. A new langmuir probe concept for rapid sampling of space plasma electron density. *Measurement Science and Technology*, 21(8):085902, 2010.

[185] D Johanning, W Seifert, and A Best. Analytical density correction for cylindrical Langmuir probes showing end effects. *Plasma physics and controlled fusion*, 27(2): 159, 1985.

[186] AR Hoskinson and Noah Hershkowitz. Effect of finite length on the current–voltage characteristic of a cylindrical Langmuir probe in a multidipole plasma chamber. *Plasma Sources Science and Technology*, 15(1):85, 2006.

[187] Sigvald Marholm and Richard Marchand. Finite-length effects on cylindrical Langmuir probes. *Physical Review Research*, 2(2):023016, 2020.

[188] Sigvald Marholm, Richard Marchand, Diako Darian, Wojciech J Miloch, and Mikael Mortensen. Impact of miniaturized fixed-bias multineedle Langmuir probes on cubesats. *IEEE Transactions on Plasma Science*, 47(8):3658–3666, 2019.

[189] Kenneth H Wright, Charles M Swenson, Donald C Thompson, Aroh Barjatya, Steven L Koontz, Todd A Schneider, Jason A Vaughn, Joseph I Minow, Paul D Craven, Victoria N Coffey, et al. Charging of the international space station as observed by the floating potential measurement unit: Initial results. *IEEE transactions on plasma science*, 36(5):2280–2293, 2008.

[190] Ogasawara Keiichi, Don E George, Jerry Goldstein, Hwang Kyoung-Joo, Nishimura Yukitoshi, David A Ruggles, and Jason L Stange. 3di: A novel ion composition and three-dimensional velocity analyzer for the topside ionosphere. *Scientific Reports (Nature Publisher Group)*, 10(1), 2020.

[191] MM Huddleston, CR Chappell, DC Delcourt, TE Moore, BL Giles, and MO Chandler. An examination of the process and magnitude of ionospheric plasma supply to the magnetosphere. *Journal of Geophysical Research: Space Physics*, 110 (A12), 2005.

[192] Keiichi Ogasawara. personal communication.

[193] Nikhil Shastri, Alexandria Western, Abhishek Cauligi, Roshan Radhakrishnan, Bret Bronner, Rupak Karnik, Siju Varughese, Brian GilChrist, Jesse McTernan, and Sven Bilén. Exploring the potential of miniature electrodynamic tethers and developments in the miniature tether electrodynamics experiment. 2014.

[194] Iverson C Bell III, Brian E Gilchrist, Jesse K McTernan, and Sven G Bilén. Investigating miniaturized electrodynamic tethers for picosatellites and femtosatellites. *Journal of Spacecraft and Rockets*, 54(1):55–66, 2017.

[195] JC Riviere. Contact potential difference measurements by the Kelvin method. *Proceedings of the Physical Society. Section B*, 70(7):676, 1957.

[196] Sven Gunnar Bilén. *Pulse propagation along conductors in low-density, cold plasmas as applied to electrodynamic tethers in the ionosphere*. PhD thesis, University of Michigan, 1998.

[197] Sven G Bilen and Brian E Gilchrist. Pulse propagation along electrodynamic tethers in the ionoshere. In *6th Spacecraft Charging Technology*, pages 181–186, 1998.

[198] JP McClure, WB Hanson, and JH Hoffman. Plasma bubbles and irregularities in the equatorial ionosphere. *Journal of Geophysical Research*, 82(19):2650–2656, 1977.

[199] Aroh Barjatya. Langmuir probe measurements in the ionosphere. *All Graduate Theses and Dissertations*, page 274, 2007.

[200] VA Davis, BM Gardner, and MJ Mandell. Nascap-2k version 4.3 users manual. Technical report, LEIDOS HOLDINGS INC SAN DIEGO CA SAN DIEGO United States, 2016.

[201] Myron J Mandell, Victoria A Davis, David L Cooke, Adrian T Wheelock, and Christopher J Roth. Nascap-2k spacecraft charging code overview. *IEEE Transactions on Plasma Science*, 34(5):2084–2093, 2006.

[202] VA Davis and MJ Mandell. Nascap-2k version 4.3 scientific documentation. Technical report, Leidos, Inc. San Diego United States, 2016.

[203] Lee W Parker. Plasma sheath effects and voltage distributions of large high-power satellite solar arrays. In *Spacecraft Charging Technology-1978*, volume 2071, page 341, 1979.

[204] Éric Coggiola and Amaury Soubeyran. Mesothermal plasma flow around a negatively wake side biased cylinder. *Journal of Geophysical Research: Space Physics*, 96(A5):7613–7621, 1991.

[205] Lee W Parker. Calculation of sheath and wake structure about a pillbox-shaped spacecraft in a flowing plasma. 1977.

[206] Fridrik Magnus and Jon Tomas Gudmundsson. Digital smoothing of the langmuir probe I-V characteristic. *Review of Scientific Instruments*, 79(7):073503, 2008.

[207] William H Press and Saul A Teukolsky. Savitzky-Golay smoothing filters. *Computers in Physics*, 4(6):669–672, 1990.

[208] Claude Elwood Shannon. Communication in the presence of noise. *Proceedings of the IRE*, 37(1):10–21, 1949.

[209] Harry Nyquist. Certain topics in telegraph transmission theory. *Transactions of the American Institute of Electrical Engineers*, 47(2):617–644, 1928.

[210] TL Thomas and EL Battle. Effects of contamination on langmuir probe measurements in glow discharge plasmas. *Journal of Applied Physics*, 41(8): 3428–3432, 1970.

[211] Francis F Chen. Langmuir probe analysis for high density plasmas. *Physics of Plasmas*, 8(6):3029–3041, 2001.

[212] Jonas Olson, Nils Brenning, J-E Wahlund, and H Gunell. On the interpretation of langmuir probe data inside a spacecraft sheath. *Review of Scientific Instruments*, 81 (10):105106, 2010.

[213] Robert L Merlino. Understanding Langmuir probe current-voltage characteristics. *American Journal of Physics*, 75(12):1078–1085, 2007.

[214] MB Hopkins and WG Graham. Langmuir probe technique for plasma parameter measurement in a medium density discharge. *Review of scientific instruments*, 57 (9):2210–2217, 1986.

[215] Mari Johan Druyvesteyn. Der niedervoltbogen. *Zeitschrift für Physik*, 64(11-12): 781–798, 1930.

[216] Isaac D Sudit and R Claude Woods. A study of the accuracy of various Langmuir probe theories. *Journal of applied physics*, 76(8):4488–4498, 1994.

[217] HK Fang and CZ Cheng. Retarding potential analyzer (RPA) for sounding rocket. *An Introduction to Space Instrumentation*, pages 139–153, 2013.

APPENDIX A

NASA/Air Force Spacecraft Charging Analyzer Program Modeling

In this discussion of *Nascap-2K*, the following topics are covered:

- The potential structure of a 3U CubeSat under various Debye lengths and ion drift energies.
- An overview of ion motion around a CubeSat biased negative of the plasma.
- Estimates of the current balance between a Langmuir probe and satellite for a restrictive area ratio.

A.1 NASA/Air Force Spacecraft Charging Analyzer Program Overview

Nascap-2K is a powerful tool, developed as a joint effort by the Air Force Research Laboratory (AFRL) at Hanscom Air Force Base (AFB) and by NASA's Space Environments and Effects (SEE) program, for simulating the interaction between a space plasma and a satellite . An overview is provided by *Mandell et. al.* [201] and the full manual is given by *Davis et. al.* [200].

The *Nascap-2K* user interface is divided into multiple tabs corresponding to various input parameters and configuration options, such as the properties of the ambient plasma environment and the type of numerical simulation (e.g. analytic equations, PIC, and hybrid PIC). In this section, each option used to model the spacecraft and the ambient plasma environment is detailed and discussed, concluding with a presentation of several results of interest. This section is divided as follows:

- The object and grid: The mesh and three-dimensional object that the plasma interacts with is described.
- Numerical calculations: A general study of the numerical methods is detailed.
- The plasma environment: The general plasma properties and external current sources (e.g. solar intensity) are chosen.

- Model options: This subsection covers the following *Nascap-2K* input parameters:
  - The types of problem being solved (e.g the potentials around the spacecraft being determined, time-dependent plasma behavior, etc.)
  - The potential structure around conductors (e.g. potentials resolved using non-linear schemes, in accordance to Debye shielding, self-consistent with particle trajectories, etc.)
  - Particle generation for both time-dependent and time-independent simulations.
- Results: Here multiple results are detailed as an overview of general behaviors observed during simulations, including:
  - Sheath size and shape variation with respect to spacecraft potential and Debye length
  - Wake filling effect of low energy ions
  - Spacecraft charging behavior

A.1.1 Object and Grid

Nascap-2K numerically computes the potentials and electric fields on surface elements and in space using the Boundary Element and Finite Element Methods (discussed in appendix A.1.2). The objects, defined using the *Object Toolkit* program, and the grids, defined using *GridTool* program, determine the geometry of the simulations within *Nascap-2K*. All *Nascap-2K* results focus on either the object or the grid; therefore, it is necessary to carefully delineate the requirements of both to understand specific simulation choices, such as grid resolution.

Beginning with objects, a full description of the *Nascap-2K* objects can be found between pages 15 and 19 of *Davis et. al.* [200]; a summary of the object and its requirements is given here. The *Object Toolkit* program is used to create finite-element representations of spacecraft surfaces, including object dimensions, element resolution, and material properties. Objects are defined by two characteristics: nodes, which are points in space, and surface elements, which are defined using the nodes as vertices. Each surface element is attributed to either a conductor (e.g. gold or aluminum) or an insulator (e.g. Kapton). The choice of material impacts surface charging, the surface elements' interaction with the ambient plasma, and photoelectron and secondary electron emission. Furthermore, each element is either a triangle or quadrilateral with an aspect ratio (length/width) no greater than 2, whose dimensions are within a factor of 2 of the local grid's resolution. Individual surface element area should be at most a few percent from the total object size, but coarser resolutions are allowed for flat, conductive areas. In the interest of computational speed, and to remain within the upper limit of 4095 total elements for an object, the individual surface element is roughly $10\,\%$ of the total object size while maintaining a dimension no greater than two Debye lengths.

Figure A.1 provides an example object used in these simulations depicting a 3U CubeSat, a boom structure, and a guarded Langmuir probe. Each surface element of an

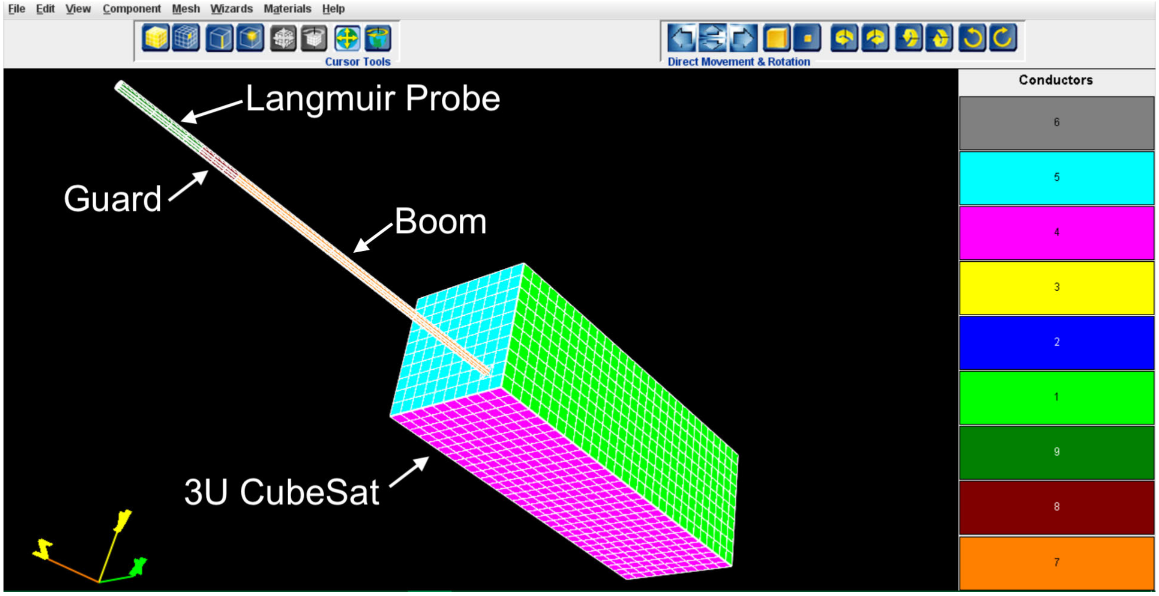

Figure A.1: Example of simulated 3U CubeSat, guarded Langmuir probe, and boom structure.

object has two important attributes: material property and ”conductor number”, which ranges from 1 to 100. Additionally, the conductor number 1 has the special designation of being considered spacecraft common. The individual faces of the CubeSat structure will always have the same conductor number assigned at their initial creation which will correspond to the coordinate direction normal to the plane of each face (listed on the right side of fig. A.1). Odd-numbered conductor numbers are always initially facing in the ”positive” coordinate direction (e.g. +x, +y, +z), and even-numbered conductor numbers correspond to faces whose normal vector is in the ”negative” coordinate direction. The CubeSat material is always fully conductive, either aluminum or gold. When the LP and boom structures are attached to the CubeSat, the smallest available conductor number is assigned to the boom structure and the conductor number is incremented for the guard, and then once more for the Langmuir probe. For example, in fig. A.1, the boom has a conductor number of 7, the guard’s conductor number is 8, and the LP’s conductor number is 9. The boom structure is always attributed an insulating material, Kapton, and the guard and Langmuir probe are always attributed conductive materials, typically gold.

Regarding *Nascap-2K*’s *GridTool* program, a full description is found between pages 19 and 24 of *Davis et. al.* [200]; a summary of the grid and its requirements is given here. The *GridTool* program is used to define an arbitrarily nested grid structure about the object (example shown in fig. A.2). A grid is necessary to simulate potentials in space, track particles, and compute wake structure. To properly resolve these plasma structures, the grid resolution in the ”sheath region” should be as few Debye lengths as possible, with no more than 2 Debye lengths being ideal. Understandably, creating a single grid that is two Debye lengths long for the entire simulation can lead to situations where the computation times are unnecessarily long as computational resources are being expended on the quasi-neutral region of the plasma. To resolve this issue, the *GridTool* program allows for nested grids by using a parent-child system where the outer most parent grid, called the primary grid, encloses the full simulation space, and is far enough from the object that a quasi-neutral plasma exists between the object's sheath structure and the simulation space's boundary. Child grids are nested within their respective parent grid, with a grid resolution that is a factor of 2 finer than their parent grid. Additionally, at the boundary between a parent and child, the resolution of the parent grid is always taken. Therefore, the outermost boundary of the child grid should not overlap with the outermost boundary of their parent to avoid sudden changes in resolution. This is especially true if the child's parent grid is itself a child of a larger parent grid. In fig. A.2, the primary grid is the coarsest grid and all subsequent grids are nested grids. The right-most side of the figure shows a collapsible list of nested grids. In this example, grid 4 is a child of grid 3, and grid 1 is the primary grid.

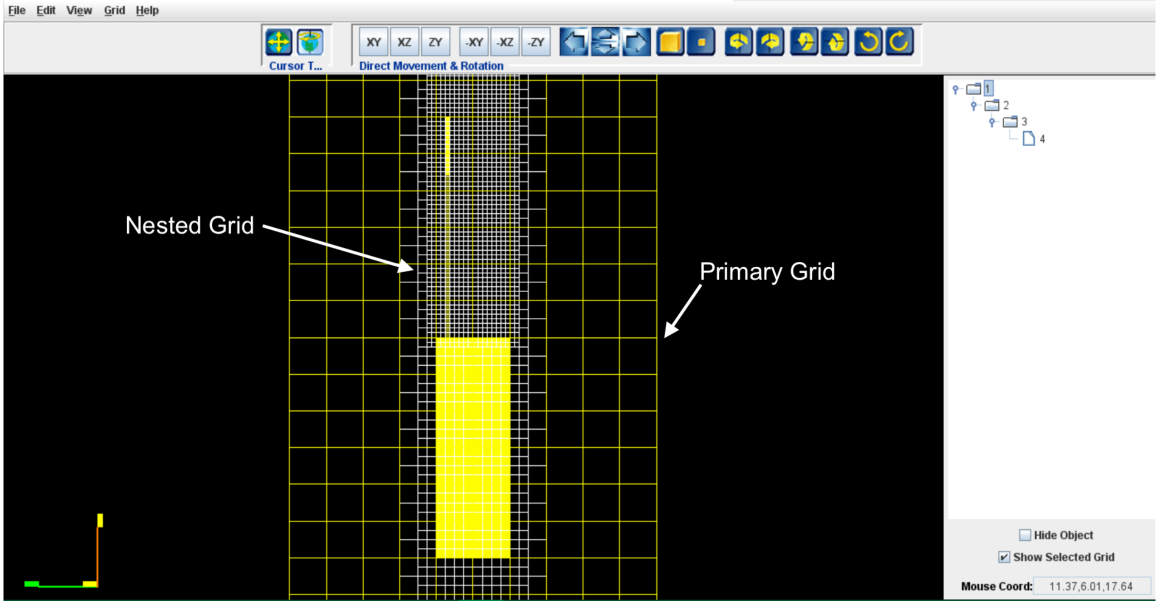

☐ Hide Object
☑ Show Selected Grid
Mouse Coord: 11.37,6.01,17.64

Figure A.2: Nested grid example surrounding an object composed of a CubeSat and Langmuir probe.

A.1.2 General Numerical Calculations

Nascap-2K is capable of solving for multiple types of physical effects including currents to a surface, electric fields and potentials surrounding a spacecraft, and determining spacecraft charging behavior in the presence of photoelectrons, secondary electrons, and similar current sources. An in-detail description of the calculations is provided by *Davis et. al.* [202]. In this subsection a general overview is presented for how *Nascap-2K*: 1) calculates currents to a surface; 2) performs boundary element analysis; and 3) uses finite element methods to compute potentials in space.

A.1.2.1 Currents to a Surface

When studying surface charging using analytic currents, the current density to a surface at a potential, ϕ, is given by

$$j = q\int_{L}^{\infty}\left(\frac{E}{E\pm\phi}\right)F\left(E\pm\phi\right)dE$$

where q is the charge of the particle, e is the charge of an electron, E is the energy at the collector's surface, L is 0 for repelled species and $|\phi|$ for attracted species, and $F\left(E\right)$ is the flux at infinity. In the case of $E\pm\phi$, the upper sign is for ions and the lower sign is for electrons. In this work, analytic methods were used, but not highlighted, to validate the current-voltage curves produced by tracking particles to a surface when employing PIC methods.

As expected, $F\left(E\right)$ is dependent on the model selected to describe the ions and electrons. In the situation of a moving satellite, the charged particle flux model is described using a convected Maxwellian,

$$F\left(E,\chi\right) = \sqrt{\frac{e}{2\pi mT}}\frac{E}{T}n\exp\left(-\frac{E+\frac{mU^2}{2}-\sqrt{\frac{Em}{2}}U\cos\chi}{T}\right)$$

where U is the plasma velocity from the object reference frame, n is the number density, and χ is the angle between the flow vector and the incident velocity. Since the convected Maxwellian requires integration over all possible angles and velocities, the full integral for the current density is then given by

$$\begin{aligned}
j &= A\left[\int_{L}^{\infty}dv_{\infty}v_{\infty}\left(v_{\infty}^{2}\mp\frac{2e\phi}{m}\right)\exp\left(-\frac{m}{2eT}v_{\infty}^{2}\right)\int_{0}^{\frac{\pi}{2}}d\theta\right.\\
&\quad\left.\exp\left(\frac{m}{eT}v_{\infty}U\cos\theta_{\infty}\cos\theta_{u}\right)I_{0}\left(\frac{m}{eT}v_{\infty}U\sin\theta_{\infty}\sin\theta_{u}\right)\sin\theta\cos\theta\right] \qquad \text{(A.1)}\\
I_{0}\left(x\right) &= \frac{1}{2\pi}\int_{0}^{2\pi}d\psi\exp\left(-x\cos\psi\right)\\
A &= qn\sqrt{\frac{eT}{2\pi m}}\exp\left(-\frac{m}{2eT}U^{2}\right)\left(\frac{m}{eT}\right)^{2}
\end{aligned}$$

where $I_0\left(x\right)$ is a zeroth order modified Bessel function of the first kind; θ_{∞} is the polar angle of the incident velocity at infinity, $\vec{v}_{\infty}$; and θ_u is the polar angle of the flow velocity [202, pg. 34].

A.1.2.2 Charging Using the Boundary Element Method

To calculate the electric fields on the surface of an object, *Nascap-2K* employs the Boundary Element Method (BEM). Improved estimates of the electric field, in both steady state and transient conditions, allow for more accurate numerical computation of a spacecraft's charging behavior. Ultimately, BEM relates electric fields on the exterior of the spacecraft to the charged surface of the spacecraft itself. The spacecraft is described by surface elements (a summary of object surface elements given in appendix A.1.1) and each surface element, j, has a constant charge density, σ_j. The relation between the potential and electric field of a point charge is then

$$\begin{aligned}\phi &= \frac{q}{4\pi\epsilon_0 r} \rightarrow 4\pi\epsilon_0\phi_i = \sum_j \int d^2\vec{r}_j \frac{\sigma_j}{|\vec{r}_{ij}|} \\ \vec{E} &= \frac{q}{4\pi\epsilon_0 r^2} \rightarrow 4\pi\epsilon_0\vec{E}_i = \sum_j \int d^2\vec{r}_j \frac{\sigma_j}{|\vec{r}_{ij}|^3}\left(\vec{r}_i - \vec{r}_j\right)\end{aligned}$$

where ϕ_i and $\vec{E}_i$ correspond to the potential and electric field, respectively, of the center of a surface element. The matrix representation of the potentials, electric fields, and charge densities are related in the following manner:

$$\begin{aligned}\phi_i &= \left[C^{-1}\right]_{ij}\sigma_j \\ \left(\vec{E}\cdot\vec{n}\right)_i &= F_{ij}\sigma_j \\ \left(\vec{E}\cdot\vec{n}\right)_i &= F_{ik}C_{kj}\phi_j\end{aligned}$$

where C and F are the matrix representations of the integral sums shown above.

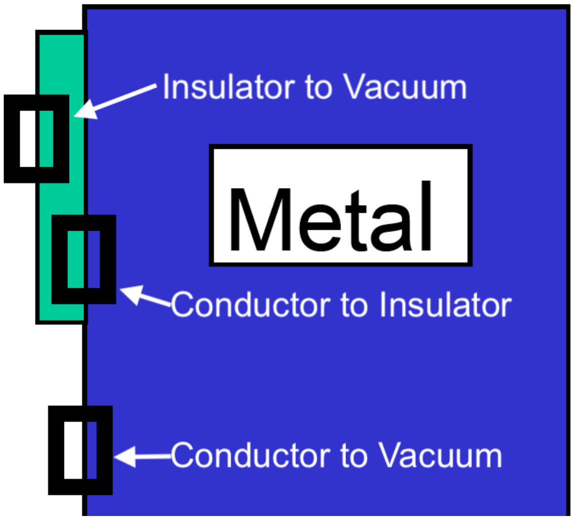

Figure A.3: Gaussian pillboxes to calculate surface charges on insulators (in green) and on conductors (in blue). Image adapted from *Davis et. al.*[202, p.43]

While BEM provides the external electric fields normal to each surface element, it does not account for internal fields between a surface insulator and its underlying conductor (see fig. A.3). Such cases are frequently encountered for *Nascap-2K* objects, which can be composed of both conducting and insulating surfaces. To account for surface element charge attributed to both external and internal fields, the total charge on an insulating surface element is given by

$$q_i = A_i \left(\vec{E} \cdot \vec{n}\right)_i + C_{ic} \left(\phi_i - \phi_c\right)$$

where A_i is the surface area, C_{ic} is the capacitance between the insulator and conductor, and ϕ_c is the potential of the conductor. For conductors, only the total charge, Q_c, needs to be known due to the mobility of charges, which is given by

$$Q_c = \sum_{bare} A_i \left(\vec{E} \cdot \vec{n}\right)_i - \sum_{insulator} C_{ic} \left(\phi_i - \phi_c\right).$$

When calculating Q_c a distinction is made between bare conductors (conductors exposed to the plasma), and insulated conductors (conductors coated in insulation). The charge on an object can now, again, be represented using matrices such that

$$\begin{aligned} Q &= \{q_1, q_2, \ldots, q_n, Q_c\} \\ \Phi &= \{\phi_1, \phi_2, \ldots, \phi_n, \phi_c\} \\ Q &= G\Phi \end{aligned}$$

where G is a charging matrix relating the surface element charge and surface element potential. *Nascap-2K* computes currents to surface elements through either analytic expressions or PIC methods, and so with an expression for the charge of the object, the currents to the surface elements are related to the potentials such that

$$\begin{gathered} I = \dot{Q} = G\dot{\Phi} \\ \left[G - \dot{I}\right] \Phi\left(t\right) = \left[G - \dot{I}\right] \Phi\left(0\right) + I\left(0\right) t \end{gathered}$$

While the exact derivations and treatments are found in pages 39 and 47 of the *Nascap-2K Scientific Documentation* [202], charging rate issues attributed to the BEM calculations do not affect steady state potentials, which are the focus of the simulations performed for this thesis.

A.1.2.3 Calculated Potentials in Space Using Finite Element Methods

To calculate the potential at any point in the simulated space, *Nascap-2K* requires an object and a grid (detailed in appendix A.1.1) where a finite element approach is applied at every element of the grid with interpolants along the edges. An example of calculated space potentials is shown in fig. A.4. The quasi-neutral plasma is shown in orange, the potential structure of a positively biased LP is shown in green and beige, and the potential structure of negatively biased CubeSat is in black and purple.

Nascap-2K solves Poisson's equation through its associated variational principle,

$$\frac{\partial}{\partial \phi}\left(\int dV \left[\frac{1}{2}\left(\nabla\phi\right)^2 + \frac{\rho\phi}{\epsilon_0}\right] + \int \phi\nabla\phi \cdot d\vec{S}\right) = 0,$$

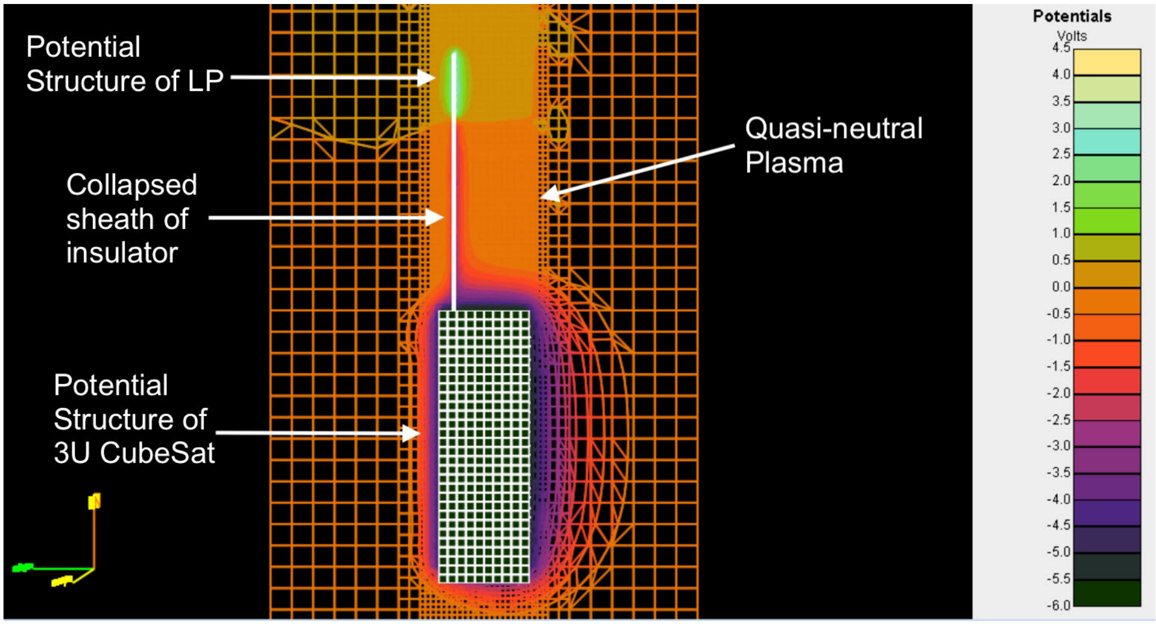

Figure A.4: Potential structure of quasi-neutral plasma and biased structures within simulation space.

where each term corresponds to the Laplacian operator, the space charge contribution, and the surface charge contribution, respectively. Poisson's equation is always solved with fixed surface potentials. Furthermore, the potential and electric field are defined at each grid node where the potential inside each grid volume element is interpolated from the value of each of its vertices. The interpolation scheme allows for only continuous electric fields, ensuring proper electric fields for computing particle trajectories. Each node in a grid is assigned 4 interpolation functions corresponding to the potential and a 3-axis potential gradient. A detailed description of how each term of the integral is numerically computed and interpolated is provided in pages 51 and 53 of the scientific documentation [202].

For grid spaces that contain surface elements of the object, the approach for interpolating the potentials and electric fields depends on the type of grid element. The elements of interest are bounded by three types of surfaces: 1) square surfaces bounded by grid edges and shared with adjacent, empty elements; 2) object surfaces; and 3) surfaces bounded by both object nodes, or edges, and grid points, or edges. On type 1 surfaces, the interpolation scheme does not change from the interpolation between empty grid elements since the boundary is between two grids. For type 2 boundaries, the object's surface element potentials and electric fields describe the potential and electric field in the space immediately surrounding the object. Finally, for type 3 surfaces, the electric field and potential must be interpolated using a combination of techniques from type 1 and 2 surfaces, and is described on page 54 of the scientific documentation [202].

When solving Poisson's equation, the ratio between Debye length and the grid spacing, Λ, is critical for determining the stability of the calculations. *Nascap-2K* uses a two-pronged scheme to help improve the stability of the calculations. The first method uses partial implicitization of the repelled density, which was determined to be a more stable numerical algorithm than explicit forms. The second method limits the charge in a node depending on Λ. When $\Lambda \geq 1$, no charge limiting occurs since the potential within a volume element of the plasma is altered by no more than the plasma temperature. However, for $\Lambda << 1$, several Debye lengths can be needed to fill the space of one volume element, amplifying numerical noise and plasma features such as sheath thickness. In such situations, the charge is limited to a reduced value such that potential variations are more appropriate to the spatial resolution of the grid. In practice, when a simulation is created where a boundary potential is screened within the code's lower limit of resolution, one to two grid elements, *Nascap-2K* redistributes the sheath charge to allow the potential to be screened over enough elements for stable computation. Further discussion on the charge density model used in the potential solver for the simulation problems of interest can be found in section A.1.4.3.

A.1.3 The Plasma Environment

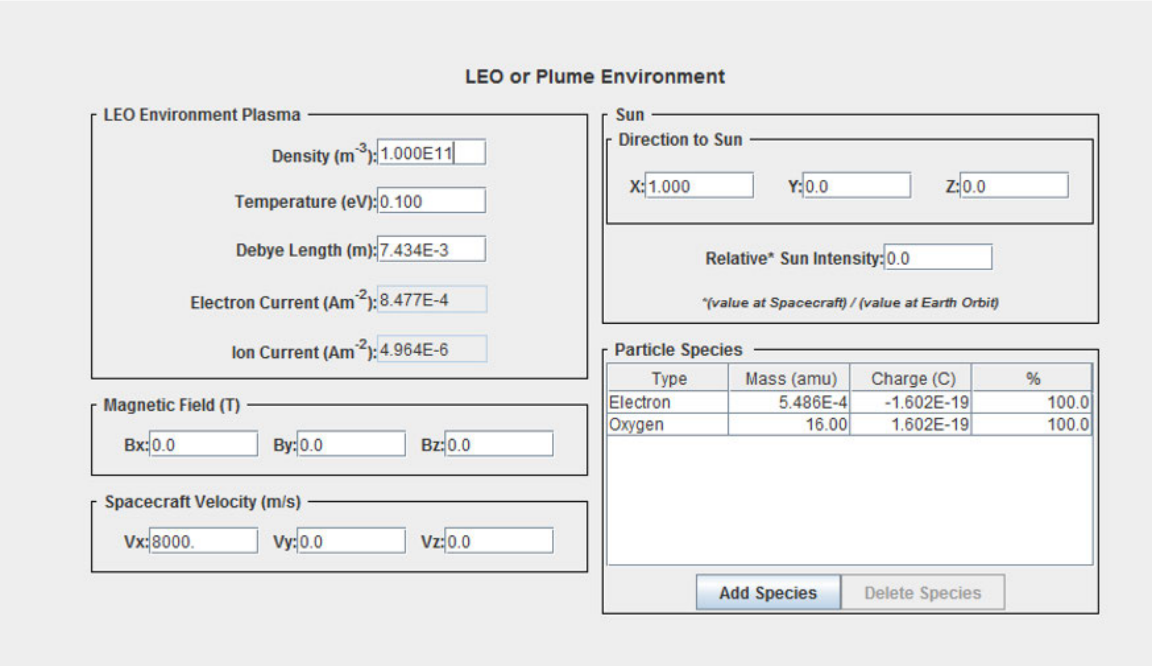

LEO or Plume Environment

LEO Environment Plasma

Density (m^{-3}): 1.000E11

Temperature (eV): 0.100

Debye Length (m): 7.434E-3

Electron Current (Am^{-2}): 8.477E-4

Ion Current (Am^{-2}): 4.964E-6

Magnetic Field (T)

Bx: 0.0 By: 0.0 Bz: 0.0

Spacecraft Velocity (m/s)

Vx: 8000. Vy: 0.0 Vz: 0.0

Sun

Direction to Sun

X: 1.000 Y: 0.0 Z: 0.0

Relative* Sun Intensity: 0.0

*(value at Spacecraft) / (value at Earth Orbit)

Particle Species

Type	Mass (amu)	Charge (C)	%
Electron	5.486E-4	-1.602E-19	100.0
Oxygen	16.00	1.602E-19	100.0

Figure A.5: General plasma properties are inputted in the LEO environment tab.

The *Nascap-2K* environment tab changes depending on the plasma environment. *Nascap-2K* is programmed to handle the plasma environments found in LEO, a plasma plume, geosynchronous orbits, an auroral environment, and the interplanetary environment. For the results presented in this section, the LEO option was always chosen as the representative plasma environment. Figure A.5 displays the environments tab for LEO. To simulate a satellite in LEO, the spacecraft velocity was always chosen such that the ion drift energy was roughly $5\,\mathrm{eV}$. Additionally, the relative solar intensity was always set to 0 to eliminate the effects of photoelectrons, and the magnetic field strength was also $0\,\mathrm{T}$ to eliminate the effects of magnetic drift for electrons. While these physical phenomena can exist in LEO, they are ignored in these simulations to focus on the relationship between spacecraft charging and area ratio, as well as, spacecraft current collection and each of the following properties: plasma density and electron temperature, ion drift energy, and conductor orientation relative to the plasma flow. Electron temperatures were within $0.1\,\mathrm{eV}$ to $0.35\,\mathrm{eV}$, with the ion temperature being equal to the electron temperature. Finally, as discussed in, section $2.1.1$, the plasma density in the F-region of the Earth's ionosphere ranges from roughly $1 \times 10^{10}\,\mathrm{m}^{-3}$ to $0.5 \times 10^{12}\,\mathrm{m}^{-3}$. However, to properly model the spacecraft and LP for the larger area ratios of interest, their individual dimensions were sometimes increased by a factor of 10. As a result, the Debye length also had to be increased by a factor of 10, and so, for enlarged CubeSats, the plasma density was modeled to be a factor of 100 less than what has been measured in orbit (approximately $1 \times 10^{8}\,\mathrm{m}^{-3}$ to $0.5 \times 10^{10}\,\mathrm{m}^{-3}$). Simple simulations of a 3U CubeSat structure at the standard size ($0.1\,\mathrm{m}\times0.1\,\mathrm{m}\times0.3\,\mathrm{m}$), with the appropriate plasma density, and the enlarged 3U CubeSat ($1\,\mathrm{m}\times1\,\mathrm{m}\times3\,\mathrm{m}$), with a reduced plasma density, collect identical thermal currents and have nearly identical current collection behavior for a biased structure.

A.1.4 Modeling Options

The benefit of *Nascap-2K* as a simulation tool is its capacity to numerically calculate plasma-spacecraft interactions through a variety of analytic models and PIC algorithms. To properly present the available options that *Nascap-2K* can handle, this subsection is divided into *Nascap-2K*'s individual tabs, presented in the following order: problem, applied potentials, space potentials, and particles.

A.1.4.1 Problem Tab

The problem tab (example shown in fig. A.6) is key in determining the type of analysis performed, referred to as the problem type (e.g. potentials in space, surface charging, time dependent plasma); specifying the plasma environment; and loading the aforementioned object and grid into the *Nascap-2K* program. While many options are available for a LEO environment, not all simulation options are exercised to solve the central questions of this dissertation. *Nascap-2K* is primarily used to estimate spacecraft charging behavior while an LP is swept across a range of potentials referenced against the satellite. However, to understand the estimated spacecraft charging behavior, the individual current collection of the CubeSat and LP, as well as the potential structure of the CubeSat, also needs to be modeled.

To understand the potential surrounding the CubeSat, the ”Potentials in Space” problem type is chosen with analytic space charge. Further discussion is highlighted in section A.1.4.3, but ultimately, this option calculates the electric potential surrounding the object using analytic charge density models. Current collection to the CubeSat structure or LP are studied using the ”surface currents” problem type where currents collected by the surface elements are computed using tracked particles. Finally, the current balance between the LP and the spacecraft is numerically solved using the time-dependent plasma option where the surface potentials are self-consistent with tracked particle currents, or the

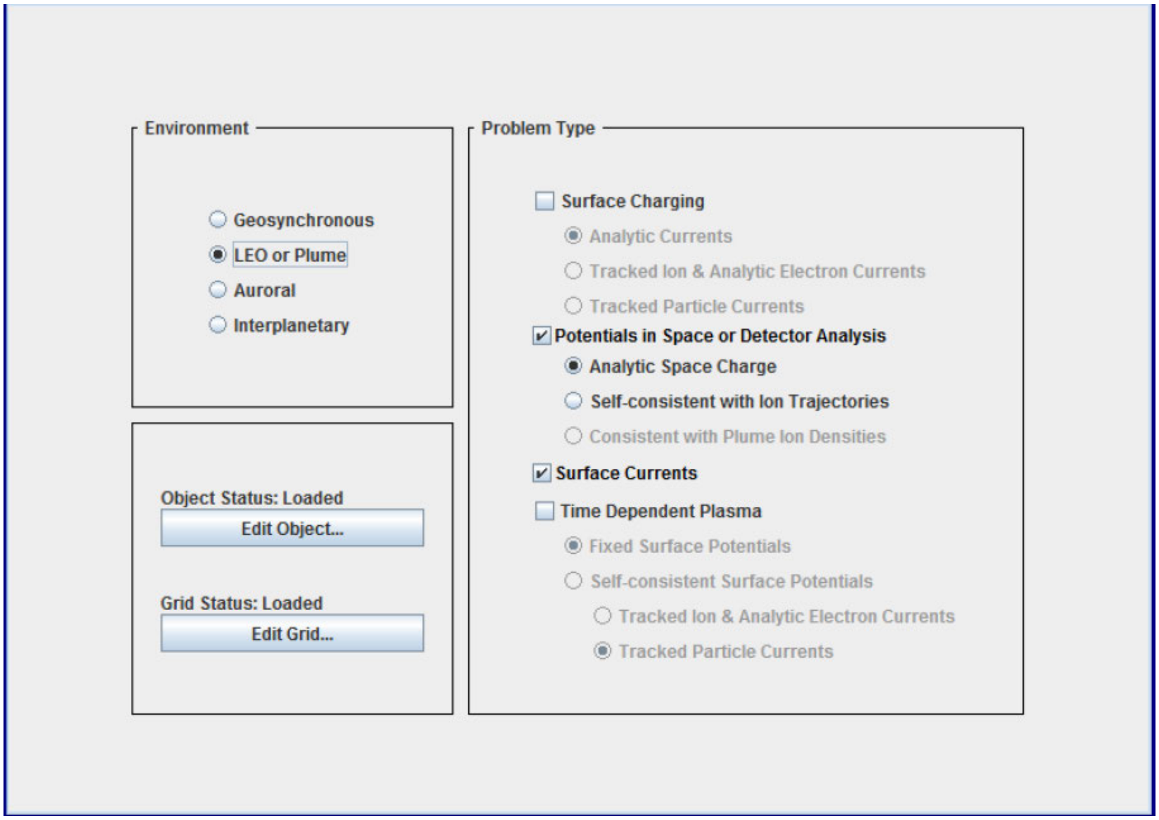

Environment

- ○ Geosynchronous
- ● LEO or Plume
- ○ Auroral
- ○ Interplanetary

Object Status: Loaded

Grid Status: Loaded

Problem Type

- ☐ Surface Charging
  - ● Analytic Currents
  - ○ Tracked Ion & Analytic Electron Currents
  - ○ Tracked Particle Currents
- ☑ Potentials in Space or Detector Analysis
  - ● Analytic Space Charge
  - ○ Self-consistent with Ion Trajectories
  - ○ Consistent with Plume Ion Densities
- ☑ Surface Currents
- ☐ Time Dependent Plasma
  - ● Fixed Surface Potentials
  - ○ Self-consistent Surface Potentials
    - ○ Tracked Ion & Analytic Electron Currents
    - ● Tracked Particle Currents

Figure A.6: Problem tab of *Nascap-2K* that determines which properties are calculated. Image adapted from *Davis et. al.* [200, p.14].

surface charging option with tracked particle currents. The charging behavior for either case generally agreed with one another and typically differed by at most a few tenths of a volt.

A.1.4.2 Applied Potentials Tab

Regardless of the type of problem being considered, the surface potentials, and how the surface potentials change with respect to the plasma, must be specified in *Nascap-2K*'s applied potentials tab (example shown in fig. A.7). The top half of the applied potentials tab deals specifically with conducting surfaces. For each conductor number there are three options: 1) floating potential, where the potential can freely vary based on plasma-spacecraft interactions; 2) fixed potential; and 3) fixed bias relative to spacecraft common. To study the current collection of a CubeSat, all faces of the satellite were equipotential, and a script was written to ”sweep” the CubeSat potential relative to the ambient plasma at fixed potentials from $-10\,\mathrm{V}$ to $10\,\mathrm{V}$. The lower half of the tab is related to insulated materials, where the conductor number related to the LP boom structure can be fixed to $0\,\mathrm{V}$. When validating Langmuir probe current as a function of potential relative to the plasma, the boom structure was designated as an insulator, and the LP and guard were ”swept” from $-10\,\mathrm{V}$ to $10\,\mathrm{V}$. Finally, for current balance modeling using PIC simulations, spacecraft common is allowed to float, the remaining sides of the CubeSat are equipotential to spacecraft common, and the LP and guard are biased relative to spacecraft common (again, swept from $-10\,\mathrm{V}$ to $10\,\mathrm{V}$).

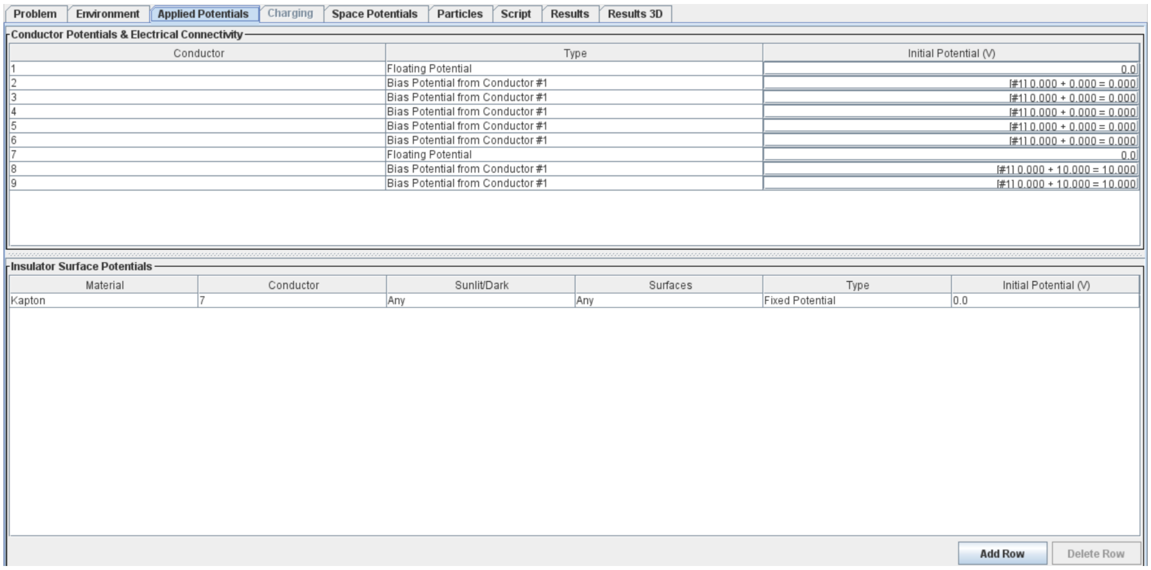

Conductor Potentials & Electrical Connectivity

Conductor	Type	Initial Potential (V)
1	Floating Potential	0.0
2	Bias Potential from Conductor #1	[#1] 0.000 + 0.000 = 0.000
3	Bias Potential from Conductor #1	[#1] 0.000 + 0.000 = 0.000
4	Bias Potential from Conductor #1	[#1] 0.000 + 0.000 = 0.000
5	Bias Potential from Conductor #1	[#1] 0.000 + 0.000 = 0.000
6	Bias Potential from Conductor #1	[#1] 0.000 + 0.000 = 0.000
7	Floating Potential	0.0
8	Bias Potential from Conductor #1	[#1] 0.000 + 10.000 = 10.000
9	Bias Potential from Conductor #1	[#1] 0.000 + 10.000 = 10.000

Insulator Surface Potentials

Material	Conductor	Sunlit/Dark	Surfaces	Type	Initial Potential (V)
Kapton	7	Any	Any	Fixed Potential	0.0

Figure A.7: Applied potentials tab of *Nascap-2K* that determines the initial surface potentials of the object.

A.1.4.3 Space Potentials Tab

As described in section A.1.2.3, *Nascap-2K* numerically calculates for the potential surrounding the object by solving Poisson's equation. Space charge is computed by either particle tracking, using analytical expressions, or in a hybrid manner. For these specific simulations, *Nascap-2K*'s predefined non-linear charge density model was used, as it is appropriate for LEO. As detailed in *Davis et. al.* [202, p. 18], the non-linear charge model is given as

$$\frac{\rho}{\epsilon_0} = -g\frac{\phi}{\lambda_D^2}\left[\frac{\max\left(1, C\left(\phi, \left|\vec{E}\right|\right)\right)}{1+\sqrt{4\pi}\left|\frac{\phi}{T}\right|^{\frac{3}{2}}}\right]$$

where g is a plasma density reduction factor that ranges between 0 and 1; T is the temperature in eV; $\vec{E}$ is the electric field; and $C\left(\psi, \left|\vec{E}\right|\right)$ is a convergence model developed by solving the Langmuir-Blodgett problem, given by

$$\begin{aligned} C\left(\phi, \left|\vec{E}\right|\right) &= \min\left(\left(\frac{R_{sh}}{r}\right)^2, 3.545\left|\frac{\phi}{T}\right|^{\frac{3}{2}}\right) \\ \left(\frac{R_{sh}}{r}\right)^2 &= 2.29\left(\frac{\left|\vec{E}\right|\lambda_D}{T}\right)^{1.262}\left|\frac{\phi}{T}\right|^{-0.509} \end{aligned} \tag{A.2}$$

This scheme interpolates between Debye screening at low potentials and an accelerated particle distribution. Furthermore, because the spacecraft potentials are adequately screened by the plasma, due to relatively small potentials and a large primary grid, the boundary potential is 0 V at the boundary of the simulation space.

A.1.4.4 Particles Tab

Nascap-2K can generate macroparticles to represent electrons and ions in the simulation space. This allows users to study particle trajectories, calculate surface currents, and study spacecraft charging. Particle creation options are available in the particles tab and there are two subtabs of interest for this work: surface currents and time-dependent.

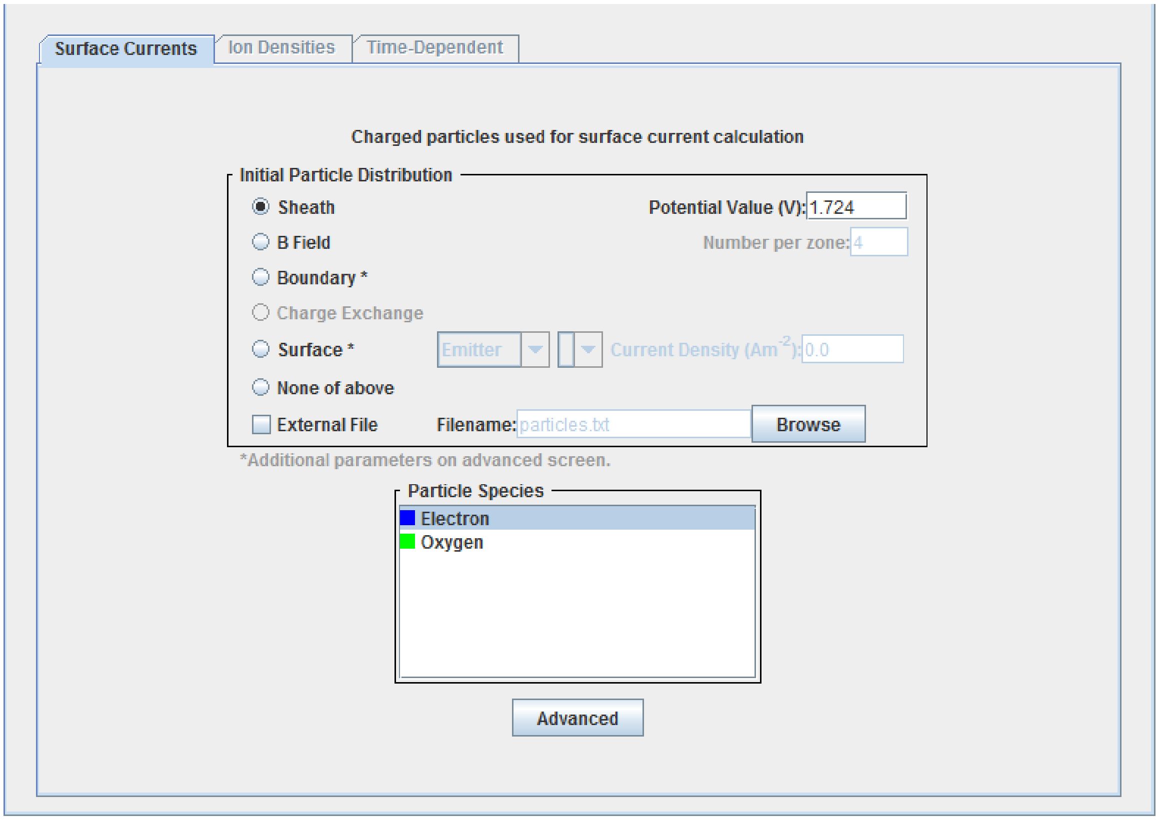

● Sheath

○ B Field

○ Boundary *

○ Charge Exchange

○ Surface * Emitter Current Density (Am^{-2}): 0.0

○ None of above

☐ External File Filename: particles.txt

Potential Value (V): 1.724

Number per zone: 4

Particle Species:
- 🟦 Electron
- 🟩 Oxygen

Figure A.8: Surface current subtab of the particles tab. Image adapted from *Davis et. al.* [200, p.50].

As shown in fig. A.8, the surface currents subtab generates particles at different regions of the simulation space. For these simulations the boundary generation method was chosen. When boundary generation is chosen, the outer surface of each primary grid boundary element is divided into squares and particles are generated in their centers. The macroparticles created in these squares represent current passing through the area. The macroparticles can be created to sample different regions of a Maxwellian distribution (see dialog box in fig. A.9). While there are many options available in the advanced particle parameters dialog box, we are interested mainly in 3 input sections: 1) the fraction

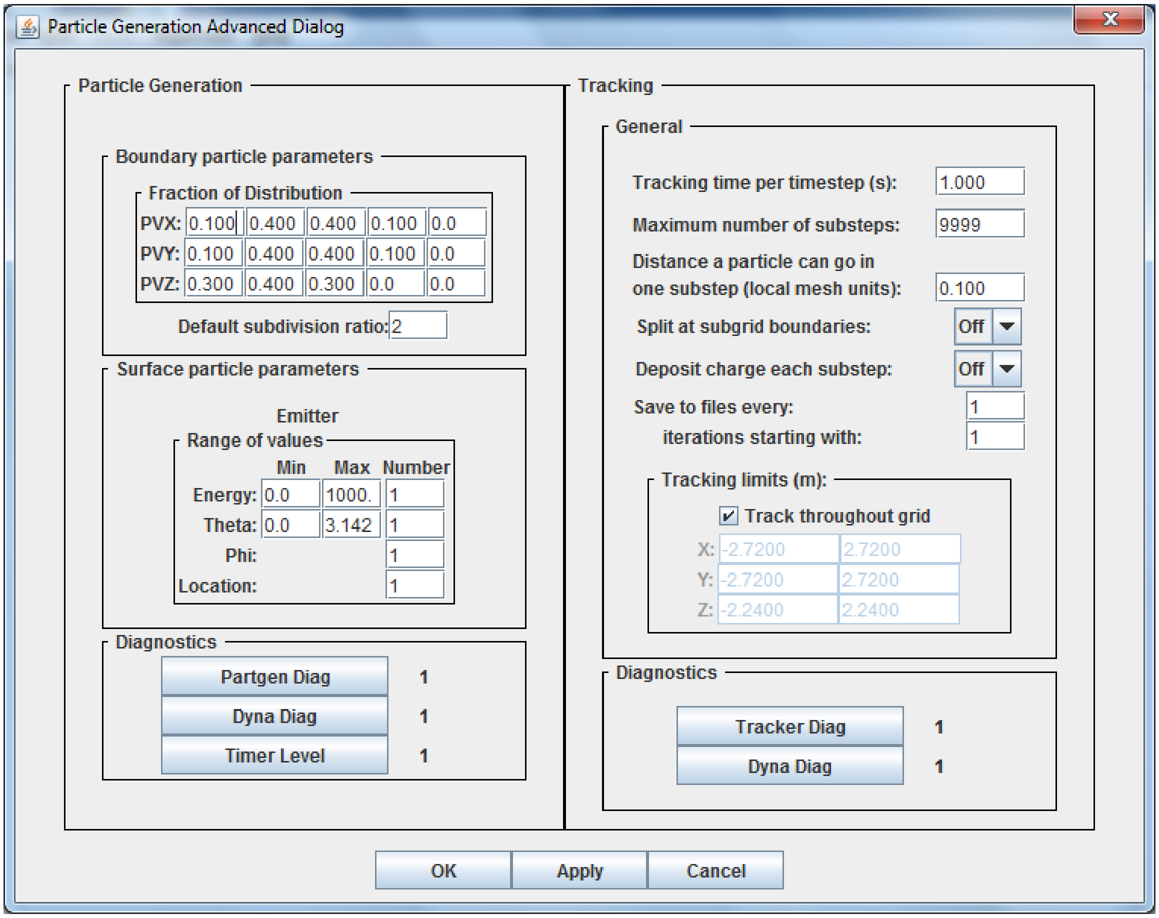

PVX:	0.100	0.400	0.400	0.100	0.0
PVY:	0.100	0.400	0.400	0.100	0.0
PVZ:	0.300	0.400	0.300	0.0	0.0

Default subdivision ratio: 2

	Min	Max	Number
Energy:	0.0	1000.	1
Theta:	0.0	3.142	1
Phi:			1
Location:			1

Partgen Diag 1
Dyna Diag 1
Timer Level 1

Tracking time per timestep (s): 1.000
Maximum number of substeps: 9999
Distance a particle can go in one substep (local mesh units): 0.100
Split at subgrid boundaries: Off
Deposit charge each substep: Off
Save to files every: 1
iterations starting with: 1

☑ Track throughout grid

X: -2.7200 2.7200
Y: -2.7200 2.7200
Z: -2.2400 2.2400

Tracker Diag 1
Dyna Diag 1

Figure A.9: Particle generation advanced options window. Image adapted from *Davis et. al.* [200, p.59].

of distribution, 2) the subdivision rate, and 3) the particle splitting option. The fraction of distribution section specifies how the Maxwellian velocity distribution in each axis is to be divided. The Maxwellian is divided into 5 sections: a negative tail, a negative bulk, a positive bulk, a positive tail, and a high-energy tail. For these simulations, the distribution is sampled as follows: $10\,\%$ of the distribution is on the negative tail, $40\,\%$ of the distribution constituting the bulk of the negative velocity particles, $40\,\%$ of the distribution constituting the bulk of the positive velocity particles, and finally $10\,\%$ of the distribution is on the positive tail. The high-energy tail is not included. The particle splitting option governs the density of particles created along grid boundaries. Typically, the default subdivision rate of 2 is kept, but for some calculations subdivision rates of 4 and 8 were chosen for more exact current estimates. Finally, the particle splitting option will split the particles at the boundaries between a parent and child. This option is only exercised if the particle that is split carries more charge than a similar particle created in the subgrid, and if its temperature is greater than $0.05\,\mathrm{eV}$. Particle splitting is used sparingly in these simulations. The surface current particle generation option is used to study the current collection to individual CubeSat and Langmuir probe objects to understand ram/wake currents, the impact of orientation on current collection, to understand how current collection changes when the ion population is composed of two species, and during current balance simulations.

When a time-dependent problem is being performed, macroparticles can be generated at the boundary, or through the entire simulation space, as shown in fig. A.10. When the boundary injection option is chosen, the macroparticles are generated at the primary grid boundary exactly as described above. However, instead of the macroparticles representing current through the surface, the macroparticles represent charge passing through the boundary during a user-specified time. The charge is equal to the plasma thermal current multiplied by the time interval that is user-defined. If instead the initial uniform distribution is chosen, the macroparticles are created throughout the simulation space at points appropriate for the system's weighting functions. If the splitting option is chosen, each macroparticle is split into eight particles in the plasma's frame of reference to maintain the proper momentum and energy distribution. Time-dependent calculations, using both the boundary injection and uniform distribution together, were performed to balance the current between the LP and spacecraft, and estimate the steady-state spacecraft potential as a function of applied bias to the LP. Finally, during current balance when using either the time-dependent or surface charging options, time steps of no more than 2 μs were used per applied bias.

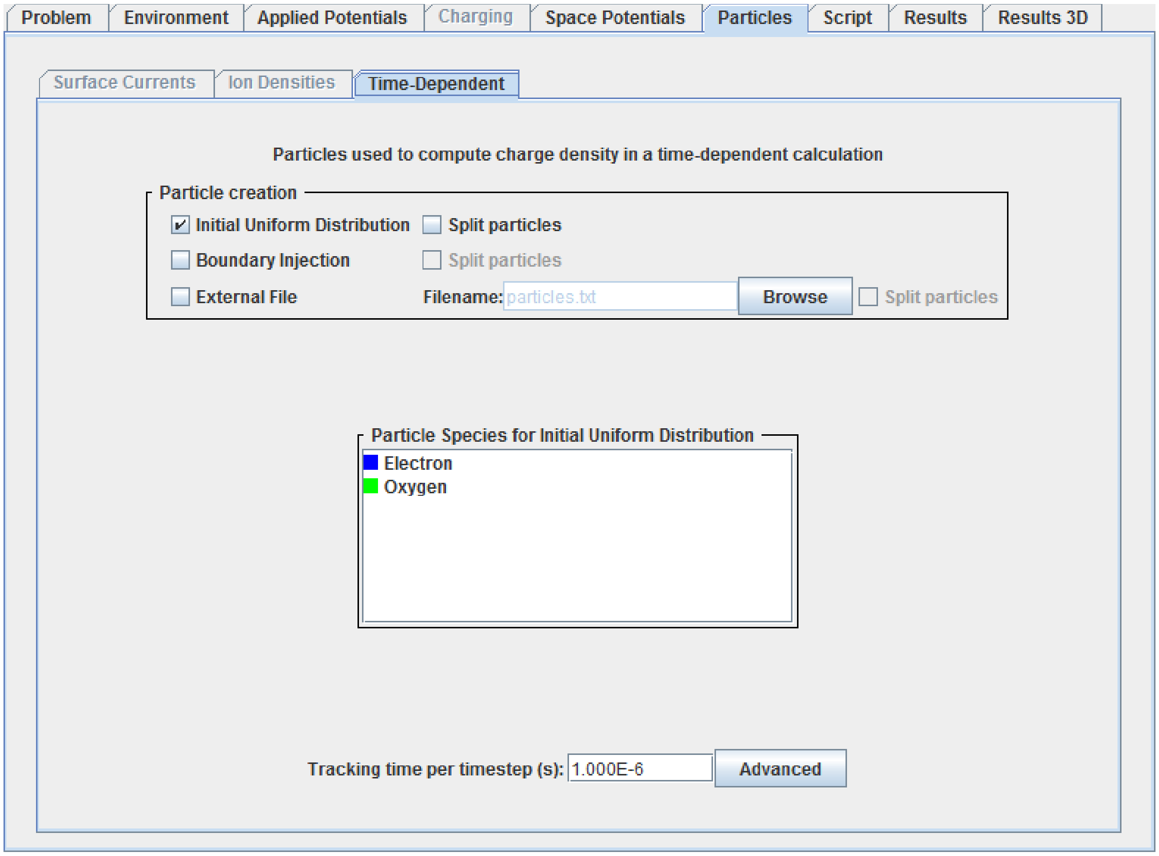

Particles used to compute charge density in a time-dependent calculation

Particle creation

☑ Initial Uniform Distribution ☐ Split particles
☐ Boundary Injection ☐ Split particles
☐ External File Filename: particles.txt ☐ Split particles

Particle Species for Initial Uniform Distribution

🟦 Electron
🟩 Oxygen

Tracking time per timestep (s): 1.000E-6

Figure A.10: Time-dependent subtab of the particles tab. Image adapted from *Davis et. al.* [200, p.51].

Regardless of how the macroparticles are generated, they are tracked in the simulation space. Particle are tracked along electric and magnetic field lines using a third-order energy-conserving algorithm that accounts for position and velocity [202, p.68]. Particles are tracked until one of the following conditions are met: 1) the particle strikes the object, 2) the particle exits the simulation space, 3) the trajectory time reaches the maximum tracking time, or 4) the number of substeps exceeds the maximum substep number. Once tracking is complete, *Nascap-2K* records the total current to the object, as well as the current lost due to particles leaving the simulation space.

A.2 Modeling Results

To quickly reiterate, potential structures around an object were always calculated using the potentials in space option with analytic space charge. Examples of spacecraft potential structures shown in appendices A.2.1 to A.2.3 indicate the direction of the drifting ion population in the top left with an arrow marked v_i. The left side of the spacecraft are in the ram region and the right side of the spacecraft are in the wake region (a description of ram and wake is provided in section 2.1.1). Surface currents were always calculated using PIC simulations. Finally, spacecraft charging simulations were accomplished using the surface charging option with tracked particle currents and were supported using the separate time-dependent plasma with tracked particle currents. The results discussed in this section give an overview of qualitative behaviors observed; more precise simulations are planned for future works, as discussed in appendix A.2.6.

A.2.1 Potential Effect on Sheath Form

The first effect studied is the impact of satellite potential on the CubeSat's sheath when immersed in a plasma with a $5\,\mathrm{eV}$ drifting oxygen ion population. Three accelerating potentials relative to the plasma are shown in fig. A.11: $-1\,\mathrm{V}$, $-10\,\mathrm{V}$, and $-50\,\mathrm{V}$. Additionally, the ambient plasma density is $5 \times 10^{12}\,\mathrm{m}^{-3}$. For this discussion, fig. A.11 is used as a reference. First, the sheath is compressed against the CubeSat on its ram side, even at the largest modeled accelerating potentials. Furthermore, the sheath is extended behind the CubeSat, its wake region. This wake is due to an ion deficit region (further discussed in appendix A.2.3). When the accelerating potential is a fraction of the ion drift energy, the sheath is mostly parallel to the sides of the CubeSat, and the sheath thickness is a fraction of the lengths and widths of the CubeSat (see fig. A.11a). However, as the accelerating potential increases and surpasses the ion drift energy, fewer ions have sufficient energy to overcome the spacecraft's potential barrier, and so the sheath expands and begins to round (see fig. A.11b). Once the accelerating potential is ten times the drift energy, the CubeSat sheath is nearly centered around the spacecraft and almost ellipsoidal (see fig. A.11c). This transition from a "thin sheath" form with a wake tail to a nearly ellipsoidal structure has not been captured using exact analytic expressions for a cuboid, requiring numerical simulations or spherical analytic approximations.

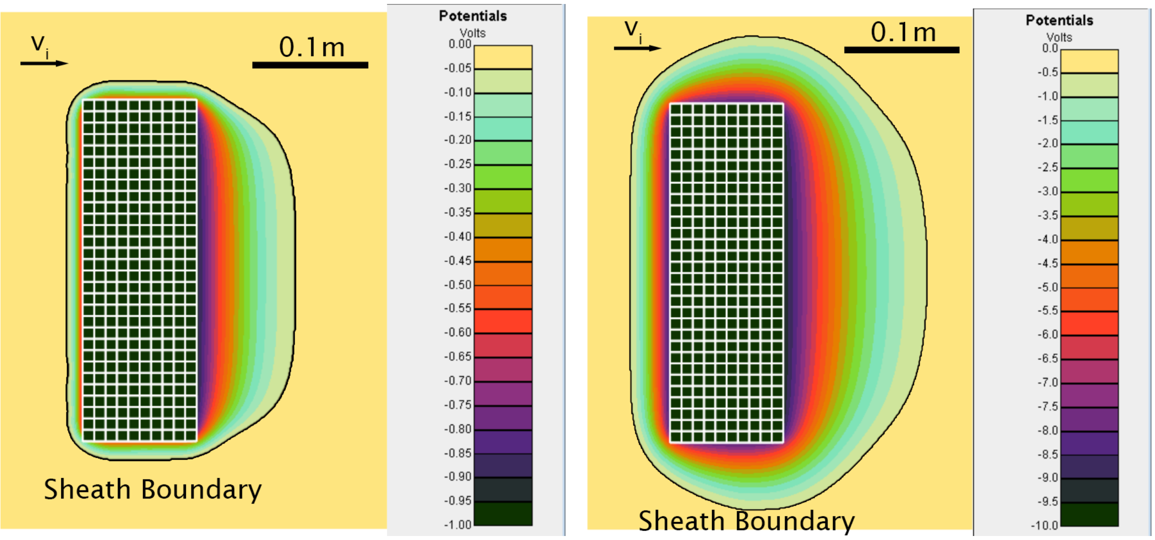

(a) Plasma sheath shape around a 3U CubeSat, biased to $-1\,\mathrm{V}$ relative to the plasma, due to a roughly $5\,\mathrm{eV}$ drifting oxygen ion population.

(b) Plasma sheath shape around a 3U CubeSat, biased to $-10\,\mathrm{V}$ relative to the plasma, due to a roughly $5\,\mathrm{eV}$ drifting oxygen ion population.

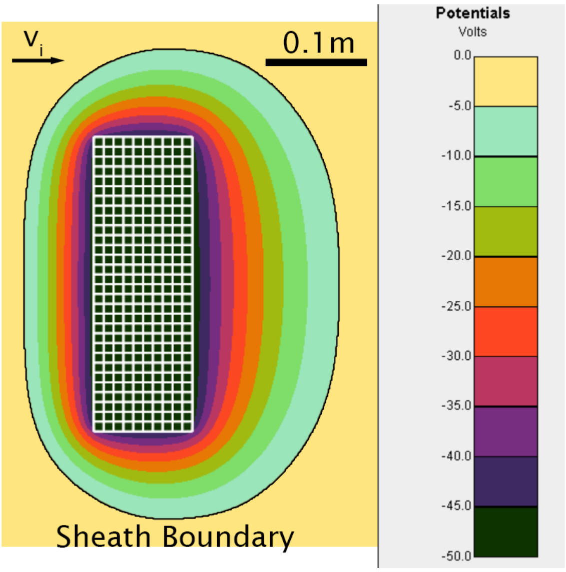

(c) Plasma sheath shape around a 3U CubeSat, biased to $-50\,\mathrm{V}$ relative to the plasma, due to a roughly $5\,\mathrm{eV}$ drifting oxygen ion population.

Figure A.11: Sheath size and shape variation with potential changes for the densest ionospheric plasma. v_i indicated the direction of the ion velocity, and the black outline provides a rough estimate of the sheath edge.

A.2.2 Debye Length Effect on Sheath Size

When the plasma density is decreased to $1 \times 10^{11}\,\mathrm{m}^{-3}$ (and all other parameters kept the same), the Debye length relative to the high-density cases increases by a factor of 7. If the sheath thickness is assumed to be at least three times the Debye length before accounting

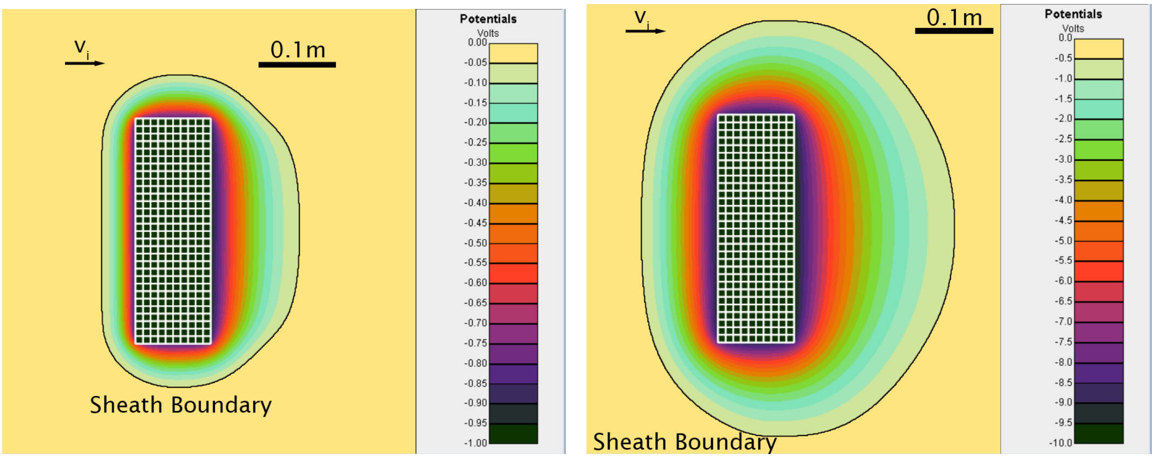

(a) Plasma sheath shape around a 3U CubeSat, biased to $-1\,\mathrm{V}$ relative to the plasma, due to a roughly $5\,\mathrm{eV}$ drifting oxygen ion population.

(b) Plasma sheath shape around a 3U CubeSat, biased to $-10\,\mathrm{V}$ relative to the plasma, due to a roughly $5\,\mathrm{eV}$ drifting oxygen ion population.

Figure A.12: Sheath size and shape variation with potential changes for the sparsest ionospheric, F-region plasma. v_i indicated the direction of the ion velocity, and the black outline provides a rough estimate of the sheath edge.

for accelerating potentials, this would imply that the sheath of the lower density scenarios is at least 21 times greater than the densest modeled plasmas. Indeed, when comparing the examples shown in fig. A.12 for accelerating potentials of $-1\,\mathrm{V}$ and $-10\,\mathrm{V}$ to the same accelerating potentials in fig. A.11, it is clear that the sheath dimensions for lower densities are much larger than high densities. However, while there is still some semblance of ram/wake effects at the lowest accelerating biases, such effects are not apparent when the spacecraft potential is twice the ion drift energy. While it is possible that the enlarged sheath at lower spacecraft potentials do mask ram/wake effects, more precise simulations where the spacecraft sheath is self-consistent with ion trajectories should be performed to better understand sheath shape as a function of plasma density [203].

A.2.3 Low Energy Ion Wake Filling Effect

To glean some understanding in the changes of sheath structure as a function of satellite potential, shown in appendix A.2.1, oxygen ions were tracked in the ram and wake sides of the CubeSat. The tracked oxygen ion trajectories are shown in fig. A.13. For clarity, the plasma and satellite properties in this section are the identical to those in appendix A.2.1. At potentials below the ion drift energy, most particles are collected on the ram side and the sides parallel to the ion drift velocity. Few oxygen ions are collected on the wake side, as most have sufficient energy to escape the satellite's potential barrier (fig. A.13a). Furthermore, while both bias cases demonstrate an ion focusing region behind the spacecraft, it is clearer in the smaller biases, where ion trajectories that originated ”above” the satellite intersect with ion trajectories that began ”below” the CubeSat. This ion focusing effect has been observed for similar simulations using cylinders, cubes, and pillbox geometries for the biased structure [204, 171, 205]. At biases greater than the ion drift energy, fewer ions escape the potential well created by the spacecraft, producing larger, rounded sheath structures in the ”wake” (fig. A.13a). These traced ion trajectories highlight an underlying physical process that explains the diminishing ram/wake effects as the spacecraft accelerating potential increases, as shown in fig. A.11. That is, as the spacecraft becomes increasingly negative, the attractive potential dominates over the ion drift energy, and so the CubeSat will increasingly collect current isometrically as the sheath expands.

When lighter hydrogen ions are present with the heavier oxygen ions, these previously empty wake zones are now filled by hydrogen, which is less affected by the CubeSat’s orbital velocity (see hydrogen lines filling empty wake region in fig. A.14). For comparison, while oxygen’s drift energy is approximately $5\,\mathrm{eV}$, hydrogen’s drift energy is roughly $0.3\,\mathrm{eV}$. Therefore, hydrogen’s drift energy is much closer to the ion temperatures used in these models, being either equal to or a factor of three greater than the thermal temperature, where as oxygen’s drift energy is 16 to 50 times greater than the ion temperature, depending on the ion temperature. As a result of hydrogen’s wake filling effect, more ion current is collected in the CubeSat’s wake region, as hydrogen makes up larger fractions of the total ion population (see table A.1). Additionally, fig. A.15 demonstrates that as hydrogen plays a more prominent role in the wake region, the sheath structure collapses toward the CubeSat, when compared to fig. A.11. These potential effects in the wake region are very apparent when the ion population is composed solely of hydrogen.

Spacecraft Bias = $-1\,\mathrm{V}$

Ion Comp.	Ram Current (µA)	Fraction of Total Current	Wake Current (µA)	Fraction of Total Current	Total Current (µA)
O^+	19.2	0.69	0.0	0.0	28.0
0.9 O^+ 0.1 H^+	19.2	0.66	0.2	0.01	29.4
0.8 O^+ 0.2 H^+	19.3	0.63	0.4	0.01	30.8
H^+	20.5	0.48	1.7	0.04	42.6

Spacecraft Bias = $-10\,\mathrm{V}$

Ion Comp.	Ram Current (µA)	Fraction of Total Current	Wake Current (µA)	Fraction of Total Current	Total Current (µA)
O^+	20.4	0.44	1.5	0.03	46.9
0.9 $^+$ 0.1 H^+	20.9	0.40	3.3	0.06	51.7
0.8 O^+ 0.2 H^+	21.3	0.38	5.1	0.09	56.5
H^+	27.2	0.28	16.6	0.17	96.7

Table A.1: Simulated ram and wake currents for various ion compositions.

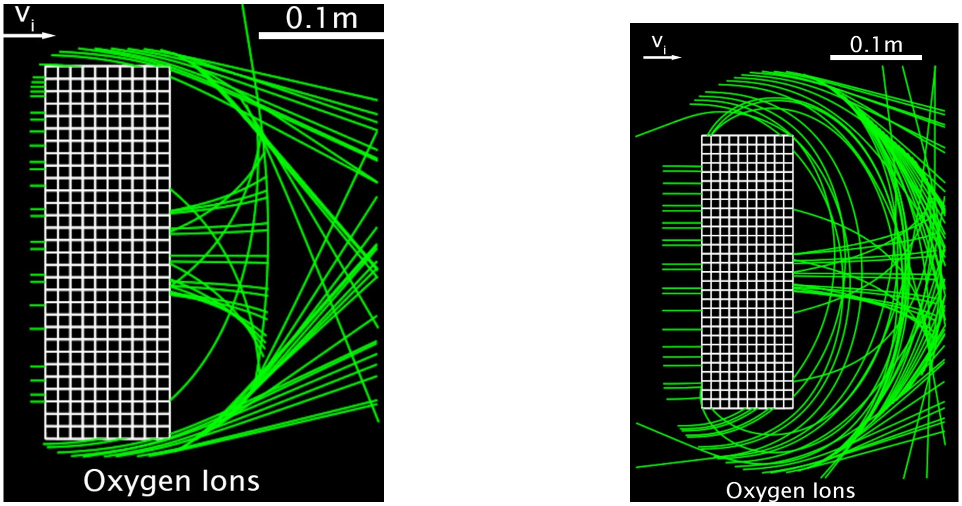

(a) Oxygen particle tracking for CubeSat biased to $-1\,\mathrm{V}$ below the ambient plasma with an ion composition that is comprised of only oxygen.

(b) Oxygen particle tracking for CubeSat biased to $-10\,\mathrm{V}$ below the ambient plasma with an ion composition that is comprised of only oxygen.

Figure A.13: Tracked oxygen particles around a 3U CubeSat object. 1 out of every 7 tracked macroparticle is shown.

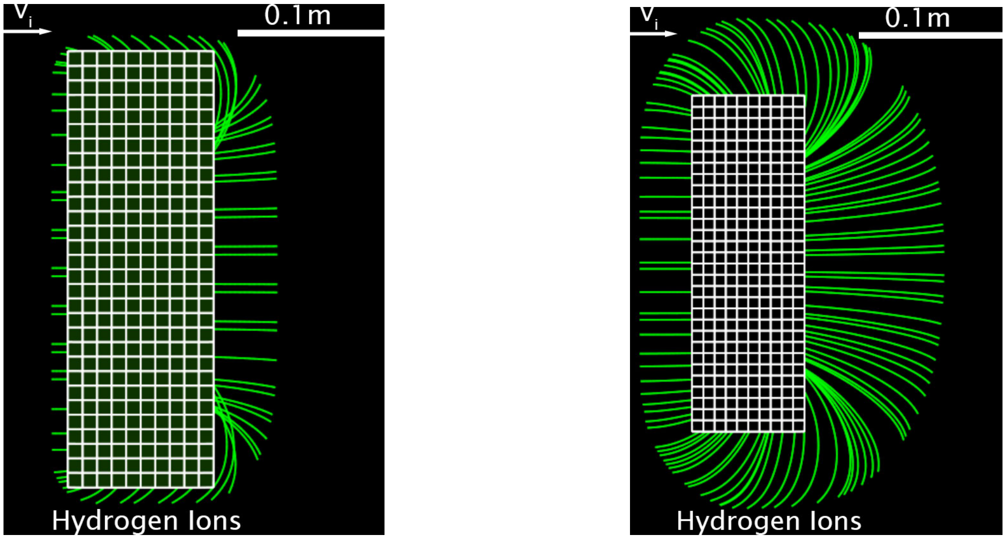

(a) Hydrogen particle tracking for CubeSat biased to $-1\,\mathrm{V}$ below the ambient plasma with an ion composition that is only hydrogen.

(b) Hydrogen particle tracking for CubeSat biased to $-10\,\mathrm{V}$ below the ambient plasma with an ion composition that is only hydrogen.

Figure A.14: Tracked hydrogen particles around a 3U CubeSat object. 1 out of every 7 macroparticles are shown.

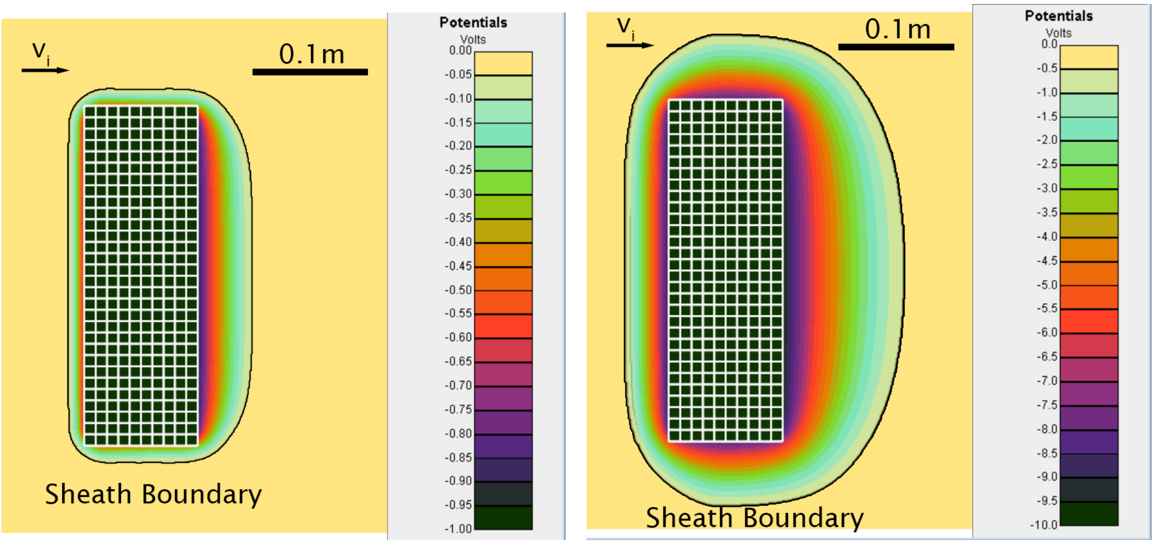

(a) Plasma sheath shape around a 3U CubeSat, biased to $-1\,\mathrm{V}$ relative to the plasma, due to a roughly $0.33\,\mathrm{eV}$ drifting hydrogen ion population.

(b) Plasma sheath shape around a 3U CubeSat, biased to $-10\,\mathrm{V}$ relative to the plasma, due to a roughly $0.33\,\mathrm{eV}$ drifting hydrogen ion population.

Figure A.15: Sheath size and shape variation with potential changes for the densest ionospheric plasma composed of various ratios of oxygen and hydrogen ions.

A.2.4 CubeSat Ion Current Collection

Current balance between an LP and CubeSat depends on multiple factors including the primary grid size, the angle between the object and ion drift velocity, and the particle generation method. Any CubeSat that is not symmetric along all three central axes of rotation will collect different total currents based on its axis of rotation. Therefore, understanding the change in ion current collection of each face for different orientations informs the amount of charging that one can expect when operating an LP. There are two axes of rotation considered, as shown in fig. A.16: a rotation about the CubeSat's Z-axis and a rotation about its Y-axis. Additionally, all estimated currents in these studies are due to PIC simulations using a boundary particle generation scheme. Furthermore, for figs. A.17 to A.19, the 3U CubeSat was scaled to be $1\,\mathrm{m}\times1\,\mathrm{m}\times3\,\mathrm{m}$, but the density was adjusted to $1\times10^{9}\,\mathrm{m}^{-3}$. Finally, rotation in this context refers to how the CubeSat changes orientation; the satellite was not rotating during simulations. Instead, I-V curves are calculated for each discrete angle.

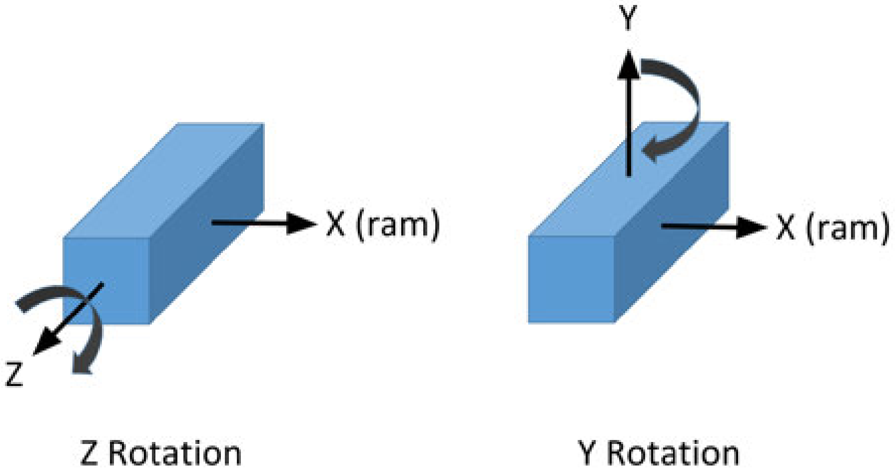

Figure A.16: Rotation about the CubeSat's Z-axis and Y-axis. Rotation arrows not necessarily indicative of true rotation.

The first type of rotation is about the CubeSat's Z-axis, which is $\pi/2$ symmetric, due to the fact that a $1\,\mathrm{m}\times3\,\mathrm{m}$ face, referred to as a large face, is always ram-facing (see fig. A.17). Under Z-axis rotation, the large faces are always parallel to the axis of rotation; that is, a vector normal to their surfaces is always perpendicular to the Z-axis. By extension, the CubeSat's small faces (dimensions of $1\,\mathrm{m}\times1\,\mathrm{m}$ each) are always perpendicular to the Z-axis. In the left-most panels, the current collection of the two large faces displayed are initially in the ram (blue line) and wake (red line). As the CubeSat rotates $180°$ counter-clockwise (using a "right-hand rule" approach–the curl of your fingers when your thumb is pointed upward indicates counter-clockwise rotation), these faces will end in the wake and ram regions, respectively, as indicated by the appearance that the two lines are near equal reflections about the $90°$ mark. The middle panels depict two large faces that are initially parallel to the ion drift velocity. As the CubeSat rotates, one large face passes through the ram region and the other passes through the wake. This is most noticeable at $90°$ when one face is fully ram-facing and the other is wake-facing, resulting in the largest separation. The right-most panels display the current collection of the two small faces as the CubeSat rotates. As expected, under a Z-axis rotation, the small faces do not change their angle relative to the ion drift velocity, and so their ion current does not change significantly under this rotation. The rotational current collection behavior of all faces is identical, regardless of whether the bias is $-1\,\mathrm{V}$ or $-10\,\mathrm{V}$, suggesting that as long as ram/wake effects are significant, this $\pi/2$ rotational symmetry should be expected for faces parallel to the axis of rotation.

The other rotation is a rotation about the CubeSat's Y-axis (results shown in fig. A.18). This rotation is orthogonal to both the ion drift velocity and the satellite's Z-axis. A Y-axis rotation is π symmetric, as the large faces and small faces alternate being in the ram-facing direction every $90°$ rotation. Therefore, two large faces will always be parallel to the axis of rotation, while the remaining two large faces and the two small faces are always

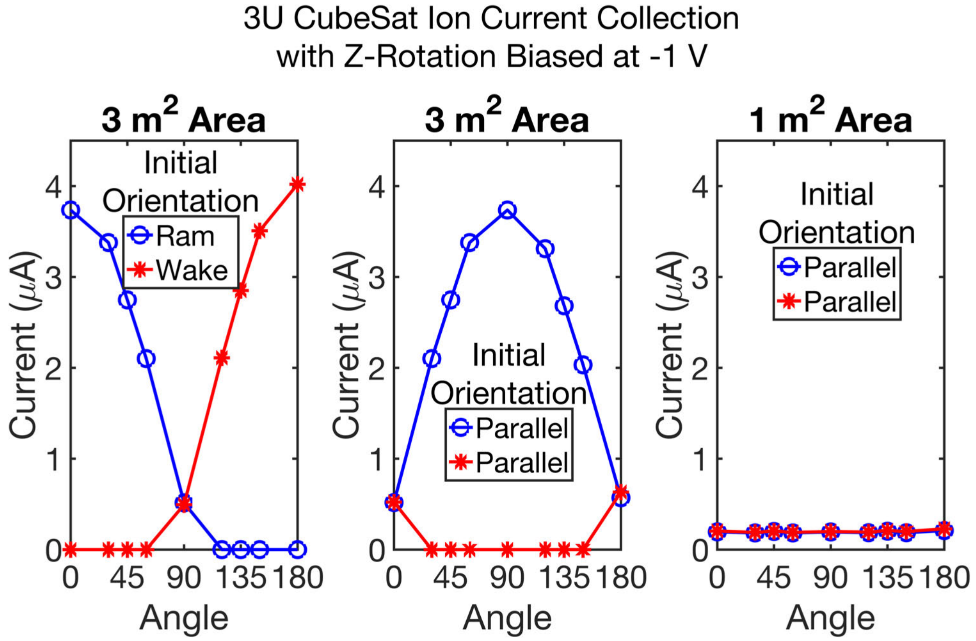

(a) Ion current collection by a 3U CubeSat biased to -1 V rotating about its Z-axis.

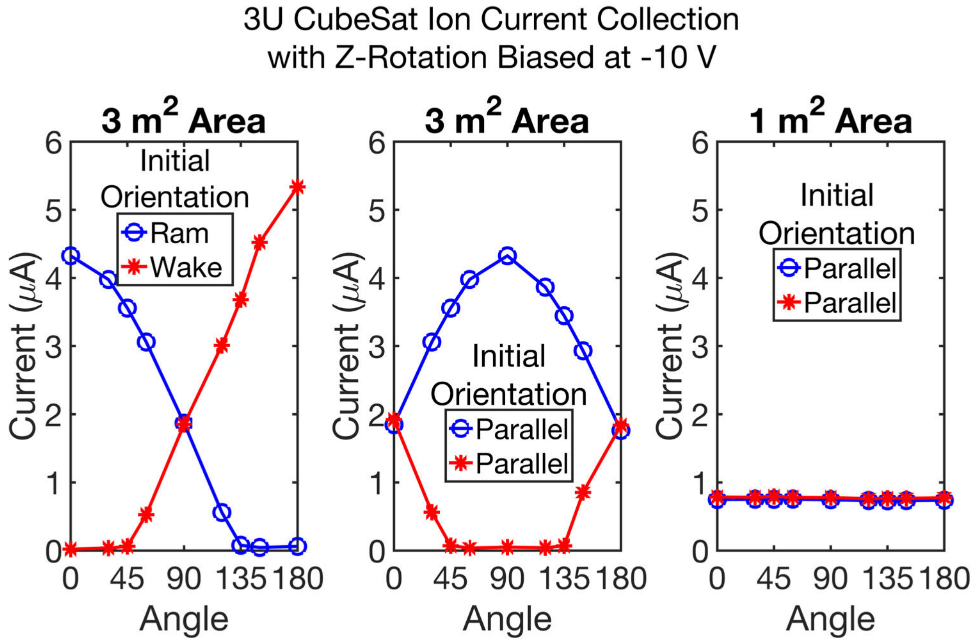

(b) Ion current collection by a 3U CubeSat biased to -10 V rotating about its Z-axis.

Figure A.17: Ion current collection dependence on Z-axis rotation.

perpendicular to the axis of rotation. Comparisons between fig. A.17 and fig. A.18 can now be drawn in order to highlight the different symmetries. Comparing the left-most panels of fig. A.18 to the left-most panels of fig. A.17, it can be seen that the general behavior is identical. This is expected, as the CubeSat is initialized in the exact same manner, and the faces represented in these panels will rotate to switch between the ram-facing and

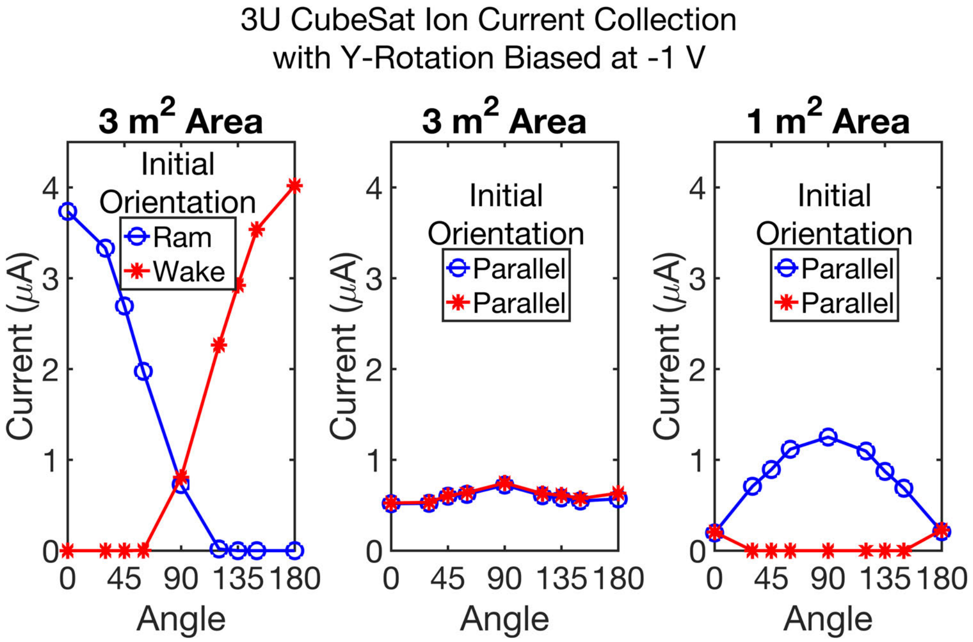

(a) Ion current collection by a 3U CubeSat biased to $-1\,\mathrm{V}$ rotating about its Y-axis.

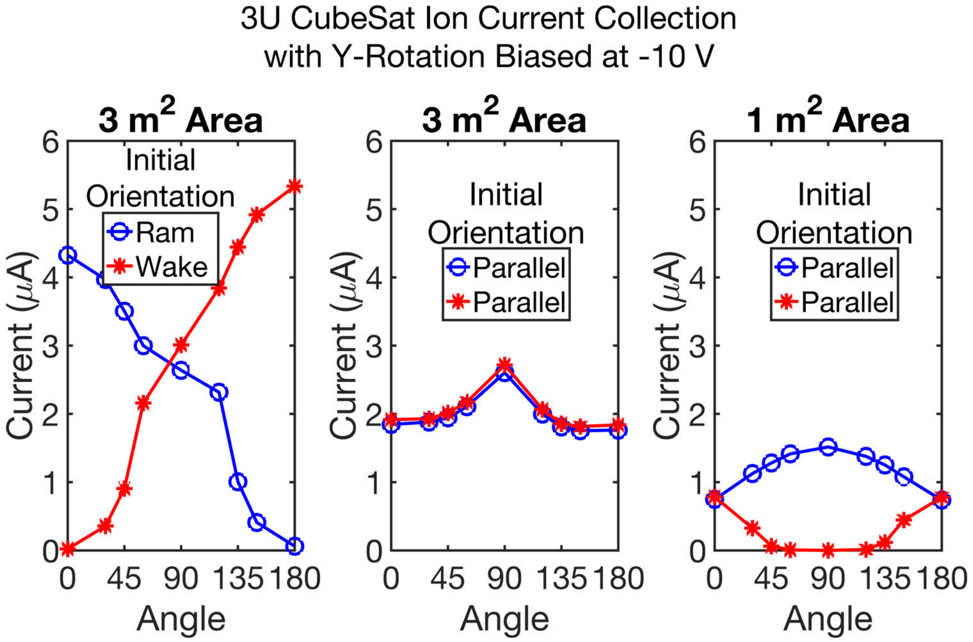

(b) Ion current collection by a 3U CubeSat biased to $-10\,\mathrm{V}$ rotating about its Y-axis.

Figure A.18: Ion current collection dependence on Y-axis rotation.

wake-facing regions regardless of the axis of rotation (Z-axis or Y-axis). The middle panels of fig. A.18 must be compared to the right-most panels of fig. A.17. In fig. A.18, the large faces are always perpendicular to the axis of rotation, and they are always parallel to the ion drift velocity. There is a noticeable peak in the large face's current collection at 90° for a Y-axis rotation, in contrast to the generally constant current collection of the small face for a Z-axis rotation. When a large face is in the ram direction, corresponding to 0° and 180°, the drifting ions must be collected as they travel over the $1\,\mathrm{m}$ thickness of the CubeSat. However, when a small face is in the ram direction, the full $3\,\mathrm{m}$ vertical length of the CubeSat is parallel with the drift velocity, and so the ions are attracted to the CubeSat over a longer period of time before the ions reach the wake region, making it more likely that they would be collected on these parallel sides. This indicates that for CubeSat sides that are not squares, the orientation of the CubeSat will impact the magnitude of its ion current collection. Finally, the right-most plots of fig. A.18 must be compared to the middle plots of fig. A.17. Like before, when the small face current collection peaks at 90°, the other small face is in the wake.

The X-axis rotation, a rotation about the axis parallel to the drift velocity, is not highlighted here because it is the only case where the current collection does not change with rotation. This is because the angle of each face of the CubeSat relative to the ion drift speed does not change, so the ion current as a function of angle for any side is similar to the right-most plots of fig. A.17.

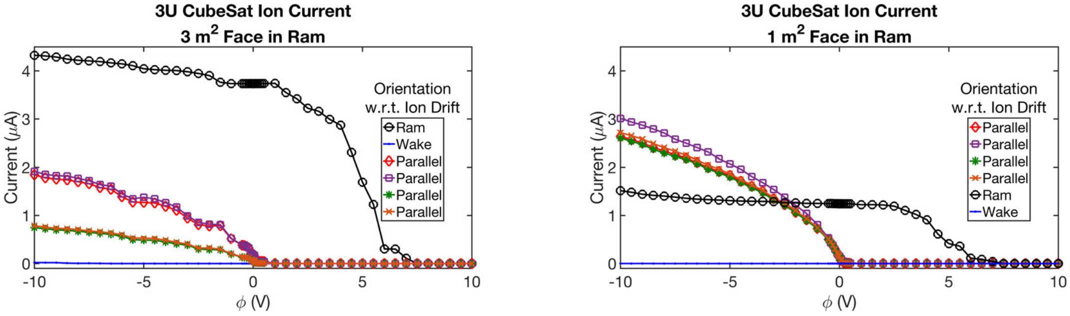

(a) Ion current collection by a swept 3U CubeSat with a large face in the ram direction.

(b) Ion current collection by a swept 3U CubeSat with a small face in the ram direction.

Figure A.19: Ion current collection by a scaled up 3U CubeSat for various potentials and ram surface areas.

Understandably, the collected ion current also changes with attractive spacecraft potential, and the collected current behavior is different for each side of the CubeSat. Starting with a large face in the ram direction, fig. A.19a demonstrates the current collection of each side of the CubeSat when a large face collects ram ion current. For small attractive and retarding potentials, the ram ion current represents a considerable fraction of the total collected ion current. As the attractive potential increases, the currents collected by the sides of the CubeSat parallel to the ion drift velocity increase as well, but they never individually surpass the current collected by the ram-facing side of the CubeSat. Additionally, there are two distinct pairs of collected ion currents, which correspond to one pair of large faces and one pair of small faces. Finally, the wake current collection is nearly negligible at the considered potentials. The wake ion current only begins to show a noticeable increase until the potential is nearly $-10\,\mathrm{V}$.

Figure A.19b depicts the ion current collection when a small face is in the ram direction. In this scenario, the 4 sides of the CubeSat parallel to the ram direction are all large faces, so their collected currents are nearly equal for all applied biases relative to the plasma. At small attractive potentials and retarding potentials, the ion current to the small ram face will also represent a majority of the total corrected current. However, the large parallel faces will collect more current than the ram face for attractive potentials greater than the ion drift energy, due to the size discrepancy between large and small CubeSat faces.

Comparing the net current between the two orientations suggests that if the CubeSat is expected to charge very negatively, there may be little difference between the net current collection of a 3U CubeSat with a large face or small face in the ram direction. Therefore, other factors such as the drag on the satellite can be weighed more heavily when determining the ideal satellite orientation. However, if minimal charging is expected (i.e. the LP sweep range is reduced, or the system has a large area ratio), then orienting the satellite to have a large face in the ram direction is crucial in minimizing possible charge buildup on the spacecraft due to LP operation.

A.2.5 Spacecraft Charging Estimates

Finally, we have reached the spacecraft charging estimates where the currents between the LP and CubeSat are balanced using PIC simulations. In the presented simulations, the area of the LP is $7.15 \times 10^{-4}\,\mathrm{m}^2$ with a guard area of $3.41 \times 10^{-4}\,\mathrm{m}^2$ to simulate the guarded ProSEDS Langmuir probe [159]. The probe and guard are biased at the same potential relative to a 1U (area ratio=50), 2U (area ratio=84), and 3U (area ratio=117) CubeSat. The ambient plasma density is $1 \times 10^{11}\,\mathrm{m}^{-3}$; the plasma temperature is $0.1\,\mathrm{eV}$; and the 1U, 2U, and 3U CubeSats and probe are not enlarged. Two probe orientations are considered in fig. A.20: an orientation perpendicular to the plasma flow and an orientation parallel to the flow. In the case where the probe is perpendicular to the flow, a large face of the 2U and 3U CubeSat are in the ram direction. When the probe is parallel to the flow, the small face of the CubeSat is in the ram direction. Regardless of area ratio or probe orientation, the spacecraft potential remains at a near constant level when the probe is biased negative, and the spacecraft potential has a considerable, nearly linear decrease in potential when the applied bias is positive and increasing. The numerical noise when the applied bias is negative is likely due to noise in the estimated ion currents to the LP. Furthermore, it is difficult to obtain low-noise results near the plasma potential as *Nascap-2K* has issues resolving spacecraft charging behavior in this regime. However, some additional expected results are observed. The magnitude of the most negative charging decreases with increased area ratio and the charging is less severe for larger ram-facing surface areas. In the case of the 1U CubeSat reference (left-most panels of fig. A.20), it is expected that the charging behavior would be nearly symmetric due to the symmetry of a 1U CubeSat. However, the parallel case likely experiences slightly more negative charging that the perpendicular case, due to an increase in electron current collection to the probe tip.

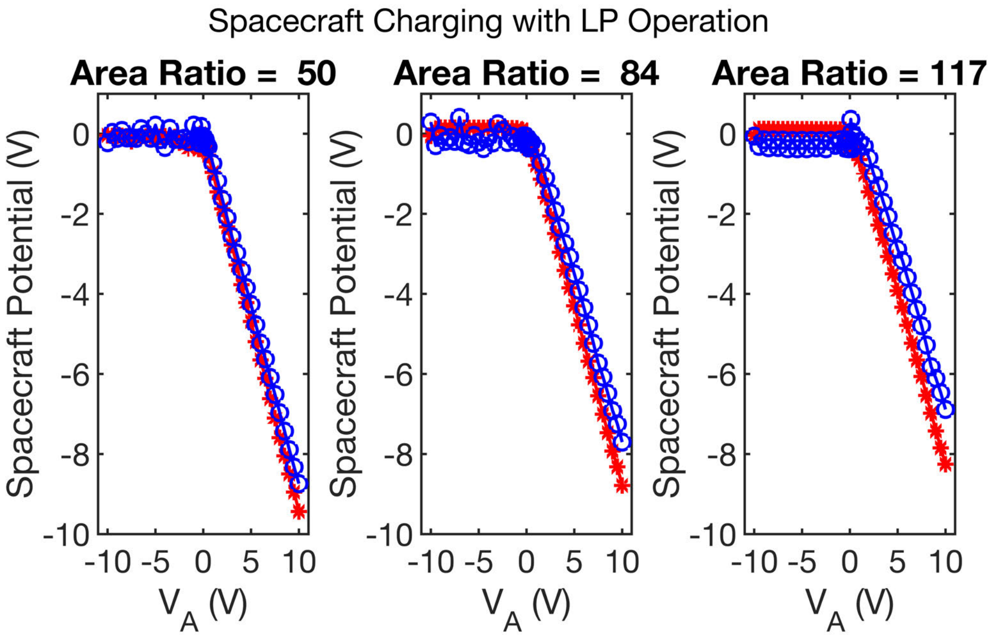

Figure A.20: Spacecraft charging behavior for the same probe operated from 1U, 2U, and 3U CubeSat reference.

A.2.6 Summary and Improvements

Nascap-2K highlighted many physical processes that can affect current collection to a spacecraft, and in turn, the stability of the satellite's floating potential, such as changes in the sheath structure due to bias and density, and the wake filling effects of low energy ions (see appendices A.2.1 to A.2.3). These processes are not captured in the most recent version of the PSIC-LEO model, which has a strict upper bound on the ion current that a satellite can collect (refer to section 4.2.2). By updating PSIC-LEO to include more of these physical processes, the modeled spacecraft charging behavior will likely estimate less negative charging and produce more realistic effects on the LP's I-V characteristics due to the greater, non-asymptotic ion current collection. Discussion for future work on advancing the PSIC-LEO model is provided in section 7.2.1.

Nascap-2K has proven to be a powerful program for modeling current collection to cuboids and cylinders. First and foremost, it is necessary to improve the latest PIC simulations to obtain more accurate Langmuir probe and CubeSat current voltage characteristics. Improvements include reducing the size of the primary grid, while increasing the number of elements in the primary grid. By reducing the size and increasing the number of elements, the macroparticle density at the edge of the primary grid increases when using the Boundary method, making it more likely that macroparticles will collide with object surfaces. This would produce more stable and accurate current collection curves, especially for applied biases near $0\,\mathrm{V}$.

The new currents to the CubeSat body can be validated using *Nascap-2K*'s surface detector scheme. Using the *Object Toolkit*, elements on the surface of an object can be designated as detectors. Macroparticles are then created at the detectors and tracked backwards to determine their origin. If the particles leave the simulation boundary, they are considered to be from the ambient plasma and counted as current to the surface [200]. Using both PIC simulations and reverse trajectory calculations, the currents to a 1U, 2U, 3U, and 6U CubeSat can be modeled for various potentials and angles relative to the plasma flow. By compiling multiple I-V curves for various cuboid sizes and orientations, analytic expressions can be derived for use in PSIC-LEO.

APPENDIX B

Plasma Spacecraft Interaction Codes for Low Earth Orbit Code

This appendix provides the full source code for the PSIC-LEO program. PSIC-LEO has one main script where the problem parameters are defined. This example is setup for a single area ratio case, but it is capable of calculating several cases in one execution. The brunt of the calculations are done in the current balance function. It numerically determines the potential of the satellite required to balance the LP and spacecraft currents. The remaining functions provide the current collection models and normalization constants.

B.1 Main File

```
% Main executable file for PSIC−LEO.

%% Conversions and Constants

amu2kg = 1.66054e−27; % kg/AMU
q = 1.6e−19; % Unit Charge
Electron_mass = 9.1e−31; %kg

%% Setup for Problem

% Problem can be defined by area ratio

% Area Ratios
Area_ratio = 285.;

% Problem can be defined by probe dimensions

Probe_length = 0.1143; %meters
Probe_diameter = 0.0013; % meters


```

```
% Sweep Start and End

VS = -10;% Start Voltage
VE = 10; % Stop Voltage
dV = 10e-3; % Voltage Step Size
points = abs(VE-VS)/dV+1; % Points in a sweep

% Plasma Parameters

Te = 0.25; % Electron Temperature [eV]
Density = 1e+12; % Plasma Density [m^-3]
Drift_speed = 8; % Ion Drift Speed [km/s]

Ion_mass = 16.; % Ion mass in amu

% Probe Parameters

Probe_area = pi*Probe_length*Probe_diameter;

%% Functions to Calculated Actual Floating Potential

Kmps2eV = @(x) 0.5*Ion_mass*amu2kg*(x*1e3).^2/1.6e-19;

% Currents

% Electron Retarding

I_ret = @(Te,V) Probe_area*Density*q*...
            sqrt(q*Te/(2*pi*Electron_mass))*exp(V/Te);

% Ion Accelerating

Ion_current_model = @(v_drift,Ti,V)(Probe_area*q/pi)*Density*...
      sqrt(q*Ti./(2*Ion_mass*amu2kg)).*2*sqrt(V/Ti+v_drift/Ti+...
            (V/Ti+0.5*v_drift/Ti)./(V/Ti+v_drift/Ti));

% Fzero calculates potential where currents are equal
FP_actual_LP = fzero(@(x) I_ret(Te,x)-...
      Ion_current_model(Kmps2eV(Drift_speed),Te,-x),[-10,0]);

%% Preallocating Matrices

FP_actual_SC = zeros(1,numel(Area_ratio)); % Spacecraft floating potential
Area_ratio_check = FP_actual_SC; %Check to verify area ratio correct
I_LP_all = zeros(points,numel(Area_ratio)); % Matrix of Net LP Current
```

```
I_e_LP_all = I_LP_all; % Matrix of LP Electron Current
I_i_LP_all = I_LP_all; % Matrix of LP Ion Current
I_SC_all = I_LP_all; % Matrix of Net SC Currents
V_A_all = I_LP_all; % Applied Voltages
Phi_SC_all = I_LP_all; % SC Potential w.r.t. Plasma
Phi_LP_all = I_LP_all; % LP Potential w.r.t. Plasma

%% Running Current Balance Function

for i=1:numel(Area_ratio)
    % Calculating Current Balance Using Probe Length and Diameter
    % N_S1 and N_S2 denote the number of same sized CubeSat faces
    % A_S1 is the area [m^2] of the sides counted by N_S1
    % A_S2 is the area [m^2] of the sides counted by N_S2

    [I_LP,I_e_LP,I_i_LP,I_SC,...
        V_applied,Phi_SC,Phi_LP,...
        Area_Ratio,SC_float] = CurrentBalance(VS,VE,...
        'Step_Size',dV,'Electron_Temperature',Te,...
        'Plasma_Density',Density,'Ion_Mass',Ion_mass,...
        'Ion_Drift_Speed',Drift_speed,...
        'Guard_Diameter',0,'Guard_Length',0,...
        'Probe_Length',Probe_length,...
        'Probe_Diameter',Probe_diameter,...
        'N_S1',4,'N_S2',2,...
        'A_S1',0.03,'A_S2',0.01);

    I_LP_all(:,i) = I_LP(:);
    I_e_LP_all(:,i) = I_e_LP(:);
    I_i_LP_all(:,i) = I_i_LP(:);
    I_SC_all(:,i) = I_SC(:);
    V_A_all(:,i) = V_applied(:);
    Phi_SC_all(:,i) = Phi_SC(:);
    Phi_LP_all(:,i) = Phi_LP(:);

    Area_ratio_check(i) = Area_Ratio;
    FP_actual_SC(i) = SC_float;
end
```

B.2 Current Balance

```
function [I_LP,I_e_LP,I_i_LP,I_SC,...
    V_applied,Phi_SC,Phi_LP,AreaRatio,SC_float] = ...
    CurrentBalance(VS,VE,varargin)

```

```
% This function calculates the spacecraft potential as a function of
% applied bias to the LP. The fzero function is used to balance the
% currents and determine the spacecraft potential.


    %% Constants

    in2cm = 2.54; % inches to cm
    cm2m = 1e−2; % cm to meters
    amu2kg = 1.6605389e−27; %AMU to kg
    km2m = 1e3; % km to meters

    %% Parse User Inputs

    % Default Options

    %%%%%%%%%%Sweep Options%%%%%%%%%%%

    dV = 10e−3;

    %%%%%%%%%%Probe Dimensions%%%%%%%%%%

    pd = 0.168∗cm2m∗in2cm; % Probe Diameter [m]
    pl = 2.1∗cm2m∗in2cm; % Probe Length [m]

    %%%%%%%%%%Guard Dimensions%%%%%%%%%%

    gd = 0.15∗cm2m∗in2cm; % Guard Diameter [m]
    gl = 1∗cm2m∗in2cm; % Guard Length [m]

    %%%%%%%%%%Probe Orientation%%%%%%%%%%

    theta = 90.; % Angle of SC vertical axis relative to ion flow

    %%%%%%%%%%CubeSat Dimensions%%%%%%%%

    N_S1 = 4; % Number of sides of type 1. Ram facing side.
    N_S2 = 2; % Number of sides of type 2. Non−ram or wake facing side.
    N_S3 = 0;

    A_S1 = 30.∗10.∗cm2m^2; % Area in m^2
    A_S2 = 10∗10∗cm2m^2; % Area in m^2
    A_S3 = 0;

    AR = []; %Possible variable to force area ratio
```

```
%%%%%%%%%%Plasma Properties%%%%%%%%%%

Te = 0.1; % Electron Temperature [eV]
Ti = 0.1; % Ion Temperature [eV]
M = 16; % Ion Species mass [amu]
W = 7.8; % Ion Drift speed [km/s]
N = 1e12; % Plasma Density [1/m^3]

% Parse Variable Arguments into their name valued pairs.

p = inputParser;

% Probe Dimensions

addOptional(p,'Probe_Diameter',pd,@isnumeric)
addOptional(p,'Probe_Length',pl,@isnumeric)

% Probe Sweep Options

addOptional(p,'Step_Size',dV,@isnumeric)

% Guard Dimensions

addOptional(p,'Guard_Diameter',gd,@isnumeric)
addOptional(p,'Guard_Length',gl,@isnumeric)

% Probe Orientation

addOptional(p,'Probe_Orientation',theta,@isnumeric)

% CubeSat Dimensions

addOptional(p,'N_S1',N_S1,@isnumeric)
addOptional(p,'N_S2',N_S2,@isnumeric)
addOptional(p,'N_S3',N_S3,@isnumeric)
addOptional(p,'A_S1',A_S1,@isnumeric)
addOptional(p,'A_S2',A_S2,@isnumeric)
addOptional(p,'A_S3',A_S3,@isnumeric)
addOptional(p,'Area_Ratio',[],@isnumeric)

% Plasma Properties

addOptional(p,'Electron_Temperature',Te,@isnumeric)
addOptional(p,'Ion_Temperature',Ti,@isnumeric)
```

```
    addOptional(p,'Ion_Mass',M,@isnumeric)
    addOptional(p,'Ion_Drift_Speed',W,@isnumeric)
    addOptional(p,'Plasma_Density',N,@isnumeric)

    parse(p,varargin{:})

    [New_Param] = setdiff(p.Parameters,p.UsingDefaults);

    for i=1:numel(New_Param)
        a = char(New_Param(i));
        switch a
            case 'A_S1'
                A_S1 = p.Results.A_S1;
            case 'A_S2'
                A_S2 = p.Results.A_S2;
            case 'A_S3'
                A_S3 = p.Results.A_S3;
            case 'Step_Size'
                dV = p.Results.Step_Size;
            case 'Electron_Temperature'
                Te = p.Results.Electron_Temperature;
            case 'Guard_Diameter'
                gd = p.Results.Guard_Diameter;
            case 'Guard_Length'
                gl = p.Results.Guard_Length;
            case 'Ion_Drift_Speed'
                W = p.Results.Ion_Drift_Speed;
            case 'Ion_Mass'
                M = p.Results.Ion_Mass;
            case 'Ion_Temperature'
                Ti = p.Results.Ion_Temperature;
            case 'N_S1'
                N_S1 = p.Results.N_S1;
            case 'N_S2'
                N_S2 = p.Results.N_S2;
            case 'N_S3'
                N_S3 = p.Results.N_S3;
            case 'Plasma_Density'
                N = p.Results.Plasma_Density;
            case 'Probe_Diameter'
                pd = p.Results.Probe_Diameter;
            case 'Probe_Length'
                pl = p.Results.Probe_Length;
            case 'Probe_Orientation'
                theta = p.Results.Probe_Orientation;
```

```
            case 'Area_Ratio'
                AR = p.Results.Area_Ratio;
    end
end

%% Calculations Based on Inputs%%%

pr = pd/2; % Probe Radius

AreaLP = pd*pl*pi;% [m]

AreaGuard = gd*gl*pi;% [m]

AreaInst = AreaLP+AreaGuard; % Area of Probe and Guard

% Calcualting Spacecraft Surface Areas for Current Collection

if isempty(AR)

    Electron_area = A_S1*N_S1+A_S2*N_S2+N_S3*A_S3;

else

    A_T = AR*AreaInst;

    % Calculates the area of a 3U CubeSat

    A_S1 = (3/14)*A_T; % Type 1 Face
    A_S2 = A_S1/3; % Type 2 Face

    Electron_area = A_S1*N_S1+A_S2*N_S2+N_S3*A_S3;
end

AreaRatio = Electron_area./AreaInst;

%% Calculations

%%%%%%%%%Generating Random Currents and Normalized Speeds%%%%%%%

[Ier,Ionr,S]= RanCur(N,Te,Ti,M,W*sind(theta));

%%%%%%%%%%Calculating Spacecraft Floating Potential%%%%%%%%%%%%%%

options = optimset('Display','off');

```

```
SC_float = fzero(@(x) CubeSat_Collection(x,W*km2m,Te,Ti,M*amu2kg,...
    Ier*Electron_area,Ionr*A_S1,Ionr*A_S2),[-10,0],options);

%%%%%%%%%Probe Sweep Properties%%%%%%%%%

V_applied = VS:dV:VE;

% Allocating array for spacecraft potential

Phi_SC = zeros(1,numel(V_applied));

%%%%%%%%%Determining Plasma Debye Length and Sheath Size%%%%%%%%%

Lambda_D = 740*cm2m*sqrt(Te/(N*power(cm2m,3))); % Debye Length

a = 3*Lambda_D+pr; % Sheath radius measured from probe center

Ratio = a/pr; % Ratio between sheath radius and probe radius

%%%%%%%%%%Calculating Spacecraft Potential%%%%%%%%%%%%%%

% Defining current balance function
myfun = @(x,V_applied) CubeSat_Collection(x,W*km2m,Te,Ti,M*amu2kg,...
    Ier*Electron_area,Ionr*A_S1,Ionr*A_S2)+...
    (AreaLP+AreaGuard)*...
    LP_collection(x+V_applied,Ratio,Te,Ti,S,Ier,Ionr);

% Iterating through applied bias for current balance

for i=1:numel(V_applied)
        Phi_SC(i) = ...
            fzero(@(x) myfun(x,V_applied(i)),...
            max(V_applied)*[-2,2],options);
end

% Calculating LP potential w.r.t. plasma

Phi_LP = V_applied+Phi_SC;

%%%%%%%%%Generating LP and Guard Current%%%%%%%%%

% Normalized Net Current
[I_N,Ie_N,Ii_N] = ...
    LP_collection(Phi_LP,Ratio,Te,Ti,S,Ier,Ionr);

```

```
    % Electron current to LP
    I_e_LP = AreaLP*Ie_N;

    % Ion current to LP
    I_i_LP = AreaLP*Ii_N;

    % Net Current to LP
    I_LP = AreaLP*I_N;

    %%%%%%%%%%Generating CubeSat Current%%%%%%%%%%%%%%%

    I_SC = CubeSat_Collection(Phi_SC,W*km2m,Te,Ti,M*amu2kg,...
        Ier*Electron_area,Ionr*A_S1,Ionr*A_S2);
end
```

B.3 Normalization Constants

```
function [Ie_ran,Ion_ran,S_long]= RanCur(density,Te,Ti,Mass,DSC_long)

% Calculates the random ion and electron currents of an Ionospheric Plasma
% and a necessary drift term. The random currents are area normalized.

% Density in 1/m^3
% Temperature in eV
% Mass in amu

%% Constants

me=9.10938215e-31;% Mass of Electron
amu=1.6605389e-27;% Atomic Mass Unit in kg
q=1.602177e-19;% Charge of Electron
km2m = 1e3; % kilometer to meter

Mass = Mass*amu;

N_q=q*density;% Charge Density

v_i_therm=sqrt(Ti*q/(2*pi*Mass)); % Ion Thermal Speed

v_e_therm = sqrt(Te*q/(2*pi*me)); % Electron Thermal Speed

%% Normalized Thermal Currents

% Electron Current

```

```
Ie_ran=v_e_therm*N_q; % Randome

% Ion Current

Ion_ran=v_i_therm*N_q;

%% Normalized Drift Speeds

% Drift Term

S_long=DSC_long*km2m/(v_i_therm*2*sqrt(pi)); % Normalized Drift Speed
end
```

B.4 Langmuir Probe Current Collection Model

```
function [I,Ie,Ii] = LP_collection(V,ratio,Te,Ti,K,Ier,Ionr)

% Modeling Langmuir Probe Current Collection
% Refer to Kanal 1964 for Ion Current Theories

%% Preallocating Arrays for Currents

array_length =numel(V);

Ie = zeros(1,array_length); % Electron Current
Ii = Ie; % Ion Current

%% Creating General Constants Based on Sheath-to-Probe Ratio

gamma2=1./((ratio.^2)-1);
gamma=sqrt(gamma2);

alpha = sqrt(gamma2+1);

%% Calculating Electron Current

% Retardation Regime

Ie(V<=0) = exp( V(V<=0)/Te);

% Acceleration Regime

V_acc = V(V>0);

% Creating Specific Constants
```

```

rtV=sqrt(V_acc/Te);
beta_1=alpha.*rtV;
beta_2=gamma.*rtV;

Ie(V>0) = exp(V_acc/Te).*erfc(beta_1)+ratio.*erf(beta_2);

%% Calculating Ion Current

for i=1:array_length

    V_n = -V(i)/Ti;

    % Acceleration Regime

    if V_n>=0


       Ii(i) = IonAcc(V_n,K,gamma);%IonAcc(V_n,K);%

    else

    % Retardation Regime
        ion_temp1 = IonRet(V_n,K);
        Ii(i)= ion_temp1;
        %{
        if ion_temp1<=1e-3
            Ii(i:array_length)=0;
            break
        else
            Ii(i) = -1*ion_temp1;
        end
        %}
    end

end

%% Total Current

Ie = Ie*Ier;

Ii = Ii*Ionr;

I = Ie-Ii;
end
```

```
%% Ion Current Models

function Ia=IonAcc(V,K,gamma)
    % Ion Acceleration Current

    f = @(x,K,V) x.*sqrt(x.^2+V).*exp(-(x-K).^2).*...
        besseli(0,2.*x.*K,1);

    g = @(x,K) x.^2.*exp(-(x-K).^2).*besseli(0,2.*x.*K,1);

    gamma2 = gamma.^2;

    split = gamma*sqrt(V);

    int1 = integral(@(x) f(x,K,V),split,inf);
    int2 = integral(@(x) g(x,K),0,split);

    Ia = 4/sqrt(pi)*(int1 + sqrt((1+gamma2)/gamma2)*int2);

end


function Ia=IonRet(V,K)

    % Ion Retardation Current

    f = @(x,K,V) x.*sqrt(x.^2+V).*exp(-(x-K).^2).*...
        besseli(0,2.*x.*K,1);

    split = sqrt(-V);

    int1 = integral(@(x) f(x,K,V),split,inf);

    Ia = 4/sqrt(pi)*int1;
end
```

B.5 Spacecraft Current Collection Model

```
function I = CubeSat_Collection(V,v0,Te,Ti,m,...
    e_therm,Ion_therm_1,Ion_therm_2)

% Modeling Spacecraft Current Collection
% v0 is the initial drift in m/s
% V is the bias in Volts
% T is the temperature in eV
```

```
% m is the mass in kg

%% Preallocating Arrays

Ie = zeros(size(V)); % Electron Current
Ii = Ie; % Ion Current

%% Calculating SC Currents

% Electron Retardation Regime

V_ret = V(V<=0);

Ie(V<=0) = ElectronRet(V_ret/Te);
Ii(V<=0) = -Ion_therm_1*((IonACC(v0,Ti,m))+...
    2*IonACC(0,Ti,m))-2*Ion_therm_2*IonACC(0,Ti,m);

% Accelerating Regime

V_acc = V(V>0);

Ie(V>0) = ElectronACC();
Ii(V>0) = -Ion_therm_1*(IonRet(v0,-V_acc,Ti,m)+...
     2*IonRet(0,-V_acc,Ti,m))-2*Ion_therm_2*IonRet(0,-V_acc,Ti,m);

% Total Current

I = Ii+e_therm*Ie;

end

%% Current Models

function Ia = IonACC(v0,T,m)
     % Accelerated Ion Current

     % Constants

     q = 1.6e-19;

     v_d = v0./sqrt(2*q*T/m); % Normalized Drift Speed

     Ia = exp(-power(v_d,2))+sqrt(pi).*v_d.*erfc(-v_d);
end

```

```
function Ia = IonRet(v0,V,T,m)
    % Retarded Ion Current

    % Constants

    q = 1.6e-19;

    v_d = v0./sqrt(2*q*T/m); % Normalized Drift Speed

    V0 = sqrt(-V./T); % Normalized Potential

    Ia = exp(-power(V0-v_d,2))+...
    sqrt(pi).*v_d.*erfc(V0-v_d);
end

function Ia = ElectronACC()
    % Accelerated Electron Current

    Ia = 1;
end

function Ia = ElectronRet(V)
    % Retarded Electron Current

    Ia = exp(V);
end
```

APPENDIX C

Langmuir Probe Analysis with Uncertainties

Here we present a full analysis of LP sweeps that have been generalized for a cylindrical probe in a non-magnetic, drifting plasma in the absence of additional current sources such as photoelectrons. All of the methods detailed in this appendix can be programatically applied, and any method which can not be numerically automated is not included in this appendix.

Consider a generic LP sweep (fig. 1.2) where there are three areas of interest: the ion saturation regime, the electron retardation regime, and the electron saturation regime. We will break down the analysis in the same order as is required for real data. Several methods are demonstrated for each plasma characteristic that can be determined, from an LP sweep. Furthermore, each method will have two uncertainties: 1) the method's intrinsic uncertainty and 2) systematic uncertainties. The square root of the sum of squares of these uncertainties determines the total uncertainty for the method (eq. C.1)

$$\sigma_{Total} = \sqrt{\sigma_{method}^2 + \sigma_{systematic}^2}. \tag{C.1}$$

Furthermore, the instrumental uncertainties affect all methods, as they affect both the measured current and the sourced voltage. Since Keithley sourcemeters were used to source voltage in a 20V range and measure currents up to a 100 μA range, the instrumental uncertainties of the source meters are [177]

$$\begin{aligned} \sigma_{V_{inst}} &= V_{sourced} * 0.02\% + 2.4 \times 10^{-3}\,\mathrm{V} \\ \sigma_{I_{inst}} &= I_{measured} * 0.025\% + 6 \times 10^{-9}\,\mathrm{A} \end{aligned}$$

A typical LP analysis procedure broadly looks as follows:

1. Use a smoothing algorithm to minimize the effects of noise. A Savitsky-Golay algorithm is typically sufficient with a window size of $1\,\%$ to $2\,\%$ of the total number of points and a polynomial of order 4 [206, 207].
2. Determine the floating potential and the plasma potential.
3. Use the floating and plasma potentials to roughly estimate the electron temperature.

4. Calculate the ion density.
5. Determine the ion current and subtract it from the net current to calculate the electron current.
6. Calculate the electron temperature and density.

C.1 Floating Potential

The floating potential, V_F, of a Langmuir probe is the potential at which the current is net zero. As a result, the floating potential exists when the ion current and electron currents are equal but opposite. Any plasma characteristic that affects these currents, such as electron temperature or ion drift speed, will in turn affect the magnitude of the floating potential.

C.1.1 Systematic Uncertainties

Due to the complex nature of instrument electronics and plasmas themselves it is difficult to accurately "land" on the floating potential during a sweep. V_F is calculated by averaging the two potentials attributed to the currents closest to a net zero current (eq. C.2). The systematic uncertainty is the square root of the sum of the squares of the uncertainties of each measured potential (eq. C.3). Naturally, the uncertainty of each potential contains the instrumental uncertainty of the sourced voltage. However, the uncertainty due to the measured current is also a factor, since these voltages were chosen based on their respective current's proximity to 0. This relationship between the instrumental uncertainty of the measured current and the voltage's uncertainty is correlated by the inverse of the first derivative of the net current with respect to the voltage evaluated at the two potentials of interest.

$$\begin{aligned} V_F &= \frac{V_1 + V_2}{2} \qquad \text{(C.2)} \\ V_1 &= V(max(I < 0)) \\ V_2 &= V(min(I > 0)) \\ \sigma_{V_F} &= \frac{1}{2}\sqrt{\sigma_{V_1}^2 + \sigma_{V_2}^2} \qquad \text{(C.3)} \\ \sigma_{V_i} &= \sqrt{\sigma_{V_{inst}}^2 + \left[\left(\frac{dI}{dV} \right)^{-1} \sigma_{I_{inst}} \bigg|_{V_A = V_i} \right]^2} \end{aligned}$$

C.1.2 Minimum Uncertainty due to Method

Programmatically, the floating potential is found using the follow procedure:

1. Search the measured currents for a current value that is exactly zero. If the zero current exists, the corresponding voltage is the floating potential, and the uncertainties are purely due to systematic uncertainties.

2. If no current is exactly zero, search through measured currents of the I-V curve for two adjacent current measurements where one is positive and the other is negative.
3. Average the corresponding voltages of the two currents.

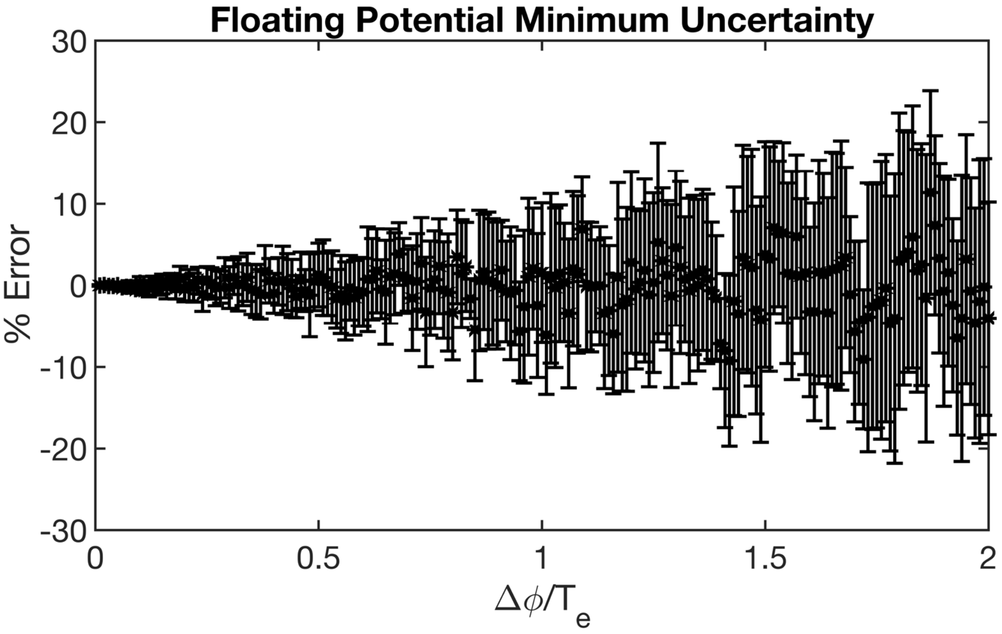

Figure C.1: Minimum uncertainty of the floating potential method.

Figure C.1 shows the minimum uncertainty of the floating potential method as a function of bias step size normalized by the electron temperature. To determine the percent error, LP I-V curves were modeled using the difference between the retarded electron current (eq. 2.13) and the accelerated ion current (eq. 2.19) over a range of electron temperatures ($0.1\,\mathrm{eV}$ to $0.2\,\mathrm{eV}$) and a 5 eV drifting Maxwellian ion population. Assuming perfectly known currents and voltages, the floating potential was numerically calculated using a the *fzero* MATLAB function that determines the root of nonlinear functions using a combination of interpolation schemes [169]. This numerically determined floating potential was compared to the floating potential obtained using the four step procedure previously detailed. The minimum uncertainty shown in fig. C.1 is the average of the percent errors of the floating potential measurements for all temperatures at a given step size. The error bars are the standard deviation of the set. Generally speaking, if the bias step size is equal to the electron temperature, the uncertainty in this method is roughly $10\,\%$. To achieve a minimum uncertainty of $5\,\%$, the voltage step size must be roughly $0.5T_e$, and a $1\,\%$ minimum uncertainty is achieved at a step size of roughly $0.25T_e$.

C.2 Plasma Potential

The plasma potential, V_P, is the bias along an LP sweep where the probe is at the same potential as the surrounding plasma. In the current-voltage curve, this point is characterized by a change in concavity and is a maximum in the first derivative of the current with respect to the applied voltage.

C.2.1 Systematic Uncertainties

The numerical scheme used to determine the first derivative is shown in eq. C.4. To ensure the voltage and current array sizes remain constant, the derivative scheme uses forward and backward differentiation at the appropriate end points and a midpoint scheme everywhere else. The equation and systematic uncertainty of the plasma potential are shown in eqs. C.6 and C.7. The systematic uncertainty is governed by the accuracy of the sourced voltage and the error in the numerical differentiation scheme.

$$\frac{dI}{dV} \approx \begin{cases} \frac{4I_{n+1}-I_{n+2}-3I_n}{2V_{Step}} & n \leq 2 \\ \frac{I_{n-2}-8I_{n-1}+8I_{n+1}-I_{n+2}}{12V_{Step}} & 2 < n < N-1 \\ \frac{3I_n-4I_{n-1}+I_{n-2}}{2V_{Step}} & n \geq N-1 \end{cases} \tag{C.4}$$

$$\sigma_{\frac{dI}{dV}} \propto \begin{cases} \frac{V_{Step}^2}{3} & n \leq 2 \\ \frac{V_{Step}^4}{30} & 2 < n < N-1 \\ \frac{V_{Step}^2}{3} & n \geq N-1 \end{cases} \tag{C.5}$$

$$V_P = V_B \ s.t. \ \left.\frac{dI}{dV}\right|_{max} \tag{C.6}$$

$$\sigma_{V_P} = \sqrt{\sigma^2_{V_{inst}} + \sigma^2_{\frac{dI}{dV}}} \tag{C.7}$$

C.2.2 Minimum Uncertainty due to Method

Programmatically, the plasma potential is found using a derivative procedure as follows:

1. Using eq. C.4 calculate the first derivative of the I-V curve using the measured currents and voltages.
2. Normalize the first derivative by the local maximum. This should be the peak.
3. Employ a peak-finding algorithm such as the *findpeaks* MATLAB function [169] to determine the voltage corresponding to the peak. Peak characteristics such as a minimum height can be used to help select the peak amongst any smaller local maxima that appear due to noise.

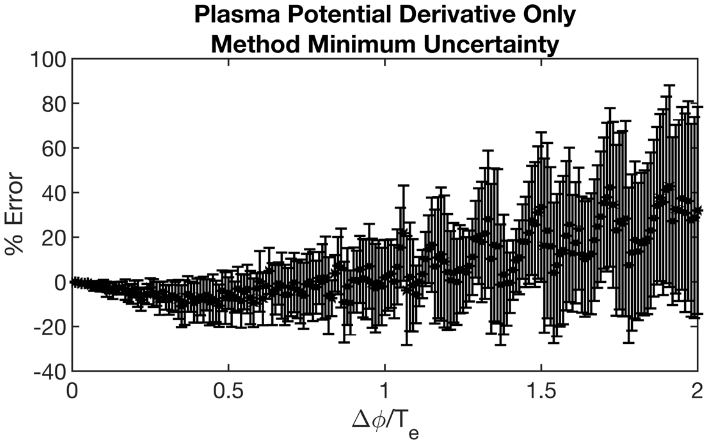
Plasma Potential Derivative Only
Method Minimum Uncertainty

(a) Minimum uncertainty of the plasma potential using only the derivative method.

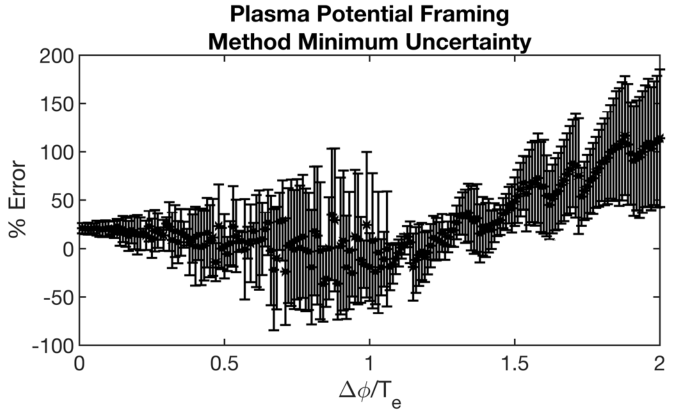
Plasma Potential Framing
Method Minimum Uncertainty

(b) Minimum uncertainty of the plasma potential using only the framing method.

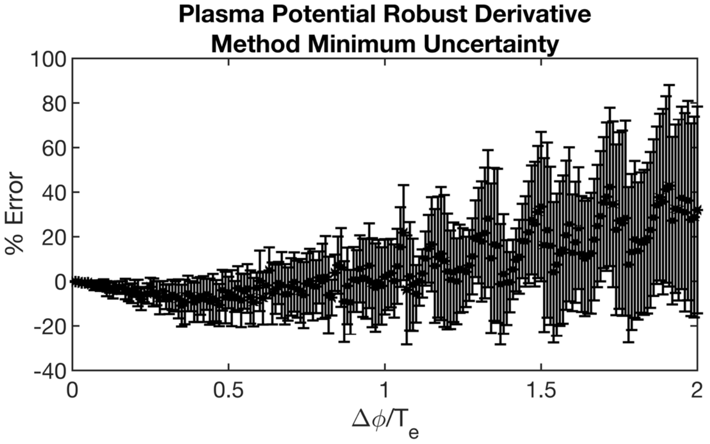
Plasma Potential Robust Derivative
Method Minimum Uncertainty

(c) Minimum uncertainty of the plasma potential using the robust derivative method.

Figure C.2: Minimum uncertainties of plasma potential measurements using various methods.

Figure C.2a shows the minimum uncertainty of the simple derivative method for determining the plasma potential as a function of bias step size normalized by the electron temperature. The plasma potential is exactly zero for the purposes of the simulation, and so the percent error is simply a factor of 100 greater than the calculated plasma potential. LP I-V curves were modeled using the retarded electron current (eq. 2.13) and the accelerated electron current (eq. 2.11) for the thick sheath condition over a range of electron temperatures ($0.1\,\mathrm{eV}$ to $1\,\mathrm{eV}$). The minimum uncertainty is the average percent error of plasma potential for all temperatures that were considered. The error bars are the standard deviation of the set.

Generally, there is a distinct shift between underestimating and overestimating the plasma potential when the voltage step size is roughly half the electron temperature. Additionally, the smaller the voltage step size relative to T_e, the better the accuracy of the plasma potential measurements. This behavior can be broadly attributed to the Nyquist–Shannon sampling theorem [208, 209] where the sampling rate must be less than or equal to half of the frequency of interest to avoid aliasing. In this case, the bias step size is analogous to the sampling rate and the electron temperature is analogous to the frequency. It is typically appropriate to sample at a voltage step size that is half of the plasma temperature, although smaller step sizes are preferred.

To achieve a minimum uncertainty of $20\,\%$, the voltage step size must be roughly $0.5T_e$ and a $5\,\%$ minimum uncertainty is achieved at a step size of roughly $0.1T_e$. This simple method is highly susceptible to problems related to large signal-to-noise ratios or effects that round the knee of the first derivative, such as probe surface contamination, operating in the sheath of another conductor, or ambient magnetic fields [210, 211, 212]. Therefore, it is useful to have an estimate of the plasma potential, which doesn't rely on the derivative, in order to determine a window of potentials to search for the peak in the first derivative. Such an estimate was derived by Brace and is detailed in the *University of Michigan's Langmuir Probe Spacecraft Potential (LPSP) instrument's end item specification document* [159]. The framing method is accomplished as follows:

1. Choose a current, I_1, that is in the ion saturation regime. This current is assumed to be the ion current, devoid of any electron current.

2. Since the ion current is typically much smaller than the electron current, a new current, $I_2 = -I_1$, is assumed to be close enough to the floating potential such that the potential at I_2, V_2, is a reasonable approximation to V_F. As an additional point, the electron current at V_2 is given by

$$\begin{aligned} I_2 &= I_{e_2} - I_i = -I_1 = I_i \\ \implies I_{e_2} &= 2I_i \end{aligned} \tag{C.8}$$

3. Estimate the electron temperature by finding the voltage, V_3, that is one T_e greater

than V_2. The net current at V_3 is

$$\begin{aligned}
I_3 &= I_{therm} exp\left(-\frac{V_P - V_3}{T_e}\right) - I_i \\
&= I_{therm} exp\left(-\frac{V_P - (V_2 + T_e)}{T_e}\right) - I_i \\
&= exp\,(1)\, I_{therm} exp\left(-\frac{V_P - V_2}{T_e}\right) - I_i \\
&= exp\,(1)\, I_{e_2} - I_i \\
&= 2exp\,(1)\, I_i - I_i \\
\therefore I_3 &= -4.436 I_1
\end{aligned}$$

4. If it is assumed that the potential difference between the floating potential and plasma potential is roughly $3T_e$, then the estimate of the plasma potential, V_4, is given by

$$V_4 = V_2 + 3\left(V_3 - V_2\right) \tag{C.9}$$

Equation C.9 gives an estimate of the plasma potential without any prior knowledge of the additional plasma characteristics, such as temperature and floating potential. However, as shown in fig. C.2b, it is a fairly inaccurate approximation of the plasma potential. In the voltage step size of interest, V_4 is typically $50\,\%$ off from the true plasma potential, and as the voltage step size approaches and grows greater than an electron temperature, this estimate can be very inaccurate surpassing $200\,\%$. Therefore, the window to search for the plasma potential using the first derivative is given by

$$V_2 \leq V_A \leq V_4 + \alpha\left(V_3 - V_2\right)$$

where α defines the upper bound of the applied voltages considered as a possible candidate for the plasma potential and typically ranges from 3 to 5 depending on the voltage step size. Figure C.2c demonstrates the end result of the robust derivative method (the global maximum of the first derivative is found within a window determined by the framing method) using modeled currents and voltages. As expected, it is identical to fig. C.2a, but predetermining a range of potentials that can be the plasma potential circumvents issues that can arise due to noise or rounded knees in the first derivative.

C.3 Ion Density

To determine the ion density, refer back to the current collection theory of a cylindrical probe in a drifting plasma detailed in section 2.3.2. There are three methods used to determine ion density using the current collection theory to a cylindrical probe in a moving plasma. They are

1. Use assumed or measured values of the ion temperature and drift speed to use the

full expression in eq. 2.21

$$I_i = \frac{qA_pN_iv_i}{\pi}\sqrt{1 + \frac{k_BT_i}{m_iv_i^2} + \frac{2q\left(V_P - V_A\right)}{m_iv_i^2}} \tag{C.10}$$

2. Assume the ion drift speed dominates over the effects of the attracting potential and random thermal motion such that

$$I_i = \frac{qA_pN_iv_i}{\pi} \tag{C.11}$$

3. Assume the attracting potential dominates over the effects of drift speed and random thermal motion such that

$$I_i = \frac{qA_pN_i}{\pi}\sqrt{\frac{2q\left(V_P - V_A\right)}{m_i}} \tag{C.12}$$

C.3.1 Full Ion Current Collection Expression

In orbit, the ion drift speed is equivalent to the orbital drift speed of the satellite and the temperature can typically be assumed to be equal to the electron temperature, if an ion energy analyzer is not available. However, in ground experiments, an ion energy analyzer, such as a retarding potential instrument, must be used to determine drift speed and temperature. These terms are necessary to obtain the ion density as the equation would have 3 unknowns and the system would be underdetermined otherwise.

C.3.1.1 Systematic Uncertainties

There are two ways to use the full expression to determine the ion density: 1) a single point approximation or 2) a fitting algorithm. As the name implies, the single point approximation will evaluate the measured ion current at a single applied bias to extract the ion density. The ion density given by the single point method is given by

$$N_i = \frac{I_i\pi}{qA_pv_i}\left(1 + \frac{k_BT_i}{m_iv_i^2} + \frac{2q\left(V_P - V_A\right)}{m_iv_i^2}\right)^{-\frac{1}{2}}. \tag{C.13}$$

To make the calculation of the uncertainty easier to understand, let

$$\alpha = \frac{I_i}{A_pv_i} \qquad\qquad \beta = \left(1 + \frac{k_BT_i}{m_iv_i^2} + \frac{2q\left(V_P - V_B\right)}{m_iv_i^2}\right)^{-\frac{1}{2}}.$$

Then the systematic uncertainty of the single point method is

$$\sigma_{N_I} = \frac{\pi}{q}\sqrt{(\beta\sigma_\alpha)^2 + \left(\frac{\alpha\beta^3}{2}\sigma_\beta\right)^2} \tag{C.14}$$

$$\sigma_\alpha = \sqrt{\left(\frac{\sigma_{I_i}}{A_p v_i}\right)^2 + \left(I_i\frac{\sigma_{A_p}}{A_p^2 v_i}\right)^2 + \left(\frac{I_i\sigma_{v_i}}{A_p v_i^2}\right)^2}$$

$$\sigma_\beta = \sqrt{\left(\frac{k_B\sigma_{T_i}}{m_i v_i^2}\right)^2 + \left(2q\frac{\sigma_{V_P}}{m_i v_i^2}\right)^2 + \left(2q\frac{\sigma_{V_B}}{m_i v_i^2}\right)^2 + \left(\frac{2k_BT_i + 4q\left(V_P - V_B\right)}{m_i v_i^3}\sigma_{v_i}\right)^2}$$

Notably, some of the terms in this uncertainty have minimal impact on the overall calculation. For instance, the probe area is very accurately known, and the ion temperature has little effect compared to the accelerating bias. These terms can generally be safely ignored but are included here for completeness.

To determine the ion density from a fitting algorithm, begin by linearizing eq. C.10 by squaring both sides. Then, the ion density is calculated from the slope of the line as follows

$$I_i^2 = \alpha V_B + \beta$$

$$\beta = \frac{1}{m_i}\left(\frac{qA_pN_i}{\pi}\right)^2\left(m_i v_i^2 + k_BT_i + 2qV_P\right)$$

$$\alpha = -\frac{2q^3}{m_i}\left(\frac{A_pN_i}{\pi}\right)^2$$

$$N_i = \frac{\pi}{A_p}\sqrt{\frac{\alpha m_i}{2q^3}} \tag{C.15}$$

$$\sigma_{N_i} = \sqrt{\frac{\pi^2 m_i}{2q^3}}\sqrt{\left(\frac{\sqrt{\alpha}\sigma_{A_p}}{A_p^2}\right)^2 + \left(\frac{\sigma_\alpha}{2A_p\sqrt{\alpha}}\right)^2} \tag{C.16}$$

where α is the slope, which is negative due to the decreasing ion current with increasing applied bias. Similar to the single point approximation, the probe area should be much more accurate than the errors due to fitting, and uncertainties due to the measured probe area can likely be ignored.

C.3.1.2 Minimum Uncertainty due to Method

When using the single point approximation, the ion density is found by simply choosing a current in the ion saturation regime and using eq. C.13. To determine the percent error, LP I-V curves were modeled using the difference between the accelerated ion current (eq. 2.19) over a variety of ion drift speeds between $1\,\mathrm{eV}$ to $10\,\mathrm{eV}$ and an ion temperature of $0.1\,\mathrm{eV}$. Figure C.3 shows the minimum uncertainty of this method as a function of probe potential normalized by the ion drift speed and for three ratios between electron and ion temperature. That is the electron temperature was modeled as being 1, 5, and 10 times greater than the ion temperature. Then, the ion temperature was assumed to be equal to the electron

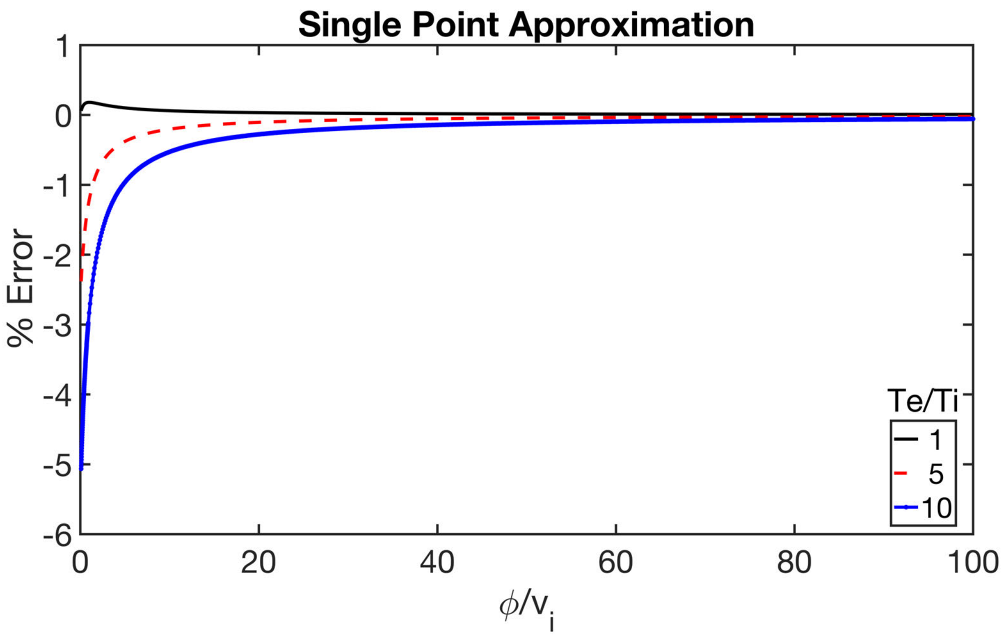

Figure C.3: Minimum uncertainty of the ion density using the single point approximation of the full ion current expression.

temperature when calculation the ion density. As can be seen from fig. C.3, even when the ion temperature is overestimated by a factor of 10, the greatest percent error is roughly $5\,\%$. Therefore, an acceptable approximation for in-orbit conditions is that the ion and electron temperatures are equal. Unsurprisingly, for large probe potentials relative to the ion drift speed, the percent error reaches a maximum of $0.5\,\%$. Physically, this is due to the fact that the accelerating potential completely dominates any effects due to drift speed or random thermal motion. This is also seen numerically, as eqs. 2.16, 2.19 and 2.21 all give nearly identical results for large probe potentials. Therefore, when using this single point approximation, the uncertainties will mostly likely be dominated by systematic uncertainties, as opposed to the method's intrinsic uncertainty.

Another analysis method that employs the full ion current collection expression is to use it as a model to fit to the measured ion current. The procedure for this method would go as follows:

1. Linearize the measured I-V curve by squaring the currents. An example of the linearized current is given in fig. C.4a.
2. Fit the appropriate region of the linearized ion current using a first order polynomial. The difficulty here is determining the range of potentials to apply the fit to.
3. Use eq. C.15 to determine the ion density from the resulting slope of the fit.

From fig. C.4a, it is apparent that the net current is linear when squared until the probe potential is near the floating potential. This is due to the electron current beginning to dominate the collected currents. The difficulty in employing this fitting method is deciding

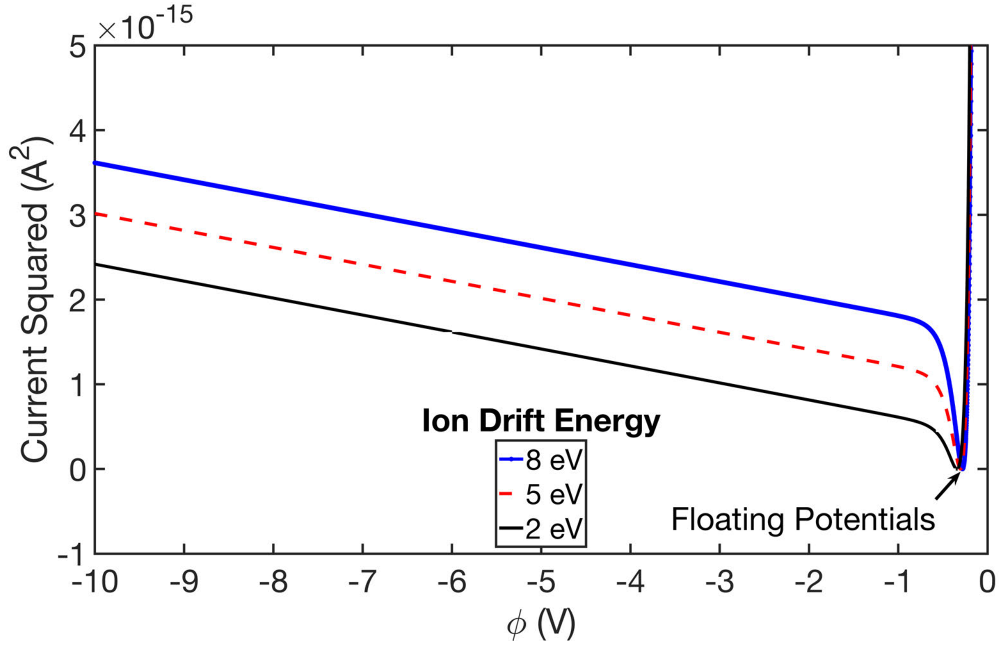

(a) Linearized ion current for three example ion drift speeds. The local minimum is the floating potential.

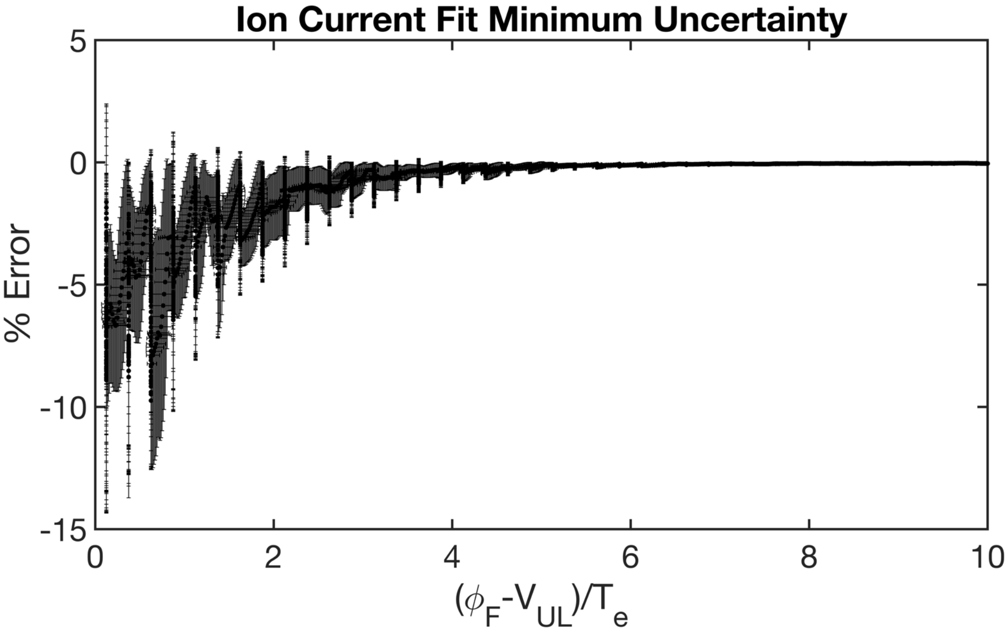

(b) Minimum uncertainty of the ion density using the fit of the full ion current expression. V_{UL} is the upper limit of the fit. The normalization is the ratio of difference between the floating potential and this upper limit and the electron temperature.

Figure C.4: Minimum uncertainties of ion density measurements using a fit of the full ion current collection expression.

the most positive potential that is still within the ion saturation regime (assuming the lower bound is the most negative potential to which the probe was biased). As shown in fig. C.4b, choosing an upper potential limit that is seven to ten electron temperatures below the floating potential ensures the intrinsic percent error of this method is below $1\,\%$. Choosing an upper potential limit that is too close to the floating potential can drastically affect the minimum uncertainty of the ion density depending on the electron temperature and ion drift speed. Generally, hotter electron temperatures and faster ion drift speeds have greater errors. This relationship with drift speed and electron temperature, combined with window of the moving average filter, produces the sawtooth pattern in fig. C.4b. To determine the percent error, LP I-V curves were modeled using the difference between the retarded electron current (eq. 2.13) and the accelerated ion current (eq. 2.19) over a range of electron temperatures ($0.1\,\mathrm{eV}$ to $1\,\mathrm{eV}$) and a range of ion drift speeds ($1\,\mathrm{eV}$ to $10\,\mathrm{eV}$). The ion density used to model the currents was then compared to the ion density obtained using the three step fitting procedure previously detailed. The minimum uncertainty is obtained using a moving average filter with a window size of $0.1\,\%$ of the total number of calculated percent errors. The error bars are calculated using a moving standard deviation filter with the same window size. From fig. C.4b, a potential that is at least $7T_e$ below the floating potential should be chosen as the upper bound of the fit.

C.3.2 Drift Speed Dominant Approximation

The benefit of the drift speed dominant approximation (eq. C.11) is its independence of ion temperature, which is rarely known unless specifically measured. However, its lack of potential dependence implies that it will begin to deviate strongly for sufficiently large attracting potentials.

C.3.2.1 Systematic Uncertainties

By manipulating eq. C.11, the ion density and its systematic uncertainties are given as

$$N_i = \frac{\pi I_i}{q A_p v_i} \tag{C.17}$$

$$\sigma_{N_i} = \frac{\pi}{q}\sqrt{\left(\frac{\sigma_{I_i}}{A_p v_i}\right)^2 + \left(\frac{I_i \sigma_{A_p}}{A_p^2 v_i}\right)^2 + \left(\frac{I_i \sigma_{v_i}}{A_p v_i^2}\right)^2} \tag{C.18}$$

The most likely dominant source of error here is the ion drift speed, as it requires either an RPA to make direct measurements of the ion's energy distribution function, or accurate knowledge of a spacecraft's orbital velocity.

C.3.2.2 Minimum Uncertainty due to Method

When assuming the ion drift speed is the dominant term in the collected ion current, the ion density is found by simply choosing a current in the ion saturation regime and using eq. C.17. Figure C.5 shows the minimum uncertainty of this method as a function of probe potential normalized by the ion drift speed. To determine the percent error, LP I-V curves were modeled using the difference between the accelerated ion current (eq. 2.19) over a variety of ion drift speeds between $1\,\mathrm{eV}$ to $10\,\mathrm{eV}$ and an ion temperature of $0.1\,\mathrm{eV}$. The minimum uncertainty shown in fig. C.6 is obtained by averaging over the results of all ion drift speeds at each potential to drift speed ratio. The error bars are the standard deviation of the same set. The probe bias must be less than the ion drift speed for this approximation to be valid, as the minimum uncertainty grows nearly exponentially for all cases of a probe bias larger than an ion drift speed. To achieve a minimum uncertainty of $10\,\%$, the bias must be roughly $0.2v_i$ and a $5\,\%$ minimum uncertainty is achieved at a potential of roughly $0.1v_i$.

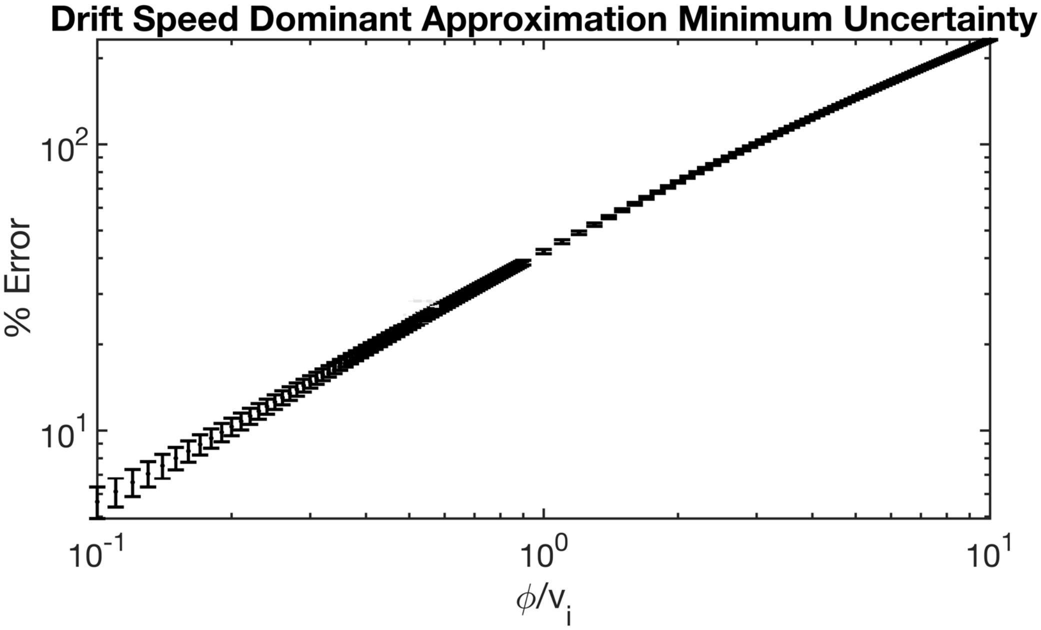

Figure C.5: Minimum uncertainty of the dominant ion drift speed approximation.

C.3.3 Dominant Accelerating Bias Approximation

The benefit of the dominant accelerating bias approximation (eq. C.12) is its ability to approximate the density without needing to know the ion drift speed nor ion temperature. The ion temperature does not typically affect the collected currents greatly, however this approximation is best applied for large biases relative to the ion drift speed.

C.3.3.1 Systematic Uncertainties

By manipulating eq. C.12, the ion density and its systematic uncertainties are given as

$$N_i = \frac{\pi I_i}{qA_p}\sqrt{\frac{m_i}{2q\phi}} \tag{C.19}$$

$$\phi = -\left(V_A - V_P\right)$$

$$\sigma_{N_i} = \frac{\pi}{q}\sqrt{\frac{m_i}{2q}}\sqrt{\left(\frac{\sigma_{I_i}}{A_p\sqrt{\phi}}\right)^2 + \left(\frac{I_i\sigma_{A_p}}{A_p^2\sqrt{\phi}}\right)^2 + \left(\frac{I_i\sigma_{V_P}}{2A_p\phi^{\frac{3}{2}}}\right)^2 + \left(\frac{I_i\sigma_{V_A}}{2A_p\phi^{\frac{3}{2}}}\right)^2} \tag{C.20}$$

The most likely dominant sources of error is error due to the plasma potential. Additionally, this approximation diverges as the probe bias approaches the plasma potential and so it should not be applied when the probe potential relative to the plasma potential, ϕ, is less than the ion drift speed.

C.3.3.2 Minimum Uncertainty due to Method

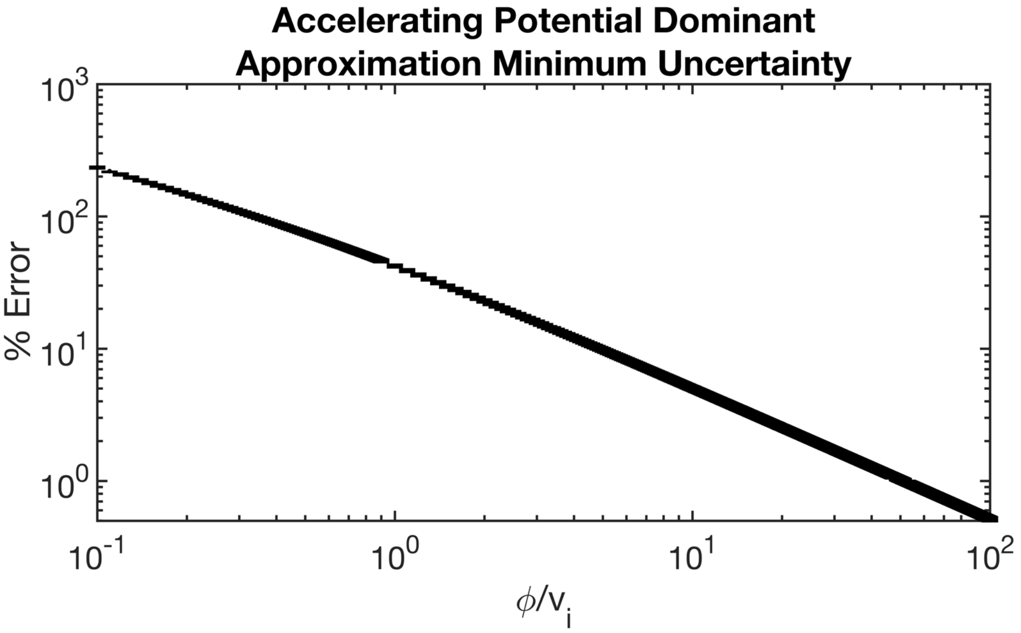

Figure C.6: Minimum uncertainty of the dominant accelerating potential approximation.

When assuming the accelerating potential is the dominant term in the collected ion current, the ion density is found by simply choosing a current in the ion saturation regime and using eq. C.19. Figure C.6 shows the minimum uncertainty of this method as a function of probe potential normalized by the ion drift speed. To determine the percent error, LP I-V curves were modeled using the difference between the accelerated ion current (eq. 2.19) over a variety of ion drift speeds between $1\,\mathrm{eV}$ to $10\,\mathrm{eV}$ and an ion temperature of $0.1\,\mathrm{eV}$. The minimum uncertainty shown in fig. C.6 is obtained by averaging over the results of all ion drift speeds at each potential to drift speed ratio. The error bars are the standard deviation of the same set. The probe bias must be greater than the ion drift speed for this approximation to be valid. The uncertainties grow nearly exponentially for all cases of a probe bias smaller than an ion drift speed. To achieve a minimum uncertainty of $10\,\%$, the bias must be roughly $5v_i$, and a $5\,\%$ minimum uncertainty is achieved at a bias of roughly $10v_i$.

Interestingly, the ion drift speed dominant and accelerating potential dominant approximations are the reciprocals of one another in terms of minimum uncertainty. Their minimum uncertainties agree at their shared limit where the probe potential is equal to the ion drift speed. At that point, their minimum uncertainty is approximately $44\,\%$.

C.4 Electron Current Determination

Regardless of the appropriate ion current collection scheme, the electron current is always obtained using the following method:

1. Perform a linear fit of the ion saturation region.
2. Evaluate the fit result for all biases between the plasma potential and the most negative applied probe potential.
3. Subtract the calculated currents from the net current to estimate the electron current.

C.4.0.1 Systematic Uncertainties

The linear fit can be interpreted as a first order Taylor expansion of the true ion current whose error is the difference between the ion current scheme (i.e. thin sheath, OML, drifting Maxwellian), $I_{i_{scheme}}$, and the linear fit. The electron current equation and its corresponding uncertainty are shown in eqs. C.21 and C.22. Using the electron current, the electron density and temperature can now be determined.

$$I_e = I - I_{i_{fit}} \tag{C.21}$$

$$\sigma_{I_e} = \sqrt{\sigma^2_{I_{inst}} + \sigma^2_{I_{i_{fit}}}} \tag{C.22}$$

$$\sigma_{I_{i_{fit}}} = I_{i_{scheme}} - I_{i_{fit}}$$

C.4.0.2 Minimum Uncertainty due to Method

Figure C.7 shows the minimum uncertainty of this method as a function of probe potential normalized by the electron temperature. To determine the percent error, LP I-V curves were modeled using the difference between the retarded electron current (eq. 2.13) and the accelerated ion current (eq. 2.19) over a range of electron temperatures ($0.1\,\mathrm{eV}$ to $1\,\mathrm{eV}$), a range of ion drift speeds ($1\,\mathrm{eV}$ to $10\,\mathrm{eV}$), and an ion temperature of $0.1\,\mathrm{eV}$. For clarity, the average value at each ratio of potential to electron temperature is reported. The electron current used to model the currents was then compared to the calculated electron current obtained using the three step fitting procedure previously detailed. In the electron retardation regime, the minimum uncertainty of this method ranges from less than $1\,\%$,

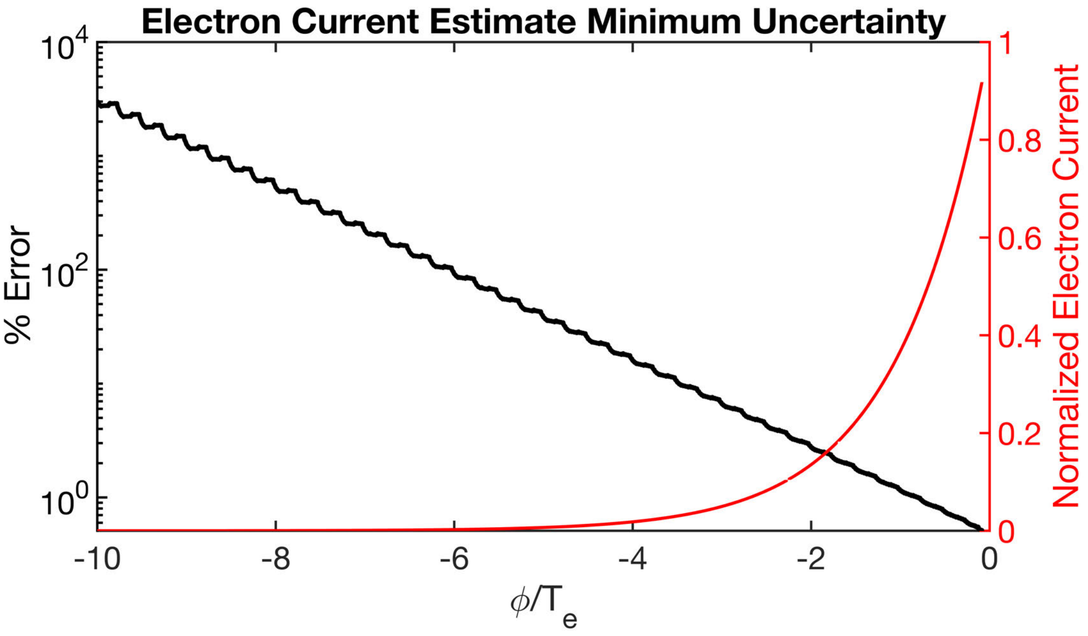

Figure C.7: Minimum uncertainty of the electron current calculation using a linear ion current estimate.

when within an electron temperature from the plasma potential, to roughly $30\,\%$, when the electron current is nearly extinguished at $5T_e$ below the plasma potential. Below $5T_e$ from the plasma potential, the error increases exponentially because the calculation is effectively dividing a linear polynomial by an exponential function that is approaching 0. Eventually, the calculation is no different than attempting to divide by zero. As a result, this uncertainty becomes meaningless beyond seven to ten electron temperatures below the plasma potential.

C.5 Electron Temperature

There are many methods used to determine the electron temperature with a variety of assumptions. The methods that are analyzed here are:

1. Potential difference methods: These methods estimate the electron temperature based on the difference between the plasma and floating potential.

2. Integral method: This method focuses on integrating the calculated electron current.

3. Log-linear fitting method: This method linearizes the calculated electron current and determines the temperature from the inverse of the slope of the fit.

4. Single point method: This method evaluates the ratio between the electron thermal current and derivative at the plasma potential to produce the electron temperature.

5. EEDF method: This method starts by estimating the electron energy distribution from the calculated electron current and then analyzing the EEDF to determine the temperature.

C.5.1 Potential Difference Method

There are two possible estimates of electron temperature based on the potential difference between the plasma and floating potential. If the plasma is stationary, the relationship between these two potentials is [213]

$$T_e = \frac{V_F - V_P}{ln\left[0.6\sqrt{\frac{2\pi m_e}{m_i}}\right]}. \tag{C.23}$$

where the ion current is assumed to be due to ions moving with the Bohm velocity, and the electron current is given by eq. 2.13. If the plasma has a directional flow, then the ion current, given by eq. C.10, and the electron current, modeled using eq. 2.13, are equal at the floating potential and the temperature can be estimated as follows

$$\begin{aligned}
&\frac{qA_pN_iv_i}{\pi}\sqrt{1+\frac{k_BT_i}{m_iv_i^2}+\frac{2q\left(V_P-V_A\right)}{m_iv_i^2}} = qA_pN\sqrt{\frac{k_BT_e}{2\pi m_e}}\exp\left(\frac{-\left(V_P-V_F\right)}{Te}\right)\\
\Longrightarrow\ &\frac{qA_pN_iv_i}{\pi} \approx qA_pN\sqrt{\frac{k_BT_e}{2\pi m_e}}\exp\left(\frac{-\left(V_P-V_F\right)}{Te}\right)\\
\Longrightarrow\ &\frac{v_i}{\pi}\sqrt{\frac{2\pi m_e}{k_BT_e}} \approx \exp\left(\frac{-\left(V_P-V_F\right)}{Te}\right)\\
\Longrightarrow\ &\ln\left(\sqrt{\frac{2v_i^2m_e}{\pi k_BT_e}}\right) \approx -\frac{V_P-V_F}{Te}\\
&\therefore T_e\ln\left(\frac{\pi k_BT_e}{2v_i^2m_e}\right) \approx 2\left(V_P-V_F\right)
\end{aligned} \tag{C.24}$$

where eq. C.10 is assumed to be dominated by the drift current (see eq. C.11).

C.5.1.1 Systematic Uncertainties

The systematic uncertainty in eq. C.23, is given by

$$\sigma_{T_e} = ln\left[\frac{1}{0.6}\sqrt{\frac{m_i}{2\pi m_e}}\right]\sqrt{\sigma_{V_F}^2+\sigma_{V_P}^2} \tag{C.25}$$

The error in the potential difference method with a drifting plasma is calculated using Monte Carlo methods to vary the plasma potential, floating potential, and ion drift speed within their respective uncertainties. The total error is then the square root of the sum of squares of the standard deviations of the calculated temperature due to uncertainties in the measurements.

C.5.1.2 Minimum Uncertainty due to Method

The intrinsic uncertainty of the electron temperature estimate of the potential difference method, assuming a stationary plasma (shown in fig. C.8), was calculated using two separate models. LP I-V curves were modeled using the difference between the retarded electron current (eq. 2.13) and the accelerated ion current (eq. 2.19) over a range of electron temperatures ($0.1\,\mathrm{eV}$ to $1\,\mathrm{eV}$) and a range of ion drift speeds ($1\,\mathrm{eV}$ to $10\,\mathrm{eV}$). For the non-drifting ion case, the ion current was modeled using eq. 2.19 for the case where $s = 0$. The calculated electron temperature for both cases are then compared to the temperature used to model the currents. The minimum uncertainty for both cases are then averaged at each drift energy to electron temperature ratio. The error bars are the standard deviation of each set.

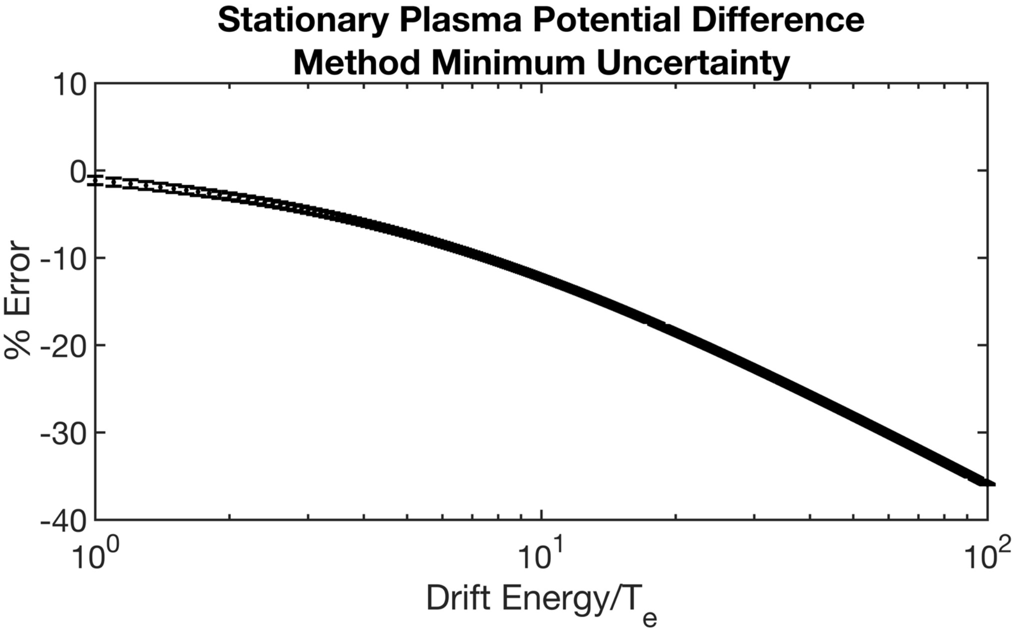

Figure C.8: Minimum uncertainty of the potential difference method in a stationary plasma.

As expected, when the currents were modeled with a non-drifting ion population, the stationary plasma temperature approximation is highly accurate, with less than a $1\,\%$ error regardless of temperature. However, if the plasma was modeled with a drifting ion population, the error in the method would grow as the drift energy to electron temperature ratio increases. For typical ionospheric temperatures, this ratio ranges from 10 to 50 and so the minimum uncertainty would be roughly $10\,\%$ to $30\,\%$, with colder plasmas having higher uncertainties. If it is assumed that the ion population had a non-zero drift speed, the flowing plasma drift potential temperature estimate is $10\,\%$ to $20\,\%$ over the same range (shown in fig. C.9). The drifting plasma approximation runs into problems at both extremes of the ratio. As the drift energy to electron temperature ratio approaches 0, the logarithmic portion approaches infinity. When the ratio is very large, the logarithmic portion of eq. C.24 tends towards negative infinity. Since this method is divergent at its boundaries, it is usually safer to use the non drifting potential difference method.

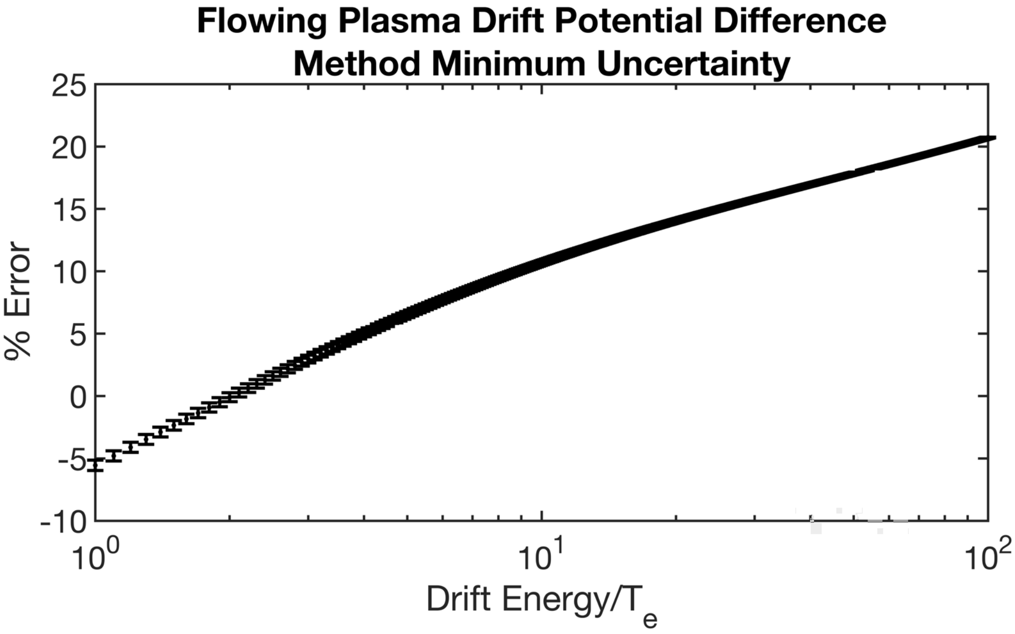

Figure C.9: Minimum uncertainty of the potential difference method in a flowing plasma.

C.5.2 Integration of Measured Current Method

The integral method, highlighted in [150], is a general method that is independent of the electron distribution and provides an average electron temperature. Therefore, for an electron population with a single peak distribution, such as the Maxwellian distribution, the average electron temperature is the electron temperature. However, if the distribution has a high energy tail or is double peaked, like the Bi-Maxwellian distribution, the resultant calculated temperature would be the average of the temperatures for each distinct segment of the distribution.

While the integral method for determining electron temperature can be used for a general EEDF [150], the scope of the following proof will focus solely on a Maxwellian electron energy distribution. Assuming the majority of the electron current is between the floating and plasma potentials,

$$\int_{V_f}^{V_P} I_e(\phi)\,d\phi = I_{e_{therm}} k_B T_e \exp\left(\frac{\phi}{T_e}\right)\Bigg|_{V_f}^{V_P}$$

$$\implies T_e = \frac{1}{I_{e_{therm}}\left(1-\exp\left(\frac{V_F}{T_e}\right)\right)}\int_{V_f}^{V_P} I_e(\phi)\,d\phi$$

$$\therefore \implies T_e \approx \frac{1}{I_{e_{therm}}}\int_{V_f}^{V_P} I_e(\phi)\,d\phi \tag{C.26}$$

where $I_{e_{therm}}$ is the electron current at the plasma potential and ϕ is the potential difference between the LP bias and the ambient plasma potential. A simplification is made by assuming that $\exp\left(\frac{V_F}{T_e}\right) << 1$. Since the magnitude of the electron current at the floating potential is negligible when compared to the electron saturation current this simplification is generally valid.

C.5.2.1 Systematic Uncertainties

While a strong benefit of this method is its independence on the underlying electron distribution, it has multiple sources of error that could affect its final result,such as the number of points used for integration and properly selecting the boundaries of integration. The method and error analysis are shown in eqs. C.27 and C.28.

$$T_e = \frac{1}{I_{sat}} \int_{V_F}^{V_P} I_e(V_B) dV_B = \frac{(V_P - V_F)}{2 N I_{sat}} \sum_{n=1}^{N} \left[I(V_n) + I(V_{n+1}) \right] \tag{C.27}$$

$$\begin{gathered}
S = \frac{(V_P - V_F)}{2N} \sum_{n=1}^{N} \left[I(V_n) + I(V_{n+1}) \right] \\
\implies \begin{array}{c} \frac{\partial S}{\partial V_P}\sigma_{V_P} = \frac{S}{V_P - V_F}\sigma_{V_P} \quad \frac{\partial S}{\partial V_F}\sigma_{V_F} = -\frac{S}{V_P - V_F}\sigma_{V_F} \quad \frac{\partial S}{\partial N}\sigma_{\phi_N} = -\frac{S}{N}\sigma_N \\ \frac{\partial S}{\partial I(V_n)}\sigma_{I(V_n)} = \frac{(V_P - V_F)}{2N}\sum_{n=1}^{N}\left[\sigma_{I(V_n)} + \sigma_{I(V_{n+1})}\right] \end{array} \\
\therefore \sigma_{T_e} = \frac{1}{I_{sat}} \left(\left[\frac{S}{I_{sat}} \sigma_{I_{sat}} \right]^2 + \left[\frac{S}{V_P - V_F} \sigma_{V_P} \right]^2 + \left[\frac{S}{V_P - V_F} \sigma_{V_F} \right]^2 + \right. \\
\left. \left[\frac{S}{N} \sigma_N \right]^2 + \left[\frac{(V_P - V_F)}{2N} \sum_{n=1}^{N} \left[\sigma_{I(V_n)} + \sigma_{I(V_{n+1})} \right] \right]^2 \right)^{\frac{1}{2}}
\end{gathered} \tag{C.28}$$

It should be noted that the last term of eq. C.28 will simplify to $(V_P - V_F)\,\sigma_{I_e}$ if the error of each current term is equal. Additionally, in eqs. C.27 and C.28, N is the number of points used in the integral.

C.5.2.2 Minimum Uncertainty due to Method

The intrinsic uncertainty of the electron temperature estimate using an integral method follows a trend similar to that of the plasma potential method's uncertainty. From fig. C.10, there are three regions of interest to discuss. When the step size is larger than about half the electron temperature, the percent error consistently increases. This is likely due to under-sampling the electron retardation regime resulting in an increasingly larger overestimation of the electron temperature. The upper bound for when this technique should be used is when the voltage step size is roughly a quarter of the electron temperature, as all step sizes at or below this limit have a minimum uncertainty that ranges from $1\,\%$ to $3\,\%$. When the retardation regime is properly sampled, this method will always underestimate the electron temperature, as the highest energy electrons are still being collected at potentials below the floating potential, and are therefore unaccounted for.

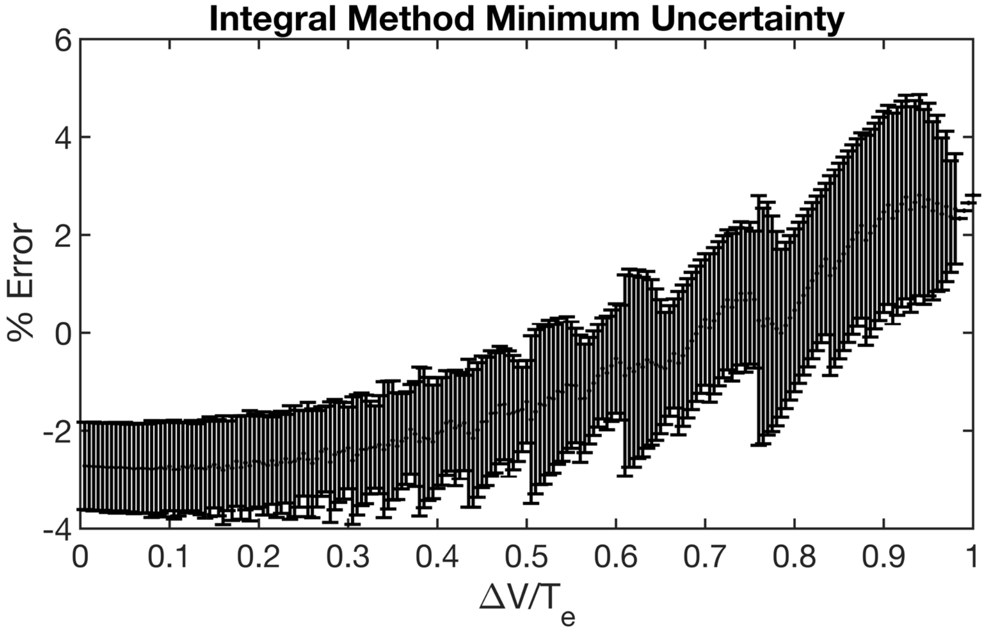

Figure C.10: Minimum uncertainty of the integral method in a flowing plasma.

LP I-V curves were modeled using the retarded electron current (eq. 2.13) over a range of electron temperatures ($0.1\,\mathrm{eV}$ to $1\,\mathrm{eV}$). The minimum uncertainty is reported as the average of all percent errors for a given ratio of voltage step size to electron temperature. The error bars are the standard deviation of the same data set.

C.5.3 Log-Linear Fitting Method

Assuming the electron population is described by a Maxwellian distribution, the collected electron current is described by eq. 2.13. The calculated electron current can then be linearized such that

$$\ln\left(I\left(\phi\right)\right) \approx \frac{\phi}{T_e} + I_{e_{therm}} \tag{C.29}$$

where $I_{e_{therm}}$ is the electron thermal current.

C.5.3.1 Systematic Uncertainties

To determine the temperature from the log-linear fit method,

1. Linearize the the calculated electron current by taking the natural logarithm of the current between the floating potential and plasma potential.

2. Fit a first degree polynomial to the linear region.

3. The inverse of the slope of the fit is the electron temperature estimate.

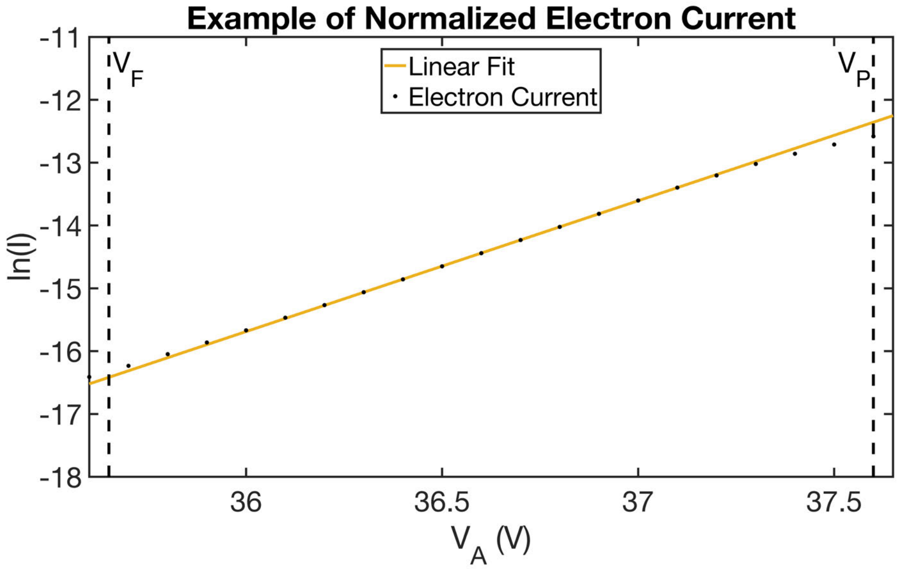

(a) Example of first degree polynomial fit to linearized electron current using measured currents.

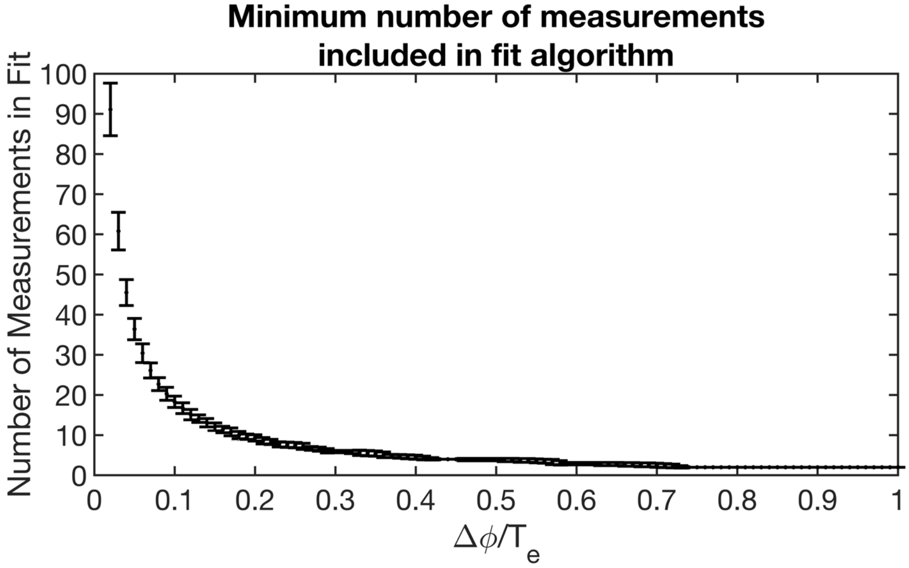

(b) The number of points included in the fitting algorithm based on ratio between step size and temperature.

Figure C.11: Linear fit to determine electron temperature example and estimate of step size required for proper fitting.

Following the last line of the procedure, the electron temperature is given as

$$T_e = \frac{1}{\alpha} \tag{C.30}$$

where α is the slope of the line. The uncertainty of this method is estimated using Monte Carlo schemes where the plasma potential, floating potential, electron current, and voltages are varied.

C.5.3.2 Minimum Uncertainty due to Method

With the analytic schemes that have modeled the electron and ion currents so far, it is not possible to replicate the issues observed with this method near the floating and plasma potential when analyzing physically measured currents. This is because near these potentials, the plasma behavior between retarded and accelerated currents tends to overlap slightly. Generally, there are non-linear behaviors near the floating potential and plasma potential that must be avoided to minimize the uncertainty due to this method (see fig. C.11a). Assuming the retardation regime is properly sampled, the simplest way of avoiding the non-linear segments of the linearized electron current is to fit the currents that correspond to potentials ranging from

$$V_F + \frac{1}{4}\left(V_P - V_F\right) \leq \phi \leq V_P - \frac{1}{4}\left(V_P - V_F\right).$$

This range effectively fits the electron retardation region with a $25\,\%$ spread above and below the midpoint between the plasma and floating potentials. As shown in fig. C.11b, a ratio of $0.25T_e$ or below is the ideal voltage step size for a proper fit, but a voltage step size of $0.5T_e$ would be the absolute upper limit for applying this method. LP I-V curves were modeled using the retarded electron current (eq. 2.13) over a range of electron temperatures ($0.1\,\mathrm{eV}$ to $1\,\mathrm{eV}$). The minimum number of measurements in the fit are then averaged over all temperatures for each ratio.

C.5.4 Single Point Method

The single point method takes advantage of the exponential behavior of the retarded electron current. The first derivative of the current is also exponential, just like the calculated electron current, and so the electron temperature is given by the ratio of the electron current and its first derivative [214] (eq. C.31).

$$\left.\frac{I_e\left(\phi\right)}{\frac{dI_e(\phi)}{d\phi}}\right|_{\phi=V_P} = \left.\frac{I_{e_{therm}}\exp(\frac{\phi}{T_e})}{\frac{I_{e_{therm}}}{T_e}\exp(\frac{\phi}{T_e})}\right|_{\phi=V_P} = T_e \tag{C.31}$$

The ratio is evaluated specifically at the plasma potential such that the exponentials are both 1.

C.5.4.1 Systematic Uncertainties

The uncertainty of the single point method is given by

$$\sigma_{T_e} = \sqrt{\left(\left. \frac{\sigma_{I_e(\phi)}}{\frac{dI_e(\phi)}{d\phi}} \right|_{\phi=V_P} \right)^2 + \left(\left. \frac{I_e(\phi)\, \sigma_{\frac{dI_e(\phi)}{d\phi}}}{\left(\frac{dI_e(\phi)}{d\phi}\right)^2} \right|_{\phi=V_P} \right)^2} \tag{C.32}$$

C.5.4.2 Minimum Uncertainty due to Method

As is generally the case with single point methods, the single point method for determining electron temperature has high uncertainties and should be used as a rough estimate at best. Even when the step size of the potential is a quarter of the electron temperature, the minimum uncertainty can be as high as $20\,\%$ at the larger electron temperatures that we considered (see fig. C.12). LP I-V curves were modeled using the retarded electron current (eq. 2.13) and the accelerated electron current (eq. 2.11) for the thick sheath condition over a range of electron temperatures ($0.1\,\mathrm{eV}$ to $1\,\mathrm{eV}$). The minimum uncertainties for both cases are then averaged over all temperatures for the same voltage step size ratio.

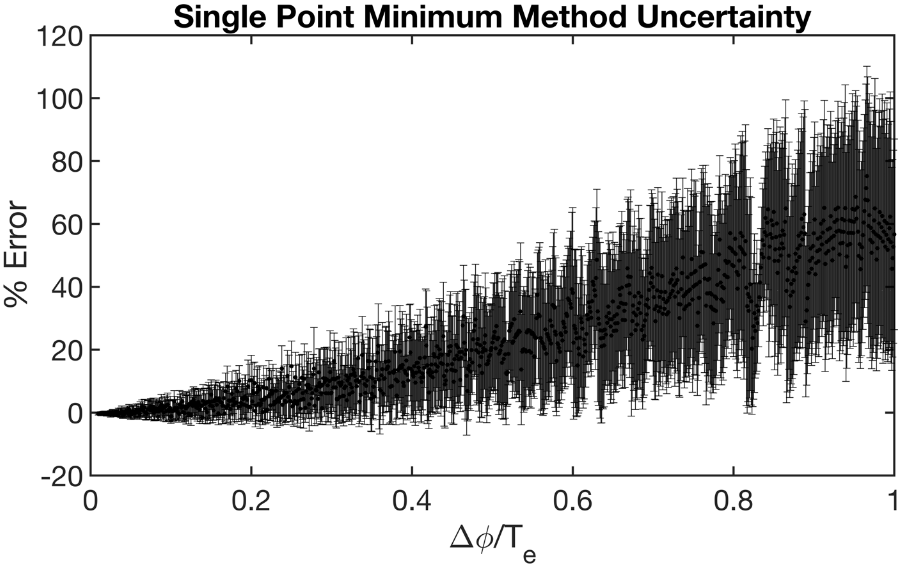

Figure C.12: Minimum uncertainty of the single point method as a function of step size relative to electron temperature.

C.5.5 EEDF Method

The final temperature determination method analyzes the electron energy distribution function. In the 1930s, Druyvesteyn determined that, for isotropic distribution functions, the retarded electron current is related to the energy distribution function as follows [215]

$$f\left(\epsilon\right) = \frac{2}{q^2 A_p} \sqrt{\frac{2m\left(-\phi\right)}{q}} \frac{d^2 I}{dV^2} \tag{C.33}$$

where ϵ is the particle energy. Since the electron energy distribution function is Maxwellian, the second derivative of the calculated electron current must be compared to the energy-dependent form of the Maxwellian distribution,

$$f\left(\epsilon\right) = \frac{2}{T_e^{\frac{3}{2}}} \sqrt{\frac{\epsilon}{\pi}} \exp\left(-\frac{\epsilon}{T_e}\right). \tag{C.34}$$

To determine the electron temperature:

1. Calculate the second derivative of the calculated electron current.
2. Evaluate eq. C.33 and normalize it by its peak.
3. Fit eq. C.34, when normalized by its own peak, to the normalized form of eq. C.33.

C.5.5.1 Systematic Uncertainties

Since all equations are normalized, the systematic uncertainty is due purely to the plasma potential measurement's uncertainty, the error in the fit, and the error in the sourced voltage. To calculate the error, a Monte Carlo method is used to vary the plasma potential and sourced voltage, within their respective limits due to its uncertainty. Then the total uncertainty is

$$\sigma_{T_e} = \sqrt{\sigma_{V_p}^2 + \sigma_{\phi}^2 + \sigma_{fit}^2} \tag{C.35}$$

where σ_{V_p} is the standard deviation of the electron temperature due to the error in the plasma potential, σ_{ϕ} is the standard deviation of the electron temperature due to the error in the sourced potential, and σ_{fit} is the standard error of the mean of all of the fits used in the Monte Carlo method.

C.5.5.2 Minimum Uncertainty due to Method

Figure C.13 demonstrates the minimum uncertainty of EEDF fit method over a range of ratios between the voltage step size and the electron temperature. As has been the case with all other methods, for voltage step sizes greater than half an electron temperature, the minimum uncertainty grows dramatically. At $0.5T_e$ the minimum uncertainty is roughly $12\,\%$; however, voltage step sizes at half of a T_e are the extreme upper bound of this method. To achieve a minimum uncertainty of $6\,\%$, the bias must be roughly $0.25T_e$, and a $2\,\%$ minimum uncertainty is achieved at a bias of roughly $0.2T_e$. This method doesn't improve much for voltage step sizes smaller than $0.2T_e$.

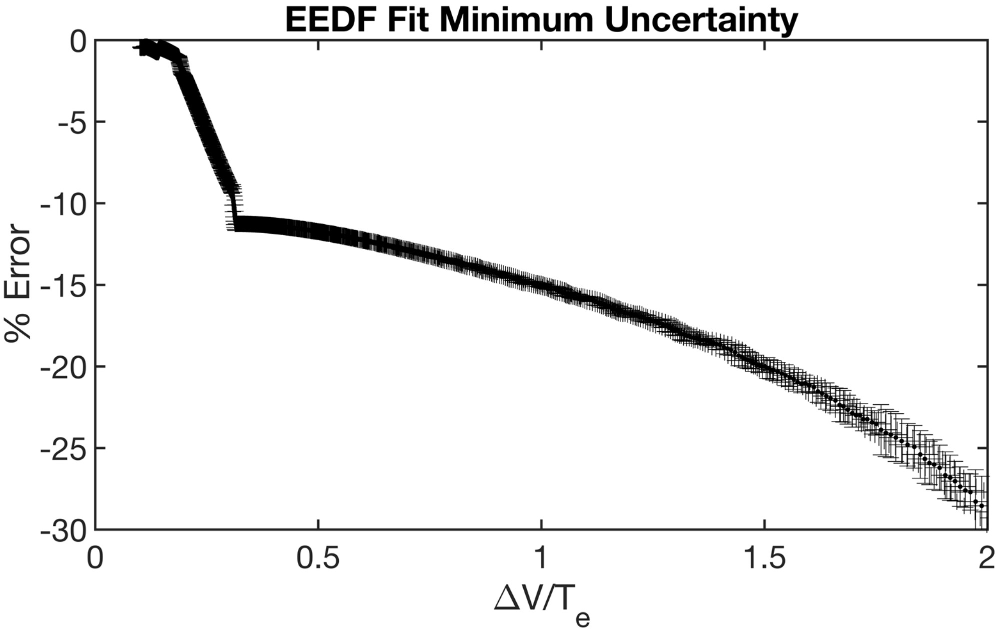

Figure C.13: Minimum uncertainty of the EEDF fit method as a function of the ratio between the potential step size and electron temperature.

LP I-V curves were modeled using the retarded electron current (eq. 2.13) over a range of electron temperatures ($0.1\,\mathrm{eV}$ to $1\,\mathrm{eV}$). The minimum uncertainty for both cases are then averaged using a moving average filter with a window size of $1\,\%$ of the total number of calculated percent errors. The error bars are calculated using a moving standard deviation filter with the same window size.

C.6 Electron Density

The last plasma characteristic to determine is the electron density. Like the ion density and electron temperature, there are many methods used to determine the electron density with a variety of assumptions. The methods analyzed here are:

1. Thermal current method: This method determines the electron thermal current to calculate the electron density.
2. OML current approximation: This method analyzes the electron saturation regime under orbit motion limited conditions.
3. EEDF method: This method starts by estimating the electron energy distribution from the calculated electron current and then analyzing the EEDF to determine the density.

C.6.1 Thermal Current Method

The thermal current method determines the electron density through the electron current at the plasma potential, otherwise known as the electron thermal current,

$$\begin{aligned} I_{e_{therm}} &= qA_pN_e\sqrt{\frac{k_BT_e}{2\pi m_e}} \\ \therefore N_e &= \frac{I_{e_{therm}}}{qA_p}\sqrt{\frac{2\pi m_e}{k_BT_e}} \end{aligned} \tag{C.36}$$

C.6.1.1 Systematic Uncertainties

This method generally has large uncertainties due to its dependence on both the plasma potential and the electron temperature. Its systematic uncertainty is

$$\begin{aligned} \sigma_{N_e} &= \sqrt{\frac{2\pi}{q^2k_B}}\sqrt{\left(\frac{\sigma_{I_{e_{therm}}}}{T_e^{\frac{1}{2}}}\right)^2 + \left(\frac{I_{e_{therm}}\sigma_{T_e}}{2T_e^{\frac{3}{2}}}\right)^2} \\ \sigma_{I_{e_{therm}}} &= \sqrt{\left.\sigma_{I_e}\right|^2_{\phi=V_P} + \left(\frac{dI_e}{dV}\sigma_{V_{inst}}\right)^2\Bigg|_{\phi=V_P}} \end{aligned} \tag{C.37}$$

where the uncertainty of the thermal electron current is related to both the uncertainty of calculated electron current and the electron current's dependence on the probe potential.

C.6.1.2 Minimum Uncertainty due to Method

Since this method relies on a single measurement, it is incredibly sensitive to the choice of electron current. Specifically, the electron current must be evaluated as close to the actual plasma potential as possible. As seen in fig. C.14, deviations from the plasma potential as large as one electron temperature above or below the plasma potential results in minimum uncertainties of $60\,\%$. Furthermore, to achieve about a $10\,\%$ minimum uncertainty, the electron current must be evaluated within $0.1T_e$ of the plasma potential. However, these constraints are typically difficult to meet as both the plasma potential and electron temperature have uncertainties that are roughly $20\,\%$ each. Additionally, overestimating the plasma potential results in slightly more accurate measurements, but the difference is typically $1\,\%$ to $2\,\%$.

LP I-V curves were modeled using the retarded electron current (eq. 2.13) and the accelerated electron current (eq. 2.11) for the thick sheath condition over a range of electron temperatures ($0.1\,\mathrm{eV}$ to $1\,\mathrm{eV}$). There was no averaging done for the analysis of this method.

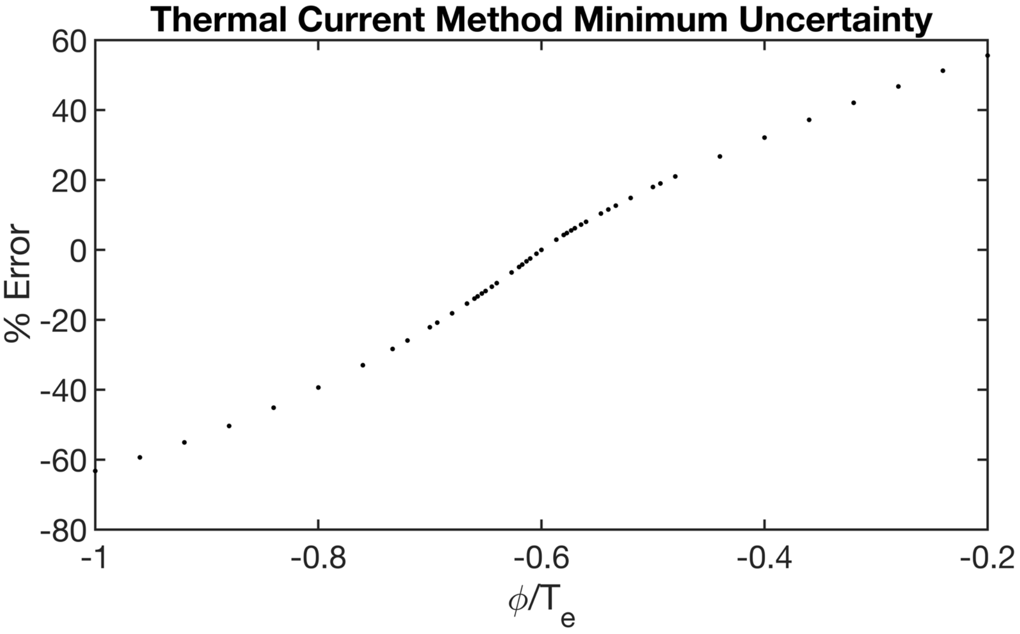

Figure C.14: Minimum uncertainty of the thermal current method as a function of the ratio between the probe potential and electron temperature.

C.6.2 OML Current Method

The OML current method analyzes the electron current at least $2T_e$ above the plasma potential using a model of the form

$$I_e = qA_pN_e\sqrt{\frac{k_BT_e}{2\pi m_e}}\beta\left(1+\frac{\phi}{T_e}\right)^\gamma \tag{C.38}$$

where β ranges from 1.02 to 1.13 depending on the probe radius to Debye length ratio [216]. γ also varies with this ratio where γ approaches 0 when the radius is much larger than the Debye length (a thin sheath approximation). For a thick sheath approximation, γ, would in theory, approach 0.5 and agree with eq. 2.11 in the thick sheath limit for large voltages. To determine the electron density, two methods are available: 1) a fitting algorithm and 2) a single point approximation. The procedure for the fitting algorithm is

1. Linearize eq. C.38 by taking the natural logarithm to both sides.
2. Fit a first order polynomial to the linearized form of eq. C.38. γ is the slope of the line. The intercept of the line provides the β parameter such that $\beta = exp(y_{int})/I_{therm}$.
3. Linearize eq. C.38 again by raising both the electron current by a power of γ^{-1}.
4. Fit a first order polynomial to the re-linearized form of eq. C.38. The density is then

given by

$$N_e = \frac{\sqrt{2\pi m_e}}{q^{\frac{3}{2}} A_p \beta} T_e^{\gamma - \frac{1}{2}} \alpha^{\gamma} \tag{C.39}$$

where α is the slope of the linearly fit line.

For the single point approximation, γ is again assumed to be 0.5, $\beta = 2/\sqrt{\pi}$, and $\phi >> T_e$ such that the electron density is approximated as follows

$$I_e(\phi) \approx \frac{2qA_pN_e}{\sqrt{\pi}} \sqrt{\frac{k_BT_e}{2\pi m_e}} \sqrt{\frac{q\phi}{k_BT_e}} \tag{C.40}$$

$$\implies N_e \approx \frac{\pi I_e(\phi)}{A_p} \sqrt{\frac{m_e}{2q^3\phi}} \tag{C.41}$$

C.6.2.1 Systematic Uncertainties

Due to the non-linearity of many of the sources of error, such as the choice of γ, an estimate of the error can be determined using a Monte Carlo scheme. The varied variables would be the plasma potential, the electron temperature, the electron current, the sourced voltage, the probe area, β, and γ.

For the single point method, the systematic uncertainty is

$$\sigma_{N_e} = \sqrt{\frac{m_e \pi^2}{2q^3}} \sqrt{\left(\frac{\sigma_{I_e}(\phi)}{A_p\sqrt{\phi}}\right)^2 + \left(\frac{I_e(\phi)\,\sigma_{A_p}}{A_p^2\sqrt{\phi}}\right)^2 + \left(\frac{I_e(\phi)\,\sigma_{\phi}}{2A_p\phi^{\frac{3}{2}}}\right)^2} \tag{C.42}$$

$$\sigma_\phi = \sqrt{\sigma_{V_{inst}}^2 + \sigma_{V_P}^2}$$

where the smallest source of uncertainty is due to the error in the probe area.

C.6.2.2 Minimum Uncertainty due to Method

The OML fit method requires both a large sheath relative to the probe radius, and to fit a sufficient number of points for biases greater than $2T_e$. Referencing fig. C.15a, ratios greater than 30 are sufficiently linear for any temperature above $0.1\,\mathrm{eV}$. Effectively, this can be thought of as a blurry boundary for current collection that is considered orbit motion limited, or "thick sheath". Figure C.15b, provides an example of log linearization for 3 sheath-to-probe radius ratios. When the current collection is undoubtedly in the OML region, a ratio of 100, applying a natural logarithm to both sides of eq. C.38 produces a clearly linear line. However, when the ratio is on the boundary of thin sheath current collection, $a/r = 3$, there is still clear curvature after attempting to linearize the current. LP I-V curves were modeled using the accelerated electron current (eq. 2.11) over a range of electron temperatures ($0.1\,\mathrm{eV}$ to $0.5\,\mathrm{eV}$), a range of a/r values that range from 3 to 100. There was no averaging done for the analysis of this method.

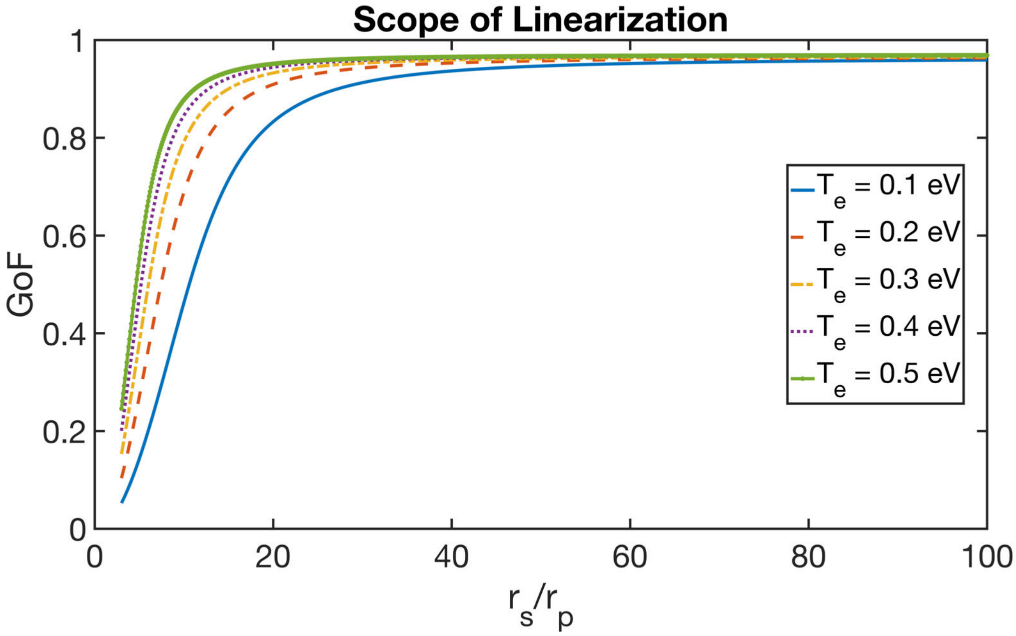

(a) Measure of linearity due to logarithmic linearization as a function of the ratio between the sheath and probe radii. A GoF of one is perfectly linear.

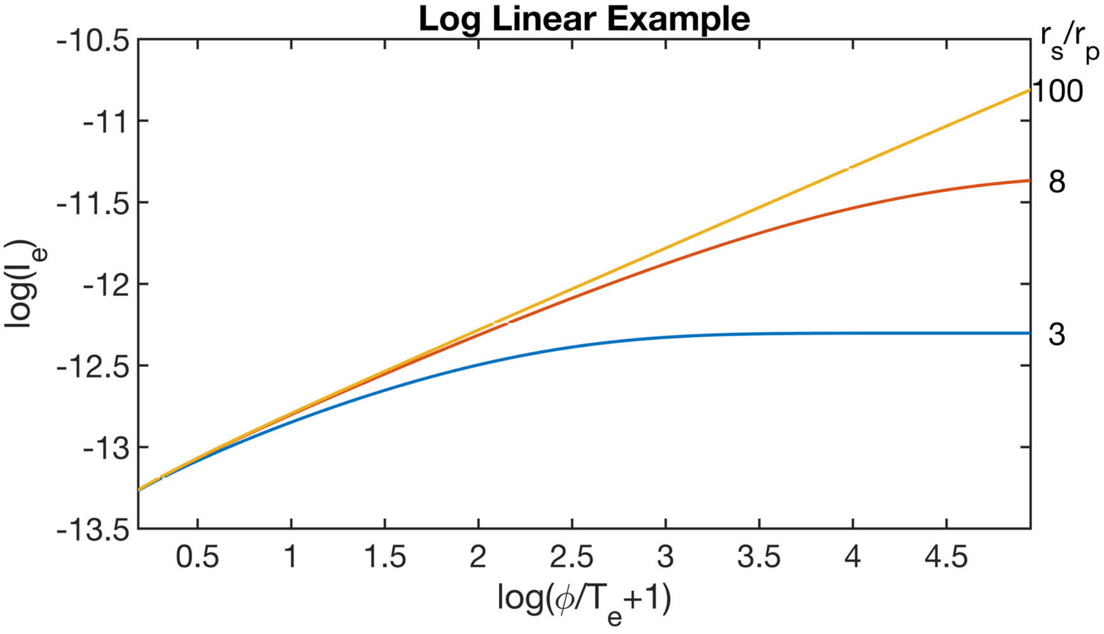

(b) Example of linearization for an accelerated electron current with an electron temperature of $0.5\,\mathrm{eV}$. When the sheath to probe radius ratio is too small, there is clear non-linear behavior at higher voltages.

Figure C.15: Linearizing electron saturation regime using natural logarithms.

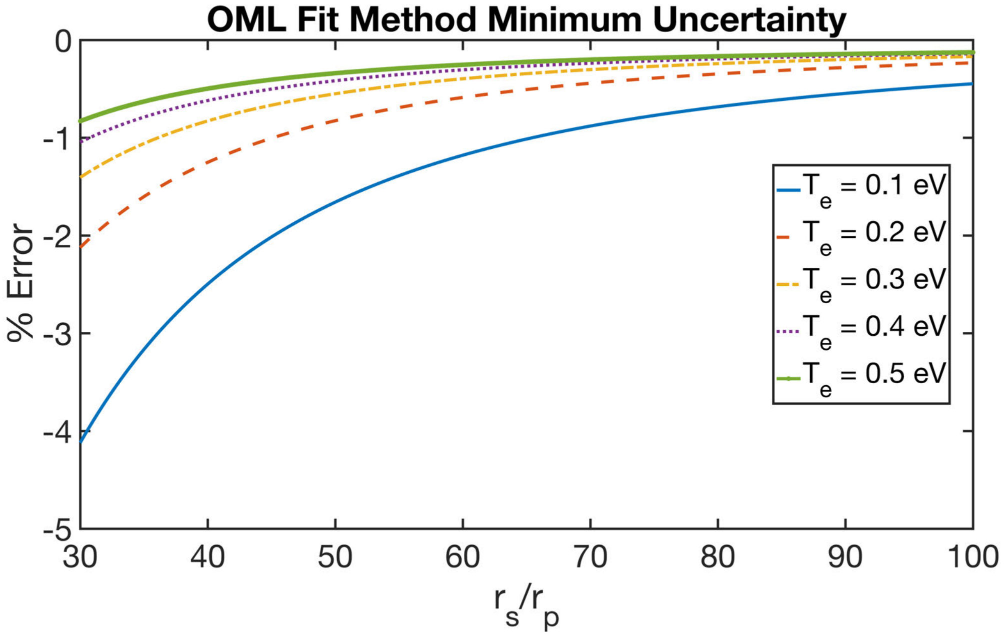

(a) Minimum uncertainty of the OML fit method as a function of the ratio between the probe potential and electron temperature.

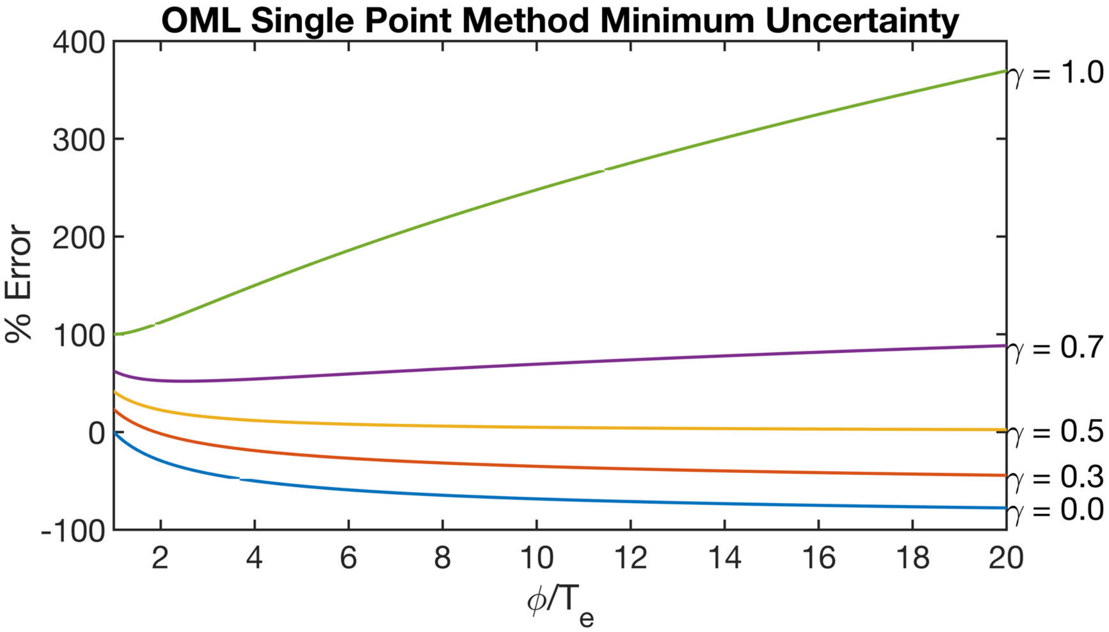

(b) Minimum uncertainty of the OML single point method as a function of the ratio between the probe potential and electron temperature.

Figure C.16: Minimum uncertainty for estimating electron density using an OML approximation.

From fig. C.16a, it clear that when properly applied, the OML fit method is incredibly accurate relative to other methods that are analyzed. At its most uncertain, the minimum percent error is $4\,\%$ and as the ratio increases, the minimum uncertainty asymptotically approaches 0 for all temperatures considered. However, both γ and β had to be determined from the logarithmic linearization to achieve the low percent errors. If a static β is chosen, the minimum uncertainty will be larger than the minimum uncertainties presented here. LP I-V curves were modeled using the accelerated electron current (eq. 2.11) over a range of electron temperatures ($0.1\,\mathrm{eV}$ to $0.5\,\mathrm{eV}$), a range of a/r values that range from 30 to 100. The calculated density was then compared to the density used to model the currents. As before, there was no averaging done for the analysis of this method.

As shown in fig. C.16b, the minimum uncertainty of the OML single point method has a complex relationship with the ratio between the probe potential and electron temperature and the actual value of γ. LP I-V curves were modeled using the accelerated electron current (eq. C.38) over a range of electron temperatures ($0.1\,\mathrm{eV}$ to $1\,\mathrm{eV}$), a range of γ values that range from 0 to 1, and $\beta = 2/\sqrt{\pi}$. The modeled current and its corresponding potential were then used to estimate the electron density using eq. C.41. There was no averaging done for the analysis of this method. When the probe potential to temperature ratio is 1, the effect of the attractive potential doesn't overtake random thermal motion, and so the electron density will always be overestimated. In this scenario, the amount of overestimation increases with γ where only $\gamma = 0$ has a nearly 0 percent error simply because the modeled current is a straight line whose value is exactly

$$I_e = qA_pN_e\sqrt{\frac{k_BT_e}{2\pi m_e}}\beta.$$

For all values of $\gamma < 0.5$, the minimum uncertainty decreases with increasing bias eventually underestimating the density for sufficiently large attractive potentials. At a ratio of 20, the range of percent error ranges from $24\,\%$ to $78\,\%$ for a range of γ values between 0.4 and 0 where the more accurate approximations are for values of γ that approach 0.5. When $\gamma = 0.5$, the minimum uncertainty when $\phi/T_e = 1$ is about $44\,\%$ and this uncertainty will asymptotically approach 0 as the potential increases (e.g. at $\phi/T_e = 20$, the minimum uncertainty is roughly $2\,\%$). Finally, for all values of γ greater than 0.5, the percent error curves will increase with greater accelerating biases; however, there is a local minimum in all curves corresponding to $\gamma > 0.5$. For example, when $\gamma = 0.9$, the local minimum exists at a potential that is $1.25T_e$, and when $\gamma = 0.6$, the local minimum exists when the potential is $5T_e$. Ultimately, the OML single point method is best used for reasonably large potentials relative to the electron temperature when γ is close to 0.5. Otherwise, the method can be used when the potential is equal to the electron temperature as long as $\gamma < 0.5$.

C.6.3 EEDF Method

Just as was done for electron temperature determination, the electron density can be obtained from the electron energy distribution function. However, while a fitting algorithm was used to calculated electron temperature, the electron density requires integration of the EEDF. As shown by *Sudit et. al.* the electron density is given by [216]

$$N_e = \int_0^\infty \frac{4}{qA_P}\sqrt{\frac{m_e\phi}{2q}}\frac{d^2I_e}{d\phi^2}d\phi \tag{C.43}$$

C.6.3.1 Systematic Uncertainties

To determine the systematic uncertainty of the EEDF integral method for electron density, the most straight forward approach is to use Monte Carlo methods. The probe area, measured current, and ϕ are all varied within their respective uncertainties and the electron density is calculated for each individual iteration. The error in the electron density is the the square root of the sum of squares of the standard deviation in electron density due to variations in each variable. The largest source of uncertainty is due to ϕ, whose uncertainty depends on both the sourced voltage and the error in the plasma potential.

C.6.3.2 Minimum Uncertainty due to Method

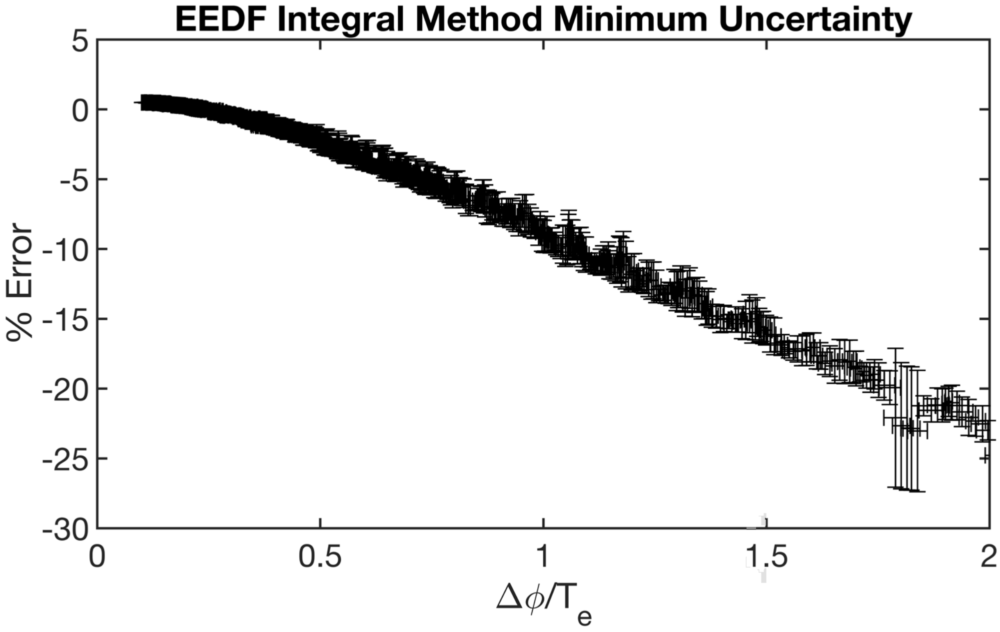

Figure C.17: Minimum uncertainty of the EEDF integral point method as a function of the ratio between potential step size and electron temperature.

As expected, a voltage step size that is less than or equal to $0.25T_e$ is necessary for proper application of the EEDF integral method (refer to fig. C.17). Above this limit, the integral method will increasingly underestimate the density, due to undersampling of the electron retardation regime. LP I-V curves were modeled using the retarded electron current (eq. 2.13) and the accelerated electron current (eq. 2.11) for the thick sheath condition over a range of electron temperatures ($0.1\,\mathrm{eV}$ to $1\,\mathrm{eV}$). The minimum uncertainty for both cases are then averaged using a moving average filter with a window size of $1\,\%$ of the total number of calculated percent errors. The error bars are calculated using a moving standard deviation filter with the same window size.

APPENDIX D

Retarding Potential Analyzer Analysis with Uncertainties

Here we present a full analysis of RPA sweeps that have been generalized for a non-magnetic, drifting plasma, in the absence of additional current sources such as secondary electron emission. The method detailed in this appendix can be programmatically applied.

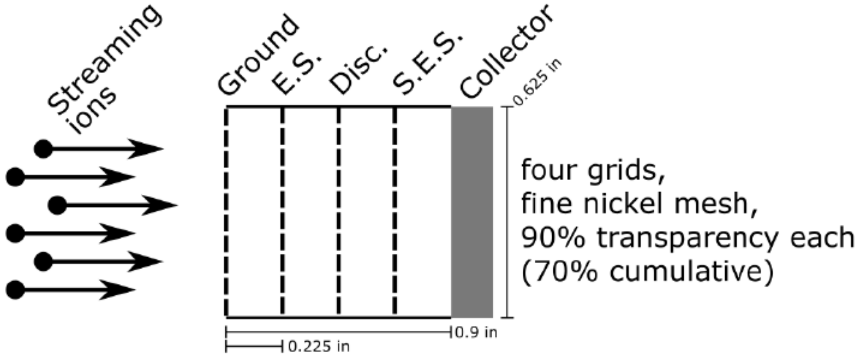

Figure D.1: Retarding potential analyzer mechanical drawing. Image adapted from *McTernan et. al.* [173, p. 3893].

The RPA used to study the plasma's ion energy distribution function is composed of four grids and a collector plate, as shown in fig. D.1. The first grid is the grounded grid, and it minimizes the effects of the internal electric fields of the RPA on the quasi-neutral plasma. The second grid, the electron suppression grid (E.S.), is biased negative of the plasma to reject any electrons, and ensure that only ions are collected by the collector plate. The E.S. grid is followed by the discriminator grid. This grid is biased from $0\,\mathrm{V}$ to a sufficiently positive potential such that the collected current is $0\,\mathrm{A}$. At this positive voltage, all ions are fully suppressed and the entire ion energy distribution function has been sampled similarly to how an electron energy distribution function is sampled using a Langmuir probe. The final grid is the secondary electron suppression (S.E.S.) grid. This is typically the most negatively biased grid in the set, whose function is to repel any secondary electrons emitted from the collector plate's surface due to ions colliding with the plate.

An RPA is crucial in understanding the energy distribution function of the ion population. While it isn't possible to determine the mass of the ions, it is possible to determine the ion drift velocity and temperature with known ion mass. In the case of multiple ion populations, an estimate of the magnitude of the contribution of each population to the total ion current can also be made.

Just like in appendix C, the method described in this appendix has two uncertainties: 1) the method's intrinsic uncertainty and 2) systematic uncertainties. The square root of the sum of squares of these uncertainties determines the total uncertainty for the method (eq. D.1)

$$\sigma_{Total} = \sqrt{\sigma_{method}^2 + \sigma_{systematic}^2} \tag{D.1}$$

Furthermore, the instrumental uncertainties affect all methods, as they are properties of both the measured current and the sourced voltage. A National Instrument's data acquisition system was used to measure the currents to the collector plate. A high voltage power supply in conjunction with a voltage divider was used to sweep the discriminator grid. The instrumental uncertainties of the measured current and sourced voltage are estimated to be $1\,\%$ of the value, such that

$$\begin{aligned} \sigma_{V_{inst}} &= V_{measured} * 1\% \\ \sigma_{I_{inst}} &= I_{measured} * 1\% \end{aligned}$$

A typical RPA analysis procedure broadly looks as follows:

1. Use a smoothing algorithm to minimize the effects of noise. A Savitsky-Golay algorithm is typically sufficient with a window size of $10\,\%$ to $15\,\%$ of the total number of points and a polynomial of order 4 [206, 207].
2. Adjust the discriminator bias by subtracting the ambient plasma potential. This shifts the reference from chamber ground to the ambient plasma.
3. Take the first derivative of the measured current with respect to the adjusted bias.
4. Normalize the derivative by its greatest peak.
5. Determine the bias at the highest peak; this is the ion drift energy of the main population.
6. Determine the full-width half maximum of the main ion peak to estimate the ion temperature.
7. Fit a normalized drifting Maxwellian model (eq. D.4) to the main peak. This validates the estimated ion temperature.
8. Use the unnormalized magnitude of the main peak to estimate the ion density this distinct population.

9. Search the first derivative at potentials below and above the primary peak for additional peaks. For instance, in the presence of charge exchange (CEX) ions, there will be a second peak at potentials below the primary peak, as long as the primary peak is due to a drifting ion population. A method of determining whether additional peaks exist would be as follows:
    (a) Reflect the normalized first derivative over the x-axis and add 1 to the full distribution. This converts any local minimum in the distribution, referred to as valleys, to local maximum in the reflected case.
    (b) Use a peak finding algorithm, such as MATLAB's *findpeaks* function [169], to find local maxima in the reflected derivative and their corresponding potentials.
    (c) If any valleys exist, search for peaks in the original normalized first derivative at potentials below the valley, if the valley exists at a potential below the main peak; and at potentials above the valley, if the valley exists at a potential above the main peak.
10. If a second peak exists, determine the potential of the peak.
11. Determine the full-width half maximum of the secondary ion peak and fit a drifting Maxwellian model to the peak to determine its ion temperature.
12. Use the amplitude of the second peak to estimate the ion density of this additional, distinct population.
13. Calculate the ratio of the ion density of each population to the total ion density. This is an estimate of how prominent each ion population is in the total ion distribution.

The magnitude of the unnormalized peaks can be used to estimate the ion density using the equation described by *Feng et. al.* [217], as shown in

$$N_i = -\frac{1}{q^2\eta A_p}\sqrt{\frac{\pi m_i k_B T_i}{2}}\left(\frac{dI}{d\phi}\right)_{Max} \tag{D.2}$$

where η is the transparency of the RPA (assumed to be 1 in this appendix). For this analysis, currents due to oxygen ions are modeled as if they are collected by a planar plate using eq. 2.7. Drifting ions have a drift energy of $5\,\mathrm{eV}$ and a temperature that ranges from $0.1\,\mathrm{eV}$ to $0.5\,\mathrm{eV}$. Charge exchange ions have an ion drift energy near $0.5\,\mathrm{eV}$ and an ion temperature that is half of the temperature of drifting ions (refer to discussion in section 5.3.2 for examples of IEDFs with two ion populations and how CEX attain non-negligible drift energies).

D.1 Single Peak Population

The single peak population will generally be the cleanest measured single and so the analysis method is relatively straightforward. The ideal measured current and first

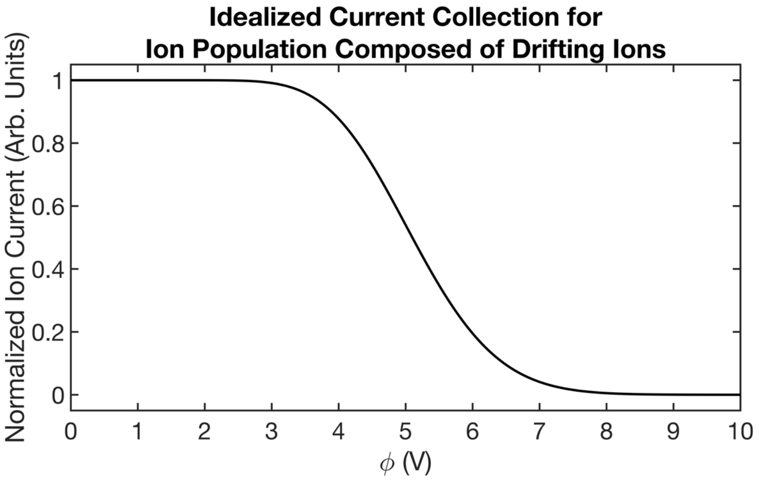

(a) Modeled ion current for an ion distribution composed of only oxygen drifting at $5\,\mathrm{eV}$.

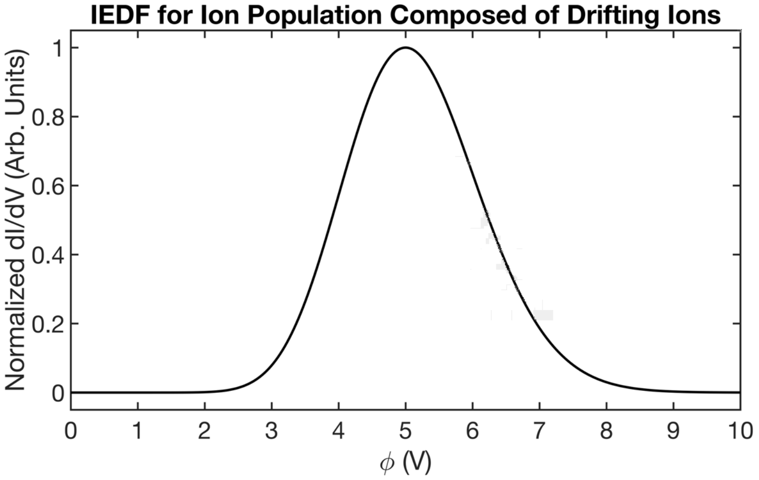

(b) Modeled ion distribution for singly ionized oxygen drifting at $5\,\mathrm{eV}$.

Figure D.2: Ideal I-V characteristics of RPA measurements of a single drifting ion species.

derivative for an oxygen ion drifting at $5\,\mathrm{eV}$ is shown in fig. D.2. In this scenario, the amplitude will always be one, as the normalization factor is the magnitude of the peak as determined by the fourth step in the procedure detailed above. The ion drift energy is then given by the potential that corresponds to the peak of the distribution. The only measurement that is left to calculate is the ion temperature. The full width half maximum (FWHM) of the normalized distribution can be used to estimate the ion temperature as follows

$$
\begin{aligned}
0.5 &= \exp\left(-\frac{m_i}{2qT_i}\left[\sqrt{\frac{2q\phi}{m_i}} - v_i\right]^2\right) \\
\log(0.5) &= -\frac{m_i}{2qT_i}\left[\sqrt{\frac{2q\phi}{m_i}} - v_i\right]^2 \\
\implies T_i &= -\frac{m_i}{2q\log(0.5)}\left[\sqrt{\frac{2q\phi}{m_i}} - v_i\right]^2 . \qquad \text{(D.3)}
\end{aligned}
$$

There are two potentials, ϕ, that satisfy the requirement for the full width half maximum of the distribution; therefore, the average of the estimated temperatures from both potentials should be used when possible. Furthermore, it is difficult to have a value at exactly 0.5 in the first derivative; in practice, it is best to use whichever potentials are closest to the 0.5 value and then use a nonlinear fitting algorithm to fit a peak-normalized drifting Maxwellian model to the top half of the distribution to obtain a more accurate ion temperature, shown in eq. D.4,

$$
I_{norm}\left(\phi\right) = A\exp\left(-\frac{m_i}{2qT_i}\left[\sqrt{\frac{2q\phi}{m_i}} - v_i\right]^2\right) \qquad \text{(D.4)}
$$

where A is the amplitude of the distribution and v_i is the ion drift speed in $\mathrm{m\,s^{-1}}$.

D.1.1 Systematic Uncertainties

The systematic uncertainties of the ion drift speed and temperature have a non-linear relationship with the underlying instrumental uncertainties. Therefore, a Monte Carlo scheme where the plasma potential, measured currents, and sourced voltage are varied within their respective uncertainties is required. The total error is then the square root of the sum of squares of the standard deviations of the calculated temperature due to uncertainties in the measurements.

D.1.2 Minimum Uncertainty due to Method

Figure D.3 shows the minimum uncertainty of ion property measurements as a function of bias step size normalized by the ion temperature. The minimum uncertainty is obtained by averaging the percent errors for every ratio. The error bars are the standard deviation for each ratio. The main source of error for a single drifting ion distribution function will not come from uncertainties in the method, but rather systematic uncertainties, as the minimum uncertainty in the model will be below $3\,\%$ for both temperature and drift speed. If only the charge exchange ions are modeled, the uncertainty in drift speed peaks at roughly $15\,\%$, but is below $5\,\%$ when the step size is a quarter of the ion temperature. Similarly, the

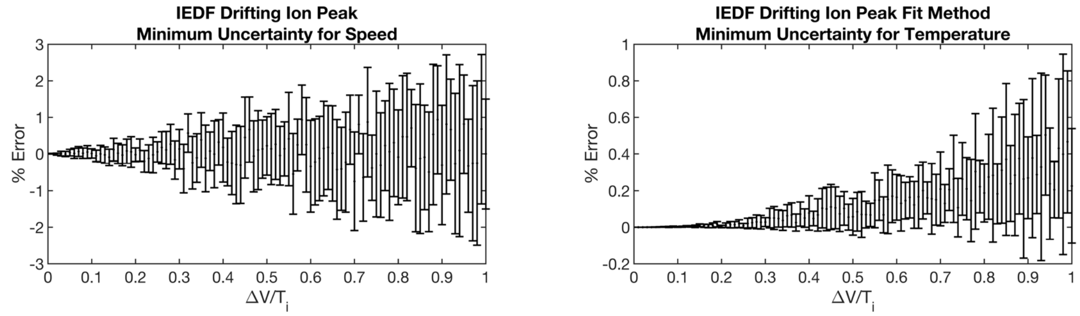

(a) Minimum uncertainty for the drift speed measurement of a single drifting population IEDF.

(b) Minimum uncertainty for the temperature measurement of a single drifting population IEDF.

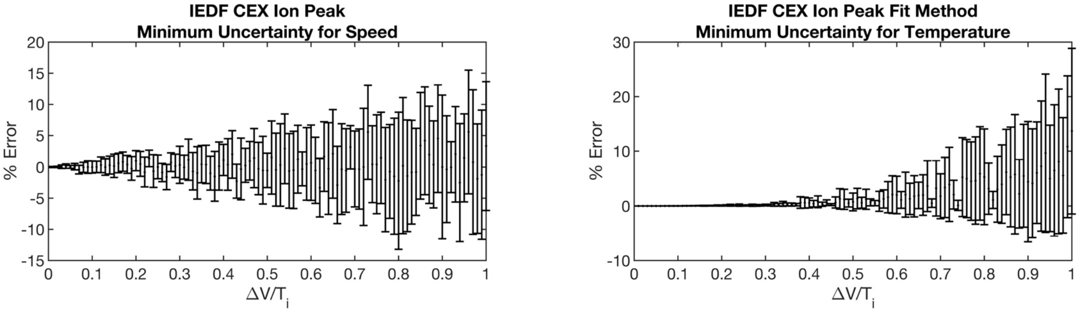

(c) Minimum uncertainty for the drift speed measurement of a single CEX population IEDF.

(d) Minimum uncertainty for the temperature measurement of a single CEX population IEDF.

Figure D.3: Minimum uncertainty of ion properties measured by an RPA when a single ion population is present.

ion temperature estimates are more uncertain for CEX ions than drifting ions. When the voltage step size is half of the CEX ion temperature, the minimum uncertainty peaks at $3\,\%$, and the minimum uncertainty is below $1\,\%$ when the step size is a quarter of the ion temperature. Therefore, the model presented in eq. D.4 has more difficulty fitting the ion distribution for ion populations of lower drift energies.

D.2 Mixed Ion Distribution

An example of the possible current and first derivative of collected ions due to an ion population that is composed of $75\,\%$ drifting ions and $25\,\%$ charge exchange ions is shown in fig. D.4. In reality, these curves will vary greatly depending on individual ion temperatures, drift speeds, and the ion population's prominence in the total ion distribution. The first drop in in the current shown in fig. D.4a is mainly due to the CEX ions being discriminated and the second drop is due to the main drifting population being discriminated. In the first derivative (see fig. D.4b), there are two distinct peaks corresponding to CEX ions and a main drifting population with a valley in between the two peaks. The relative magnitude of each peak does not correspond to the fraction of the composition they make up in the total current due to their differences in ion temperature (see discussion in appendix D.2.2).

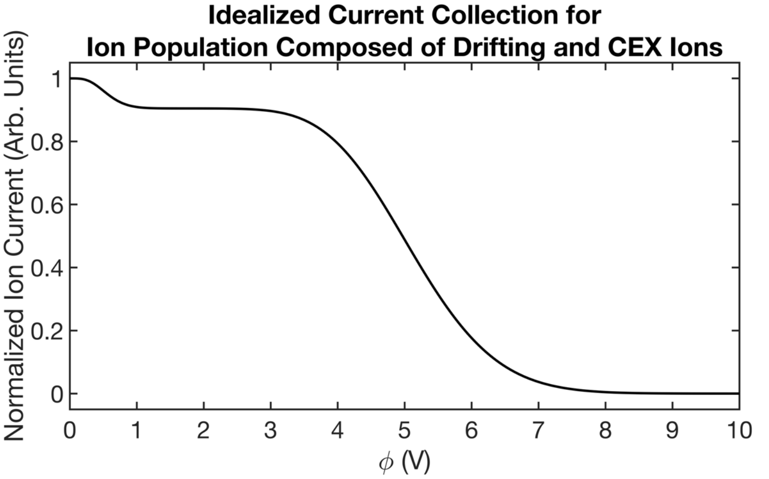

(a) Modeled ion current for an ion distribution composed of a drifting Maxwellian population mixed with a CEX ion population.

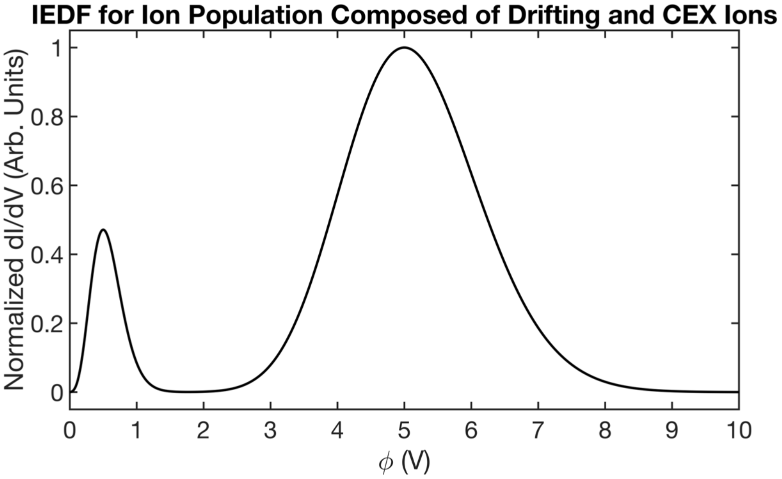

(b) Modeled first derivative for an ion distribution composed of a drifting Maxwellian population mixed with a CEX ion population.

Figure D.4: Ideal I-V characteristics of RPA measurements of a drifting ion species and a smaller CEX ion population.

D.2.1 Systematic Uncertainties

The systematic uncertainties of the ion drift speed and temperature have a non-linear relationship with the underlying instrumental uncertainties. Therefore, a Monte Carlo scheme must be performed where the plasma potential, measured currents, and sourced voltage are varied within their respective uncertainties. The total error is then the square root of the sum of squares of the standard deviations of the calculated temperature due to uncertainties in the measurements.

D.2.2 Minimum Uncertainty due to Method

To begin, for this discussion, ”amplitude” is the fractional percent of the ion density that corresponds to a particular population of ions. For instance, the amplitudes of an ion population whose density is $25\,\%$ CEX ions and $75\,\%$ drifting ions would be 0.25 and 0.75, respectively. Using this definition, the magnitudes of the peaks in the full distribution do not correlate with the percentage of the ion current that corresponds to the individual ion population. The ratio of temperature between the charge exchange ions and the main drift population drastically affects the magnitudes of the peaks relative to one another. As shown in fig. D.5a, the minimum uncertainty of the amplitude is related to the ratio of CEX and drifting ion temperatures. The smaller the ratio, the more uncertain the the estimates of the amplitude become. When the CEX ion temperature is a factor of 100 less than the main drift species, the average uncertainty in the amplitude of the main drift population approaches $75\,\%$ underestimation, while the uncertainty of the amplitude for CEX ions approaches $150\,\%$. Therefore, both the magnitude of the peaks and the individual ion temperatures must be taken into account to determine the amplitude of each ion population. Using eq. D.2, the individual densities of each population can be calculated and the amplitude would then be the ratio between the individual ion density and the total ion density, shown here as

$$A_j = \frac{N_j}{\sum_{j=1}^{N} N_j}, \tag{D.5}$$

where A_j is the amplitude of the ion population, N_j is the ion density of the ion population, and N is the total number of distinct ion populations, typically 1 or 2 for this work, depending on the prevalence of the CEX ion population. Figure D.5b shows the calculated amplitudes using eq. D.5 and is the proper method to use, as the minimum uncertainty is approximately zero regardless of temperature ratio. Even when the potential step size is on the order of the CEX ion temperature, the minimum uncertainties of the amplitudes are roughly $2\,\%$ (refer to fig. D.5c). Therefore, the uncertainties of the amplitudes will be dominated by systematic uncertainties due to the error of the measured current and changes in the distribution due to filtering the data.

When analyzing the peaks for ion drift speed and ion temperature, two cases were studied: 1) a case where the ion distribution is originally $25\,\%$ CEX ion and $75\,\%$ drifting ions and 2) a case where the ion distribution is originally $50\,\%$ CEX ion and $50\,\%$ drifting ions. Figures D.6 and D.7 demonstrate the minimum uncertainties for various ion speeds and temperatures, which are plotted as a function of voltage step size normalized by the CEX ion temperature. The minimum uncertainty is obtained by averaging the calculated percent errors at each ratio and the error bars are the standard deviation. The peak uncertainty for CEX ions reaches $15\,\%$ regardless of whether it was the main peak (fig. D.7a) or the secondary peak (fig. D.6c). The uncertainty in the ion drift speed for a drifting Maxwellian ion population remains below $2\,\%$. In terms of temperature estimates, for drifting ions, the minimum uncertainty in the temperature reaches a maximum of roughly $10\,\%$. Similarly, the minimum uncertainty for the temperature measurements of CEX ions remains near $10\,\%$ when it is the secondary peak and $5\,\%$ when it is the

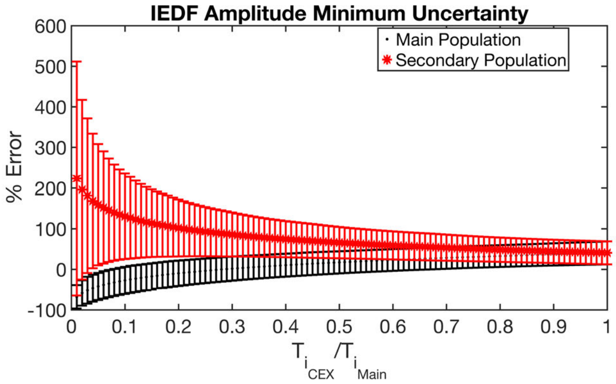

(a) Minimum uncertainty of the measured amplitudes of the ion distributions using only the relative size of the amplitudes as a function of temperature ratios and preset amplitude.

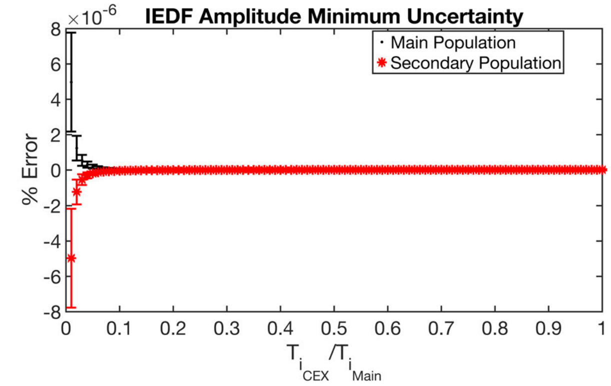

(b) Minimum uncertainty of the measured amplitudes of the ion distributions using the ratio of calculated densities as a function of temperature ratios and preset amplitude.

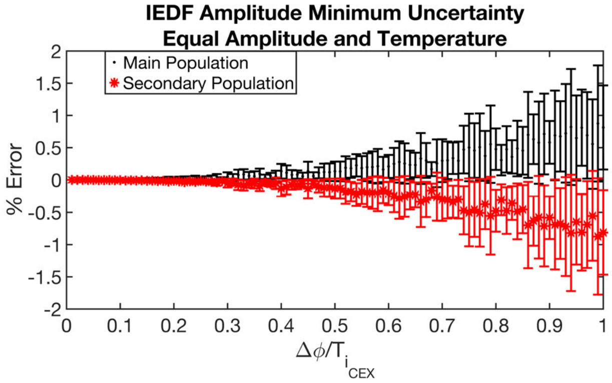

(c) Minimum uncertainty of the measured amplitudes of the ion distributions using the ratio of calculated densities as a function of voltage step size normalized by CEX ion temperature.

Figure D.5: Minimum uncertainty of amplitude of distribution under various constraints.

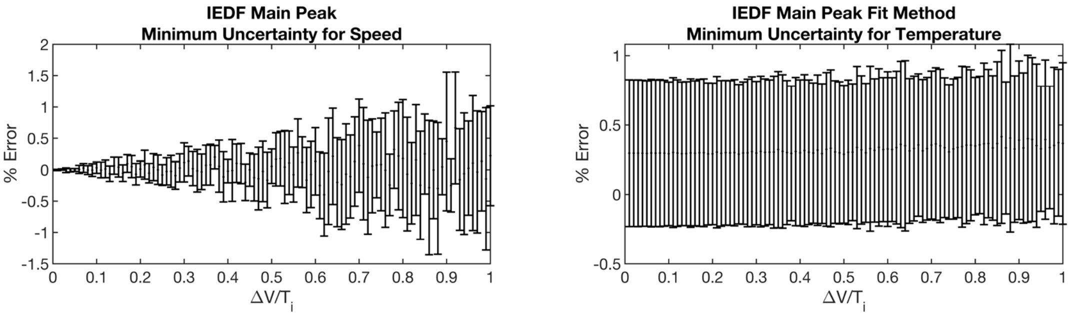

(a) Minimum uncertainty of ion drift speed of the main ion population.

(b) Minimum uncertainty of ion temperature of the main ion population.

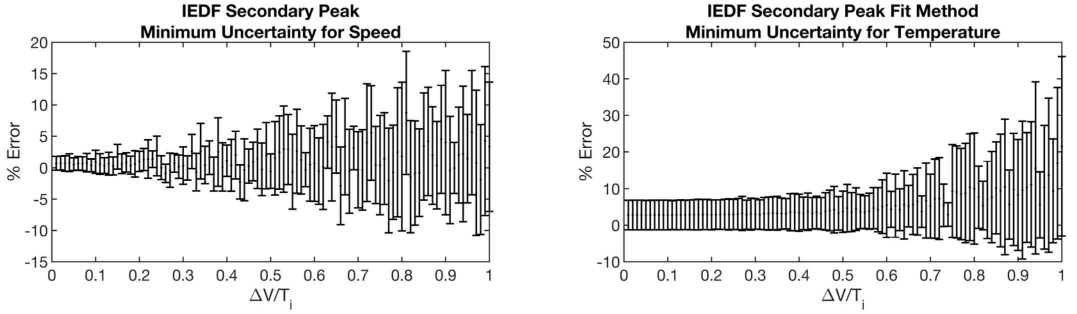

(c) Minimum uncertainty of ion drift speed of the secondary ion population.

(d) Minimum uncertainty of ion temperature of the secondary ion population.

Figure D.6: Minimum uncertainties of the properties of each ion energy distribution functions composed of $25\,\%$ CEX and $75\,\%$ main population.

primary peak, at voltage step sizes that are less that half the ion temperature of the CEX ion population.

There is some interdependence between the uncertainties of each ion population due to the fact that as the CEX ions are being discriminated, the very low-energy tail of the drifting ions are also being discriminated. As a result, the IEDF of the CEX ions are being affected by low-energy tail of the drifting Maxwellian. Similarly, the high-energy tail of the CEX IEDF affects the low energy portion of the drifting Maxwellian IEDF. A possible solution to the issue of cross-contamination is to limit the fitting bounds on the side where the distribution mixing occurs. For instance, in the case of fitting CEX ions, the upper bounds of the fit would be restricted by some potential below the valley.

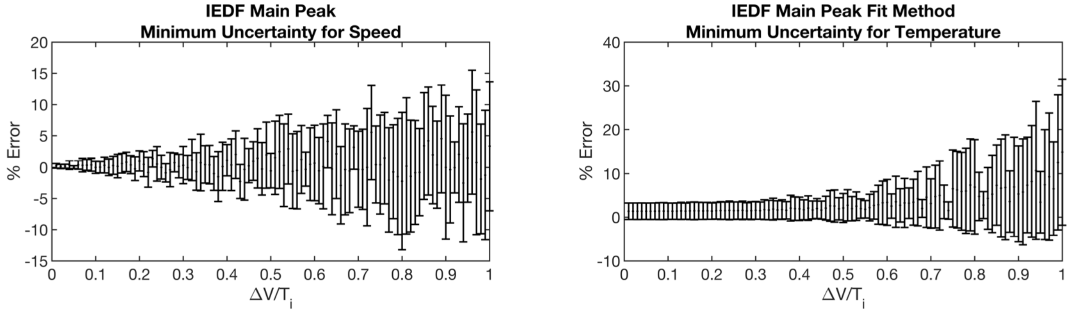

(a) Minimum uncertainty of ion drift speed of the main ion population.

(b) Minimum uncertainty of ion temperature of the main ion population.

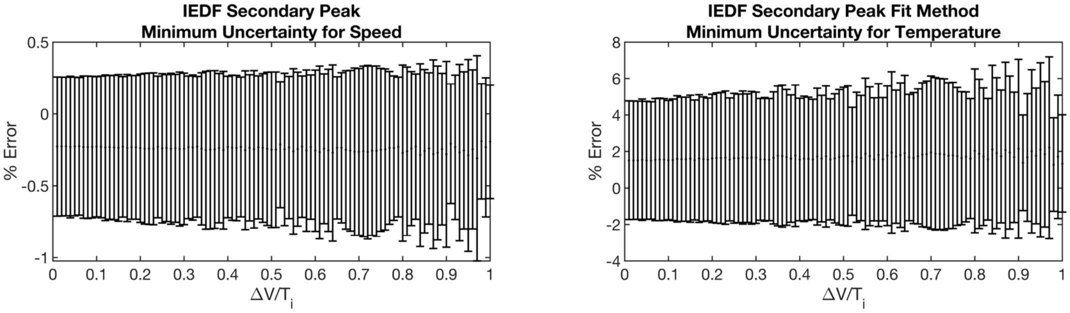

(c) Minimum uncertainty of ion drift speed of the secondary ion population.

(d) Minimum uncertainty of ion temperature of the secondary ion population.

Figure D.7: Minimum uncertainties of the properties of each ion energy distribution functions composed of $50\,\%$ CEX and $50\,\%$ main population.